DISSERTATION

CRYO-ELECTRON MICROSCOPY OF CLONEABLE INORGANIC NANOPARTICLES

Submitted by

Bradley Forrest Guilliams

Department of Chemistry

In partial fulfilment of the requirements

For the Degree of Doctor of Philosophy

Colorado State University

Fort Collins, Colorado

Fall 2024

Doctoral Committee:

Advisor: Christopher J. Ackerson

Justin Sambur
Debbie Crans
Tim Stasevich

ABSTRACT

CRYO-ELECTRON MICROSCOPY OF CLONEABLE INORGANIC NANOPARTICLES

Our understanding of biology is best understood through direct, empirical measurements of biomacromolecules and biological systems. The functions of proteins are directly linked to both their structure and their intracellular organizations. Single particle cryo-electron microscopy has revolutionized modern structural biology by enabling the structural determination of proteins and protein-complexes in purified samples without the need to form large crystals as required by X-ray crystallography. With single particle cryo-EM, atomic and near-atomic resolution structures are now routine which offer insight into the functions of biomacromolecules. While these insights are invaluable, there is increasing momentum for integrative structural biology which aims to accomplish structural determination of biomacromolecules in their cellular, tissue, or organismal context. There remains a grand challenge in biological imaging where biological materials have low innate contrast. Cloneable contrast labels that impart contrast to discrete protein densities do not reliably exist for cryo-electron microscopy. In contrast, fluorescent proteins are reliable and routine for localizing fluorescent protein / protein of interest genetic fusions in visible-light microscopies. We have proposed and developed intracellularly synthesized inorganic nanoparticles called ‘cloneable nanoparticles’ as a solution to this grand challenge. Cloneable nanoparticles are inorganic nanoparticles, synthesized by a protein/peptide (or combination thereof) which controls and defines the properties of the inorganic nanoparticle. Here we have defined the cloneable nanoparticle paradigm and described the development of a cloneable selenium nanoparticle. Further, we show the application of the cloneable selenium nanoparticle as a cloneable contrast label for biological electron microscopy and correlative light-electron microscopy and detail

progress towards adapting the cloneable selenium nanoparticle for use in cryo-electron tomography. With the aim to later expand cloneable nanoparticles to include a myriad of orthogonal cloneable contrast labels (analogous to different colored fluorophores), and to gain understanding about enzymatic nanoparticle synthesis, a single particle cryo-EM study is on-going. Lastly, we have shown the application of directed evolution for cloneable nanoparticles, suggesting that this is a viable path, alongside rational protein design, towards developing future cloneable nanoparticle cryo-electron microscopy labels.

ACKNOWLEDGEMENTS

When I reflect on my PhD, it looks a lot different from what I imagined. I never could have anticipated the personal growth over such a short period of time. Ultimately, there are many people throughout my life that have helped bring me to where I am today. Below, I wish to thank some of them in what is a comparatively small selection of words in a ridiculously long document representing some of the science I have been a part of in the last 4 years.

None of this would have been possible without my adviser Prof. Chris Ackerson. I have immense respect for Chirs and cannot speak highly enough about him as a mentor and as a human. I chose to come to Colorado State University largely to work for Chris with whom I share a very similar scientific philosophy. I have greatly enjoyed working for and working with Chris—so much so that I am going to continue working with him as long as he'll have me around. Hopefully soon, we'll have a new Cryo-EM facility to extend the lab's scientific playground. It's been great getting to know Chris and his partner Meg outside the lab too; this summer we all got to spend a relaxing day together in Morocco ahead of a conference in Barcelona.

Alex Hendricks was one of the first people I met at CSU and I later became his lab-mate in the Ackerson lab. If you know anything about Alex, you'll know that he's really good at getting you to look at things from a different perspective. Alex has been my biggest mentor after Chris and has helped me grow as a person more than he realizes. I always admired his writing and I've done my best to translate what I've learned into my own writing (which as you'll see later, still needs some work). He's someone I consider a good friend, and I continue to learn from him.

While Scott Compel and I never overlapped in the Ackerson lab, he was another very important mentor for me and someone that I am also glad to call a friend. He's one of the most charismatic and humble scientists that I know, and I respect Scott a great deal.

The Ackerson lab has been a great place to grow as a human and do science (in that order). I think the culture and people in the lab exist in a way that prioritizes making good humans before good scientists—and there are some truly excellent scientists in the lab and among the alumni. While Alex and Scott had major impacts on my life as mentors, there are many other past and present lab members with whom I've had countless positive experiences with.

A big thanks to Olve Peersen and Nancy Levinger for many thoughtful conversations throughout the last few years—and hopefully many more! I appreciate your honesty and curiosity—both things that I hold as core values.

I've had a great time working with Roy Geiss, Rebecca Miller, and Karolien Denef. It was Roy who taught me how to use an electron microscope—the scientific instrument that currently holds my obsession and serves as the lens through which I view many scientific questions. It was through Rebecca and Karolien that I learned to appreciate an alternative career path in science, one supporting shared use research instrumentation. Working with Roy, Rebecca, and Karolien has led me down the career path I find myself on now (and is one that I enjoy).

When I met Charlie Sither, I was a 17 year old kid in my first week of organic chemistry lab. Charlie was my first scientific mentor in a way. He had returned to WCU for a graduate degree (and for some reason I still don't quite understand) and was stuck with me as a lab partner. Sometime after Charlie (to no one's surprise) helped me through organic chemistry lab, we became roommates. At some point, he recommended me for a research job with Brian Byrd and Scott Huffman—who would later become co-advisers for my Chemistry M.S. Brian and Scott taught me how to do science and helped to prepare me for the world of science after graduating. I have many great anecdotes about Scott—but most of those are probably best left out of press. Scott would

joke that by the time I started my PhD he would have gotten me to be ‘almost useful’ as a researcher—emphasizing the immense learning curve that is science.

During my time at WCU, I found community working at Motion Makers bicycle shop. Kent, Marla, Larry, Simon, Sam, Kathy, and Johnny ‘Ray’ Hicks, all helped me to find myself as a human following many years of mental health struggles growing up. With you all, I was able to call Western North Carolina my home.

One of the biggest differences from my expectations about my PhD was just how much I enjoyed working with other people after considering myself very introverted for a long time. Working with and getting to know other people has been one of the best parts of my PhD. The impact of scientific friends and collaborators cannot be understated and listed here are just a few: Garry Morgan, Erik Hartwick, Kasahun Neselu, Eugene Chua, Ed Eng, Savic Serbynovskyi, Christina Zimanyi, Jake Johnston, Susan Tsunoda, Lauren Young, Laurel Haines, Bridget Carragher, Clint Potter, David Agard, Dave Bushnell, Reza Paraan, Julia Peukes, Bisco Hill, Michael Elbaum, Caitlyn McCafferty, Michelle Fry, Yuliia Mironova, Rasmus Jensen, Hamish Brown, Florian Fäßler, Emmanuel Smith, Stefan Huber, Cathy Spangler, Elissa Moller, Chris Russo, James Streetley, David Bhella, Gabriella Ruiz, and many more that I’ve had the pleasure of getting to know. Science is more fun when it’s shared with others.

Thanks to Mr. McCaffrey who gave me a second chance when I needed one.

Thanks to Erick for helping me to appreciate life’s imperfections through beautiful art.

I can’t finish this without thanking my family and friends. To my Mom, Dad, Steve, my brother Stephen, my cousin Phillip, and the rest of my family—thanks for your unwavering support and love. To my best friends Ian and Sabari—love you guys, thanks for all of the adventures and “hiking.” Can’t wait to see what stupid hat you got for me this time.

To my wife Hannah—thanks for agreeing to come to Colorado with me 2 weeks after we started dating and for actually moving here less than 2 years after that. Life with you is so much fun and I’m so glad we get to keep building our life together, I love you.

In loving memory of Uncle Wesley, Uncle Danny, Ms. Arnold, and D.O.G.

TABLE OF CONTENTS

CHAPTER 1: BACKGROUND AND SIGNIFICANCE

1.0 Synopsis

Over the course of the last several years, I have had the utmost pleasure of being a part of a variety of scientific projects, frequently lending my learned skills as an electron microscopist to make direct observations of both biological and inorganic systems. This dissertation represents a summation of some of the work I have contributed to (in-part or in-whole) related primarily to adapting cloneable nanoparticles as cloneable contrast labels for electron microscopy. Cryo-electron microscopy is an incredibly powerful imaging modality that currently lacks the contrast tools to take full advantage of the technique when applied to biological systems. It is through this lens that I approached the projects presented here-in.

1.1 Chapter Summaries

The first chapter introduces the cloneable nanoparticle platform and provides background necessary to understand the significance of its implementation. While recent advances in fluorescence microscopy with cloneable fluorescence proteins and super-resolution microscopy present significant advances for cellular imaging, fluorescence remains fundamentally limited in terms of what can be seen inside the cell. With fluorescence microscopy, only the cellular components labeled with fluorescent tags are resolved while the remainder of cellular components (~99% of components) is imaged at diffraction limited resolutions. Electron microscopy presents the highest resolution imaging technique for biological imaging. While electron microscopy is capable of atomic resolutions across an entire image of cellular components, it lacks a widely-applicable toolset for providing contrast to specific biomacromolecules of interest—analogous to cloneable fluorescent proteins. Cloneable nanoparticles are presented as a solution to this problem.

The second chapter is adapted from a published review article describing cloneable inorganic nanoparticles—our labs' proposed toolset for adding contrast to biological electron microscopy. In this review, cloneable inorganic nanoparticles are defined and discussed in greater detail. Here, the cloneable nanoparticle paradigm is defined through telling the story of the cloneable selenium nanoparticle (cSeNP). The cloneable nanoparticle system is analogous to traditional inorganic particle synthesis with ligands, reductants, and inorganic cations—peptides, enzyme-cofactor pairs, and dietary or supplemented metal(loid) ions, respectively. In brief, after isolating glutathione reductase-like metalloid reductase (GRLMR) from a microorganism thriving in seleniferous soil in the Colorado mountains, it was characterized and modified for use as a cloneable contrast label for biological electron microscopy.

In the third chapter, the cloneable selenium nanoparticle is used as an intracellular cloneable contrast label for multiple imaging modalities including electron tomography, correlative light-electron microscopy (CLEM), and X-ray tomography. Here, the cSeNP is evaluated in a bacterial model system using the filamenting protein FtsZ. This represents the first application of cloneable nanoparticles as an imaging tool and serves to highlight their potential as next-generation contrast tools for biological electron microscopy. It also unveils work demonstrating that in addition to being electron dense, the cloneable selenium particle can be modified to be a fluorescent quantum dot. This 'cloneable quantum dot' can be used as a single tag to provide contrast in electron microscopy and in fluorescence microscopy enabling correlative light and electron microscopy with a single cloneable contrast label.

The fourth chapter presents an on-going project using single particle cryo-electron microscopy to determine a near-atomic resolution (~3 Å) structure for GRLMR. An empirically determined structure of GRLMR will enable a more thorough investigation of structure-function

relationships. The on-going work will enhance rational protein design efforts to improve the cloneable nanoparticle platform and will inform library design for directed evolution experiments. Lastly, this project includes imaging selenium and NADPH bound within GRLMR which (alongside future work) will help to us understand enzymatic nanoparticle growth.

In the fifth chapter, continued efforts to adapt the cloneable selenium nanoparticle for cryo-electron tomography are presented in another on-going project. Progress adapting the sample preparation workflow is shown alongside some promising preliminary data. Challenges with this project are presented and discussed in detail. Adjacent and future work adapting cloneable nanoparticles as cryo-CLEM labels are also discussed which will address many of the discussed challenges.

In chapter six, metal(loid) substrate specificity is evolved by directed evolution of GRLMR. By using different selective pressures, laboratory enzyme evolution can change or add new qualities to a protein. This paper represents the first instance of changing the substrate specificity of an enzyme with respect to an inorganic (metal[loid]) substrate. Through directed evolution, enzyme activity was modified to favor selenite while reducing activity towards GRLMR's native substrate. It is through directed evolution (alongside computation) that we envision expanding our toolbox of cloneable contrast tools for electron microscopy—in the same way that fluorescence microscopy has access to a suite of different colored fluorescent proteins. With a toolbox of contrast tools, multiple biomacromolecules of interest can be simultaneously co-localized.

Finally, chapter seven reflects on the story of cloneable nanoparticles as cloneable contrast labels and looks towards the future of the platform.

1.2 Background - Imaging

In biology, seeing is believing. Contrast is what distinguishes an object from its' background and allows humans and animals to make direct observations in their environments with sight. Imaging at all scales enables scientists to make direct, empirical observations which are fundamental to advancing our understanding. These direct observations not only serve to generate data, but also to allow for unique interpretations which inspire new research and thus new discoveries. There is no ubiquitous imaging tool for making direct observations across the massive length-scales encapsulated by biology. Fortunately, there are many scientific disciplines, which together, make direct observations of biological materials across many length-scales.

For over 100 years, chemistry has enabled biological imaging by adding contrast to biological features. Beginning with German chemists who noticed that different clothing dyes highlighted different biological features and later to antibodies that can deliver contrast to specific macromolecules within a cell, scientists have been working on the so-called 'contrast-problem' for a long time. Namely, biological materials are generally comprised of the same atomic elements (e.g., carbon, oxygen, nitrogen) in relatively similar amounts which results in limited innate contrast under the lenses of an optical microscope. For visible-light microscopies, different colored dyes add contrast to regions of interest and are collected as different colors at the detector. For electron-based microscopies, electron dense materials can be used to add contrast to regions of interest where electron dense material interacts more strongly with the incident electron beam. In figure 1.1, electrons passing through the biological sample (e.g., protein of interest [POI] or cell) are weakly scattered and reach the detector largely unchanged while the electron-dense material scatters the incident electrons at high angles. An electron dense tag within a biological sample can thus highlight specific biological features by proximal correlation (Figure 1.2).

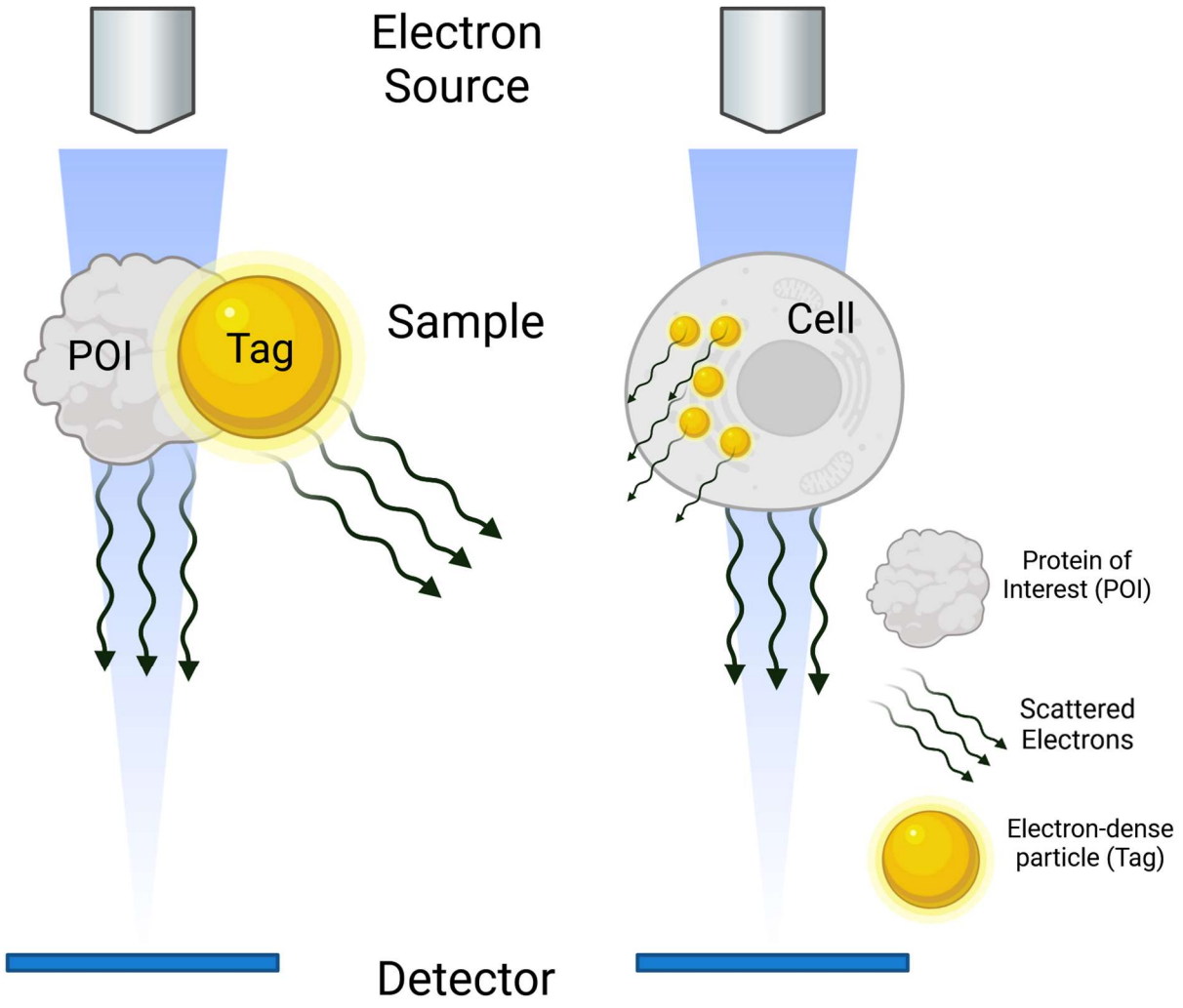

Figure 1.1. *Biological materials such as a protein of interest (POI) or a cell do not interact strongly with the electron beam, leading to low contrast. Whereas electron dense-particles (Tag) scatter electrons in the electron beam strongly, leading to high contrast with respect to biological materials.*

For visible light microscopes, dyes can add color to specific *regions* of a cell or tissue—such as staining the membranes red or the nucleus blue—while leaving the remainder of the background uncolored - creating contrast. Cloneable fluorescent proteins represent a toolbox of 'tags' to mitigate the contrast problem for visible light microscopy of biological materials. With tags such as green fluorescent protein (GFP) and its derivatives, contrast with known optical properties can be attached to a specific intracellular *molecule* of interest.[1,2] Simultaneously,

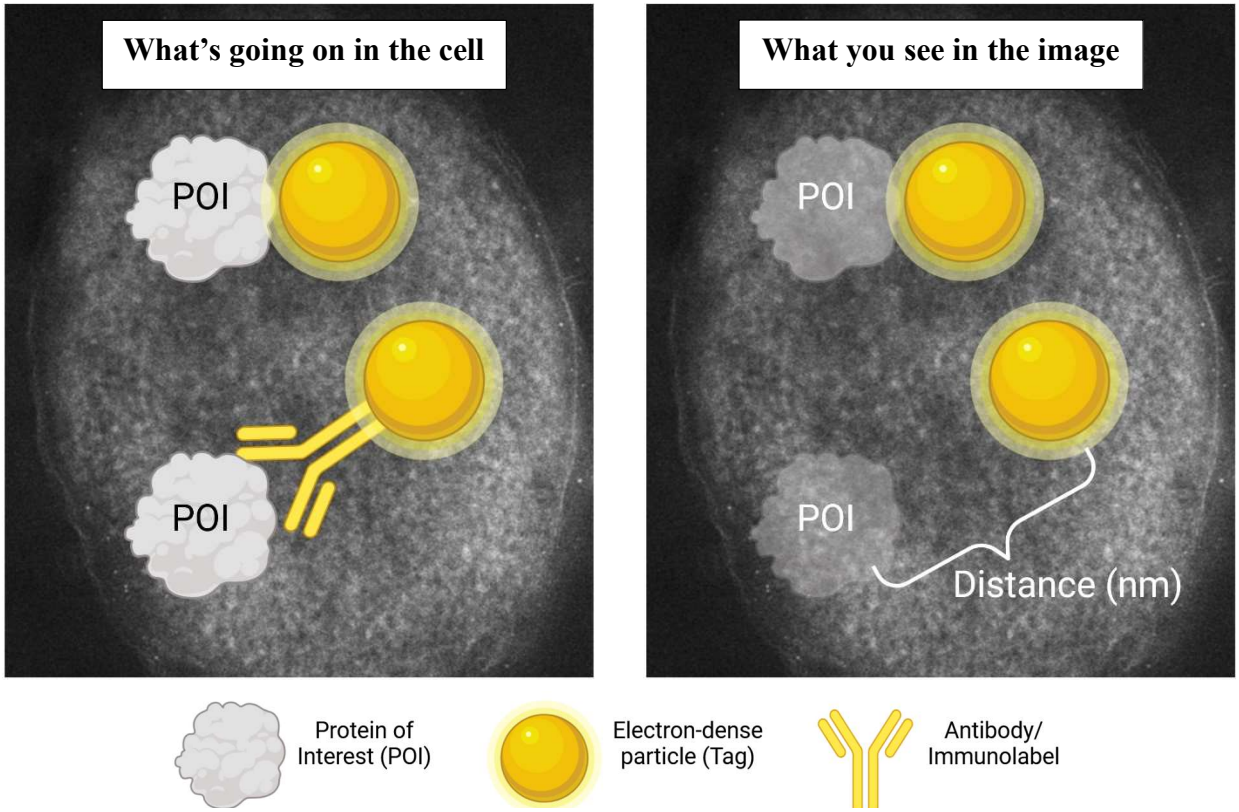

Figure 1.2. *Tags enable protein visualization by proxy. The left panel represents what is going on in the cell—two proteins of interest (POI)s are associated with electron-dense particle tags. In the right panel, the electron-dense particle tags are visible which enable the localization of the POIs by proximity to the easily identifiable tag. In this instance, the antibody/immunolabel represents one way to attach a tag to a POI; size of the antibody displaces the tag from the POI by a measurable distance related to the size of the antibody.*

cloneable fluorescent tags address the challenges with delivering fluorophore-antibody conjugates intracellularly.

Cloneable fluorescent tags have helped to answer many questions in biology and are especially good for elucidating dynamic interactions or macromolecular movements within cells because they can be visualized without needing to immobilize the system. However, visible-light microscopies are fundamentally limited in resolution by the wavelength of light to ~100 nm which serves as the illumination source for imaging (e.g., de Brogelie wavelengths).[3] Recent advancements in super-resolution fluorescence microscopy have pushed this resolution to ~10 nm, but this resolution is only for the fluorescent tag.[4] Everything else in a cell remains resolution-

limited. There is, however, a much better toolbox available for fluorescence microscopies than there is for electron microscopies. It is important to understand that fluorescence microscopies and electron microscopies are *complimentary* techniques which each have their strengths and weaknesses. Fluorescence microscopy can provide a wealth of information about dynamic systems or imaging at a much wider field of view than is possible with electron microscopy. A relatively new discipline, correlative light-electron microscopy (CLEM) extends the biological length scales for both techniques which represents a powerful and information-rich combination.[5]

Electron microscopy represents the highest resolution imaging tool (20 pm or 0.2 Å) and uses an electron beam as the illumination source to form an image.[6,7] Since the wavelength of an electron is much smaller than that of visible-light (2.74 pm at 200 keV versus 380 nm at ~3.26 eV), the image resolution is not limited in the same way. For biological materials, electron dose is usually the limiting factor for resolution where biological materials are quickly damaged by the incident electrons, which have a lot more energy than photons (more on this later). Contrast in the

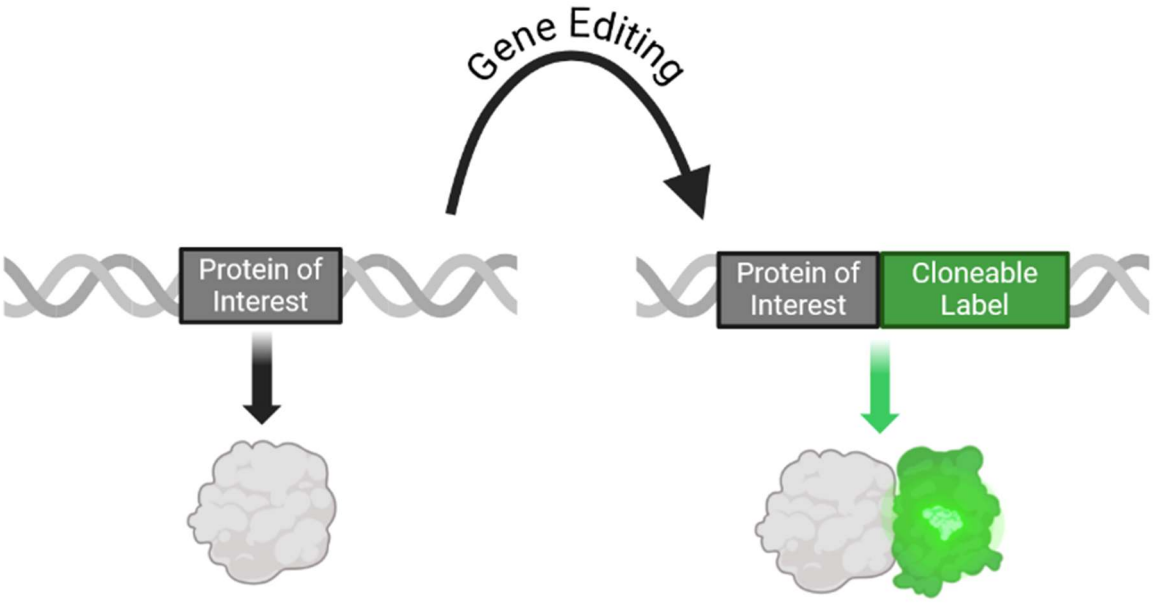

Figure 1.3. *Cloneable labels are attached to a protein of interest by editing the DNA, resulting in a covalently linked chimera of the protein of interest and the cloneable label (following transcription and translation of the DNA).*

electron microscope arises from differences in how parts of a sample interact with the incident electron beam—loosely, differences in electron density. For non-biological inorganic materials which sample regions across the periodic table, contrast is (usually) in high supply since a gold nanoparticle will appear quite different to a thin carbon film (Z = 79 versus Z = 6, respectively). Contrast in a cellular system still broadly arises from differences in electron density. For instance, this means that regions with phospholipid membranes appear quite different from the cellular background. Many larger cellular structures can be observed directly in an electron microscope, but the smaller components, the proteins, are much more difficult to image directly within complex samples, such as those within cellular milieux. Not only are the proteins smaller--presenting a 'signal above background' challenge--but the interaction with the electron beam is similar to the cellular background. Picking a protein of interest (POI) out of a complex cellular matrix remains a grand challenge in biological imaging.

Cryogenic electron microscopy involves imaging samples (usually biological in nature) at or near liquid nitrogen temperatures. When imaging with an electron microscope, the sample is under high vacuum to reduce the potential for incident electrons to collide with stray molecules in the electron microscope column, interfering with the image of the sample. Due to the high-vacuum, much work is needed to prepare biological samples for the harsh environment of the electron microscope. Traditionally, this was done first by chemically fixing the cells using aldehyde-based cross-linkers such as formaldehyde or glutaraldehyde. At this point, stains or dyes could be used to add additional contrast to the sample. This chemical fixation permanently alters the cellular ultrastructure, especially with respect to membranes. Chemical fixation was followed with dehydration and embedment with plastic which could be cut into thin slices that would be transparent to the electron beam. This process may have (unknowingly) biased our interpretations

of cellular structures throughout history due to structural artifacts added by chemical fixation and traditional labeling methods.[8]

Jacques Dubochet showed in the 1980s that it was possible to create vitreous ice--a glass-like form of solid water that does not have crystals distributed throughout. This resulted in Jacques Dubochet receiving the 2017 Nobel Prize in Chemistry alongside Joachim Frank and Richard Henderson for work related to cryo-electron microscopy, and is important to the field owing to several reasons: (1) biological materials could be preserved directly in their native aqueous environment without need for chemical fixatives, dehydration, or plastic embedment (2) vitreous ice would be transparent to the electron beam where ice crystals would strongly interact with the electron beam, obscuring anything embedded within it (3) imaging at low temperatures helped to mitigate sample damage caused by the electron beam. However, many of the contrast tools available at the time were not compatible with samples prepared for cryo-electron microscopy since live cells could not tolerate the high doses of electron dense metal stains.

1.3 Background – Contrast Tools for Electron Microscopy

Where dyes and stains lack the specificity required to deliver contrast to a POI, immunolabeling enabled protein specific labeling. Immunolabeling or immunostaining makes use of the high affinity binding of antigen-specific antibody to deliver contrast. It is common to attach a gold nanoparticle of known size or fluorescent protein to an antibody which then binds to an antigen at the POI. While immunolabels have single molecule specificity, they are very large (150 kDa) and are fundamentally limited by their diffusion into cells and into resin-embedded sections.[9,10] In order to penetrate the cell membrane, the membrane has to be permeabilized—permanently altering the membrane and ultrastructure. Moreover, the large size of antibodies (10 nm) displaces tags far away from the intended target, and can be ‘fooled’ to bind multiple isoforms of a

protein.[11,12] To remedy the fundamental limitations with immunolabeling, there has been increasing interest in a cloneable tag for EM which expresses chimerically to POIs, alleviating the need for molecular recognition that relies on interfacial chemistry.

In electron microscopy, a genetically encodable or 'cloneable' tag equivalent to the robust and widely used cloneable fluorescent proteins does not yet exist. There are a host of semi-cloneable tags such as Spytag, Halotag, or SNAP tag which have one component that is covalently attached to a protein of interest and another component that is exogenously added to the cells.[13–17] These operate in a similar manner to antibodies, but the overall size is much smaller and the system can easily be adapted to different systems (i.e., with cloning). The component added to cells is usually conjugated or attached to a contrast marker such as a gold nanoparticle. The two components of the tag are designed to have a strong binding affinity so that the contrast marker is localized to the POI when the two components of the tag come together. This category of cloneable tags are generally robust and widely used, but still rely on a binding interaction through delivery of one component to the POI.

Metallothioneins are small (< 10 kDa) cysteine-rich proteins known for bindings metals (e.g., gold, cadmium) through thiolate bonds.[18–21] Metallothioneins form particles on the order of, but smaller than, 1.4 nm Nanogold which is often used in immunolabeling. Since the particles are so small, the signal can be difficult to distinguish from the background.[21] Moreover, the ionic gold substrates often used for Metallothionein labeling can be promiscuously reduced in cells and there are additional cysteine residuals in the cell where particles could bind—both of which can lead to higher signal in the background where insoluble gold particles are not associated with POIs.[18,21]

Another class of cloneable tags are those which release molecular species that radically activate diaminobenzidine (DAB) to polymerize with itself such as adapted ascorbate peroxidases

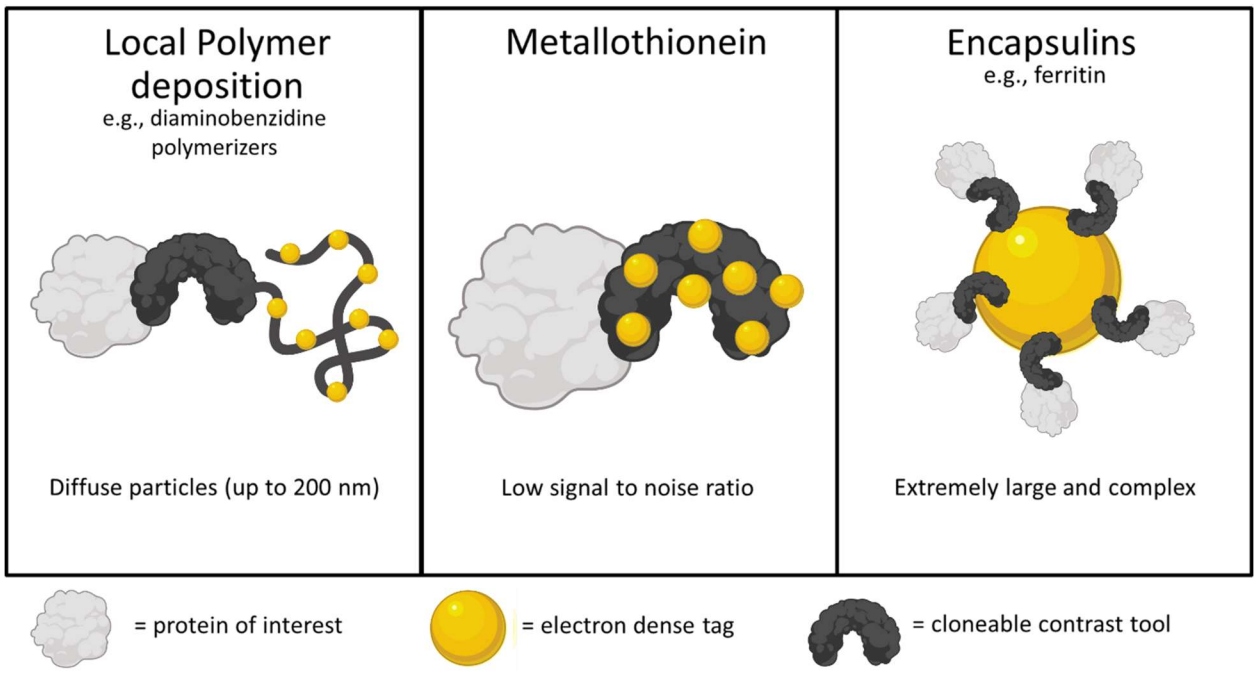

Figure 1.4. *Alternative cloneable labeling strategies for electron microscopy.*

(APEX/APEX2) and mini singlet oxygen generator (miniSOG).[11,22,23] The DAB polymers are osmiophilic and, once they are coated with osmium, serve as electron dense polymers localized near a protein of interest.[11,22] Osmium tetroxide will also preferentially bind lipids as we established previously with regard to staining. While DAB polymerization based genetic tags (i.e., APEX & miniSOG) are highly sensitive contrast enhancers, the DAB polymers can diffuse distally upwards of 200 nm away from the tagged protein, diminishing its applicability where high resolution is required.[24,25] Despite attempts to limit diffusion, approaches using miniSOG are not optimized for applications in prokaryotes and are better suited to applications at the interfaces of membranes or within enclosed vesicles.[25] Additionally, DAB-based systems are restricted to fixed cells due to harsh cell-killing conditions used to create DAB polymers (e.g., peroxides, photooxidation).[11,22,23,26]

Finally, ferritin (or apoferritin when not associated with iron) has also been proposed as a genetic tag for use in EM, but its large size (474 kDa) and composition of 24 subunits makes it

poorly suited for the job.[27,28] A ferritin based tag would be impractically large compared to the size of most proteins and the multimeric structure would result in multiple proteins per ferritin complex and significantly perturbed native protein function. Figure 1.4 shows schematic representations of these alternative cloneable labeling strategies (i.e., local polymer deposition, metallothionein, and encapsulins)

With the cloneable nanoparticle paradigm, an electron dense particle is intracellularly synthesized by an enzyme that is covalently attached to a protein of interest. A small peptide(s) helps to control the nanoparticle (e.g., size, retention). In the following chapter, the cloneable nanoparticles paradigm is described in detail. Cloneable nanoparticles are proposed as a solution to the contrast problem because they can provide intracellular contrast to a protein of interest in electron microscopy and other imaging modalities—discussed in later chapters.

CHAPTER 2: CLONEABLE INORGANIC NANOPARTICLES

2.0 Synopsis

When a defined protein/peptide (or combinations thereof) control and define the synthesis of an inorganic nanoparticle, the result is a cloneable NanoParticle (cNP). This is because the protein sequence/structure/function is encoded in DNA, and therefore the physicochemical properties of the nanoparticle are also encoded in DNA. Thus, the cloneable nanoparticle paradigm can be considered as an extension of the central dogma of molecular biology (*e.g.* DNA → mRNA → protein → cNP); modifications to the DNA encoding a cNP can modify the resulting properties of the cNP. Inorganic ion oxidoreductases (*e.g.*, mercuric reductase, tellurite reductase, *etc.*) can select and reduce specific inorganic oxyanions and coordination complexes, creating zerovalent precipitates. Other proteins/peptides (often genetically concatenated to the parent oxidoreductase) serve as ligands, directing the size, shape, crystal structure and other properties of the nanoparticle. The DNA encoding a cNP can be recombinantly transferred into any organism. Ideally, this enables recombinant production of cNPs with the same defined physiochemical properties. Such cNPs are of interest for applications ranging from molecular imaging, bioremediation, catalysis, and biomining. In this Feature Article we detail and define the cNP concept and retrace the story of our creation of a cloneable Se NanoParticle (cSeNP). We also describe our more preliminary work that we expect to result in cloneable semiconductor quantum dots, cloneable Te nanoparticles, and other cNP formulations. We highlight the application of cNPs in cellular electron microscopy and compare this approach to other cloneable imaging contrast approaches.

2.1 Introduction

Soluble inorganic nanoparticles (iNPs) typically comprise an inorganic core passivated by an organic ligand shell. *In vitro* synthetic methodology for producing iNPs of well-defined elemental composition, size, shape and crystal structure is now relatively mature; rules and guidelines exist that form starting points for synthesis of novel iNPs, based on prior work. Biogenic nanoparticles (bNPs) are those produced with biomolecules, such as crude cell extracts or sugars. These tend to be less well-controlled, relying on serendipitous interactions between biomolecules and iNP precursors; well-developed frameworks for predictive bNP synthesis do not yet exist.

A relatively new concept in nanoparticle synthesis is that of a cloneable nanoparticle (cNP), which can be considered a sub-type of bNP. When physicochemical properties of an iNP, such as elemental composition, size, shape, crystal-structure, allotrope, optical properties, and magnetism, are encoded in DNA, the iNP is a "cloneable NP" (cNP). These cNPs are synthesized by proteins, usually inside cells. Protein sequence, and therefore structure and function, are genetically encoded. Therefore, nanoparticles whose physicochemical properties are controlled by proteins during synthesis have their properties encoded in DNA. This framing implies that the DNA encoding any cNP can be recombinantly transferred into any organism, endowing that organism with the ability to make the cNP.

cNPs as defined in this article are made in living cells. cNPs *do* occur naturally. Magnetosomes[29,30], ferritins[31–33], and DNA-binding protein from starved cells (Dps)[34,35] are examples of naturally occurring cNPs. Each of these examples makes an iron oxide nanoparticle of defined size, shape, elemental composition, and magnetism.

bNPs (and therefore cNPs) attract interest for a diverse array of applications. Our primary interest in cNP engineering is to make cloneable contrast in images of biological systems generated

with electrons, X-rays, light and/or magnets (i.e., electron microscopes, CT-scanners, optical microscopes, and MRI imagers). Our secondary interest is using cNPs for environmental bioremediation of metal(loid) contaminations.

There are many ongoing studies developing bNPs for uses including catalysis[36], solar photoconversion[37], antimicrobial therapy[38,39], and theranostic (i.e., combined therapeutics and diagnostics) agents.[40,41] The applications of biogenic NPs listed here are at preliminary stages. It can be expected that the greater synthetic control of NP properties in biological contexts will become more desirable or necessary as implementations advance. cNPs may enable such means of improving synthetic control in many of the currently proposed uses of biogenic NPs.

The cNP synthesis paradigm

We have developed a modular cNP platform that links genotype (DNA) to phenotype (cNP composition). This platform adapts *in vitro* NP synthesis (Figure 2.1, top panel) approaches to use cellularly available reactants (Figure 2.1, bottom panel).

In vitro reductive iNP synthesis usually begins with three chemical components: inorganic cations, reductants, and ligands. In this synthetic approach, reductants change the oxidation states of cations from soluble (e.g., aqueous) to insoluble (particulate, solid) states. Very often, the reduced particulate oxidation state is zerovalent. Ligands present during synthesis cap growing inorganic solids at nanoparticulate size, suppressing growth into macroscopic bulk solid[42] and directing particle size, shape, fluorescence, etc.

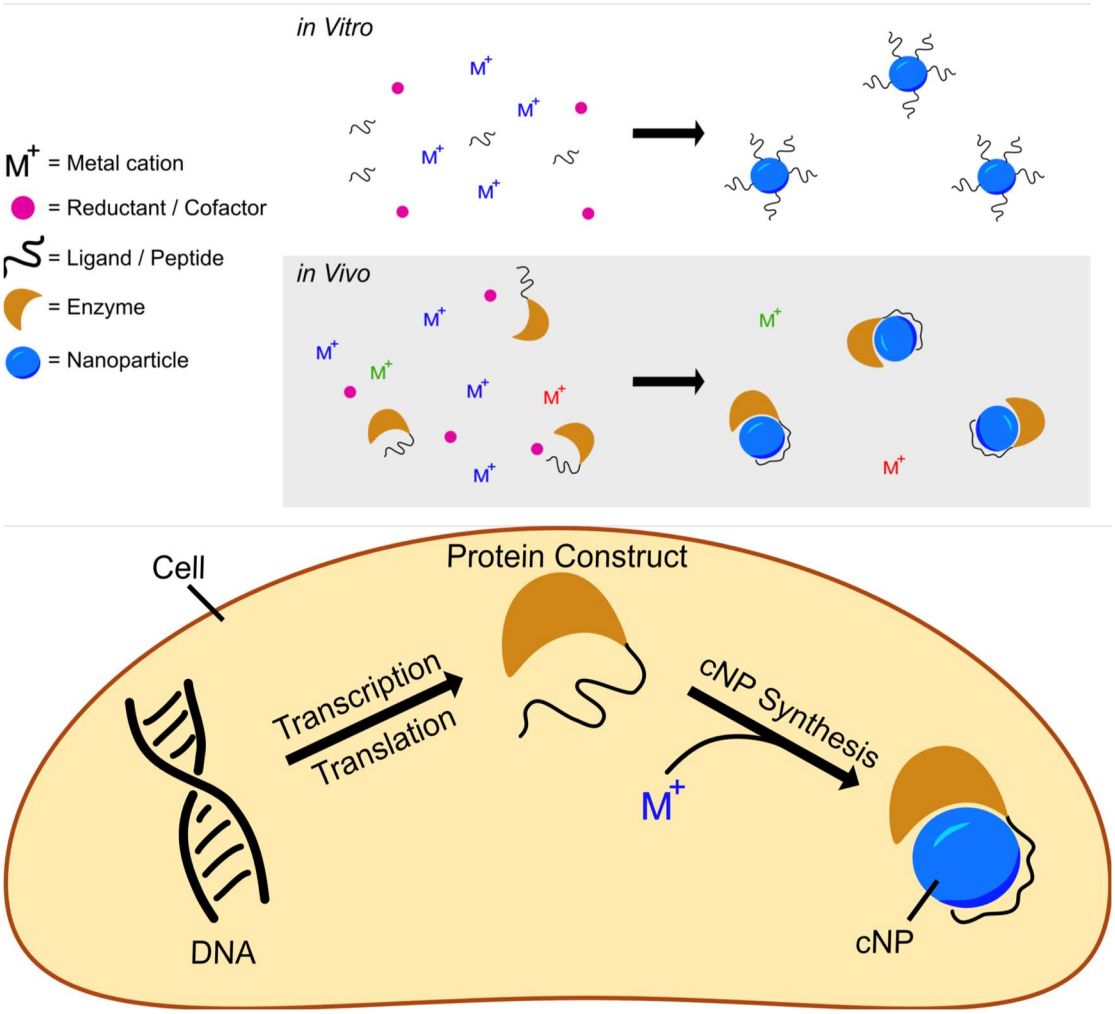

Figure 2.1. *Schematics showing reductive nanoparticle synthesis approaches in vitro (top panel) and in vivo (bottom panel).*

In adapting this paradigm to cellular environments, we similarly use three distinct chemical components, with the additional use of inorganic ion oxidoreductases. In this context, bioavailable metal(loid) cations or coordination complexes act as the metal(loid) source. Inorganic ion oxidoreductases select the 'desired' ion (coordination complex) from a background that contains all essential elements (Se, Zn, Fe, etc). Enzyme cofactors (NADH, NADPH, glutaredoxin, etc.) act in concert with enzymes as the reductant. Peptides or proteins that bind to and/or control iNP properties can be concatenated to or coexpressed with the oxidoreductase and act as ligands in cNP

synthesis; in this role, they offer the prospect of size, shape, and crystal structure definition. The combination of oxidoreductases and iNP binding peptides/proteins results in synthetic control of cNP synthesis inside cells rivalling the synthetic control that is possible with well-developed *in vitro* methods.

cNP composition parameters

cNPs require metal(loids) coordination-complex precursors that are at least transitively stable inside cells (e.g., not easily reduced by ubiquitous reducing molecules such as sugars and aromatic or thiol-containing amino acids). Such metal(loid)s include essential elements such as Fe, Co, Zn, Se, W and Mo. In addition, many non-essential metal(loids), such as Bi (a pharmaceutical component in Pepto Bismol) or Au (a pharmaceutical component of rheumatoid arthritis drugs such as Auranofin) might also form the basis for a cNP. Some metal(loids) regarded as highly toxic, such as, can even form the basis for a cNP, if the toxicity can be appropriately modulated. In the case of arsenicals, the metal complex arsphenamine (Salvarsan) is a treatment for syphilis.[43]

For metal(loid) ions to be cNP reactants, they must be enzymatically reducible by enzymes – therefore the redox potential of the metal(loid) precursor must be in a range accessible to biological reductants such as NADPH or glutaredoxin. (i.e., their oxidation state must be modulated by the enzyme). The redox potential of a metal(loid) ion is significantly impacted by ligation. The impact of ligation on redox potential exerts effects through multiple pathways, including ligand lability/inertness, the electron transfer (tunnelling) properties of the ligand, and the metal(loid) oxidation state favored by the ligand (influenced by ligand geometry). As an example of how ligation changes redox potentials, consider the reduction of $Cu^{2+}$to Cu^{0}. The reduction potential of aquated Cu^{2+} in the reaction $[Cu(H_2O)_6]^{2+} + 2e \rightarrow Cu(s) + 6H_2O(l)$ is +0.337 V versus S.H.E., whereas $[Cu(NH_3)_4]^{2+} + 2e \rightarrow Cu(s) + 4NH_4$ is at -0.05 V. [44]

Many intracellular metal ions are glutathione-ligated, in part due to the ~mM concentration of glutathione (GSH) inside most cells, combined with the high affinity of thiols for many metal(loids).[45] Many metal(loid) oxidoreductases are thus unsurprisingly related to glutathione reductase (GSHR). GSHR[46,47], mercuric reductase[48], tellurite reductase[49], and glutathione reductase-like metalloid reductase (GRLMR)[50] all belong to the class I FAD dependent oxidoreductase enzyme family. Functional differences among enzymes in this family mainly comprise substrate selection—where substrates are different metal(loids) ligated by GSH.

Enzymatic metal(loid) ion reduction is a relatively common cellular feature. Many enzymatic systems may therefore possess cNP chemistry; however, most enzymes described to date lack inherent means of enforcing uniform size/shape/elemental composition. A great deal of iNP binding peptides have, in contrast, been described for their ability to exert strong influence on NP size/shape/elemental composition yet lack intrinsic means of reducing metal(loid) cations. Thus, the combination of iNP-binding peptides with metal(loid) ion reductases represents a platform or paradigm for cNP synthesis.

iNP binding dodecapeptides were first isolated from phage display libraries.[51] So-far, peptides that bind to a about 100 iNPs of differing size/shape/elemental composition are now described in the literature. A subset of iNP binding peptides can also assist in the synthesis of iNPs. For instance, A3 peptide in the presence of Au^{3+} salts and a reductant (which can include the buffer HEPES serving as reductant) makes 10 nm AuNPs. The Ge8 peptide, in the presence of $AgNO_3$ and H_2O_2, makes chiral, curved silver nanowires.[52]

These synthesis-assisting peptides do not constitute cNPs on their own; while they are encoded in DNA and promote NP formation, they do not change the oxidation states of the ions (and therefore solubility). Thus, they do not represent a self-contained cNP system. Notably, some

of the early literature on iNP binding peptides confuses this issue, as early papers did not recognize that buffer salts can donate electrons too, and reduce many metal ions in the absence of peptides.[53,54]

Many proteins have also been identified that bind to inorganic nanoparticles and might therefore similarly control their shape and size during synthesis. Broadly speaking, there is existing literature on proteins that form a 'corona' around iNPs.[55,56] For selenium nanoparticle(s) (SeNPs) a proteomic study identified about 50 proteins that are found in the SeNP corona,[57] for SeNPs made in cells or exposed to cell extracts.

By analogy to what is now known about library isolated peptides in the context of bNP synthesis, we expect that some naturally occurring proteins can also direct cNP size and shape. That suite of proteins may include those that confer an adaptive advantage to their host (in the context of metal toxicity) and those that evolved for other functional endpoints but serendipitously control cNP size/shape.

Above we outlined cellular equivalents of reductants and ligands that can synthesize well-defined cNPs. This combination of cellular reductants and ligands can be encoded in a single chimeric DNA construct. This results in a chimeric protein that incorporates all chemical activities required to make a cNP.

Because a single protein (polypeptide chain) controls all functions, mutations to the DNA encoding the protein can subsequently change properties of the cNP. This allows the adaptation of recently developed and powerful directed evolution methods for the purpose of cellular nanoparticle synthesis.[58]

Cloneable contrast

Our primary motivation in developing the cNP platform is to develop cloneable imaging contrast. Cloneable contrast imaging agents, such as green fluorescent protein (GFP), were first described and adopted for fluorescence microscopy.[1,59] What makes GFP useful in imaging is that the DNA encoding GFP can be easily 'cloned' or concatenated to the DNA encoding any protein of interest. The protein of interest now 'lights up' in fluorescence microscopy and is distinctly visible against the cellular background, where nothing else fluoresces notably at the GFP emission wavelength of 509 nm. Meanwhile, the available toolbox of fluorescent proteins has grown to the extent that multi-color (multiplexed imaging) studies are routine—e.g., dynamic protein interactions with several players can be observed.[60]

GFP represents a 'benchmark' for cloneable imaging contrast. The properties of GFP that make it so useful are: (1) it works in both live and fixed cells; (2) it is entirely self-contained in a single DNA segment—requiring nothing further such as exogenous building blocks or upstream cellular engineering (3) there is 1 GFP for each protein that it is concatenated to. This allows straightforward quantification of protein copy number through quantification of fluorescence signal.

Cloneable contrast agents that function in electron, magnet and X-ray-based imaging modalities are extensively explored, but not yet widely adopted by biologists using these imaging methods. Such modalities are nevertheless important, as they allow tissue imaging in magnification and penetration domains outside what visible-light microscopy is capable of. Cloneable contrast in these imaging modalities may or may not use approaches that create cNPs. Approaches that use ferritin, singlet-oxygen generation proteins, and phytochelatins—such as metallothionein—are outlined below. So far, no cloneable contrast approach for EM is widely used because there are severe limitations associated with each method proposed to date:

Ferritin is a ~400 kDa protein constituted from 24 polypeptide units. Under iron-rich conditions, ferritins can store up to ~4500 iron atoms as a highly regulated mineral core, which can be easily observable in certain imaging contexts such as EM or correlative light and electron microscopy (CLEM).[31,32] Ferritin presents two substantial challenges for widespread use as a contrast agent. First, its multimericity can heavily convolute labelling strategies. Second, its comparatively large size casts a shadow in images, obscuring potentially important areas within images. The size may also impact function of ferritin-protein conjugates by slowing diffusion kinetics of concatemerized protein(s) of interest.

Certain proteins can locally deposit diaminobenzidine (DAB) polymer, such as mini singlet oxygen generator[61] (miniSOG) and engineered ascorbate peroxidase[62] (APEX2). In these cases, radical oxygen is enzymatically produced, which subsequently activates DAB to form osmiophilic polymers. These polymers then preferentially absorb electron dense osmium stains proximal to the point of polymer origination. While osmiophilic DAB polymers can be a highly sensitive method of enhancing contrast, they diffuse distally from their point of origination (in some cases to nearly 200 nm), substantially reducing the resolution at which interpretations of images (collected at much higher resolution) can be made. DAB polymerization is moreover infeasible in living cells or in frozen-hydrated cells, requiring fixation which introduces imaging artefacts.

Metallothioneins are small (0.5-14 kDa) cysteine-rich proteins which stoichiometrically bind metal atoms. Previous works have demonstrated that metallothionein can bind a wide array of metal atoms, including Au, Pt, Ag, Pb, Cd, and As. Metallothioneins have been implemented as cloneable contrast tags.[63] However, they are barely visible above the background in electron micrographs. This can also be exacerbated by competition from natively expressed metallothionein, which upregulates in the presence of high intracellular metal concentration.

Inorganic nanoparticles are known to have properties that can produce contrast in EM, visible-light, X-ray, and magnetic imaging modalities. An appropriately formulated cNP may therefore be able to produce contrast in each of these imaging modalities simultaneously, while overcoming many of the limitations of existing cloneable contrast agents.

This feature article outlines our development of a cNP platform, with some applications highlighted. The most 'mature cNP' in our lab is comprised of ~5 nm Selenium NPs—making it a cloneable selenium nanoparticle (cSeNP.)

We summarize a set of 4 papers from our group, which in concert describe the development of this cSeNP platform. The reductase is Glutathione Reductase-Like Metalloid Reductase (GRLMR), which was isolated from *Pseudomonas moraviensis* subspecies stanleyae—among the most Se tolerant microorganisms ever described. This species may show promise for bioremediation of selenium contamination—an area where previous work has been done collecting biogenically produced Se(0) from wastewater.[64,65]

Transmission electron microscopy (TEM) and electron tomography of the *P. moraviensis* stanleyae shows ~50 nm diameter intracellular SeNPs. There is no apparent membrane or protein structure surrounding these SeNPs. GRLMR can be transferred among species, endowing other species with enhanced Se tolerance.

GRLMR alone does not control SeNP size. To introduce size control, we isolated a peptide that binds to SeNPs from a phage display library. Concatenation of this peptide to GRLMR at the DNA level results in a construct that consistently makes 35 nm diameter SeNPs *in vitro* and ~5 nm diameter SeNPs *in vivo*. Furthermore, we show that inclusion of transition metals such as Cadmium in the cell cultures that make cSeNPs allows instead the production of CdSe semiconductor quantum dots.

There are 'less mature' cNPs in the pipeline in our lab. For instance, we have isolated a tellurium reductase from environmental isolates, and this may form the basis for a cloneable tellurium nanoparticle in future work.

While not a cNP, we have examined metallothionein as a cloneable contrast agent, concluding that it must be present in high copy number to be visible in EM.

We have also made some substantial and unpublished investigation of the capsule-forming and Fe-concentrating protein Dps. Here we will outline our approach and the shortcomings of that approach which precluded prior publication.

2.2 Summary of cNP Developments

Development of the cSeNP is described in 4 manuscripts, beginning with a manuscript describing the isolation of a selenium hyperaccumulating bacterium, followed by a paper describing the isolation of a selenium reducing enzyme and characterization of the SeNP products of that enzyme. A subsequent paper showed that the Se tolerance can be recombinantly transferred to other species, facilitating recombinant SeNP production. A fourth paper isolates a SeNP binding peptide and shows how incorporation of this peptide with the selenium reductase significantly alters enzyme activity and results in size-controlled, 5 nm diameter, red SeNPs which remain attached to the enzyme that synthesizes them, representing a cSeNP.

Pseudomonas moraviensis subsp. stanleyae, a bacterial endophyte of hyperaccumulator Stanleya pinnata, is capable of efficient selenite reduction to elemental selenium under aerobic conditions[65]

Our work on the cSeNP began with isolation and characterization of a bacterium specialized for high Se conditions.[65] In this paper, we report *Pseudomonas moraviensis* subspecies stanleyae, a bacterial endophyte that was isolated from the root tissue of Se hyperaccumulator *Stanleyae pinnata* (colloquial name Prince's Plume) found growing in the naturally seleniferous soil in the Pine Ridge Natural area of Colorado, USA.

The bacterium was characterized phylogenetically by fatty acid methyl ester analysis and multi locus sequence analysis. The sequence analysis showed 97.3% nucleotide identity to *P. moraviensis*. This subspecies was therefore dubbed *Pseudomonas moraviensis* stanleyae, taking the name of the plant in which it was found.

Because *P. moraviensis* stanleyae was found as an endophyte in a selenium hyperaccumulating plant, it was hypothesized that the bacterium is a selenium specialist (possibly working in symbiosis with the plant in which it lives). The bacterial strain was grown in various concentrations of SeO_4^{2-} (selenate) and SeO_3^{2-} (selenite). When grown on selenite supplemented LB-agar, the bacterial colonies appeared bright red—consistent with production of red-allotrope SeNPs (Figure 2.2, panel A). When examined by TEM, rod shaped bacteria coated with SeNPs were apparent (Figure 2.2, panel B.) Overall, we observed that the bacterium could tolerate up to 120 mM of selenite and 150 mM selenate, making this the most selenium tolerant organism so-far described.

Growth kinetics in the presence of high concentrations of Se oxyanions showed that the growth of *P. moraviensis* stanleyae was not significantly impeded by 10 mM selenate—but no red Se(0) was observed with selenate. In the presence of selenite, growth was somewhat slower, and red selenite appeared after about 10 hours (Figure 2.3).

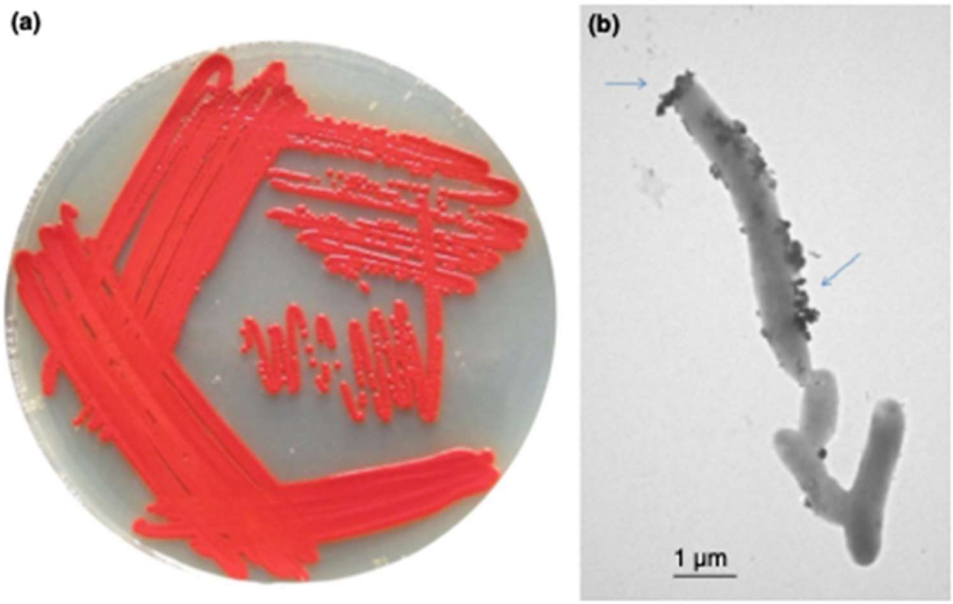

Figure 2.2. *Panel a shows P. moraviensis stanleyae growing on SeO_3^{2-} supplemented agar. The red color is indicative of red Se(0) formation as a result of selenite reduction. Panel b shows a TEM image of P. moraviensis stanleyae grown in the presence of selenite. The bacteria appear coated with SeNPs.*

The observation that *P. moraviensis* stanleyae converted SeO_3^{2-} to Se(0) while SeO_4^{2-} was not reduced was also made by observing the aerobic reduction of each selenium oxyanion. Figure 2.4 shows the concentration of SeO_3^{2-} and SeO_4^{2-} as determined by a microchip capillary electrophoresis method that we developed for this purpose.[66] This figure shows that SeO_4^{2-} concentrations persisted near their original 10 mM concentrations in the culture for as long as they were measured (up to 50 hours). SeO_3^{2-} concentration, however, diminished over time due to its reduction to red Se(0). Combined, these observations suggest that the mechanism for SeO_3^{2-} tolerance involves conversion of SeO_3^{2-} to Se(0), whereas SeO_4^{2-} tolerance must be due to other mechanisms that do not reduce selenium oxyanions (such as efflux pumping). Overall, this paper identifies the most Se tolerant organism described to date, capable of surviving in liquid culture supplemented with up to 150 mM SeO_4^{2-}. Subsequent work determines the molecular mechanism of SeO_3^{2-} reduction.

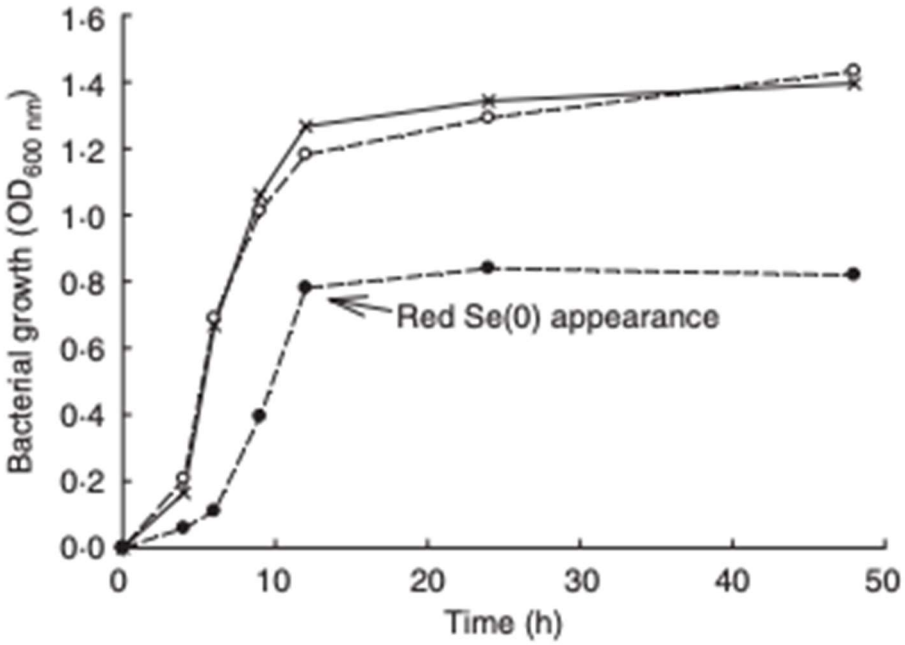

Figure 2.3. *Aerobic growth of* P. moraviensis stanleyae *in Luria Broth media without Se oxyanions (x), and in the presence of 10 mM selenite (solid circles) and 10 mM SeO_4^{2-} (open circles).*

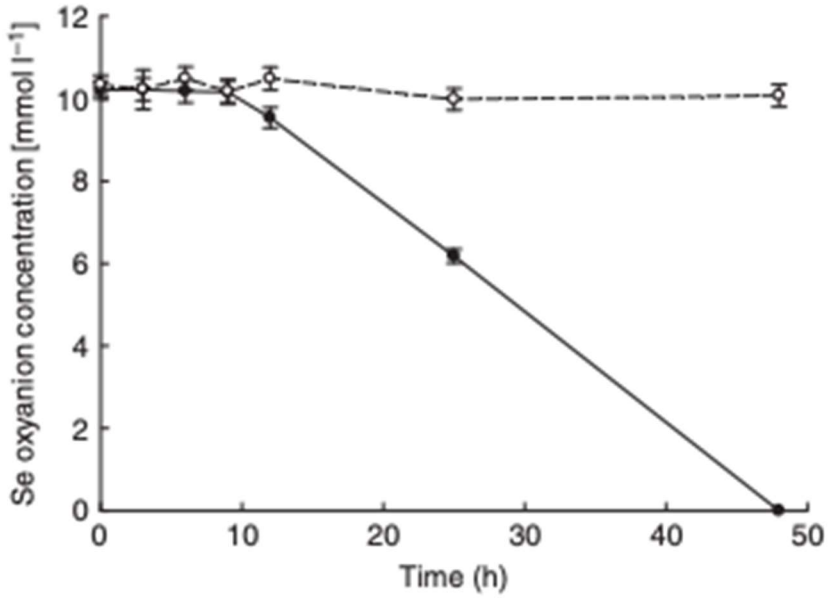

Figure 2.4. *Aerobic reduction of SeO_4^{2-} (open circles) and SeO_3^{2-} (closed circles) by* P. moraviensis *stanleyae as a function of time.*

Progress toward cloneable inorganic nanoparticles[67]

We continued the characterization of *P. moraviensis* stanleyae.[67] This paper focuses on electron microscopy characterization of *P. moraviensis* stanleyae and unraveling the mechanism of SeO_3^{2-} reduction.

The initial EM imaging of *P. moraviensis* stanleyae (Figure 2.2) left several microscopic aspects of the system ambiguous. From these images, it is unclear whether SeNPs are present inside cells as well as outside cells. This initial data also lacks elemental imaging, which could confirm that the punctate inclusions are in fact comprised of Se, as inferred.

In the present paper, *P. moraviensis* stanleyae cells were grown in the presence of SeO_3^{2-} and cells were then imaged by scanning electron microscopy (SEM) as glutaraldehyde-fixed dehydrated cells. The SEM based imaging allows energy dispersive X-ray spectroscopy (EDS) elemental analysis of the cells.

SEM imaging revealed capsule-shaped cells, most of which contained one or more dark inclusions. EDS mapping showed that these inclusions were Se rich, suggesting that these are SeNPs. The putative SeNPs were circular with an average diameter of 107 ± 35 nm (for 50 observations). These dark inclusions were not observed in control experiments where *P. moraviensis* stanleyae was grown in the absence of Se supplementation.

To this point, it was unclear if SeNPs were present inside or outside of the observed cells. Electron tomography is an imaging modality that allows 3D reconstructions of cells, which can resolve questions about particle location. *P. moraviensis* stanleyae was again grown with selenite supplementation and was preserved for electron tomographic image acquisition by freeze substitution. In this method, cells are vitrified by high pressure freezing, then the water in the cells is substituted for acetone. Following acetone substitution, the cells can be fixed and plastic

embedded. This approach is recognized as providing the highest fidelity preservation of cellular ultrastructure outside of imaging of cells that are vitrified and imaged as frozen-hydrated samples (which is technically difficult to do for cells that are as thick as *P. moraviensis* stanleyae.)

The results of electron tomographic reconstruction of *P. moraviensis* stanleyae are shown in Figure 2.5. Figure 25 panel A shows a 2D image of a *P. moraviensis* stanleyae cell, which contains two very clear large inclusions, assumed to be SeNPs. Panels B and C show a 3D reconstruction of the cell. The reconstruction is segmented so that the membrane is shown in green and putative SeNPs are shown in red. The reconstruction reveals 3 additional particles that were not apparent in the 2D image (possibly because they were distant from the focal plane and/or too small to be visible in the 2D image. It is common for 3D reconstructions to reveal details that are not visible in any of the 2D images used to perform the reconstruction.

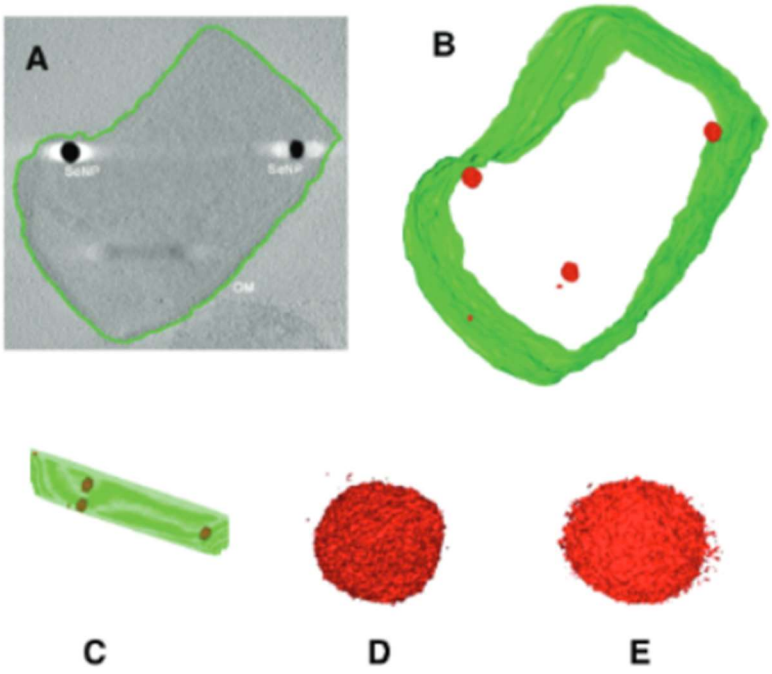

***Figure 2.5**. Electron tomographic reconstruction of P. moraviensis stanleyae grown in SeO_3^{2-} media. The reconstruction was segmented to reveal the outer membrane and SeNPs (panels A-C). Panels D and E show two of the SeNPs at higher magnification.*

Panels B and C of Figure 2.5 show unambiguously that the putative SeNPs are present intracellularly. Furthermore, there is no evidence for membrane encapsulation, which is observed for other inorganic intracellular NPs, such as magnetite within membrane encapsulated magnetosomes.[68] Panels D and E of Figure 2.5 show 2 of the SeNPs at greater magnification. The individual particles are irregular in shape, although overall they are approximately spherical. The irregularity in shape suggests that there is no structured protein coat surrounding these particles, as is the case with other intracellular NPs such as ferritin and Dps.

Most inorganic clusters and nanoparticles require an organic ligand shell to be stable; in the absence of a ligand shell, inorganic nanoparticles fuse, ultimately forming macroscopic material. Selenium, however, is one of a handful of elements for which 'naked' or un-ligated clusters and nanoparticles are stable. The reasoning for this is that Se (as well as, Bi and Sb, among others) can self-satisfy its valence bonding conditions by bonding to other Se atoms.[69] This aspect of Se chemistry suggests that the SeNPs inside *P. moraviensis* stanleyae might not have or need a well-defined biological coating, such as those found around iron oxides. It is probable that the SeNPs do maintain a so-called 'protein corona,' but that this forms as a result of direct exposure of the surface of SeNPs to bacterial cytoplasm.

To gain insight into the mechanism of intracellular SeNP formation, we assayed all soluble proteins of *P. moraviensis* stanleyae for SeO_3^{2-} reduction capability. This assay involved fractionating all the soluble proteins from *P. moraviensis* stanleyae on a non-denaturing gel, which is expected to leave enzyme function intact. Non-denaturing gels containing all soluble proteins were incubated with SeO_3^{2-} salts and various enzyme cofactors, including NADH and NADPH. With the combination of NADPH and SeO_3^{2-}, we observed a set of red bands in the gel, presumably comprised of Se(0) precipitates made by NADPH dependent enzymatic reduction of SeO_3^{2-}

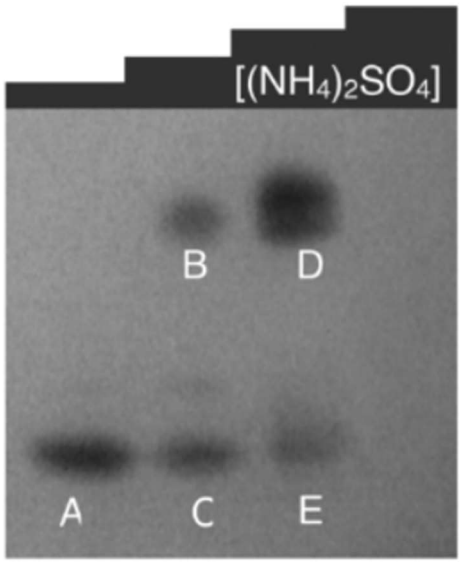

***Figure 2.6**. Non-denaturing gel of soluble proteins from P. moraviensis stanleyae, stained with NADPH and SeO_3^{2-}. The lanes correspond to fractions eluted from a hydrophobic interaction column at various concentrations of ammonium sulfate. Bands appear where NADPH dependent SeO_3^{2-} activity is spatially localized.*

(Figure 2.6). The bands did not appear in the absence of NADPH and appeared very faintly in the presence of NADH.

To identify the NADPH dependent enzyme(s) responsible for SeO_3^{2-} precipitation, we excised each band from the gel and subjected it to proteomic mass spectrometry analysis. This analysis revealed a total of 7 NADPH dependent enzymes out of 113 total proteins present in the combination of all 5 lanes. The NADPH dependent enzymes were Nitrite and sulfite reductase, isocitrate dehydrogenase, glutathione reductase, Methylenetetrahydrofolate reductase, ketoacyl-ACP reductase, Thiol peroxidase and 4-Aminobutyrate aminotransferase.

Of these enzymes, we hypothesized that a glutathione reductase-like enzyme was primarily responsible for SeNP particle formation, because glutathione reductase (GSHR) belongs to the same enzyme family as mercuric reductase, and GSHR has also been shown to reduce Au^{3+} ions.[70] To address this hypothesis, we acquired commercially produced GSHR from Sigma-Aldrich, and tested it for SeO_3^{2-} reductase activity. We observed that GSHR produced spherical SeNPs of an

average diameter of 61 ± 37 nm *in vitro,* when both SeO_3^{2-} and NADPH were present. Notably, we also observed that GSHR reduced TeO_3^{2-} as well.

Combined, this paper shows that GSHR can reduce SeO_3^{2-} intracellularly in an NADPH dependent process. The enzymatic product is SeNPs, of relatively high polydispersity. The SeNPs are thought to be 'naked' or stable without a defined and monolayer-like ligand shell. Overall, this paper postulates that GSHR or similar inorganic ion reductases form a promising basis for cNPs as enzymes that make electron dense intracellular nanoparticles from essential elements. A full adaptation of such reductases should include better SeNP size control, retention of the SeNP at the enzyme, and enzymes that reduce their metal substrates faster and more effectively than 'background' reduction by, for example, native GSHR.

Metalloid Reductase of Pseudomonas moraviensis Stanleyae Conveys Nanoparticle Mediated Metalloid Tolerance[50]

Under the hypothesis that the GSHR from *P. moraviensis* stanleyae is specialized for Se reduction, we proceeded with study of the *P. moraviensis* stanleyae GSHR. In the paper, we began by sequencing the genome of *P. moraviensis* stanleyae. From the whole genome sequence, we identified the DNA encoding the most closely related enzyme to GSHR from this organism. This sequence was cloned into a protein expression vector, and the GSHR-like protein from *P. moraviensis* stanleyae was expressed recombinantly in *Escherichia coli*.

The substrate selectivity of the *P. moraviensis* stanleyae GSHR-like protein was determined for oxidized glutathione (GSSG), selenite, and selenodiglutathione (GS-Se-SG). For comparison, commercially obtained baker's yeast GSHR was analyzed with the same substrates.

Enzyme assays for the GSHR-like enzyme and GSHR are shown in Figure 2.7. Michaelis-Menten analysis of this data revealed that the *P. moraviensis* stanleyae GSHR-like enzyme prefers GS-Se-SG as a substrate over GS-SG; the K_M for GSSG was determined to be 8.22 mM for GSSG

and 336 μM for GS-Se-SG. For baker's yeast GSHR, the K_M values for each substrate were similar (103 μM and 133 μM for GSSG and GS-Se-SG respectively)—showing a slightly greater affinity for GSSG substrates. Other investigations of substrate selectivity for baker's yeast GSHR found similar K_M values.[71]

The 25-fold difference in K_M values for the enzyme from P. moraviensis stanleyae suggests that the enzyme is adapted for reducing GS-Se-SG. Therefore, we named this enzyme "Glutathione Reductase-Like Metalloid Reductase" (GRLMR) due to its substrate preference.

Another difference between GRLMR and GSHR enzymes is the lack of a substrate binding pocket cysteine or methionine residue on GRLMR that might serve as a locus for glutathionylation. Baker's yeast GSHR, a canonical GSHR enzyme, can be glutathionated at C239, resulting in inhibition of the enzyme.[72] Similarly, E. coli and Homo sapiens GSHR contain a methionine residue in this position, which might also be glutathionylated. This is thought to be a regulatory mechanism. In GRLMR, homology models show that this residue is a serine residue, which cannot be glutathionylated (Figure 2.8). The absence of GSH based inhibition of GRLMR also suggests that this enzyme is distinct from canonical GSHR enzymes.

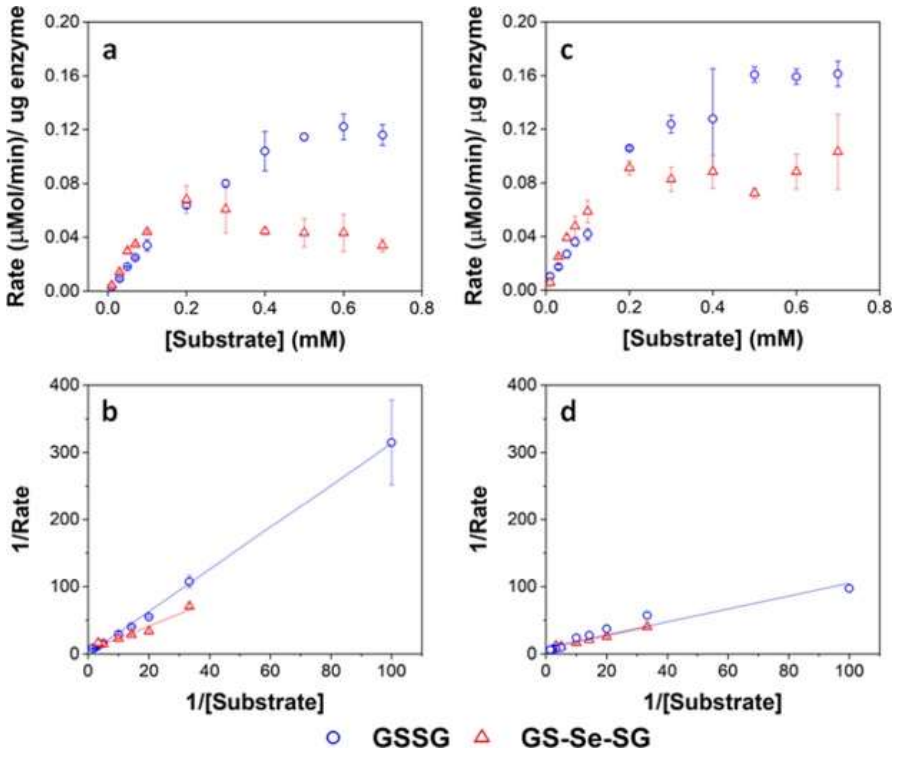

Figure 2.7*. Enzyme kinetic assays for GRLMR (panel a) and GSHR (panel c). Lineweaver-Burke plots for GRLMR (panel b) and GSHR (panel d). The drop in rate at high concentrations of GS-Se-SG is attributed to SeNP formation interfering with the optical assay.*

Expression of GRLMR in E. coli confers selenium recombinant selenium tolerance to its host species. In the presence of mM concentrations of selenite, GRLMR creates nanoparticles to impart selenium tolerance for the cells (Figure 2.9). In our testing, we defined selenium tolerance as the amount of selenium required to inhibit 90% of cell growth (IC90). By testing for the IC90

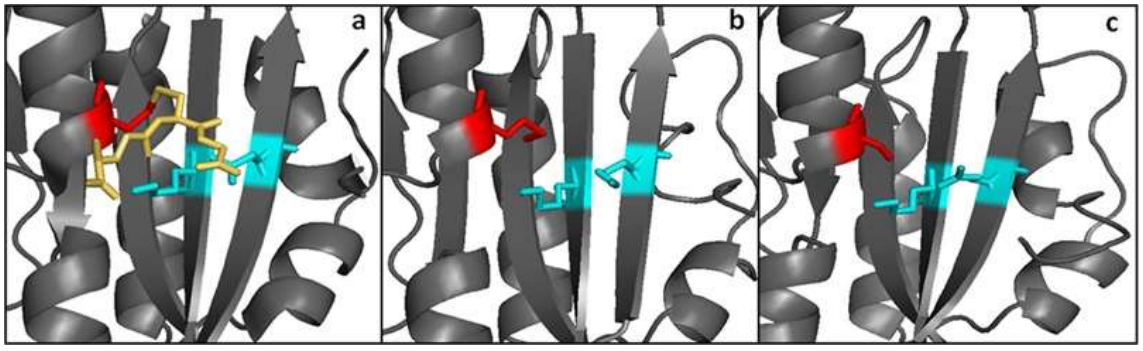

Figure 2.8*. Panels a and b show the substrate binding region from yeast and E. coli GSHR crystal structures. Panel c shows the same region for a homology model of GRLMR. The residue shown in red is glutathionylated in panel a. In panel c, the red-colored residue is not capable of being glutathionylated.*

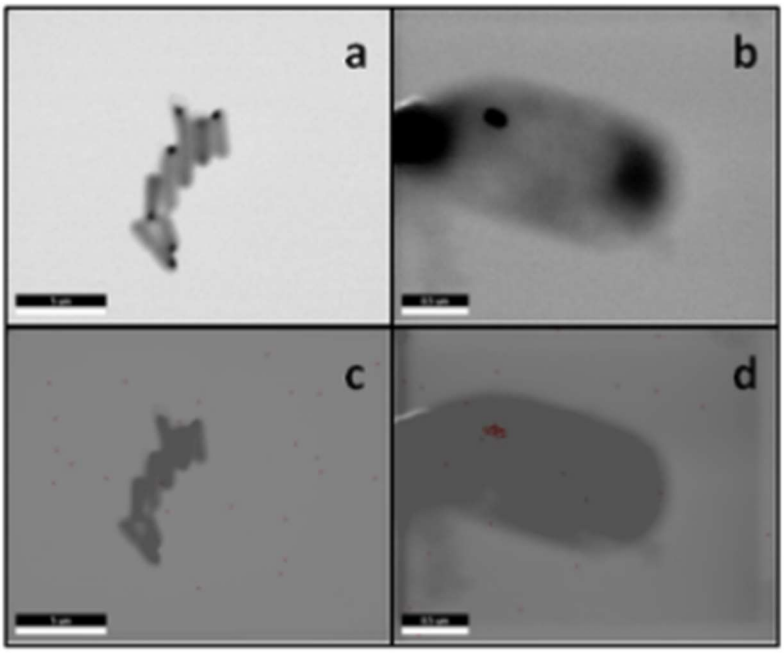

***Figure 2.9**. Panels a-d show SEM images of fixed BL21 E. coli. Panels a and c show cells without the GRLMR plasmid, whereas panels b and d show cells that include the plasmids that are expressing GRLMR. Panels c and d show EDS overlay, where areas that are mapped to Se are colored red.*

of SeO_3^{2-} in laboratory strains of Escherichia coli, cells with the GRLMR gene had an IC90 of 21.3 ± 9.8 mM, whereas without GRLMR, the IC90 was 1.89 ± 0.46 mM. We observed a similar increase in Se tolerance for the SS320 strain of E. coli. The ten-fold higher Se tolerance when GRLMR was expressed was interpreted as imparting Se tolerance. Notably, GRLMR expressing cells grew poorly unless they were supplemented with 1 μM selenite. This was interpreted as GRLMR scavenging Se to the point that cells were Se deficient.

For our ultimate goal of creating cNPs useful in EM imaging of cells, it is critical that the enzyme that synthesizes the SeNP also bind to the SeNP that it has made. We observe that about 10% of GRLMR enzymes are associated with SeNPs in pull-down assays (where the mass of the SeNP allows SeNPs and associated proteins to be collected by centrifugation). This small association makes sense—an efficient enzyme is likely to turn over its product and not be associated with the product. In fact, we observe that ~20% of baker's yeast GSHR is SeNP

associated after SeNP synthesis. The smaller fraction of GRLMR associated with SeNPs is additional evidence for the specialization of this enzyme for SeNP production.

Overall, the GRLMR enzyme accomplishes reduction of a cellularly ubiquitous and essential element, Selenium. However, the SeNPs are quite polydisperse in size and do not remain attached to the enzyme that made them. To make a cSeNP, the GRLMR enzyme needs modification.

Metalloid Reductase Activity Modified by a Fused Se^0 Binding Peptide[73]

In the paper, we describe the isolation and activity of a SeNP binding peptide. When concatenated to GRLMR, this peptide changes the activity of the enzyme so that it controls SeNP size and SeNPs remain largely associated with the enzyme.

A SeNP binding peptide (SeBP) was isolated from the New England Biolabs Ph.D. 12-mer phage display library (NEB Ph.D. Kit) after three rounds of selection versus 8.4 ± 2.7 nm SeNPs, whose size was confirmed via TEM. Following three rounds of selection, the output phage peptide library was found to be dominated by two sequences (Table 2.1). The sequence that appeared at

Table 2.1. *Sequences identified after three rounds of selection versus GRLMR-synthesized SeNPs. Sequences are described by population frequency, isoelectric point, and the amount of phage expressing the peptide sequence that bound to the three negative screen conditions (BSA, unreacted GRLMR, and SiNPs). Each titer began with an initial phage titer of 1010 pfu.*

	Pep. Seq.	Frequency	pI	Polystyrene	GRLMR	SiNP
	Wild Type	N/A	N/A	$3.9x10^4$	$1.5x10^5$	$1.8x10^6$
SeBP	LTPHKHHKHLHA	19/33	9.37	$3.7x10^4$	$2.6x10^5$	$3.0x10^5$
SeBP2	GPHHMHHHRTHH	7/33	10.47	$1.1x10^5$	$2.1x10^5$	$7.9x10^6$
SeBP3	WPRHHWHTNYMR	1/33	11.15	$2.3x10^5$	$3.9x10^5$	$1.3x10^6$
SeBP4	GWHSPHAHWRVK	1/33	10.61	$4.3x10^4$	$3.3x10^5$	$3.7x10^5$
SeBP5	THYNPLRINPIT	1/33	9.95	$9.8x10^5$	$6.8x10^5$	$1.8x10^6$
SeBP6	KVHIMHFHHHSL	1/33	9.08	N/A	N/A	N/A
SeBP7	HSWSTIKRIETM	1/33	9.07	N/A	N/A	N/A
SeBP8	WPHLQHHKATSR	1/33	10.61	N/A	N/A	N/A
SeBP9	HDRMTKSSPSPP	1/33	9.07	N/A	N/A	N/A

the highest frequency (LTPHKHHKHLHA) was designated as SeBP and was used for future experiments.

Subsequent experiments explored the effect of concatenating SeBP to GRLMR (GRLMR-SeBP) versus GRLMR alone in terms of nanoparticle size, enzyme-nanoparticle binding, and enzyme activity. It was discovered that GRLMR-SeBP exerted control over the size of nanoparticles formed. SEM images of nanoparticles formed using 40 mM, 1 mM, 5 mM, and 10 mM SeO_3^{2-} revealed that GRLMR-SeBP formed smaller and less polydisperse sized particles (Figure 2.10). For GRLMR, particle size varied with SeO_3^{2-} concentrations such that at low concentrations SeNPs were smaller, and at high concentrations particles were larger. However, the GRLMR-SeBP construct synthesized ~35 nm diameter particles independent of SeO_3^{2-} concentration at the physiologically relevant SeO_3^{2-} concentrations of 40 mM to 5 mM. This demonstrates that the SeBP exerts remarkable control over SeNP size.

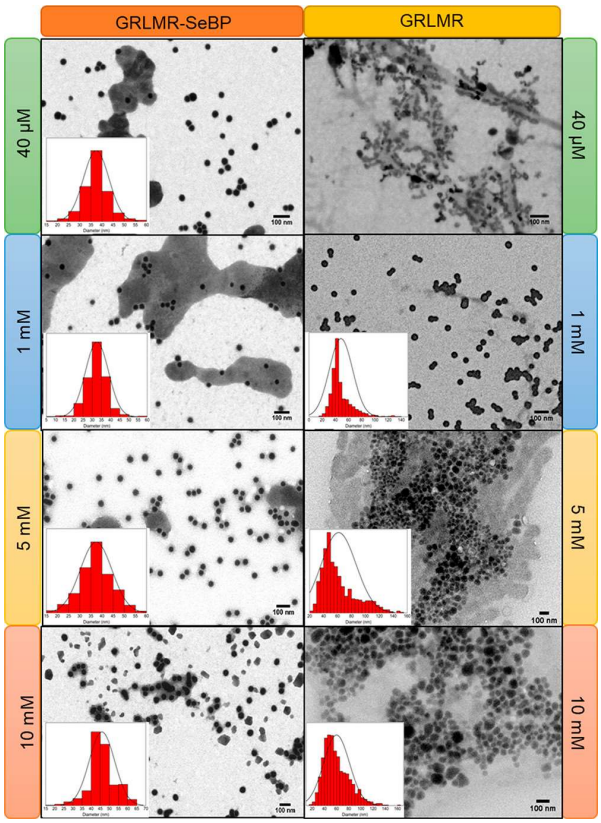

***Figure 2.10**. SEM images of nanoparticles formed using GRLMR-SeBP or GRLMR at indicated concentrations of SeO_3^{2-}. A histogram of the size distributions is shown where it could be determined.*

To compare the abilities of GRLMR-SeBP versus GRLMR to bind SeNPs, two different centrifugation assays were performed. In the first centrifugation assay, SeNPs were enzymatically synthesized, and centrifugation was then used to remove SeNPs from solution along with any associated enzyme. The percentage of bound enzyme was determined by measuring the protein concentration in the soluble fraction after precipitation. It was found that 83.1 ± 1.0% of GRLMR-SeBP was bound to SeNPs, while 14.4 ± 2.6% of GRLMR was bound to SeNPs (Figure 2.11). This demonstrates that concatenation of SeBP to GRLMR improves nanoparticle binding affinity.

In the second centrifugation assay, SeNPs were abiotically synthesized using $NaBH_4$ reduction; the percentage of bound enzyme was again determined by measuring the protein concentration in the soluble fraction after precipitation. GRLMR-SeBP preferentially binds

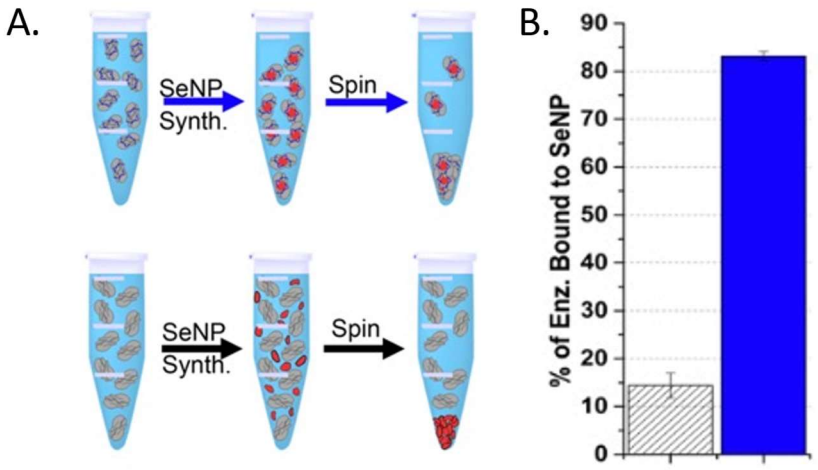

***Figure 2.11**. (a) Overview of the centrifugation assay used to assess enzyme-nanoparticle binding, (b) Percentage of enzyme that remained bound to nanoparticles following centrifugation for GRLMR (diagonal stripe) versus GRLMR-SeBP (blue).*

smaller SeNPs (30 nm or 50 nm) compared to larger SeNPs (125 nm or 900 nm). This indicates that there is an intrinsic preference of GRLMR-SeBP to bind SeNPs that are close to the typical SeNP size formed by enzymatic reduction. These results demonstrate that GRLMR-SeBP forms smaller and more monodisperse SeNPs than GRLMR. The results also demonstrate that concatenating SeBP to GRLMR improves the binding affinity for smaller SeNPs.

Raman spectroscopy was used to confirm enzyme conjugation by monitoring established histidine-metal binding modes and peptide backbone conformation in both free and SeNP bound states. The interpretation of Raman spectra suggested that the SeBP peptide forms covalent bonds to histidine residues via mono- and bivalent conjugation, which is supported by observing conformational shifts in its backbone signature from an unordered structure to a β-sheet configuration. Finally, the enzymatic activities of GRLMR versus GRLMR-SeBP were measured by spectroscopically monitoring NADPH depletion during enzymatic reactions. It was found that the K_M is significantly lower for GRLMR-SeBP than GRLMR alone when $HNaSeO_3$ was used as the substrate (0.22 ± 0.06 mM versus 1.92 ± 1.28 mM). Additionally, the k_{cat} was significantly higher for GRLMR-SeBP than GRLMR when using $HNaSeO_3$ as the substrate (40 ± 2 min^{-1}

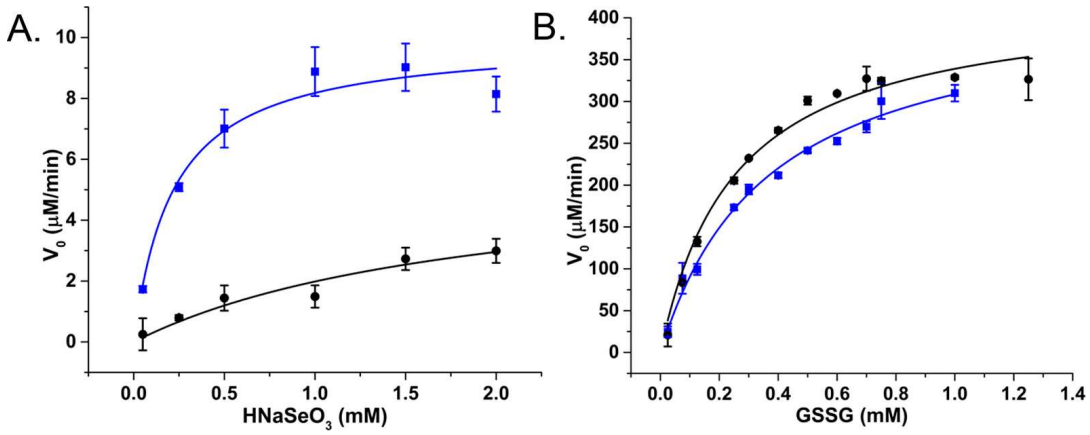

Figure 2.12. *V_0 plotted against substrate concentration of GRLMR (black) and GRLMR-SeBP (blue) using (a) HNaSeO3as a substrate, (b) GSSG as a substrate.*

versus 23 ± 9 min^{-1}). When GSSG was used as the substrate, the measured K_M or k_{cat} values were not significantly different for GRLMR versus GRLMR-SeBP (Figure 2.12). These results indicate that concatenating SeBP to GRLMR leads to a more favourable enzyme-substrate complex and faster enzyme activity when selenite is used as the substrate. A possible reason for the increased enzyme-substrate stability and faster enzyme activity is that SeBP preconcentrates selenite near the active site. This could be due to the introduction of five positively charged histidine residues near the active site.

Overall, the GRLMR-SeBP construct appears to constitute a cloneable SeNP (cSeNP). This construct selects the element (Se) from a background containing many metal(loid) ions; the construct reduces the Se in an NADPH dependent process to form Se precipitates of the red allotrope of Se(0). The SeBP arrests the particle size at a consistent size. Therefore, this construct—which is encoded in DNA—makes 35 nm diameter, spherical red Se nanoparticles that remain associated with the construct.

Assessment of molecular imaging with this cSeNP construct is ongoing and the cSeNP appears effective—localizing SeNPs to the expected intracellular positions of the proteins to which cSeNP is genetically concatenated.

2.3 Motivation for "Multi-Color" cNPs

Above is the 'story of a cSeNP'. For our goal of creating cNPs for imaging applications, multiplexed, simultaneous tagging of different proteins with distinguishable tags is a longer-term goal. Fluorescent proteins that were originally isolated as green (e.g., GFP) were subsequently evolved in laboratories to emit different colors (red, yellow, etc…).[60] The multiple colors of fluorescent protein now enables multiplexed imaging of multiple proteins of interest, each labeled with a different color of fluorescent protein. Similarly, multiple cNP proteins, each producing a distinguishable cNP, comprise a panel of cNPs that enable multiplexed tagging of proteins of interest.

Inorganic NPs can be distinguished in EM on the basis of their elemental composition, size, and/or shape. For other modalities like X-ray imaging, elemental composition of the cNP may be the chief means of distinguishing different cNPs. The basis for distinguishing different elements in EM and X-ray imaging modalities may be as simple as elemental electron density (for instance, it is straightforward to distinguish Au and Ag NPs using TEM, where Au NPs simply have notably higher contrast). However, more sophisticated spectroscopic methods such as EDS and electron energy loss spectroscopy (EELS) can also map elemental compositions in TEM.[74,75] In X-ray imaging, X-ray fluorescence methods may allow elemental mapping (although the resolution may be low) and tuning the X-ray wavelength to absorption edges of particular elements can also distinguish different elements, although variable wavelength X-rays require specialized X-ray sources such as synchrotrons.

In this context, we are working to make size/shape or elementally distinct cNPs. Most of our work to-date has been toward making elementally distinct cNPs.

Identification of a TeO_3^{2-} reductase/mycothione reductase from Rhodococcus erythropolis PR4[49]

In this paper, we began by collecting environmental samples from abandoned mine sites in Clear Creek County, Colorado, USA. Mining in this region dates to the 1851 Colorado Gold Rush, and most mines have not been active for over a century. Many of these mines leach mine runoff that carries substantial metal contamination.

The environmental sampling was facilitated by the Clear Creek Watershed Foundation—a nonprofit organization dedicated to the cleanup of mine sites in Clear Creek County, whose mine runoff contaminates Clear Creek with toxic metals.

Here, we worked under the hypothesis that microorganisms that survive in normally lethal concentrations of toxic metals may reduce these metals to zerovalent form as a means of detoxification. One of the isolates from this sample collection was able to grow on LB-Agar that contained normally lethal concentrations of Fe(II), Cu(II), AsO_3^{2-}, SeO_3^{2-}, TeO_3^{2-}, Cd(II) and Zn(II).

To discover any inorganic oxidoreductases involved in this remarkable set of metal tolerances, we followed the same procedure that we used to isolate GRLMR from the Se specialized *P. moraviensis* stanleyae. This involves first fractionating all soluble proteins on one or more non-denaturing gels, then staining gels with different metal salts and enzyme cofactors, and finally performing proteomic mass spectrometry analysis on any bands that appear from combinations of enzyme cofactors and metal salts to identify enzymes that may have precipitated the metal salts.

Figure 2.13 shows the results of this screening for metal(loid) reductase activity in this isolate. Among the inorganic ions tested, only TeO_3^{2-} was enzymatically reduced in-gel (Figure 2.13, panel A). Proteomic mass spectrometry revealed 13 proteins associated with the precipitate, 4 of which are NAD(P)H dependent enzymes (Figure 2.13, panel B). Of those enzymes, we judged

(A)

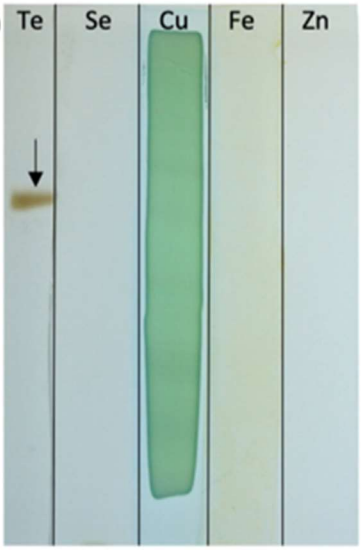

(B)

MS Identified Proteins	M_W
Putrescine Oxidase	*49 kDa*
β-ketoadipyl-CoA Thiolase	42 kDa
Mycothione Reductase	*49 kDa*
Malate Dehydrogenase	*41 kDa*
Aminopeptidase N	91 kDa
Superoxide Dismutase	23 kDa
Enoyl-CoA Hydratase	27 kDa
Thioredoxin Reductase	*35 kDa*
3-hydroxyisobutyrate Dehydrogenase	*30 kDa*
RNA Polymerase Subunit α	38 kDa
Zinc-Dependent Metalloprotease	50 kDa
Metallo-hydrolase	48 kDa
Phosphoenolpyruvate Carboxykinase	67 kDa

Figure 2.13. *(A) Native PAGE gel sections incubated in indicated metal(loid) ions and NADPH. The arrow indicates reduced insoluble Te(0) particulate. Cu(II) was precipitated in gel with and without protein. (B) Proteins associated with the excised Te(0) by LC-MS/MS. Entries in italics indicate the presence of an NAD(P)H binding domain.*

the mycothione reductase to be of the greatest interest because it belongs to the same class I pyridine nucleotide-disulphide oxidoreductase enzyme family as GRLMR and mercuric reductase. Notably, mycothione reductase fills a similar role as glutathione reductase; in mycothione containing organisms, mycothione is used to establish redox balance—whereas in most organisms, GSH accomplishes this.

Mass spectrometry identified the organism as *Rhodococcus erythropolis* PR4. The genome of this organism was already sequenced and available in published sequence databases. We used the existing genomic information to determine the sequence of the mycothione reductase, and then expressed and purified this enzyme recombinantly from BL21 *E. coli*.

In *in vitro* experiments, the mycothione reductase was found to have significant selectivity for tellurite over selenite. This was surprising because the oxyanions are very similar, and the reduction potential for selenite makes it easier to reduce than tellurite. The standard reduction of potential for the reaction $TeO_3^{2-} + 3\ H_2O + 4e^- \leftarrow\rightarrow Te + 6\ OH^-$ is −0.57 V vs Hydrogen. The

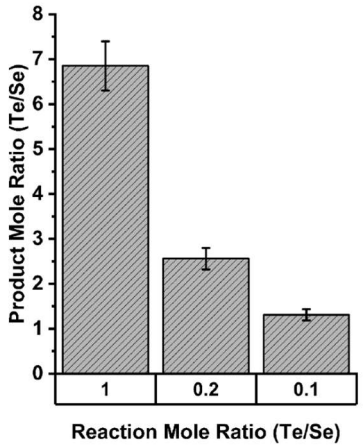

Figure 2.14. *Elemental composition of precipitates resulting from enzymatic reactions in indicated ratios of tellurite and selenite as determined by ICP MS.*

corresponding reduction of SeO_3^{2-} is −0.366 V. Thus, SeO_3^{2-} is the preferred substrate for reduction in the absence of a mechanism for substrate selectivity.

This selectivity for Te over Se was quantified in assays in which both TeO_3^{2-} and SeO_3^{2-} were present in different molar ratios. Figure 2.14 shows that in equimolar concentrations of Te and Se, the enzymatic precipitant incorporated 7 tellurium atoms for each selenium atom as determined by inductively coupled plasma mass spectrometry analysis. Even when selenium was present in a 10-fold excess to tellurium, the enzymatic products incorporated tellurium in an almost 2:1 ratio.

This selectivity was found to depend on pH. Assays done at pH values of 6, 7, 8 and 9 showed the greatest discrimination between tellurium and selenium at pH 6, with decreasing selectivity as pH rises (Figure 2.15).

In this paper, we postulated a mechanism for selectivity of tellurium over selenium by the mycothione reductase which we now view as flawed. Here, we postulate what we believe to be a more plausible mechanism for enzymatic preference of Te over Se.

A homology model for the structure of mycothione reductase was generated with Phyre2. This homology model was subsequently aligned with GRLMR in Pymol to show mutations which may contribute to the observed substrate specificity.

Several notable mutations in mycothione reductase are located in an apparent cavity that is oppositional to the putative substrate entry channel of GRLMR. Four of the seven mutations within this region result in aromatic residues for mycothione reductase, with several of these residues being Histidine. This set of aromatic residues may contract the immediately surrounding region through π-π stacking interactions; this contraction may expand the substrate entry channel, accommodating of TeO_3^{2-}, which is a larger substrate than SeO_3^{2-}. The protonation of the histidine

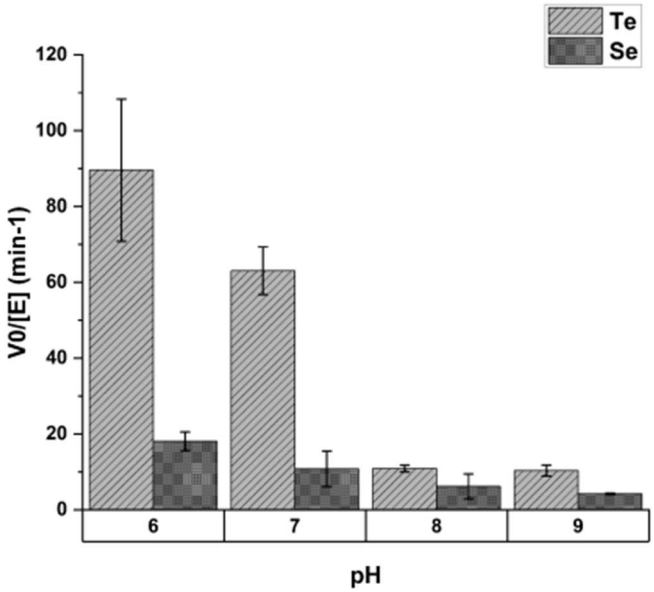

Figure 2.15*. The effect of pH on mycothione reductase substrate selectivity; Y-axis shows initial velocity of mycothione reductase with tellurite or selenite. Each substrate was present at 2 nM.*

residues at lower pH values is implicated in this structural rearrangement by the pH dependence of the observed selectivity.

In summary, we isolated a Class I pyridine nucleotide-disulphide oxidoreductase that is specialized for tellurite reduction. This is a curious finding because tellurite reduction is energetically more difficult than selenite reduction, and selenite and tellurite are otherwise very similar oxyanions. This enzyme currently represents a lower priority for our adaptation to a cNP purpose because of the toxicity of tellurium. However, it is attractive for adaptation because mycothione is not present in most cells, meaning TeO_3^{2-} will not be competing with mycothione as a substrate. (In our testing, the mycothione reductase did not act upon oxidized glutathione in any detectable manner.)

Enzyme-Catalyzed in Situ Synthesis of Temporally and Spatially Distinct CdSe Quantum Dots in Biological Backgrounds[76]

Metal chalcogenide semiconductor nanoparticles are often referred to as quantum dots. This naming reflects the observation that electrons within semiconductor nanoparticles behave like a quantum particle in a box. Quantum dots can be very bright luminescent emitters with quantum yields over 90%. This makes quantum dots attractive as potential luminescent labels in optical or fluorescence microscopy.

Many semiconductor nanoparticles are made as metal-selenides, for example, CdSe. In this paper, we found that when Cd^{2+} ions are included in the synthesis of SeNPs by GRLMR, what results are luminescent CdSe nanoparticle quantum dots, instead of the non-emissive SeNPs that we made previously. Therefore, GRLMR joins cystathionine γ-lyase from *Stenotrophomonas maltophilia*[77,78] and nitrate reductase from *Fusarium oxysporum*[79] in a category of enzymes that generate active monomers to help mediate metal nanoparticle growth.

In prior papers that identified enzymes that synthesize quantum dots, a general theme is that the enzymes generate dianionic chalcogenides (e.g., S^{2-} from cysteine). These dianionic chalcogenides then crystalize with dicationic metals (e.g., Cd^{2+}). The resulting nanocrystals comprise quantum dots.

Following this rationale, we hypothesized that GRLMR might reduce GS-Se-SG (where Se's oxidation state is +2) to Se^{2-}. The Se^{2-}ions could then crystallize with any Cd^{2+} forming fluorescent semiconductor nanocrystals. This rationale is summarized in Figure 2.16. In this rationale, the presence of dissolved oxygen oxidizes Se^{2-} to Se(0) which forms the usual observed SeNP product of GRLMR. Evidence for this hypothesis arises from the observation that the QDs only form when oxygen is excluded from GRLMR catalyzed SeNP synthesis in the presence of Cd^{2+}.

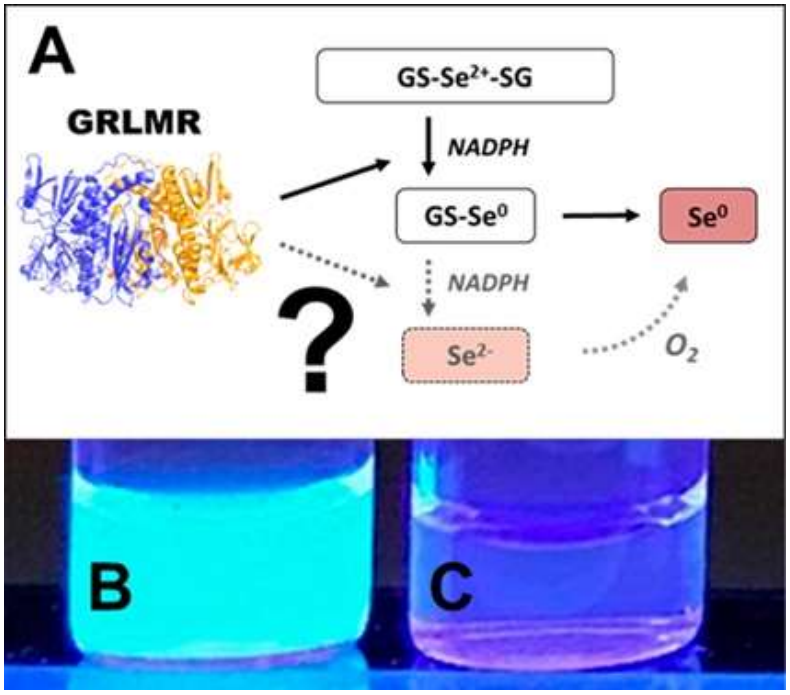

Figure 2.16. *(A) Sketch of suggested selenite reduction pathway via GRLMR. Fluorescence can be visualized through UV illumination of particles formed by reduction of Se^{2+} to Se^{2-} by GRLMR with Cd^{2+} present in (B) air-free conditions and (C) in atmosphere.*

Much of this paper describes mechanistic work showing that while GSH can also reduce SeO_3^{2-} to Se(0) and Se^{2-}, the rate of this process is slow compared to the enzymatic process. Overall, this paper shows that GRLMR can be used to form CdSe semiconductor quantum dots. This is appealing because of the possibility of making cNPs that are both electron dense and fluorescent. Such a tool is useful in the emerging field of CLEM—where fluorescence microscopy images are used to determine which parts of a sample should be examined at high resolution by EM, and which parts are of less interest.

2.4 Other Approaches to Cloneable Contrast in EM

In addition to the cNP approach, we have attempted to form cloneable contrast agents from the naturally occurring metal handling proteins Dps and metallothionein. The Dps approach failed completely and has never been published. The metallothionein approach functions in the limited circumstances of high-copy number proteins in fixed cells, as outlined below.

Metallothionein as a cloneable tag for protein localization by electron microscopy of cells[80]

We explored the use of metallothionein as a cloneable contrast tag. Metallothioneins are small cysteine rich proteins belonging to the broader class of phytochelatins. Such proteins are naturally expressed during heavy metal stress to most cells. The cysteine-rich proteins chelate metal ions, helping to sequester and reduce toxic effects of metals. There is some prior history of investigation of metallothionein as a cloneable contrast agent by others.

Previous studies demonstrated by mass-spectrophotometric measurement that metallothionein can capture enough gold atoms to theoretically be visible in cellular electron microscopy. Metallothionein can achieve this function when conjugated to a protein.[63] These studies increased the appeal of metallothionein as a cloneable contrast tag but did not demonstrate success in imaging.

We do not define cloneable contrast tags formed by metallothionein as a biogenic cNP for three reasons. First, these tags are essentially inorganic coordination complexes—which are not classically 'particulate'—even as they may appear as such in an electron microscope. Second, the chemistries developed that allow successful imaging of metallothionein are incompatible with living cells; more specifically, the chemistries developed here use Au^{n+} salts, which are quite reactive with living cells. Finally, a cNP can be modified by altering the DNA encoding the cNP. In an approach where the underlying chemistry is stoichiometric binding of metal ions to cysteine, the only way to modify the construct to modify metal activity is adding or removing cysteine residues to the protein. This manipulation is only able to modify the number of metal ions coordinated—i.e., changing the DNA cannot dramatically modify materials properties such as elemental composition, crystal structure, size, or shape.

Nonetheless, metallothionein is appealing for potential applications as a cloneable contrast tag, whose electron scattering properties could be enhanced post-fixation and before EM imaging.

In this study, we attempted to label several proteins, which provided an assessment of how well metallothionein performed as a cloneable contrast tag. Metallothioneins range in weight from 0.5-14 kDa, which satisfies the requirement of a small-size tag. To assess the ability of metallothionein to label proteins with a high copy number, wild-type desmin (a filamenting protein) was tagged with a single metallothionein and expressed in bacteria. After desmin was freeze-substituted and treated with aurothiomalate, the metallothionein-labeled desmin showed staining with small particles. Furthermore, this type of staining was not seen in the wild-type desmin, which indicated that the staining was due to metallothionein and that the staining resulted in a good signal to noise ratio (Figure 2.17).

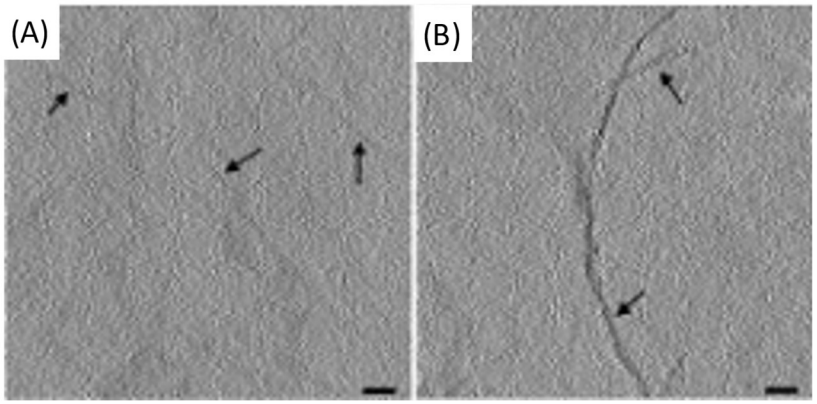

Figure 2.17*. Tomographic slices of (A) wild-type desmin (B) metallothionein -labeled desmin. Scale bars = 100 nm.*

To assess the ability of metallothionein to localize a tagged protein in the complex environment of a cell, an SPC42 protein product was tagged with two copies of metallothionein. SPC42 is a component of the yeast spindle pole body and is located approximately at the plane of the nuclear envelope. It was found that following the same procedure as followed for desmin did not yield adequate signal. Instead, use of a Nanoprobes gold enhancement kit was required (Figure 2.18). To this point, sections were stained with aurothiomalate after freeze substitution. Therefore, staining during the process of freeze substitution was assessed next.

It was found that the best signal was achieved by first staining sections with $Au(III)Cl_3$ during freeze-substitution, then treating samples with diglyme, and finally enhancing using a silver enhancement protocol.[81] Control samples not tagged with metallothionein did not show staining, regardless of whether they underwent the diglyme and silver enhancement protocol. However, metallothionein tagged samples that underwent staining during freeze-substitution, diglyme treatment, and silver enhancement showed strong labeling, which allowed single particles to be detected (Figure 2.19). The studies using desmin and spc42 provide evidence that metallothionein can reveal the location of proteins with many copies localized to a small area.

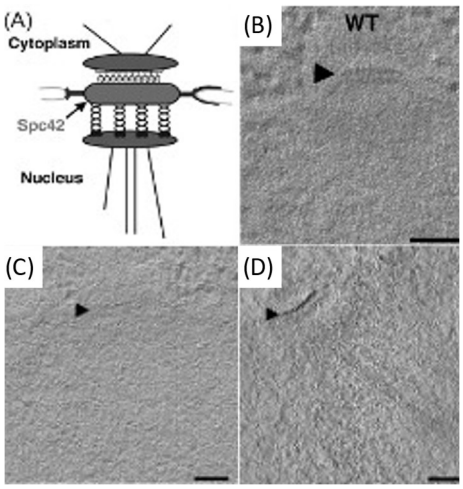

Figure 2.18. *(A) Diagram of spc42; the metallothionein tag was added to the C-terminus. (B) Tomographic slices of wild-type spc42. Tomographic slices of Spc42-2x metallothionein (C) incubated with aurothiomalate alone, and (D) first stained with aurothiomalate followed by enhancement with the Nanoprobes gold enhancement kit. Scale bars = 100 nm.*

To assess the capabilities of metallothionein as a tag for low-copy number proteins, protein components of the nuclear-pore complex were tagged with metallothionein and stained. No staining of the nuclear pore complex was observed, although many staining and enhancement protocols were attempted.

Despite unsuccessful attempts to stain components of the NPC, the successful applications of metallothionein to stain both desmin and spc42 demonstrates the potential of metallothionein as a cloneable contrast tag in fixed cells.

Overall, this paper shows that metallothionein can be effective to localize high copy number proteins that are concentrated in specific areas, such as filamentous or ultrastructural proteins. For low copy number or isolated proteins, metallothionein does not appear effective. These approaches with metallothionein also require that cells are fixed before metal incubation and are therefore somewhat limited compared to the cNP platform approach, which can use essential elements to form high contrast particles in live cells.

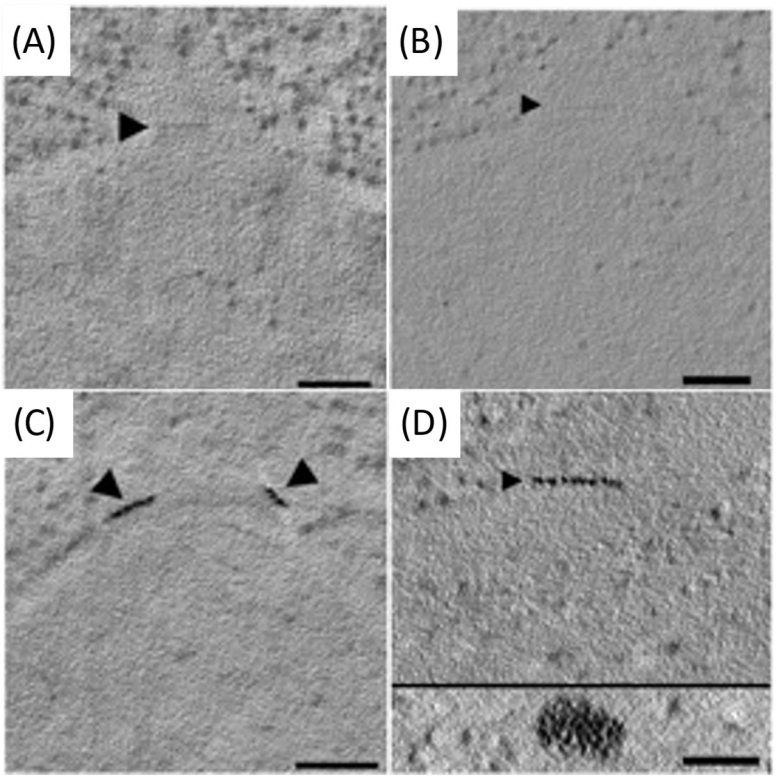

Figure 2.19. *Staining of wild-type spc42 during freeze substitution (A) without diglyme treatment and silver enhancement and (B) with diglyme treatment and silver enhancement. Staining is not observed in either condition. Staining of Spc42-2xMTH sections (C) without diglyme and silver enhancement and (D) with diglyme treatment and silver enhancement, which allowed for the detection of particles (D, inset). Scale bars = 100 nm.*

Dps as a cloneable tag

Iron oxide encapsulating proteins such as ferritin and Dps create iron oxides that can be identified in electron microscopy. Ferritin has been investigated as a cloneable tag.[3] Ferritin is comprised of 24 protein subunits that assemble into a capsule which can contain an iron oxide core of up to ~8 nm in diameter. Concatenating a ferritin subunit to a protein of interest at the DNA level can cause a ferritin capsule to become attached to that protein of interest. This approach has not become widely used because several proteins of interest can become integrated into a single ferritin capsule. This cross-linking, as well as the sheer size of ferritin, are likely to cause artifactual observations around the localization of the protein of interest.

An improvement on this approach may be to use Dps, which is sometimes described as a mini-ferritin. Dps is a capsule protein comprised of 12 subunits, which can contain an iron oxide mineral up to ~4 nm in diameter, which can be visualized in cells. A 'single-chain' Dps—where up to 12 Dps protomers are linked with a flexible linker sequence at the DNA level is in principle possible.

Our work on Dps involved making the DNA that encodes Dps from 12 Dps protomers, each linked by a flexible linker. Despite many attempts, we were unable to express functional Dps as a 12-mer, 6-mer, 4-mer or 3-mer construct. For now, we hypothesize the linker that we chose may have been incompatible with DPS folding and therefore function. We hypothesize that different linkers might allow DPS protomers to be linked into functional units, using modern computational protein folding assessment tools to identify successful linkers.

2.5 Outlook and Future Directions for cNPs

As a field, synthetic chemistry aims to develop and improve methods for creation of well-defined molecules and materials. The synthetic chemistry sub-field of organic synthesis is particularly impressive in this regard, with well-developed methods for discrete addition or removal of atoms to defined locations in complex molecules. Cyclization reactions, solid phase synthesis and enantioselective control, among other tools, facilitate the precision synthesis of carbon-rich products including pharmaceuticals, oligonucleotides, and plastics.

Outside of organic synthesis, precise 'magic number' nanoclusters are now routinely made with atomic precision and resulting defined structure, up to about ~500 metal atoms. These nanoclusters are already used as extrinsic biological contrast agents, catalysts, and their continued synthetic exploration allows advancement of fundamental knowledge of cluster physics. Improved control over NP synthesis in biological contexts is a logical (and destined) progression.

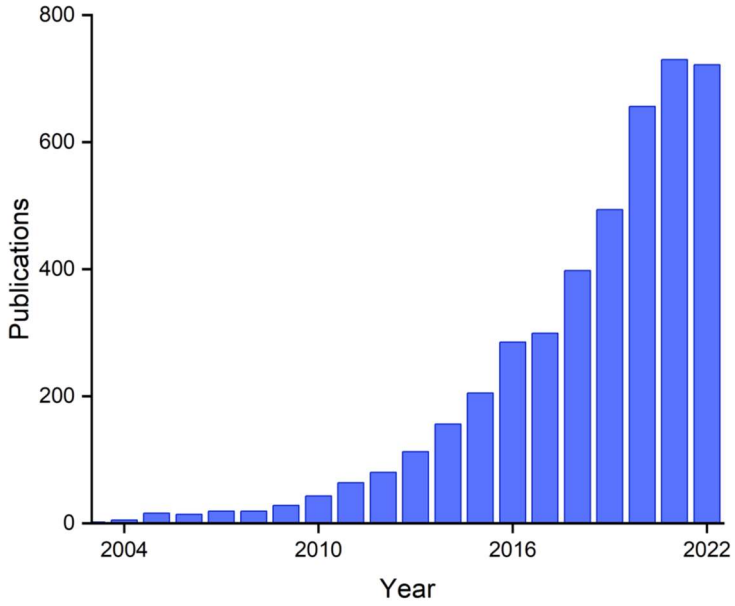

***Figure 2.20**. Papers on the topic of 'biogenic nanoparticles' per year, from Web of Science.*

Research on biogenic NPs appears to be currently in a "gold rush" era, with sharply growing numbers of active researchers and publications (Figure 2.20). These publications include those that address fundamental aspects of nanoparticle chemistry, new synthetic routes, and a wide variety of potential applications. The research area is presently highly interdisciplinary, with contributions coming from chemists, physicists, geologists, and microbiologists.

As the field of biogenic nanoparticles continues to develop, we anticipate an increasing emphasis on synthetic precision, by analogy to the development of other synthetic chemistry sub-fields. We postulate that the cNP platform approach, which mixes and matches well-defined metal oxidoreductases and proteins and peptides that enforce NP shape, provides a robust approach to improving biogenic NP precision and design. Biological evolution over eons has produced many examples of atomically precise/defined molecules. For bio-organic synthesis, biology often allows synthetic organic transformations that are difficult or impossible to achieve in vitro. It's an ambition of ours to push cNP synthesis to achieve similar levels of atomic precision in nanomaterials synthesis, using well-defined biological approaches.

One way to conceptualize this approach is as an extension of the central dogma of molecular biology. This states that DNA contains all the information to create an atomically precise protein. To convert DNA information into protein function, the DNA is transcribed into RNA, which is then translated into functional proteins.

Extending this dogma to cNP synthesis, we suggest that DNA (information) can be transcribed into mRNA (information transfer) which is then translated into protein (translating information into function). The protein then creates a cNP, translating function into discrete synthetic product. This approach suggests the possibility of next-generation nanoscale materials where the synthetic information is not contained in journal-article text, but rather in DNA sequence.

Much in the same way that unnatural amino acid incorporation has expanded the "chemical space" that biology is allowed to partake in, so too will cNPs open the door to exploring new interfaces of nanoscale inorganic nanomaterials and biosystems. As we approach this paradigm, we ask ourselves: what new and exciting things will be discovered?

cNP synthesis does have intrinsic limitations. Not every metal(loid) on the periodic table, for instance, is compatible with redox reactions that are biologically achievable. Elements with redox potentials outside the range of –1.0 V to 1.0 V relative to SHE will either be too favorable for controlled reduction or too unfavorable for any redox chemistry to occur at all. In the case of 'uncontrolled' reduction—oxidation of ubiquitous biomolecules such as sugars, tyrosine and tryptophan, and nucleobases by easily reduced elements is likely to be implicated. Such elements are likely to be reduced in nonspecific ways within biological matrices. Pourbaix diagrams describe expected redox potential versus pH and can help identify elements that are good candidates for inclusion in cNPs.[82,83]

For our target applications in imaging, electron-rich (e.g., higher-Z) elements are the most attractive, as they provide greater contrast relative to the less electron rich elements of C, O, N, H and P that comprise most of the biological matrix. Based on these considerations, Zn, As, Te, Fe, Cd, Se, Bi and Co ions are of highest interest for cNP incorporation because of relatively favorable redox potentials and Z-values. We consider comparably toxic elements as lower priority choices. Although the cNP machinery may confer tolerance to elements such as Cd and Te, their intrinsic toxicity at small concentrations presents complications that are less pronounced for biologically essential elements such as Zn, Fe and Se, as well as elements that are generally less toxic such as Bi (a component in pharmaceuticals such as Pepto-Bismol). Bismuth is particularly attractive for our future work as it is the most electron-rich non-radioactive element on the periodic table.

Many metal(loid) oxidoreductases are comparatively large proteins. Class I pyridine nucleotide-disulphide oxidoreductases, including GRLMR, are typically ~100 kDa homodimers—before they are saddled with an attached inorganic nanoparticle.[47–49,84] For comparison, widely used fluorescent proteins like GFP are ~27 kDa monomers. GFP is well known to alter the biological activity of many of the proteins that it is concatenated to, potentially resulting in artefactual observations.[85,86] It's hypothesized that larger 'tags' are more likely to alter biological activity of concatenated proteins; large size can hinder POI diffusion kinetics and position contrasting markers distally to the point of interest, whereas multimericity can convolute labelling efficiency. Therefore, one of our future directions in cNP synthesis is to develop smaller inorganic oxidoreductases.

We are investigating approaches for making GRLMR a functional monomer of decreased mass. Other metal(loid) oxidoreductase enzymes may be of interest as starting points for further engineering. For instance, a 27 kDa NADH-dependent cytochrome b_5 reductase was recently

isolated from a strain of *Muchor racemosus*[87,88]; similar to GRLMR, the enzyme conveys nanoparticle-mediated metal tolerance to silver and palladium when cloned into laboratory microorganisms. Alternatively, arsenate reductase[89] may be amenable to engineering processes that alter its substrate specificity to metals other pnictides such as Bismuth.

It is possible that newfound and promising enzymatic systems may possess kinetics or substrate specificity that nullify their otherwise ideal characteristics (e.g., mass, stability, metal(loid) reduction, monomericity, etc.). Given the discrete genetic nature of cNPs, we offer the prospect of using directed evolution as a means of manipulating enzyme function to better serve the needs of cloneable contrast. Doing so will necessitate the development of robust selection methods for metal reductases, which is a relatively unexplored area.

2.6 Conclusions

In this feature-article, we have described the development of a cNP platform technology. Our main goal is to develop cNP based cloneable contrast agents for biological imaging. It is conceivable that our approach may one day result in a single cloneable contrast agent that allows imaging in many modalities (optical, fluorescent, electron, X-ray, magnetic imaging). We are also interested, to a lesser extent, in using cNP approaches for bioremediation of toxic metals.

The platform is not limited to applications in imaging and bioremediation. Rather, we expect that many applications explored for biogenic NPs such as biomining and solar photoconversion might one day benefit from the increased precision of synthetic product made possible with the well-defined components of this platform and their intrinsic linkage to laboratory evolvable DNA sequences. The intracellular aspect of cNP synthesis further offers the prospect of integrating cNPs with other cellular processes to offer the prospect of cellular engineering to accomplish yet unimagined goals.

Manuscript adapted for dissertation submission[90]*. Author contributions: ARH (lead author),* ***BFG*** *(2nd author), RSC, GAE, TT (co-authors), and CJA (principal investigator) wrote initial draft and edited. KMB (co-author) edited.*

CHAPTER 3: CLONEABLE SELENIUM NANOPARTICLES AS MULTI-MODAL BIO-IMAGING CONTRAST AGENTS

3.0 Synopsis

Cloneable contrast in biological microscopy is exemplified by fluorescent proteins such as Green Fluorescent Protein (GFP) in biological fluorescence microscopy. There are no similarly useful cloneable contrast agents that function in biological electron microscopy. GFP doesn't impart contrast in EM because EM contrast arises from differences in electron density, and GFP does not have appreciably different electron density compared to other biomolecules. This paper reports a cloneable Selenium NanoParticle (cSeNP) that can impart protein-based molecular contrast in imaging modalities including cellular electron microscopy, fluorescence microscopy, and X-ray computed tomography. The cSeNP is a Selenium nanoparticle that is made by a protein that reduces selenodiglutathione (the intracellular form of the essential element Se) into zerovalent SeNPs. The cSeNP protein also binds to the SeNP that it synthesizes and controls its size. DNA encoding the cSeNP was concatenated to DNA encoding FtsZ, the procaryotic analog of tubulin. FtsZ is membrane associated and localizes to the mid-point of dividing cells. *Escherichia coli* cells expressing FtsZ-cSeNP fusions were examined. Transmission electron microscopy, cellular electron tomography and fluorescence light microscopy show SeNP decorated FtsZ filaments outside of cells, as well as FtsZ-cSeNP signals or densities localizing to expected FtsZ locations. CT imaging shows contrast attributable to cSeNPs is distinguishable from background in *E. coli*. The cSeNP, therefore, represents a cloneable imaging contrast agent that facilitates location and correlation of proteins-of-interest across all biological length scales.

3.1 Introduction

Cloneable contrast is well established in fluorescence microscopy, exemplified by Green Fluorescent Protein (GFP).[2,91] What makes GFP and related fluorescent proteins useful in fluorescence microscopy is that the DNA encoding GFP can be concatenated to the DNA encoding any protein of interest (POI). When that DNA is expressed in cells, a GFP-POI fusion protein is created. The physiological location of the POI can then be determined on the basis of GFP fluorescence. The widespread adoption and utility of fluorescent proteins was recognized by the 2008 Nobel Prize in Chemistry.

GFP is a 'cloneable fluorophore' because the instructions to make the fluorophore are genetically encoded in DNA. Modification of DNA encoding GFP can alter the fluorophore absorption/emission wavelengths, and therefore the color of the fluorescent protein. The DNA encoding GFP can be recombinantly inserted into other organisms, endowing those organisms with the capability of producing fluorescent proteins.

The 'cloneable contrast' paradigm of fluorescent proteins in light-based microscopy inspires cloneable (genetically encoded), protein-based, contrast approaches in other imaging modalities. Despite significant efforts, there are no widely used and robust cloneable contrast agents that function in electron microscopy of cells. A "GFP for cellular EM" is sometimes referred to by biological electron microscopists as a "holy grail."

Biological EM is currently a rapidly growing method. It is instrumental to the overarching goals of integrative structural biology.[92,93] Whereas 'classical' structural biology aimed to determine atomically resolved structures of individual biopolymers (proteins and nucleic acids), integrative structural biology aims to contextualize such structures in their cellular, tissue, and

organismal context. An ultimate goal of integrative structural biology is producing empirically informed 3D atomic resolution models of entire cells, or even tissues and organisms.

3D electron microscopy (3DEM) presently produces the highest resolution images of cells, and now outpaces x-ray crystallography in production of empirical atomistic structures of biomolecules. 3DEM overall comprises 3 distinct methods. At the largest sample volumes, volume Electron Microscopy (vEM) now produces 3D reconstruction of organs, exemplified by the drosophila brain and connectome. Cryo-electron tomography (cryo-ET) of individual cells, and sub-tomogram averaging to produce atomistic models of biomolecules. The methods of vEM and cryo-ET differ in sample preparation – in vEM, samples are typically chemically fixed and plastic embedded, facilitating serial sectioning of larger volumes. Such fixation and plastic embedding introduce artifacts, such as membrane distortion. In contrast, in cryo-ET, cells are preserved by vitrification (rapid freezing, so that solvent solidifies in a glassy, amorphous state). Vitrification can be accomplished by high-pressure freezing or plunge freezing into a liquid ethane/propane mixture, both of which allow the samples to freeze without formation of ice crystals. Cryo-ET imaging of such cells produces 3D images of cells at ~3nm resolution (where resolution is limited by beam damage to the sample).

At the ~3 nm resolution of cryo-ET, protein and nucleic acid densities are visible. However, only the largest biomacromolecular complexes, such as ribosomes and filaments, can be reliably identified. Significant machine learning efforts to identify additional proteins, based solely on their observed shapes in cryo-ET are ongoing. However, the theoretical limits on this approach mean that at least 60% of the proteome is too small to identify and therefore localize. Due to plastic embedding used in vEM, protein and nucleic acid densities are more difficult to identify than they are in cryo-ET.

To localize most POIs within vEM or cryo-ET reconstructions, therefore, most proteins will need added contrast. Four approaches to imparting contrast on POIs in TEM are previously reported. These are: (1) inorganic nanoparticle conjugates; (2) *in situ* inorganic nanoparticle synthesis on cysteine rich proteins; (3) osmium staining of osmiophilic polymers generated by singlet-oxygen generating proteins; (4) the use of large proteins with distinctive shapes. Three of these approaches deliver contrast in the form of inorganic elements, whereas one approach uses large and distinctively shaped proteins. Because inorganic elements used for EM contrast are heavier (higher Z) than the carbon/oxygen/nitrogen that comprise most of cell biology, these elements have good contrast against biological background in TEM. However, due to sample preparation and/or imaging constraints, inorganic densities need to be ~5 nm (about 4000 inorganic atoms) in diameter to be unambiguously identifiable in biological micrographs.

Targeted iNP-conjugates, where the conjugate molecule binds to a POI, is an approach used since the 1970s to localize proteins in electron micrographs of biological material. Classically accomplished with antibody-gold nanoparticle conjugates and expanded recently with more sophisticated approaches.[13–16] Another approach involves using cysteine rich proteins, such as metallothionein, to localize inorganic atoms to a protein on the basis of metal coordination to the thiol functional group of cysteine. Each cysteine binds stoichiometrically to one metal ion. Because an iNP must contain about 4000 inorganic atoms (~5 nm diameter iNP) to be unambiguously identifiable in biological EM (e.g., limited electron dose) conditions, it's infeasible to rely only on metal-cysteine interactions to develop contrast. (Typical proteins have about 400 amino acids, and the largest proteins ever described top out at 5000 amino acids). Therefore, the cysteine-rich, metal decorated proteins are subsequently enhanced with additional metal deposition in reductive metal deposition processes. A third approach uses small singlet oxygen generating (SOG) proteins to

provoke polymerization of an osmiophilic polymer at the site of the POI-SOG fusion protein. Subsequent osmium staining reveals the location of the polymer, from which the approximate location of the POI can be inferred. A fourth approach uses relatively large and distinctly shaped proteins, often hollow proteins (encapsulins). On the basis of the size and shape of the encapsuling, it can be identified in biological micrographs without added inorganics. Each of these 4 broad approaches has shortcomings that hinder their widespread adoption as contrast agents in the biological EM community.

To understand the different shortcomings of each approach, we suggest 9 criteria for evaluating biological EM contrast approaches (Table 3.1). This table summarizes each of the 4 previously reported approaches according to whether they fill criteria including cloneability, live cell compatibility, size, toxicity, and so forth. Some of the criteria are self-explanatory (e.g., visibility in electron micrographs). Other criteria (e.g., stoichiometric labeling) need additional explanation. Fluorescent proteins, even though they do not provide contrast in TEM, are included in table 1 for comparison of properties to a truly widely used contrast tool. Table 6.1 also includes the approach described in this paper, which is distinct from previously described approaches.

Table 3.1 summarizes which approaches work in live cells (*in vivo*). For cryo-ET imaging, this is an absolute requirement, because cells are not chemically fixed before the contrast agent is applied. For vEM, function *in vivo* is optional because the cells/organs are usually chemically fixed before imaging. Therefore, *in vivo* contrast that survives fixation can work, but contrast agents (such as exogenously added iNP conjugates) can also be applied after fixation.

Table 3.1 also summarizes which approaches facilitate stoichiometric labeling. A contrast approach with perfect stoichiometry will have exactly one instance of the contrast agent for every instance of the POI. As an example, adding iNP-conjugates to samples will never result in perfect

stoichiometric labeling. If more iNPs than POIs are present, there are background iNPs that complicate interpretation. If more POIs than iNPs are present, then not all POIs are localized. Stoichiometric labeling, in other words, allows quantification of the number of POIs in an image. In the case of encapsulins, SOGs, and iNPs, it is not possible to quantify the number of POIs in an image on the basis of the apparent contrast.

Table 3.1 also includes contrast in light microscopy and X-ray imaging as attractive features of an EM contrast agent. The reason that contrast in other imaging modalities is attractive for biological EM contrast agents is that such imaging modalities facilitate imaging of much larger samples than can be imaged in EM. Biological EM can image samples that are a maximum of ~300 nm in thickness, where the highest resolution reconstructions come from samples thinner than this. Because typical bacterial cells have dimensions on the order of 3 μm and eucaryotic cells have dimensions on the order of 10s of μm, only a small fraction of a cell (often less than 10% of the cell volume) can be imaged in a single biological EM section. POIs often localize to distinct areas within cells (mitochondria, nucleus, Golgi, periplasm, cellular poles, membranes). Therefore, any single 300 nm thick section of a cell may or may not contain a POI.

The method of "Correlative Light and Electron Microscopy" (CLEM) takes advantage of the much larger samples that can be imaged by light microscopy, using fluorophores (such as GFP) to identify regions of interest within a cell for higher resolution examination by EM.[94,95] By correlating the fluorescence signal of a protein in light microscopy with the same locations in electron micrographs, crude localization of POIs becomes possible. This is especially useful in cryo-ET, where samples are made thin enough for EM using a highly technical and time-consuming method of FIB-SEM. Therefore, if an EM contrast agent is also fluorescent, it's

attractive because the same tool facilitates lower resolution localization in large sample volumes and high-resolution localization in EM compatible sample volumes.

Likewise, in vEM of tissues or organs, a POI may be found in a relatively small subset of areas. In samples that are too thick for fluorescence microscopy, EM contrast agents that are also visible in X-ray images may facilitate excision of areas where the POI location is known, followed by higher resolution localization of the POI in fluorescence microscopy, followed by the highest resolution localization by vEM.

Thus, multimodal contrast agents that are visible in X-ray, fluorescence, and EM imaging modalities may facilitate the study of POIs within large organisms with both lower resolution / large area imaging modalities and also high resolution / small area imaging methods (Figure 3.1, panel A), using a single contrast construct.

Table 3.1. *Ten criteria for biological EM contrast agents for localizing proteins*

Property	***Contrast Approach***					
	Ex situ iNP contrast agents	Encapsulins	Singlet Oxygen Generators	*In situ* Metal deposition on cys-rich protein	Fluorescent Proteins	Cloneable Nanoparticles
Examples	iNP-conj VIPER SPOT[96,97]	GEMS, Ferritag, Ferritin[28,31,98]	miniSOG APEX[22,61,99,100]	Metallothionein[18,63,101,102]	GFP	cSeNP (this work)
EM Contrast	✓	✓	✓	✓	✗	✓
Fluorescent	✓	✓	✗*	✗*	✓	✓
X-Ray Contrast	✓	✗	?	?	✗	✓
In vivo contrast	**Varies**	✓	✗	✗	✓	✓
Cloneable	✗	✓	✓	✓	✓	✓
Benign	?	?	?	?	✓	?
Stoichiometric	✗	✗	✗	✓	✓	✓
Organisms	Many	Mammalian Cells	Many	Many	Many	E. coli
Size (protein / inorganic)	**Varies / Varies**	**25nm/none**	**~2nm/diffuse**	**2nm/5nm**	**3nm/none**	**6nm/5nm**
Tag to Target Distance	**Varies**	**50nm**	✗	**2nm**	**1.5nm**	**6nm**

Inorganic nanoparticles (iNPs) can produce distinctive contrast in all commonly used biomedical imaging modalities (Table 3.1),[103] however, they are not 'cloneable' and must be exogenously added to samples. To harness the contrast advantages of iNPs as well as the ease of use of fluorescent proteins, we developed a cNP paradigm (Figure 3.1, panel B).[90] Fundamentally, a cNP is an iNP that is made by a protein. The 'cloneable nanoparticle protein' determines the physicochemical properties (elemental composition, size, morphology, crystal structure, allotrope, etc…) of the iNP that it creates. Because protein sequence and structure are encoded in DNA, therefore the physicochemical properties of the iNP made by the cloneable nanoparticle protein are also encoded in DNA. Changing the DNA sequence encoding the cNP can change the physicochemical properties of the resulting cNP, just as changing the DNA encoding a fluorescent protein can change the color of the protein. Just as 'cloning' the DNA encoding a fluorescent protein into a different organism endows the receiving organism with the capability of producing a fluorescent protein, cloning the DNA encoding a cNP into other organisms endows those organisms with the capability of recombinant production of the cNP.

The DNA encoding a cNP usually encodes a modified inorganic-ion oxidoreductase. Examples include Selenium Reductase, Metalloid Reductase, Tellurite Reductase, Ferroxidase, or Mercuric Reductase.[49,104–107] The enzyme both selects a soluble inorganic ion from a milieu that can contain a variety of essential, bioavailable inorganic ions and alters the oxidation state of the ion from soluble to insoluble (particulate) form. Redox equivalents are provided by NAD(P)H or oxygen. To effect control over nanoparticle size, morphology, crystal structure and so-forth, the enzymes are genetically modified with peptides that were selected for binding to iNPs with a targeted/desired size, morphology and crystal structure.[108] In many cases, such peptides template the formation of iNPs during their synthesis, producing iNPs/cNPs of similar

size/morphology/crystal structure relative to the target/desired size. We recently reviewed the concept.[90]

We demonstrate that a cSeNP (Figure 3.1, panel C) functions as a cloneable contrast agent in electron, X-ray, and visible light-based imaging modalities. The cSeNP is comprised of an obligate homodimer, GS-Se-SG reducing enzyme – Glutathione Reductase-Like Metalloid Reductase(GRLMR) – modified to be a single-chain construct with 2 SeNP binding peptides attached.[50,73] Expression of GRLMR in cells grown in SeO_3^{2-} supplemented media results in a striking-red color, attributable to the red allotrope of intracellular SeNPs (Figure 3.1, panel D).[65]

cSeNPs produce distinctive contrast in X-ray and electron imaging modalities, arising from the higher electron density of Se ($Z = 34$) relative the C, O, N, S, and P ($6 < Z < 16$) atoms comprising cellular samples. SeNPs can react with transition metal cations, forming metal-selenide semiconductor quantum dots (Figure 3.1, panel E), which enables fluorescence contrast.[109]

The cNP paradigm as demonstrated herein fills two gaps in the current bio-imaging contrast toolset. First, because it is visible in X-ray, optical and electron images, it can facilitate correlative imaging studies across all biological length scales (Figure 3.1, panel A). Second, it is a cloneable contrast agent visible in electron microscopy that is produced *inside live cells*. This report is the first to show metal-based cloneable contrast in live cells.

An ongoing challenge in Cryo-ET is the imaging of cells thicker than ~300 nm (the maximum possible sample thickness in current TEMs). Cryo-microtomy to produce sections of vitrified cells is technically challenging and results in knife-compression artifacts. An alternative approach, use of a gallium focused ion beam (FIB) within a scanning electron microscope (SEM) to mill away thick parts of a sample, leaving behind a ~200 nm thick window, has emerged. This method is becoming more widely adopted but is also technically challenging.

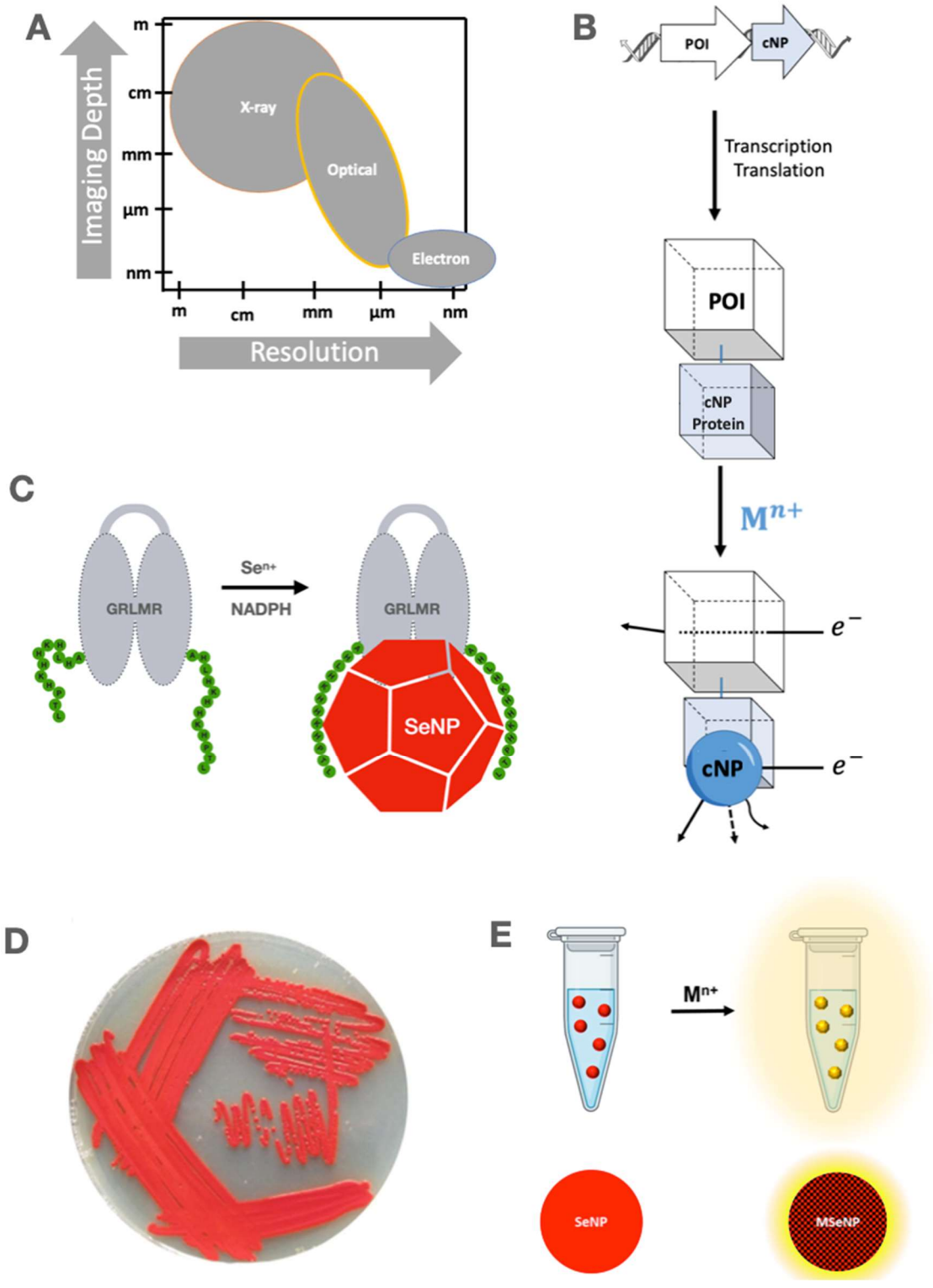

Figure 3.1. *Figure description at top of next page*

Figure 3.1. *Panel A shows a schematic of the length scales and resolution of X-Ray, Optical, and Electron based imaging methods. Panel B shows a schematic of the cNP paradigm, where 'protein of interest' is abbreviated to 'POI'. Panel C shows a schematic of the cSeNP in apo and cSeNP forms. Panel D shows an image of bacteria expressing GRLMR, grown on SeO_3^{2-} supplemented agar. The cell colonies take on the red color because they are producing SeNPs of the red allotrope of Se (α-Se). Panel E shows a schematic of the disproportionation reaction that converts SeNPs to fluorescent metal selenide nanoparticles.*

Imaging at these different length scales necessitates different imaging tools (Figure 3.1, panel A). X-ray computed tomography (X-ray CT) facilitates meter scale imaging of whole organisms at resolutions approaching 50 μm.[110] Light microscopy illuminates cells and tissues at cm length scale and up to ~200 nm resolution.[91] Electron microscopy of biomolecules operates at length scales of up to millimeters and resolutions of ~2 nm for single images and near-atomic resolution for averaged images of multiple copies of identical structures.[111,112]

3.2 Results and Discussion

Cellular EM assessment of FtsZ-cSeNP expression in Escherichia coli.

To assess the cSeNP as a contrast agent in cellular electron microscopy, we fused DNA encoding the 'filamentous temperature sensitive protein Z (FtsZ), a bacterial tubulin homologue, to cSeNP DNA. FtsZ forms protofilaments observed in two forms. In non-dividing cells, FtsZ is found in membrane associated dispersed helical protofilaments, comprised of 30 – 80 FtsZ protomers, extending to lengths of 100 nm. During cell division, protofilaments localize to the cleavage furrow of the dividing cell, forming a Z ring (Figure 3.2, panel A), which is implicated in generating mechanical force driving cell division.37 Protofilaments on average lie 16 nm from the cellular inner membrane. Expression of cSeNP-FtsZ fusion proteins in E. coli should result in SeNPs organized by FtsZ at different points in the cell cycle as shown in Figure 3.2, panels A and B.

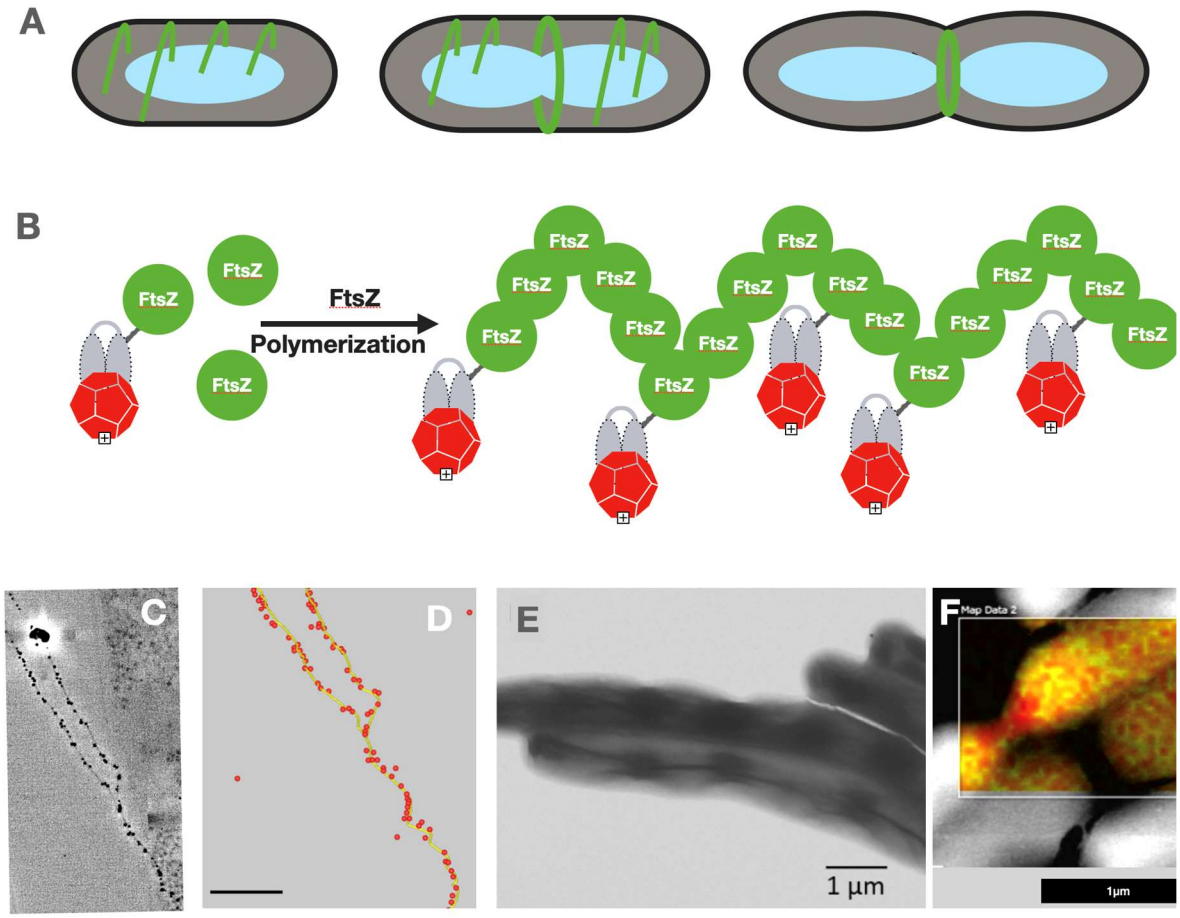

Figure 3.2. *Panel A shows a schematic of FtsZ locations in prokaryotic cells through the cell cycle. Panel B shows a schematic of FtsZ and FtsZ-cSeNP assembling into helical protofilaments. Panel C renders a portion of a transmission electron tomogram of putative FtsZ-cSeNP filaments in vitro. Panel D shows a segmentation of the filaments and cSeNPs from the tomogram in panel C, with filaments rendered in yellow and cSeNPs rendered in red. Additional particles are visible in this rendering that are not visiable in Panel C because the segmented rendering includes the entire tomographic volume (where some stray particles were apparent). Panel E shows E.coli cells grown in 2 mM SeO_3^{2-}, expressing FtsZ-cSeNP which was fixed and imaged after drop-casting on a TEM grid. Due to FtsZ overexpression, this is an elongated cell with several cleavage furrows. Density at these cleavage furrows is attributed to accumulation of FtsZ-cSeNP. We also observe a longitudinal filament. FtsZ is known to form such filaments when overexpressed. A corresponding control made without SeO_3^{2-} addition reveals none of these densities (Appendix A). Panel F shows an STEM-EDS elemental map of a dividing cell. Se is shown in red, Phospohous in yellow.*

We overexpressed FtsZ-cSeNP fusions in E. coli BL21 cells, as described in Appendix A. The population of FtsZ protomers inside the cell, therefore, is comprised of both genomic FtsZ and recombinant FtsZ-cSeNP. FtsZ overexpression interferes with completion of cell division, resulting in cells up to 20 – 30 µm in length, whereas wild-type cells are 3 – 5 µm.[113] In such

extended cells observations of helical protofilaments forming wave-like patterns along the membrane are known.[114]

Substantial optimization work was performed using a high throughput, low resolution whole cell fixation / drop-cast EM imaging method (elaborated in Appendix A). In these experiments, we identified conditions where FtsZ-cSeNP expression resulted in punctate SeNP formation. Figure 3.2 panels C and D show in vitro filaments from lysed cells induced with 1 mM IPTG and 2 mM SeO_3^{2-}. Figure 3.2, panel E shows cells grown in an optimized high expression condition (2.0 mM SeO_3^{2-},1 mM IPTG); Figure A4, panel A shows a SeO_3^{2-} omitted control. In figure 3.2 panel E, contrast increases at cleavage furrows, where FtsZ-cSeNP concentration is expected to be high. Putative longitudinal FtsZ-cSeNP filaments are also observed, consistent with prior observations of such filaments under high level FtsZ overexpression.[114–116] In the control experiment, omitting SeO_3^{2-}, contrast appears uniform across all cells. Figures 3.2 panel F and figure A3 show elemental maps of Se in a dividing cell, collected by scanning transmission electron microscopy-energy dispersive X-ray spectroscopy (STEM-EDS). These images show that the density at the cleavage furrow is Se-rich.

FtsZ filamentation and function in vivo requires a delicate balance of division proteins. High levels of FtsZ-GFP overexpression are known to disrupt its native function. We performed another series of optimizations to better mimic native FtsZ localization by modulating induction levels with an IPTG screen (Appendix A) and by moving the cSeNP tag to the N-terminus of FtsZ. We determined that a medium level expression of the cSeNP-FtsZ chimera with 100 – 250 μM IPTG was optimal regarding cell phenotype and Se-based contrast. We acquired 11 electron tomograms of E. coli BL21 plastic sections. The cells were prepared under optimized cSeNP-FtsZ expression conditions. We found that solvents typically used in plastic embedding, such as acetone,

dissolve SeNPs (Figures A11 & A12). We found that the SeNPs could be stabilized against dissolution, post-fixation, by adding $Cu(OAc)_2$ to the fixed cells. This treatment transforms amorphous SeNPs to crystalline CuSeNPs (Figure 3.1, panel E), in a process we describe elsewhere.[109] The resulting CuSeNPs resist solvent dissolution (Figure A12).

We made additional modifications to the conventional fixation and embedment protocols. We omitted the metal stains typically added to plastic sections that react with specific functional groups in biomolecules, such as osmium tetroxide (membrane staining) and uranyl acetate (nonspecific protein, nucleic acid staining). These metal stains were omitted because they may form granules that complicate the assignment of cSeNP densities. The resulting tomograms are of lower than typical contrast. Note also that fixation and embedment is known to result in some ultrastructure distortions.[117]

Figure 3.3 shows renderings and analysis of electron tomographic reconstructions of experimental and control cells. Panel A shows 75 of 340 slices through an *E. coli* cell expressing FtsZ-cSeNP, grown in 2 mM SeO_3^{2-} for 3 hours following the ramp up protocol described in appendix A. Two features are readily apparent: (1) the outer membrane (OM) and portions of the inner membrane (IM); (2) punctate densities elementally mapped to CuSeNPs.

Figure 3.3, Panel A shows a slice through the tomogram, where a few CuSeNPs are highlighted. Panel B shows a magnified view of the boxed area panel A, with the OM segmented in blue. The CuSeNPs have sufficient contrast for automatic segmentation using the findbeads3d script available in IMOD.[118,119] The user inputs the expected nanoparticle size in pixels, and the program automatically distinguishes particle contrast from cellular background, removing human bias. We demonstrated this process using an isosurface rendering (Figure 3.3 panel C, magenta objects) to compare thresholding from cCuSe cells (Figure 3.3 panel A) with control cells that do

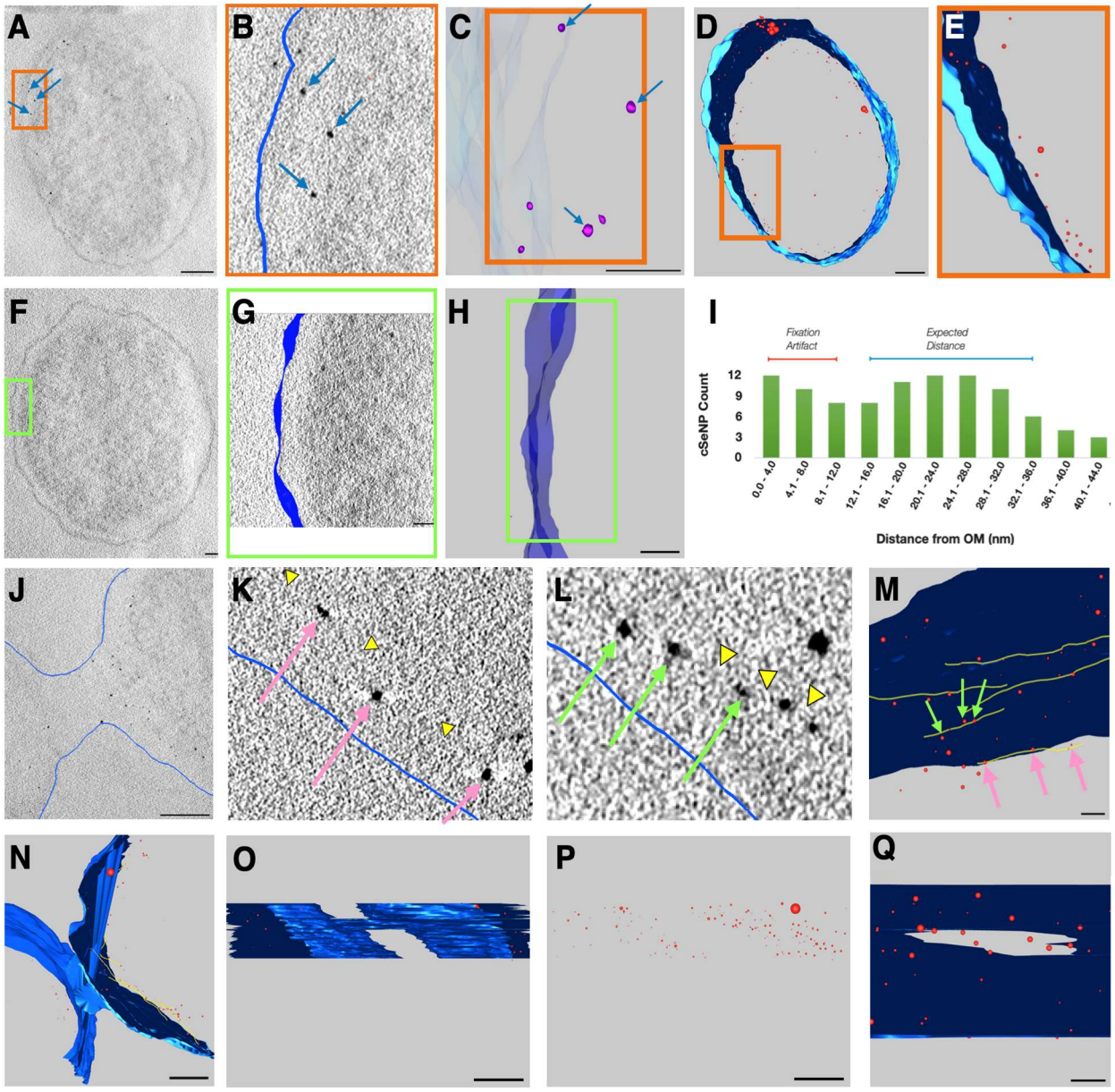

Figure 3.3. *Figure description at the top of following page*

not contain nanoparticles (Figure 3.3 panels F and H). Figure 3.3 panel D shows manual membrane and particle segmentation of a 250 nm thick tomogram; figure A2-E shows automatic nanoparticle segmentation. Figure 3.3 panel E shows a magnified image of the boxed area of figure 3.3 panel D.

Figure 3.3 panels F, G, and H show images of a control cell, grown without SeO_3^{2-}, but otherwise treated identically to the cell in figure 3.3 panel A (including Cu^{2+} exposure). There are

Figure 3.3. *Panel A shows a tomogram of E. coli expressing the cSeNP-FtsZ construct grown in 2 mM SeO_3^{2-} supplemented LB; 75 of 340 vertical slices comprise this 2D image. Visible are the outer membrane (OM), some remnants of the inner membrane (IM), and many punctate inclusions, (cSeNPs), noted with blue arrows. Panel B shows a magnified of the area within the orange box of panel A, with membrane segmented manually in blue. Panel C shows an isosurface auto-segmentation of the cSeNPs in the orange box. Panel D shows a segmented tomogram, with the membrane in blue and cSeNPs in red. Panel E shows a closer view of the area highlighted by the orange box in panel C. Panels F and G show tomograms of a cell grown in the absence of SeO_3^{2-}, but otherwise handled identically. Panel H shows the isosurface auto-segmentation of the area in the green box of panel F. Panel I shows a histogram of particle to membrane distances for the cell in panel A. Panel J shows a tomogram of a dividing cell, with the membrane segmented in blue. Panel K and L show two magnified views of sections of the dividing cell. Areas appearing to be filaments are marked with yellow triangles. Panel M shows segmented filaments in yellow, with arrows pointing to the particles noted in panels K and L. Panel N shows a fully segmented image of the dividing cell. Panels O and P show a side on view of the dividing cell, with the membrane hidden in panel P. Panel Q shows a view of the dividing cell where a small window between the two dividing cells remains.*

no obvious punctate densities in this tomogram. Automatic segmentation does not identify voxels of intensity comparable to those in experimental cells. We previously published tomograms of cells expressing unmodified GRLMR grown in SeO_3^{2-} supplemented media; in this 'control' experiment, we observed intracellular SeNPs with diameters ranging between 5 and 60 nm that were randomly distributed.[67]

An analysis of cCuSeNP locations relative to the OM suggests that 94% of observed cCuSeNPs are found in expected locations relative to the membrane. This analysis depends on known FtsZ biology. FtsZ is a membrane associated protein found 16 nm from the inner membrane in the cytosol, which translates to ~35 nm from the OM. The size of the cSeNP Protein component is ~10 nm in maximum dimension. We anticipate the cCuSeNPs to be located within a range from the OM, with 45 nm being the maximum distance a particle can be from the membrane. Of the range, we expect those that fall within 16 – 45 nm of the OM to be associated with intact filaments, where those found on the closer spectrum of the range are positions where the inner membrane has either partially or completely collapsed. Figure 3.3, panel I shows a histogram of cCuSeNP –OM distances for the cell in panel A. Of 104 observed cSeNPs, 98 are within 45 nm of the outer

membrane. Of those, 37% are closer than 16 nm to the outer membrane. We attribute particles closer than 16 nm to the outer membrane to membrane fixation artifacts, which are well-known with glutaraldehyde fixation. Therefore, over 90% of observed CuSeNPs lie in FtsZ associated locations.

Figure 3.3, panels J through Q, show a variety of renderings of a tomogram of a cell nearing completion of division; panels K and L show renderings where positive contrast putative FtsZ filaments appear; panel M shows a rendering of FtsZ filaments (yellow) decorated with cSeNPs that we could pick out; Figure A2 panels K-O show a more clearly visible extra-cellular filament. Analysis of 6 additional tomograms, including one additional control, show similar results.

Overall, electron microscopy suggests that FtsZ-cSeNP expression results in SeNPs found in locations where FtsZ is expected to be found. Evidence for this includes (1) dark densities in FtsZ locations in high-throughput 2D-samples; (2) Se elementally mapping to FtsZ locations; (3) punctate densities in locations expected for FtsZ in 3D cellular reconstructions; (4) absence of these features in control samples.

SeNPs are known to form spontaneously inside wild-type *E. coli* cells grown in Se supplementation.[120] This suggests an alternative interpretation of our observations is that some or all of the SeNPs were made by endogenous processes of *E. coli*—not by the recombinantly expressed cSeNP-FtsZ proteins. Our data in aggregate suggests that the SeNPs observed inside cells are not due to endogenous SeNP formation inside *E. coli* but can rather be attributed to recombinant cSeNP production as outlined below.

First, we note that previous reports of SeNPs in wild-type *E. coli* are done with 72 hours of growth in Se supplemented media resulting in 100 nm or larger SeNPs inside *E. coli*. In contrast, we observe 5 nm diameter cSeNPs after a maximum of 4 hours of growth in Se supplemented

media, suggesting that the process we are observing is quite distinct from endogenous SeNP formation. Other evidence suggesting that endogenous SeNP formation is minimal in our experimental approach is in figure A5 (IPTG induction screen) and Figure 3.5A (CT of cells). In figure A5, all cells are grown in 2 mM SeO_3^{2-} with varying concentrations of IPTG (from 1 μM to 1 mM). At lower concentrations of IPTG (less cSeNP-FtsZ) we do not observe densities corresponding to SeNPs (e.g., at the midpoints of dividing cells). At higher concentrations, these densities are observed, implicating a contrast-generating role (SeNP formation) by the cSeNP construct. In figure 3.5a, cells grown in 2 mM SeO_3^{2-} show dramatically different contrast (SeNP accumulation) depending upon whether the cSeNP is expressed. X-Ray contrast scales with Se supplementation concentration when the cSeNP is expressed, and X-Ray contrast does not scale in this way when the cSeNP is not expressed.

Correlative Light and Electron Microscopy of FtsZ-cSeNP expressing E. coli.

SeNPs can react with transition metal cations such as Zn^{2+} and Cd^{2+}, forming fluorescent metal selenide nanoparticles (e.g., quantum dots).[76,121] This suggests the possibility of the cSeNP as a cloneable CLEM contrast agent. We assessed this possibility by growing cSeNP-FtsZ expressing *E. coli* first in 10 mM SeO_3^{2-} supplementation, followed by a change of media and subsequent growth in ZnOAc supplemented media, as described in appendix A.

Figure 3.4 shows CLEM images of these cells; panels A and B show fluorescence and electron images, respectively, of the same cells. Figure 3.4 panel C shows an overlay of correlated light and electron images; panels E, F and G show higher magnification images of panels A, B, and C; panels D and H show fluorescence and electron images of control cells grown without SeO_3^{2-} but with $Zn(OAc)_2$.

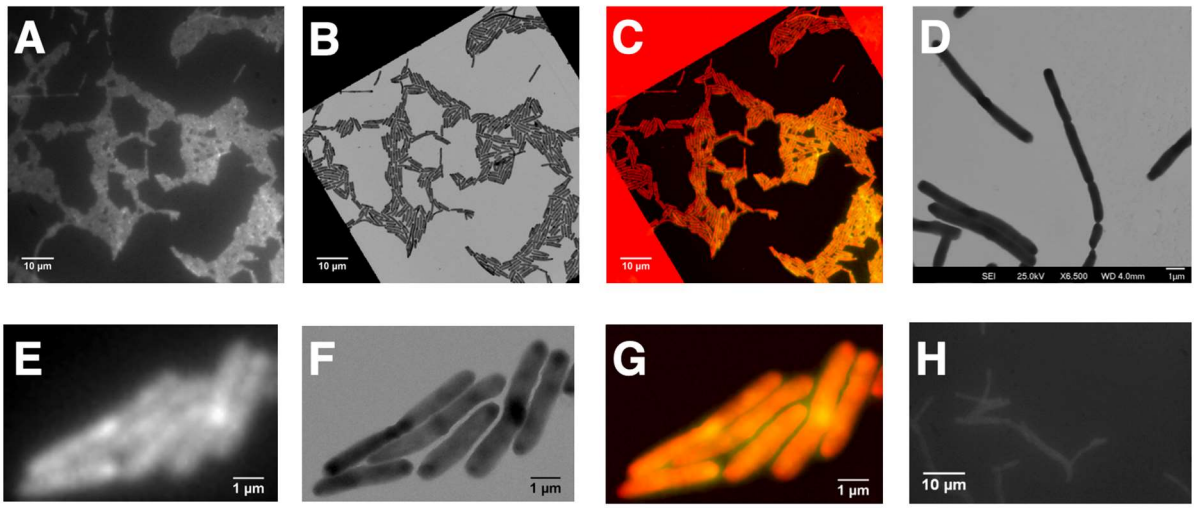

Figure 3.4. *CLEM images of E. coli expressing cSeNP-FtsZ fusions. Panels A and B show fluorescence and electron images, respectively of cells grown in 2 mM SeO_3^{2-}. Panel C shows an overlay of panels A and B. Panel D shows an electron image of cells grown without SeO_3^{2-}. Panels E, F, and G show magnified images of panels A, B and C. Panel H shows a fluorescence image of cells grown without SeO_3^{2-}.*

The fluorescence images of cZnSe-FtsZ expressing cells show the brightest emission localizing at the cleavage furrow of dividing cells, consistent with FtsZ-based contrast. The uniform background fluorescence is interpreted as arising from FtsZ-cZnSeNPs that are dispersed in the cell away from the cleavage furrow. Corresponding electron images also show the highest electron contrast at cleavage furrows. When overlayed, regions of high electron contrast overlap with areas of high fluorescence emission.

The higher magnification electron microscope image in figure 3.4 panel F shows *E. coli* cells with higher contrast densities at the midpoint of 3 dividing cells and at the poles of 3 other cells. We attribute these densities to SeNPs localized to FtsZ. The fluorescence images of figure 3.4 panel E show a relatively uniform fluorescence across the entire cells, with bright emission at the midpoints of 2 of the dividing cells and at the pole of one of the other cells. The overlay image of figure 3.4 panel F shows regions of high florescence correspond uniformly to the locations of SeNP density. The control fluorescence images in figure 3.4 panel H show typical fixed-cell autofluorescence.

Overall, the putative cZnSeNPs produce clear fluorescence emission above cellular autofluorescence, which becomes more intense in areas of high FtsZ concentration. Combined, this set of experiments suggests that the cSeNP, after conversion to cZnSeNP, is a promising approach for CLEM contrast. Furthermore, because particles were synthesized in vivo, cZnSeNPs may be an effective tool for cryo-CLEM based methods.

cSeNPs as genetically encoded X-ray contrast.

X-ray imaging modalities such as Computed Tomography (CT) provide images at length scales of meters with penetration deep into tissues and organisms. X-ray attenuation in CT is quantified with the Hounsfield Unit (HU). The HU scale is defined by the radiodensity of distilled water (0 HU) and air (-1000 HU). For biological tissues, typical HU values range from -700 (lungs) to +1900 (bone), with most soft tissues (fat, muscle, organs) having HU values between -120 and 60. Inorganic materials attenuate X-rays more effectively than biological tissues; pure copper attenuates X-rays at 14,000 HU. For inorganic nanoparticles such as the cSeNP, X-ray attenuation depends on particle concentration.

X-ray tomograms of *E. coli* cells expressing the cSeNP or GRLMR in grown in varying concentrations of SeO_3^{2-} were acquired in a Scanco micro-CT 80 instrument. CT data is presented in figure 3.5. Figure 3.5 panel A shows that cells expressing the cSeNP in varying growth conditions attenuate X-rays with an efficiency that depends on the SeO_3^{2-} concentration. Attenuation of 700 HU is observed for cells grown in 1 mM SeO_3^{2-}. Notably, cells grown in the same concentrations of SeO_3^{2-} but not expressing the cSeNP never attenuate more than 100 HU. Figure 3.5 panel B shows a voxel-parsed trace of X-ray attenuation. Here we observe that cells expressing the cSeNP grown in 2 mM SeO_3^{2-} show voxels with minor attenuation peak at 190 HU

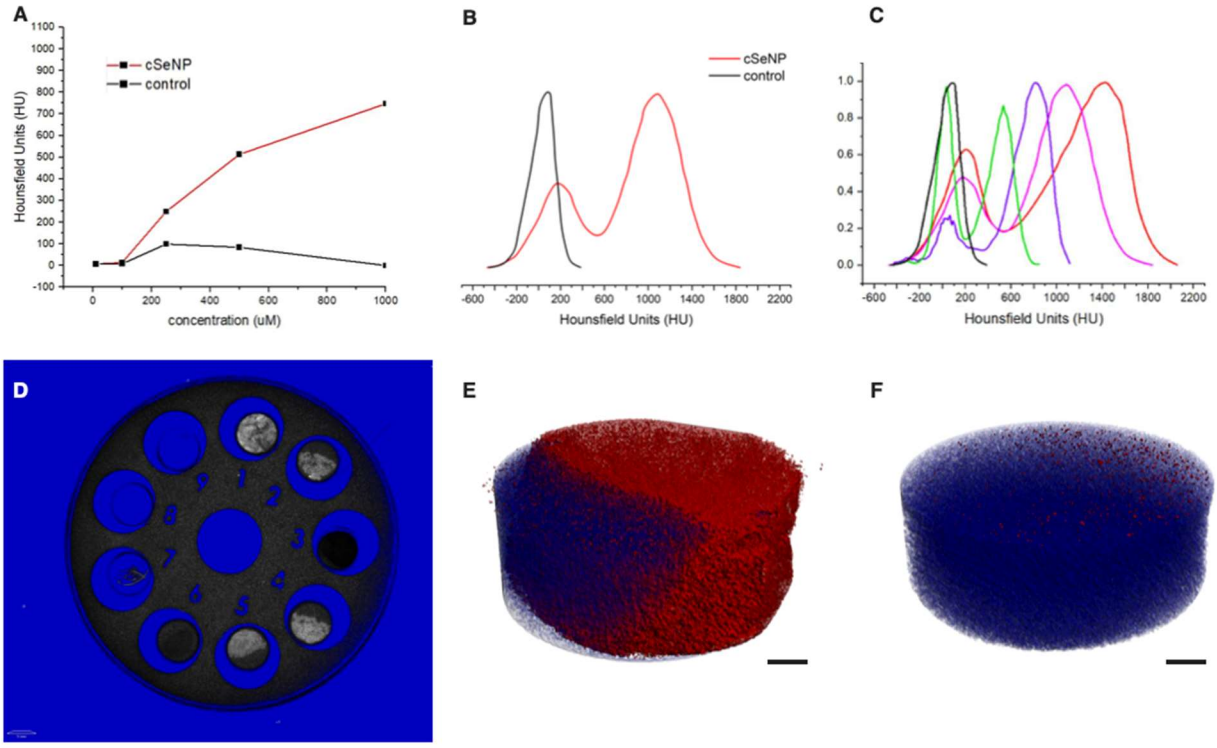

Figure 3.5. *X-Ray CT imaging of E. coli expressing cSeNPs. Panel A shows the X-ray attenuation (HU) of cells expressing the cSeNP (red) and cells not expressing the cSeNP (black) grown in the indicated concentrations of SeO_3^{2-}. Panel B shows the attenuation of cells expressing cSeNP, with the experimental cells grown in 2 mM SeO_3^{2-} and control omitting Se. Panel C shows the attenuation for cells grown in varying concentrations of SeO_3^{2-}; concentrations are 10 mM (red), 2 mM (pink), 1 mM (purple), 500 µM (green) and 1 µM (black). Panel D shows CT images of (1) GRLMR expressing cells in 10 mM SeO_3^{2-}; (2) GRLMR expressing cells in 2 mM SeO_3^{2-}; (3) GRLMR expressing cells; (4) cNP expressing cells in 10mM SeO_3^{2-}; (5) cSeNP expressing cells in 2 mM SeO_3^{2-}; (6) cSeNP expressing cells; (7) in vitro synthesized SeNP powder; (8, 9) empty tubes. Panel E shows a CT tomogram of sample 5. Se attenuation is represented in red, buffer attenuation in blue; This tube was centrifuged in a fixed-angle rotor, explaining the shape of the cell pellet. Panel F shows a tomogram of tube 6. The blue rendering indicates no Se in these cells. Scalebars in panels E and F are 1 mm.*

and a major attenuation peak at 1100 HU. Corresponding controls (without Se) show only an attenuation peak near 100 HU, comparable to soft tissue. Figure 3.5 panel C shows the attenuation of cSeNP expressing cells grown in concentrations of SeO_3^{2-} ranging from 1 µM to 10 mM. Like figure 3.5 panel A, attenuation increases with the concentration of SeO_3^{2-} in which the cells were grown. Figure 3.5 panel D shows a 9-position microcentrifuge-tube holder. Whiter color in these images corresponds to higher X-ray attenuation and thus Se absorption. Figure 3.5 panels E and F show tomograms of the samples in tubes 5 and 6, respectively. They are colored according to

attenuation, with red representing attenuation near 1100 HU and blue representing attenuation near 100 HU, as detailed in appendix A. More details on this rendering are available in appendix A. Overall, these tomograms show that cells expressing the cSeNP show clearly distinguishable X-ray contrast relative to cells grown in the same concentrations of SeO_3^{2-} that do not express the cSeNP.

Toxicity and other physiological impacts of cSeNPs.

In this work, we supplement the cell cultures with SeO_3^{2-} in to provide the Se equivalents needed for intracellular cSeNP formation. A reasonable question is whether Se supplementation alters underlying observable biology or causes toxic effects?

Selenium is an essential element. Its main biological functions are found in selenocysteine (sometimes referred to as the 21st amino acid) containing enzymes. Selenocysteine is found in the active sites of ubiquitous enzymes involved in redox homeostasis such as glutathione peroxidase and thioredoxin reductase. In the absence of Se, redox homeostasis is diminished, and cells grow slowly, if at all. At 'essential' concentrations, Se plays an antioxidant role. At high concentrations, Se becomes a pro-oxidant and exerts toxic effects (e.g., through free radical generation, which can oxidize DNA and membranes.)

In the present work, we optimized SeO_3^{2-} supplementation concentrations. We built on our prior work showing that recombinant GRLMR expression alters selenium homeostasis in *E. coli*. Overexpression of GRLMR makes *E. coli* significantly more tolerant of SeO_3^{2-}supplementation – raising the concentration of SeO_3^{2-} that inhibited 90% of cell growth (IC90) from ~2 mM to ~20 mM. GRLMR expression also resulted in a requirement to supplement cultures with ~10 μM SeO_3^{2-} in to sustain optimal growth rates.[105]

The overall conclusion from our prior work is that recombinant GRLMR overexpression alters Se homeostasis, such that the *E. coli* requires Se supplementation to thrive, and the cells also tolerate an order of magnitude more SeO_3^{2-} before growth is significantly impaired. Our study of intracellular SeNPs in *E. coli*, ongoing for a decade, leads to a hypothesis that SeNPs are a general feature of Se homeostasis in *E. coli*. This hypothesis is directly analogous to how cells handle excess of other essential inorganic elements, such as iron and phosphorous. Excess iron is stored in a bio-unavailable form in ferritin; similarly excess phosphate is stored in bio-unavailable inorganic polyphosphate nanoparticles. We suggest that excess ionic (bioavailable) Se may likewise be segregated and stored in bio-unavailable SeNPs – and that Se toxicity is observed when concentrations of Se overwhelm the cells innate capability for storage of Se in SeNPs.

In the present work, the majority of data was collected on *E. coli* supplemented with 2 mM Se when expressing GRLMR. In a few cases (e.g., experiments in figure 3.4), we used up to 10 mM Se supplementation – however in these higher SeO_3^{2-}conditions, we limited exposure to Se to 1 hour maximum.

In the Se supplementation conditions used in the present work, we observe no signs of acute Se toxicity. Cellular growth rates are normal. Cell morphologies are as expected (and altered significantly from normal due to the overexpression of FtsZ). Further, we don't observe stress granules or other signs of cellular stress. While there may be more subtle effects of Se supplementation on underlying biology than we've observed so-far, our observations in aggregate suggest that Se supplementation is not significantly altering underlying biology.

Downstream Use Cases

We show in this work the use-case of the cSeNP for revealing FtsZ locations in an *E. coli* model system. We expect that the cSeNP will function widely in *E. coli* for revealing subcellular protein

locations at electron microscope resolutions. We are presently assessing the cSeNP in other model systems (*Drosophila melanogaster*, *Caulobacter crescentus*, and some in vitro reconstituted systems). Understanding the interplay of Se supplementation and GRLMR overexpression on Se homeostasis in these systems is a key consideration. For widespread adoption, the cSeNP will need to function in all kinds of cells, analogous to the widely used fluorescent proteins. At this stage, we do not suggest that the cSeNP is 'perfect' and it is expected to cause some perturbance on underlying biology in many use cases, although we do not observe significant perturbance in the present study.

The "Cloneable labeling" approaches that find widespread success (even Nobel prize recognition in 2008) – namely the cloneable fluorophores exemplified by GFP – are imperfect labels. GFP has long been known to dimerize with itself, provoking undesirable aggregation of GFP labeled proteins. GFP can also impact the subcellular localization of GFP tagged proteins. For instance, one study showed that C- vs. N-terminal labeling of proteins with GFP impacted the subcellular localization of about 10% of proteins in yeast.

Given the need for cloneable contrast, especially in cellular electron microscopy, even imperfect tags are (1) likely to find community adoption and (2) form a basis for improved iterations/ generations of cloneable nanoparticles that reduce observed artefacts. (E.g., recent iterations of GFP largely eliminate the dimerization problems).

3.3 Conclusions

Expression of the cSeNP in an *E. coli* model system produces molecular contrast in electron and fluorescence microscopies, as well as cellular contrast in X-ray imaging (where resolutions are not molecular). This paper demonstrates a 'proof of concept' for cSeNPs as multi-modal cloneable contrast agents, using *E. coli*, a workhorse laboratory model-organism. What is true in *E. coli*,

typically translates to more complex model and experimental systems. We are presently working to extend these findings to the more complex model system of *D. melanogaster*.

Manuscript in review at ACS Nano and adapted for dissertation submission, previously published in a pre-print.[122] *Author contributions: KMB (lead author) and* ***BFG*** *(2nd author) conducted experiments, wrote initial draft, and edited. ZJB (co-author) conducted experiments and edited. CJA (principal investigator) wrote initial draft and edited.*

CHAPTER 4: SINGLE PARTICLE CRYOGENIC ELECTRON MICROSCOPY OF GLUTATHIONE REDUCTASE-LIKE METALLOID REDUCTASE

4.1 Introduction

There is a mantra within biology: "structure equals function" and this is especially true for proteins. Glutathione reductase-like metalloid reductase (GRLMR) —the protein upon which the cloneable selenium nanoparticle (cSeNP) is based—does not have an empirically determined structure nor are there closely related proteins with empirically determined structures either. For much of the story so far, GRLMR and the cSeNP have served as a proof of principle for cloneable nanoparticles with the previous chapter demonstrating the first use of cloneable nanoparticles as a cloneable contrast label for electron microscopy. Thus far, computationally determined protein structures have been sufficient to inform basic design decisions, but these do not represent the 'ground truth.' Having demonstrated that the cloneable nanoparticle platform works in the model system *E. coli*, we can continue trying to improve this platform with rational protein design and directed evolution, the latter of which is discussed in chapter 6. However, we need an empirically determined structure of GRLMR to inform more sophisticated design choices and to uncover the underlying mechanisms for cloneable nanoparticle growth. This chapter describes an on-going project to determine a near-atomic (~3 Å) resolution structure of GRLMR using single particle cryo-EM.

4.2 Background

Structural biology via NMR and X-ray crystallography

For many years, the field of structural biology relied almost entirely on nuclear magnetic resonance (NMR) based techniques or X-ray crystallography to determine 3-dimensional protein structures. NMR-based techniques are incredibly difficult and are time consuming for structural analysis of biomacromolecules, but can capture some dynamic information about proteins.[123,124] X-ray

crystallography is a robust technique for determining the 3-dimensional arrangement of atoms in a variety of samples—including biomacromolecules. X-ray crystallography relies on forming a (relatively large) crystalline sample which scatters a high energy X-ray beam to form a diffraction pattern. By rotating the crystalline sample, a series of diffraction patterns are collected at different angles. From this collection of diffraction patterns, a 3-dimensional structure can be solved after careful processing. With X-ray crystallography, thousands of protein structures and protein complexes have been solved, subsequently leading to countless scientific discoveries and breakthroughs. However, X-ray crystallography is inherently limited to protein samples that can be crystallized—any many cannot. The conditions required for crystallization can also change a proteins native structure and remove much of the dynamic movement that is present in proteins (movement which is largely linked their function).

An introduction to single particle cryo-EM

In recent years, starting with the 'Resolution Revolution' circa ~2013 single particle analysis (or single particle cryo-EM) has emerged as the foremost technique for protein structural determination. With single particle cryo-EM, purified proteins can be directly imaged suspended in vitreous ice—representing an aqueous environment close to their native state (especially when compared to a crystal). Any protein or protein complex that can be isolated with modestly high purity and of sufficient size to be imaged directly (> ~ 50 kDa currently) is theoretically amenable to single particle cryo-EM. After a protein sample is isolated in an aqueous buffer, it can be deposited on a transmission electron microscopy (TEM) grid and plunge frozen in liquid ethane cooled by liquid nitrogen. With a sufficiently thin layer of liquid—a droplet is usually wicked until only a thin film remains on the TEM grid—it will form a thin ~50 – 200 nm layer of vitreous ice. When liquid water freezes under normal circumstances, it forms a wide variety of crystals that

interact strongly with the electron beam, thus obscuring anything embedded within it. When frozen quickly enough, liquid water will form vitreous (i.e., non-crystalline) ice which is much more transparent to electrons. Thus, materials embedded within this vitreous ice can be viewed with relatively low background signal.

Since proteins and protein complexes are relatively small (< ~25 nm), they freeze effectively via plunge freezing. There are a few other cryo-fixation methods that exist, some that involve spraying the sample or 'writing' a thin layer of sample onto a TEM grid, and high-pressure freezing (usually reserved for cells or tissues).

To take further advantage of the transparent yet solid matrix provided by vitreous ice, special types of TEM grids are used to image biological materials by cryo-EM. A traditional TEM grid uses a thin (~5 nm) film (typically carbon) laid on top of a metallic (e.g., copper) substrate. The sample adheres or sits on top of the thin film and incident electrons pass through the sample and the thin carbon film before reaching the detector. The film provides relatively low signal when compared to many materials that could be imaged in an electron microscope (i.e., materials with atomic number [Z] > 6). But, when trying to image a carbon-based material (such as a protein), the carbon film represents a significant background signal. By cutting holes in the carbon film, proteins suspended in solid vitreous ice above the holes can be imaged without the carbon film background—the electron only passing through proteins and vitreous ice. Figure 4.1 shows a representation of a TEM grid with a copper mesh and a zoom in shows a representation of a holey carbon film with proteins located within the holes.

Single particle cryo-EM is done within a *transmission* electron microscope, so electrons pass *through* the sample before hitting the detector. This means that the 3-dimensional information of the protein structure is compressed into a 2-dimensional image. With X-ray crystallography, this

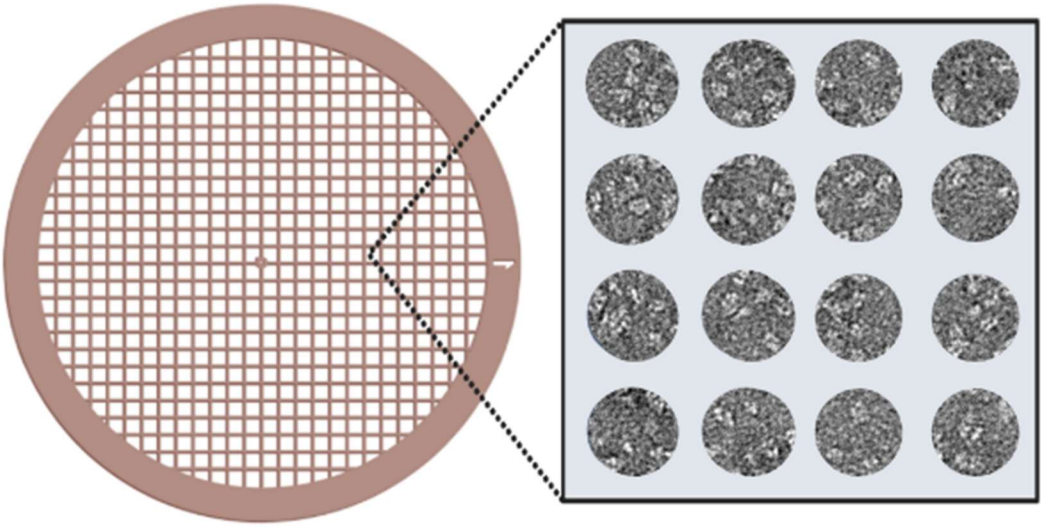

Figure 4.1. *Representation of a holey-carbon grid on a copper-mesh TEM grid. Imaging is done within the holes which are filled with proteins suspended in vitreous ice. Imaging within the holes removes background signal from the carbon film which is problematic for contrast.*

'compression' of information is mitigated by rotating the crystallized sample and collecting data as the crystal rotates. With single particle cryo-EM, the protein sample is (ideally) randomly distributed within the vitreous ice such that imaging many particles yields 2-dimensional images of the protein from many different angles. Through data processing, the 3-dimensional structural information of the protein sample can be regained by combining 2-dimensional images of a protein from all orientations.

Single particle cryo-EM workflow

Single particle cryo-EM starts with a purified, concentrated protein sample. While it is possible to do single particle cryo-EM with an unpurified sample, it adds a new layer of difficulty especially during the particle-picking stage. A purified protein sample is usually plunge-frozen to cryo-fix. Freezing conditions are determined empirically, and variables include TEM grid material (e.g., gold, copper), mesh style (e.g., holey, lacey), mesh material (e.g., carbon, gold, graphene oxide), mesh size, hole size & frequency, plasma cleaning conditions, blot time (s), blot type (e.g., front,

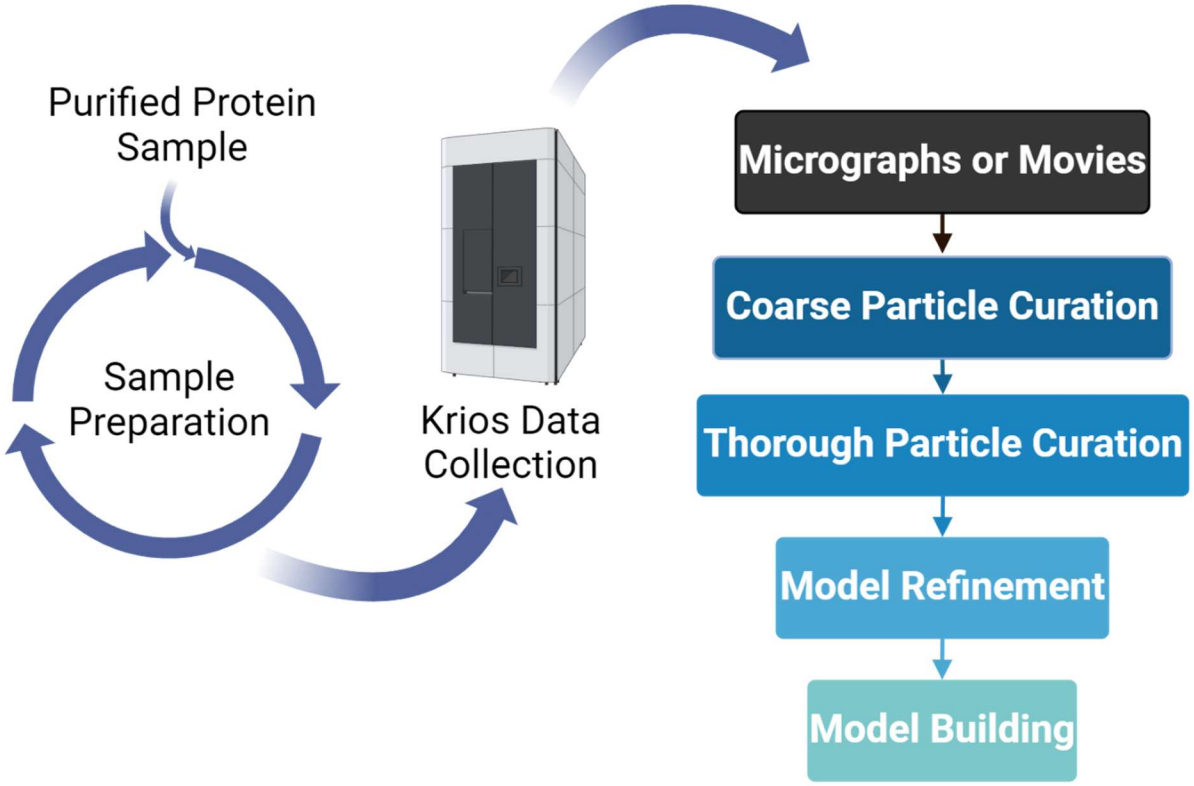

Figure 4.2. *Simplified single particle cryo-EM workflow. Starting with a purified protein sample, grids are prepared for data collection in a Krios cryo-TEM in a process that is iterative. Following data collection, electron micrographs are pre-processed and individual particles are picked from the images. Particle curation steps are highly iterative and the goal is to generate a stack of images that can be used to generate a 3-dimensional structure into which an atomic model is built.*

back), blot force, sample concentration, among others. This stage of sample preparation is a complex matrix of variables that are all loosely related to the resulting sample quality—though in isolation, some conclusions about their effects can be drawn. Ultimately, this multi-variate matrix of sample preparation conditions necessitates (often several) rounds of sample screening in a cryo-TEM.

After preparing an appropriate sample, hundreds to thousands of images are collected in a cryo-TEM from which individual particles are picked across each of the images. Data processing for single-particle cryo-EM is done with the help of programs such as CryoSPARC.[125] Particle picking can be done via 'blob picking' or 'template picking' which essentially rely on pixel intensity differences sometimes corresponding to instances of the protein of interest. More

sophisticated machine-learning approaches can be trained with subsets of particles to find particles of interest in the remainder of a dataset.[126] After particles are 'picked' they are sorted into 2-dimensional classes based on their appearance/shape. Classes corresponding to different protein orientations (versus background or noise) are then selected to reconstruct a 3-dimensional model of the protein of interest. This 3-dimensional model is an electron density which is used to build an atomic model of the protein of interest (i.e., placing in atoms, amino acids, or secondary structures). Figure 4.2 shows a simplified flow-chart of the single particle cryo-EM workflow starting with a purified protein sample and ending with atomic model building into an empirically determined electron density map.

4.3 Structural Determination of GRLMR via Single Particle Cryo-EM

The previous chapters told the story of GRLMR and the cSeNP, highlighting the importance of developing intracellular cloneable contrast agents for electron microscopy, and demonstrating the use of the cSeNP with a model filamenting protein (FtsZ) in *E. coli*. In this chapter we are looking through the lens to the future of cloneable nanoparticles—by trying to better understand the system we have been working with for a decade. Much of the work related to cloneable nanoparticles has been with the objective of implementing them, an endeavor to which I've invested a significant amount of time as well (and chapter 5 returns to this with another on-going project). Here, the goal is to determine a near-atomic resolution structure of GRLMR and to see where selenium and NADPH sit within that structure.

With a near-atomic (~3 Å) structure of GRLMR, the positions and orientations of amino acids that make up the protein structure will be resolved. This will enable a more informed analysis of structure-activity relationships, where residues or regions of the protein implicated in various functions of the enzyme can be interrogated. For instance, resolving the position and orientations

of residues in the active site or in the substrate entry channel can help to understand how the enzyme interacts with different selenium species (e.g., selenite, selenate, or selenodiglutathione).

Understanding the relationship between the structure of GRLMR and its functions will inform rational protein designs—such as designing a smaller version of GRLMR while preserving the ability to produce selenium nanoparticles (primary research of Rachel S. Cohen in the Ackerson lab). Given an empirically determined structure of GRLMR, smart libraries for directed evolution could be designed, which could introduce new functions to GRLMR (the first example of enzyme directed evolution applied to an inorganic substrate is demonstrated in Chapter 6). Lastly, comparing the structure of GRLMR to other metal reductases may offer new insights into the underlying mechanisms of enzymatic metal reduction. All told, these insights will help move the dial towards continued development of the cloneable nanoparticles platform and to expand the toolbox of cloneable contrast tools for electron microscopy.

Screening GRLMR with negative staining

Purified GRLMR was added to TEM grids and negatively stained with uranyl acetate. Uranyl acetate sticks preferentially to the carbon film over proteins adding contrast between the background and the proteins on the grid. Shown below is an electron micrograph of GRLMR negatively stained and imaged at room-temperature. This screening step is done to demonstrate a purified protein is a good candidate for cryo-EM imaging. This example helps to show that the purified GRLMR sample is pure, that it does not have any glaring preferred orientation problems, and that GRLMR does not form large aggregates. This negative stain image (along with an SDS-PAGE gel and Bradford Assay) was used to gain access to cryo-EM resources located at the National Center for CryoEM Access and Training (NCCAT)

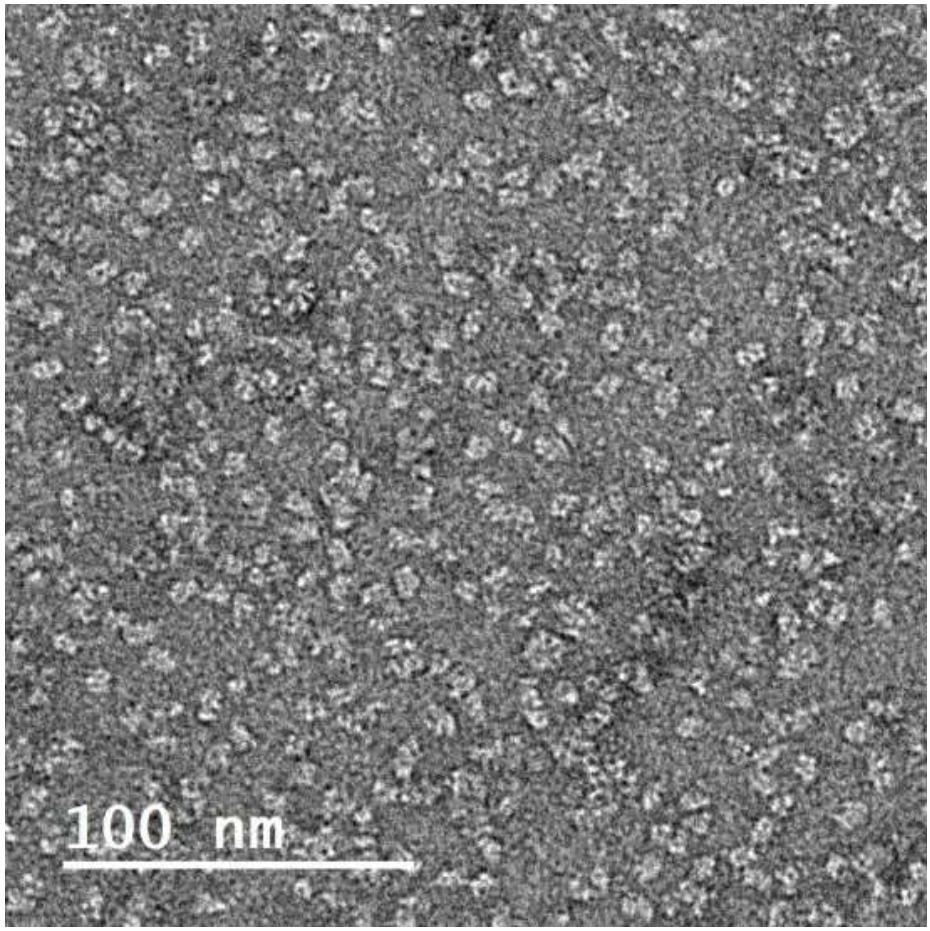

Figure 4.3. *Negative stained (2% UA) GRLMR WT (0.1 mg/mL) imaged in JEOL 2100F TEM with Gatan Ultrascan CCD camera on negatively glow discharged 200 mesh carbon support copper grid*

Cryo-EM screening of GRLMR samples

Cryo-EM sample preparation is iterative and involves testing a myriad of conditions, followed with imaging at different magnifications to evaluate the quality of the grid. Generally, changing the grid type, the sample concentration, and blot time will cover a wide variety of conditions. Samples of purified GRLMR as well as GRLMR + NADPH and GRLMR + selenite were screened at NCCAT to generate grids for automated data collection on a Krios cryo-TEM.

Samples were prepared by plunge freezing using a Leica EM GP automated plunge freezer followed by screening in a Glacios CryoTEM. Modern cryo-TEMs (such as the Glacios and Krios) are equipped with autoloaders that can load a dozen grids at a time that can all be manipulated

within the microscope—enhancing high-throughput screening and data collection. While there is no 'standard' way to screen grids for single particle cryo-EM, images are usually taken at a few different magnifications to understand the quality of the ice and the distribution of the sample within the ice. Screening data was collected using an automated protocol in Leginon.[127] Figure 4.4 shows an example of the data that was collected screening a single sample. Lower magnification images were taken across the entire grid and were stitched together in a 'montage' or 'atlas' to give an indication of ice thickness across each grid (Figure 4.4 panel A). A slightly higher magnification image of a single grid square gives more information about ice quality, here a large crack in the ice or film is visible (Figure 4.4 panel B). Data was collected at an even higher magnification to evaluate ice within the holes (Figure 4.4 panel C). Lastly, images were collected within the holes to evaluate protein distribution within the ice (Figure 4.4 panel D).

GRLMR cryo-EM data collection

After several iterations of screening as described above, grids were selected for several automated data collection sessions on a Krios cryo-TEM (adding up to ~1 week of continuous microscope time). Three datasets were collected with over 30,000 total micrographs: GRLMR, GRLMR + NADPH, and GRLMR + selenite. Data processing takes a long time for single particle cryo-EM and is on-going; I will share some of what has been done, offer some discussion about what I've learned, and outline what remains. Biological samples in cryo-EM are limited by the electron-dose they can withstand before bonds break apart.[128,129] Krios data are collected as a series of frames (or movies) that make up a micrograph after they are stitched together. Earlier frames (i.e., with less accumulated electron dose) contain the 'highest resolution information' about the sample, and the later frames are needed to 'see' the sample particles within the background.[130–137] Through the

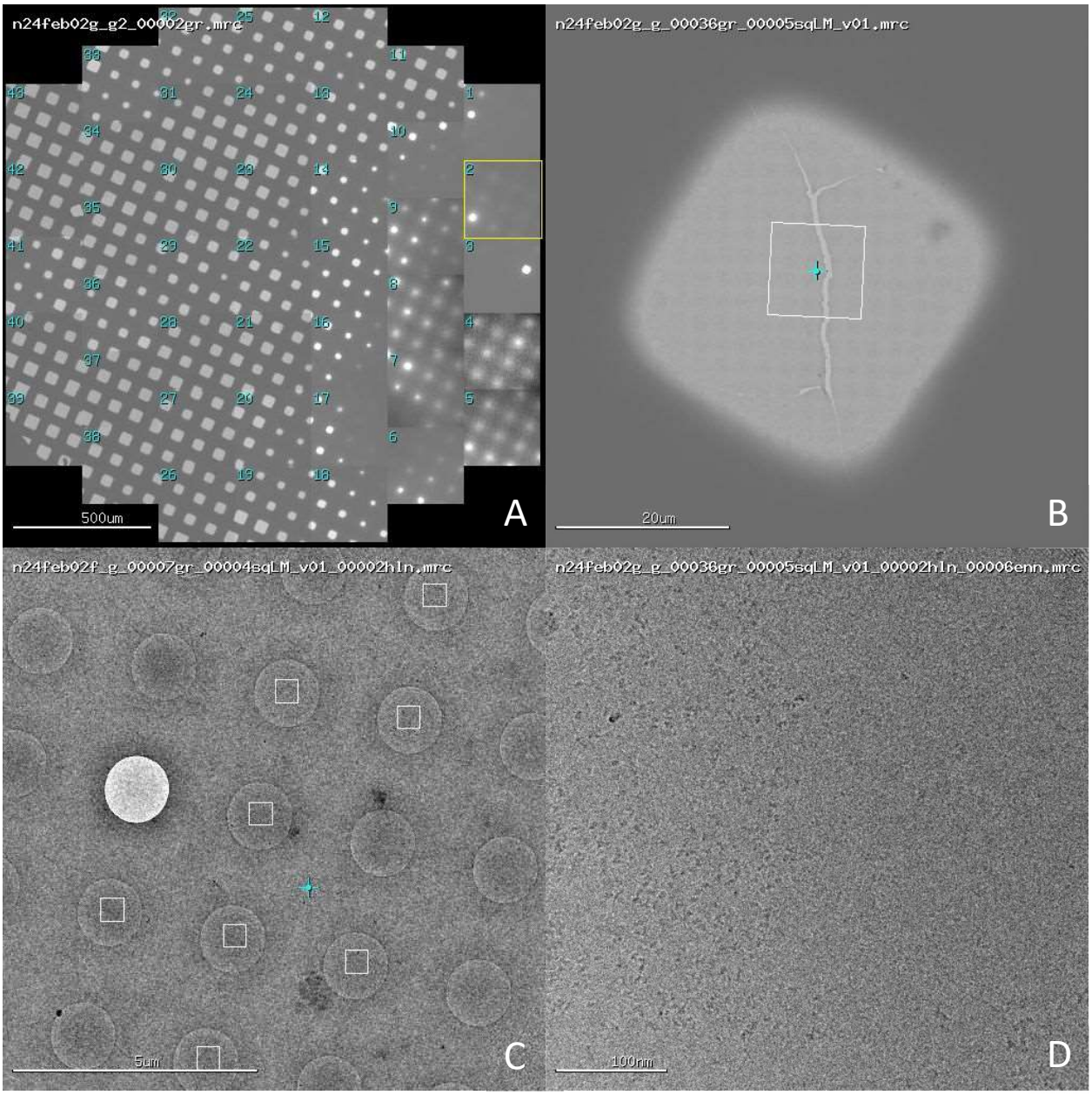

Figure 4.4. *Panel A shows an example atlas of a GRLMR cryo-EM sample; there is a gradient of ice thickness across the grid going from thin (left) to thick (right). Panel B shows an image of a single grid square that has a crack across the middle and relatively thin ice; holes are visible in the background. Panel C shows a 'hole-level' image; data is collected at a higher magnification and within the holes. The bright circle is an example of a hole with no ice in it. Panel D shows a high magnification image within a hole and includes protein distributed across the image; more protein is on the left half than on the right.*

collection of the movie, the sample moves under the electron beam. Sample motion gets corrected using software tools.[130–137]

Cryo-EM data processing with CryoSPARC

Data processing is on-going and has focused primarily on the first GRLMR dataset—without added NADPH or selenite. What follows is a summary of some of this progress followed by some commentary on what is next:

Coarse particle curation

9,869 micrographs from the GRLMR dataset were imported into CryoSPARC and the contrast transfer function (CTF) was estimated for each micrograph.[138–141] Particles were initially picked using the 'Blob Picker' job. With this approach, essentially any particle / blob of a given (input) size is selected and extracted from the micrographs. While quick, this approach treats everything as a gaussian blob and so many 'junk' particles were picked alongside particles of GRLMR.[142] For coarse particle curation, these extracted particles were sorted into 2-dimensional classes where (in principle) particles within a class are more similar to each other than to any other class. The goal for coarse particle curation was to remove some *junk* particles in favor of GRLMR particles. After a few iterations of 2D classification where classes corresponding to *junk* were rejected while others (containing GRLMR particles) were accepted, a select few of the best classes were used as templates in the 'Template Picker' job. Here, 2D classes—representing several orientations of GRLMR are used as templates to go back and pick particles from the micrographs. Figure 4.5 shows an example of some classes which were used as templates. These classes represent averages of the particles within them—i.e., the average of several hundreds or thousands of individual particles.

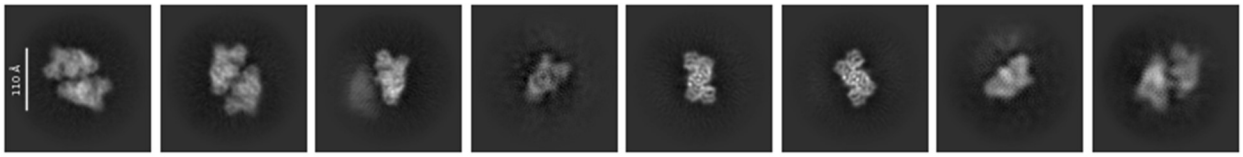

Figure 4.5. *Example 2D classes of GRLMR used as templates for 'Template Picker' job in CryoSPARC.*

Thorough particle curation

Template picking was slightly better at picking GRLMR particles, but there were still mostly *junk* particles that needed to be removed. A subset (100,000) of template particle picks were separated for quicker processing. This particle subset was classified into 2D classes (e.g., 150 classes) iteratively where classes identified as *junk* were excluded and the remaining particles were classified again. After many (~20 – 25) rounds of this, ~7,000 GRLMR particles were used to train a neural network-based particle picker called Topaz on a subset of 500 micrographs.[126] Following a small test of the model on a unique subset of 500 micrographs, the model was used to pick particles on the remaining 8,869 micrographs.

Where the blob picker identified ~5,000,000 - ~23,000,000 particles on 9,869 micrographs, the Topaz picking model identified closer to ~1,000,000 particles. Initial processing of these particles suggested that a much higher portion (~50% versus ~5%) of the Topaz picked particles were of GRLMR particles versus *junk*. The Topaz picked particles were classified again using 2D classification to get rid of some *junk* particles that remained in the particle stack. To further curate the particle stack (i.e., remove *junk particles*) the '*Ab-initio reconstruction*' and '*Heterogeneous refinement*' jobs can be used iteratively. In a similar manner to 2D classification, initial 3-dimensional reconstructions were generated, and particles were sorted by which structure they corresponded to.[125] Doing this first with 3 classes, 2 classes contained a large fraction of *junk* particles while 1 class contained mostly GRLMR particles.

Model refinement and molecular model building

After some thorough particle curation, initial models were used to generate refined structures. These initial structures are essentially electron density volumes generated by combining the 2D particle images from all orientations. Refinement of the volume (and later the atomic model) is

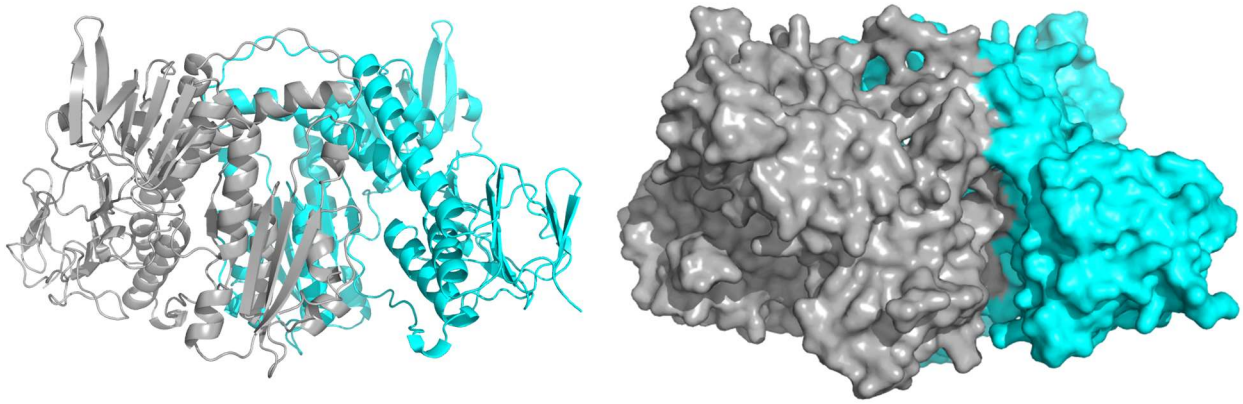

Figure 4.6. *Renderings of initial atomic models of GRLMR structure from ~4 Å resolution volume. Atomic model was generated using DiffModeler (Kihara lab) and the renderings were generated using PyMOL™ version 3.0.4*

done to improve agreement between the model and the experimental data—and is on-going. One volume at nominal 4 Å resolution was used to generate an atomic model.[143–145] The initial atomic model was generated using the DiffModeler tool from the lab of Daisuke Kihara which automatically builds a protein complex structure using a cryo-EM map and the protein sequence (recently accepted in Nature Methods, pre-print cited).[146] This model, shown in figure 4.6 with both a cartoon and surface rendering generated in PyMOL™ (version 3.0.4) represents the current state of GRLMR structural determination.

4.4 Discussion

On-going work and future experiments

While the work in this chapter ends somewhat abruptly, it is on-going and the importance has hopefully been established throughout this chapter and in the chapters before it. The particle stack can still be further curated to get rid of a sub-population of GRLMR particles that have been termed 'dimers of dimers.' These particles are visible in the 2 left-most panels of figure 4.5 and represent 2 copies of the GRLMR homodimer in close proximity (whether they are associated in a complex is still unknown). Appendix B offers a supplementary mass photometry spectum showing that this population of particles is present in the purified protein sample. There are many data processing

tools built into CryoSPARC or ChimeraX to help in separating out this population and to continue refining the molecular models of GRLMR towards near-atomic resolution.[147] With a near-atomic resolution model in hand, structure-property relationships can continue to be interrogated—one example of this is shown in chapter 6 where an inactive mutant of GRLMR was generated by mutating the cysteine residues in the active site.[104]

Furthermore, there are (2) additional GRLMR datasets (+ NADPH and + selenite) that have gone largely untouched thus far. Data processing is resource intensive and processing these datasets in parallel would significantly slow progress. With the assumption that the atomic models are similar, the data processing workflow used for the initial GRLMR dataset will help to streamline the data processing for the remaining datasets. Some additional work will likely be needed to separate sub-populations within the +NADPH and +selenite datasets (i.e., to separate particles with either NADPH or selenite bound from those without).

Lastly, future work will involve trying to uncover cloneable selenium nanoparticle growth through time-resolved single particle cryo-EM.[148] With one iteration of this new approach, samples can be mixed in a microfluidic device over a defined period of time (~ tens to hundreds of milliseconds) before plunge freezing. Generating cloneable selenium nanoparticles *in vitro* is routine in the Ackerson lab. By mixing GRLMR with all the components necessary to generate selenium nanoparticles using a microfluidic device, GRLMR should be plunge frozen at different stages of nanoparticle growth. Recent advances in data processing for heterogeneity help make this experiment conceptually possible[149,150] Through this experiment, along with the on-going work presented in this chapter, we aim to gain unique insight into enzyme-mediated nanoparticle growth through direct imaging via cryo-EM.

CHAPTER 5: CRYOGENIC ELECTRON TOMOGRAPHY OF A CLONEABLE SELENIUM NANOPARTICLE

5.1 Introduction

For many imaging techniques, the 3-dimensional information of a sample is lost during the image creation process. Shown in chapter 3, the 3-dimensional information of cellular samples can be regained through electron tomography. Within the electron microscope, a sample can be physically rotated, collecting images at different tilt angles. This 'tilt-series' is aligned and used to reconstruct a 3-dimensional volume of the original sample called a tomogram. Electron tomography (ET) using cryogenically preserved samples represents a technique for imaging cellular samples in near-native states in 3-dimensions at near-atomic (~10 - 20 Å) resolutions. If cloneable nanoparticles are going to be widely used as a cloneable contrast tool for intracellular imaging, they will need to be compatible with cryo-ET. Using a similar model system as in chapter 3, the goal is to image *E. coli* cells expressing a chimera of the cloneable selenium nanoparticle and the filamenting protein FtsZ to demonstrate the application of cloneable nanoparticles in cryo-electron tomography. Presented in this chapter is an on-going project, extending from work presented in chapter 3, adapting the cloneable selenium nanoparticle for cryo-electron tomography.

5.2 Background

Vitrification of cellular samples for cryo-ET

Samples can be prepared for cryo-electron tomography in a few different ways, but the most common are by 'plunge-freezing' and by 'high-pressure freezing.' With plunge freezing, a thin film of sample (e.g., bacterial cells or proteins) is plunged quickly into a cryogen. The sample is frozen so quickly that ice crystals don't have time to form.[151,152] A liquid ethane/propane mixture cooled by liquid nitrogen is commonly used as a cryogen since the ethane/propane mixture has

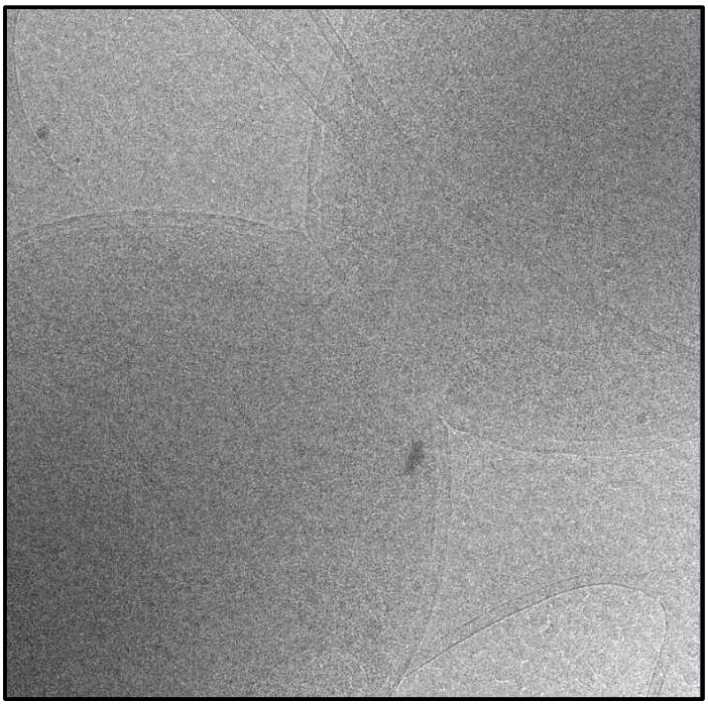

Figure 5.1. *Cryo-TEM image of a plunge frozen dividing* E. coli *cell expressing the cSeNP-FtsZ construct. Since the cell is not thinned, it is difficult to see any details inside the cytosol of the cell.*

more favorable freezing qualities than liquid nitrogen alone. Plunge freezing can effectively vitrify aqueous samples ranging from proteins to small cells. For instance, the nuclei of mammalian cells are too thick to vitrify effectively by plunge freezing. High-pressure freezing uses a combination of high-pressure and liquid nitrogen to vitrify a larger volume of biological sample (e.g., larger cells, neurons, small tissues).

Whether prepared by plunge freezing or high-pressure freezing, many cellular and tissue samples are too thick to image directly with the electron beam and have to be thinned. Figure 5.1 shows an image of a plunge frozen dividing *E. coli* cell expressing the cSeNP-FtsZ construct. From this image alone, we learned that *E. coli* cells would need to be thinned before trying to collect any tilt-series. Where high-pressure frozen samples can be dehydrated and freeze-substituted (described in Chapter 3 and Appendix A) to enable thinning via ultramicrotomy in (~50 - 150 nm), cryo-ET (by definition) requires a frozen-hydrated sample (i.e., not dehydrated and freeze-

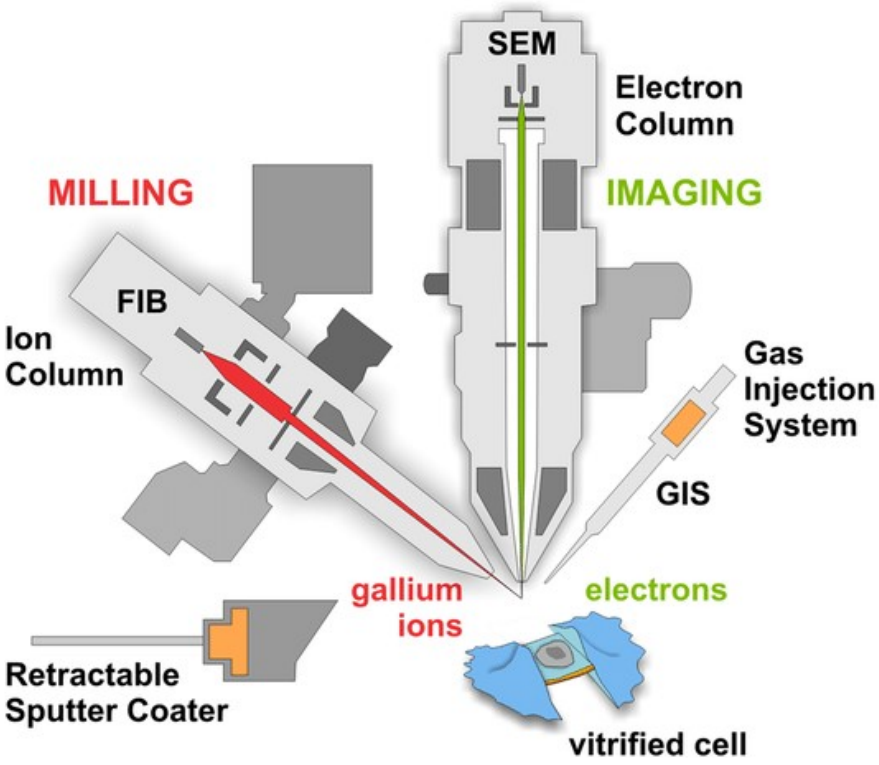

Figure 5.2. *The SEM electron beam and ion beam are coincident at the sample. In this example, the FIB uses gallium ions. The sputter coater adds a conductive platinum layer to an otherwise insulating biological sample. The gas injection system deposits an organometallic platinum gas that condenses on the cold sample which serves to protect and add structure to the lamella during and after milling. The cryo-stage is cooled to -170 ºC using a liquid nitrogen heat exchanger. Figure adapted from (Kuba et al.).*[1]

substituted). Frozen sample volumes can also be thinned without dehydration with cryo-ultramicrotomy, but this is now rarely done because of well characterized mechanical artifacts that can be introduced.[153]

Adapted from the material science world, cryo-focused ion beam scanning electron microscopes (FIB-SEM)s are now routinely used to thin frozen-hydrated cellular samples for cryo-ET. FIB-SEMs use a focused ion beam coincident with a scanning electron microscope to ablate regions of a sample to form a thin 'lamella' that is transparent to the electron beam (Figure 5.2).[154,155]

5.3 Progress towards cryo-electron tomography of cloneable selenium nanoparticles

Sample thinning via cryo-focused ion beam milling

Following nanoparticle formation inside *E. coli* cells expressing the cSeNP-FtsZ construct, samples were plunge frozen using a Leica GP2 automated plunge freezer. Vitrified samples were transferred to an Aquilos 2 cryo-FIB-SEM for milling. Following FIB-milling, samples are transferred to a cryo-TEM for tilt-series data collection. Figure 5.3 is cryo-TEM image showing one example of a cryo-FIB-milled lamella containing *E. coli* cells expressing the cSeNP-FtsZ chimera. Visible in the middle of the lamella are dozens of *E. coli* cells that have been thinned to ~200 nm to improve their transparency to the electron beam.

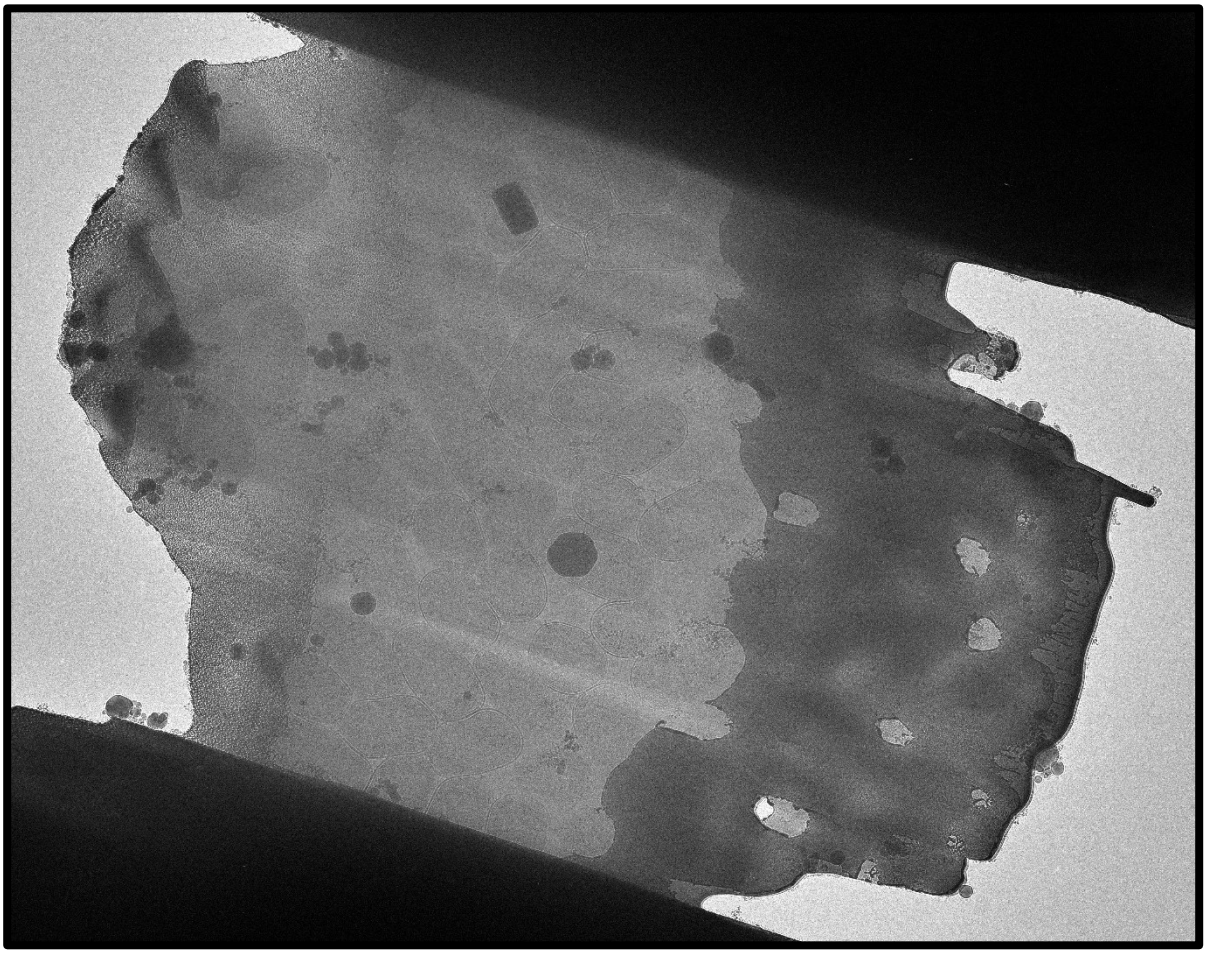

Figure 5.3. *Cryo-TEM image of a cryo-FIB-milled lamella containing frozen-hydrated E. coli cells expressing cSeNP-FtsZ chimera.*

Tilt series data collection and analysis

Tilt-series data collection was focused on collecting data at the pinch points of dividing cells—where FtsZ is known to localize and thus where cloneable selenium nanoparticles should be concentrated. Outside of cell division, FtsZ is associated with the membrane and cloneable selenium nanoparticles are similarly expected to localize there. Following tilt-series collection on the lamella shown in figure 5.3, a 3-dimenional volume (tomogram) was reconstructed using IMOD.[156,157] Figure 5.4 shows a slice from the resulting tomogram that contains (4) *E. coli* cells in close proximity, but not dividing. The large dark densities visible across the cells were attributed to ribosomes. To aid visualization of the cells in 3-dimensions, membranes were manually segmented for (3) of the cells (Figure 5.5). Also segmented were two smaller volumes (denoted in

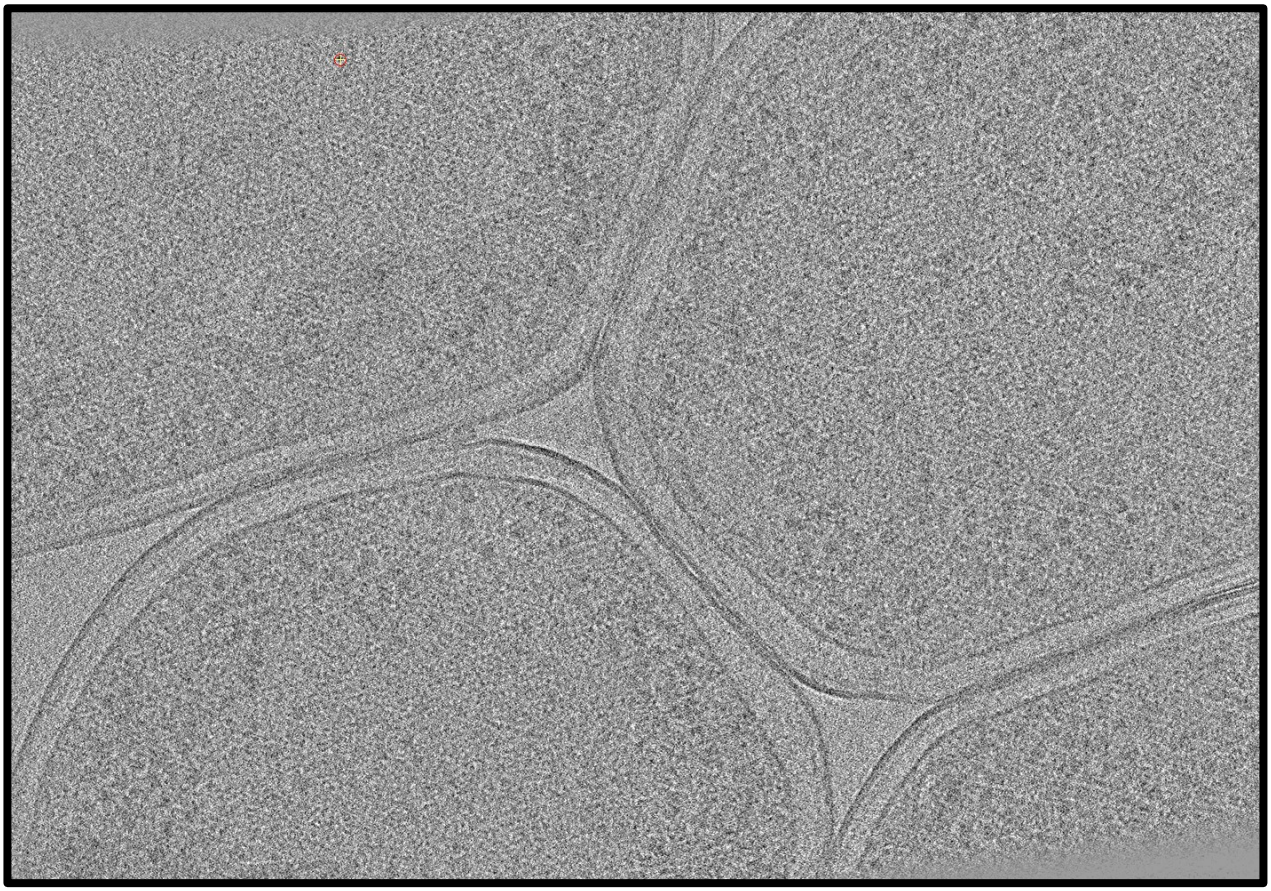

Figure 5.4. *Slice from tomogram volume. While multiple cells are present, but none appear to be actively dividing. Aside from the membranes of (4) cells that are easily identifiable, large dark densities across all of the cells are attributed to ribosomes.*

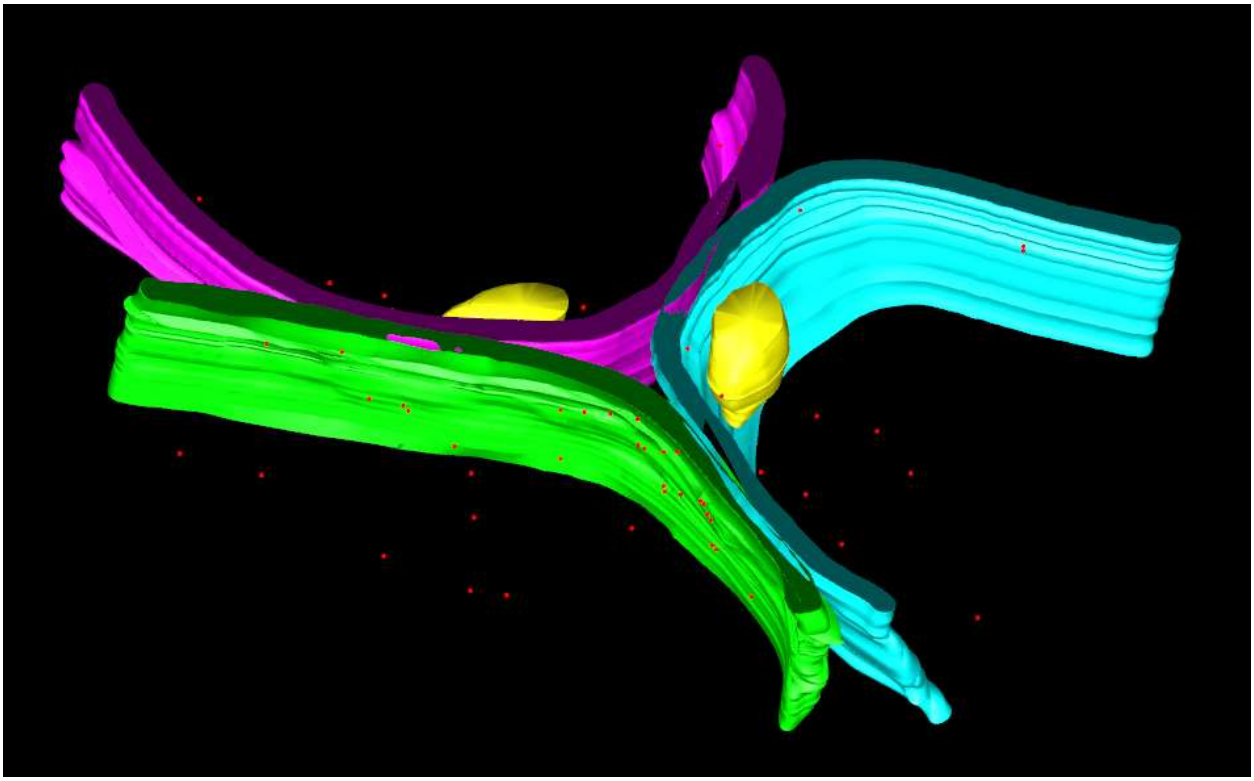

Figure 5.5. *Segmentation model of cells shown in figure 5.4. Green, blue, and magenta represent (3) of the (4) cell membranes, yellow represents the endosomes, and the red particles represent cloneable selenium nanoparticles attached to FtsZ.*

yellow) attributed to endosomes. Lastly, densities believed to be selenium nanoparticles were segmented (red spheres). Unlike in chapter 3, these densities could not be automatically segmented with the same strategy. Figure 5.6 shows a closer view of one membrane and includes segmented selenium particles. This data suggested that (while they had to be picked manually) cloneable selenium nanoparticles were localized where expected.

Still aiming to collect a tilt-series at the pinch point of dividing *E. coli* cells, fresh cells were grown, cloneable selenium nanoparticles were synthesized *in vivo*, and cells were plunge frozen. Following cryo-FIB-milling, a dividing *E. coli* cell was captured in a lamella (show in Figure 5.7). A tilt-series was collected at the region approximated by the blue box in figure 5.7. Following tomographic reconstruction, the volume had extremely low contrast. Even after using a contrast enhancing algorithm (at the expense of resolution), the reconstruction was of extremely

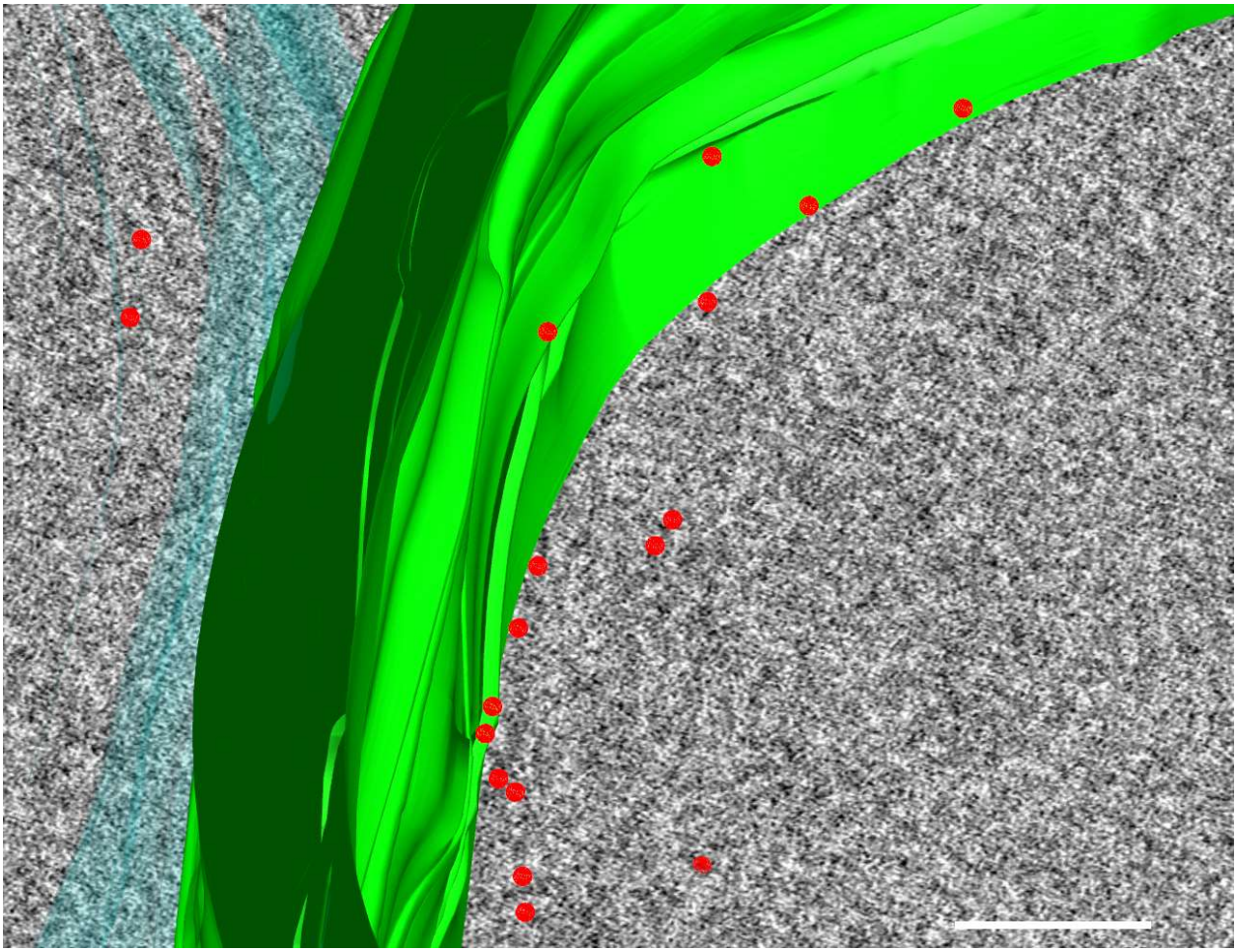

Figure 5.6. *Closer look at part of figure 5.5 showing segmented selenium nanoparticles (red) proximal to the membrane (green). (Scale bar = 50 nm.)*

low contrast with only parts of the membrane visible from the background (Figure 5.8). From this tomogram, it was not possible to segment any selenium nanoparticles. Beyond this, there were no easily identifiable FtsZ filaments, which should be visible in this region.[158] While disappointing that cloneable selenium nanoparticles were not visible in this tomogram, there are several reasonable explanations for this (discussed below) and this research is still on-going.

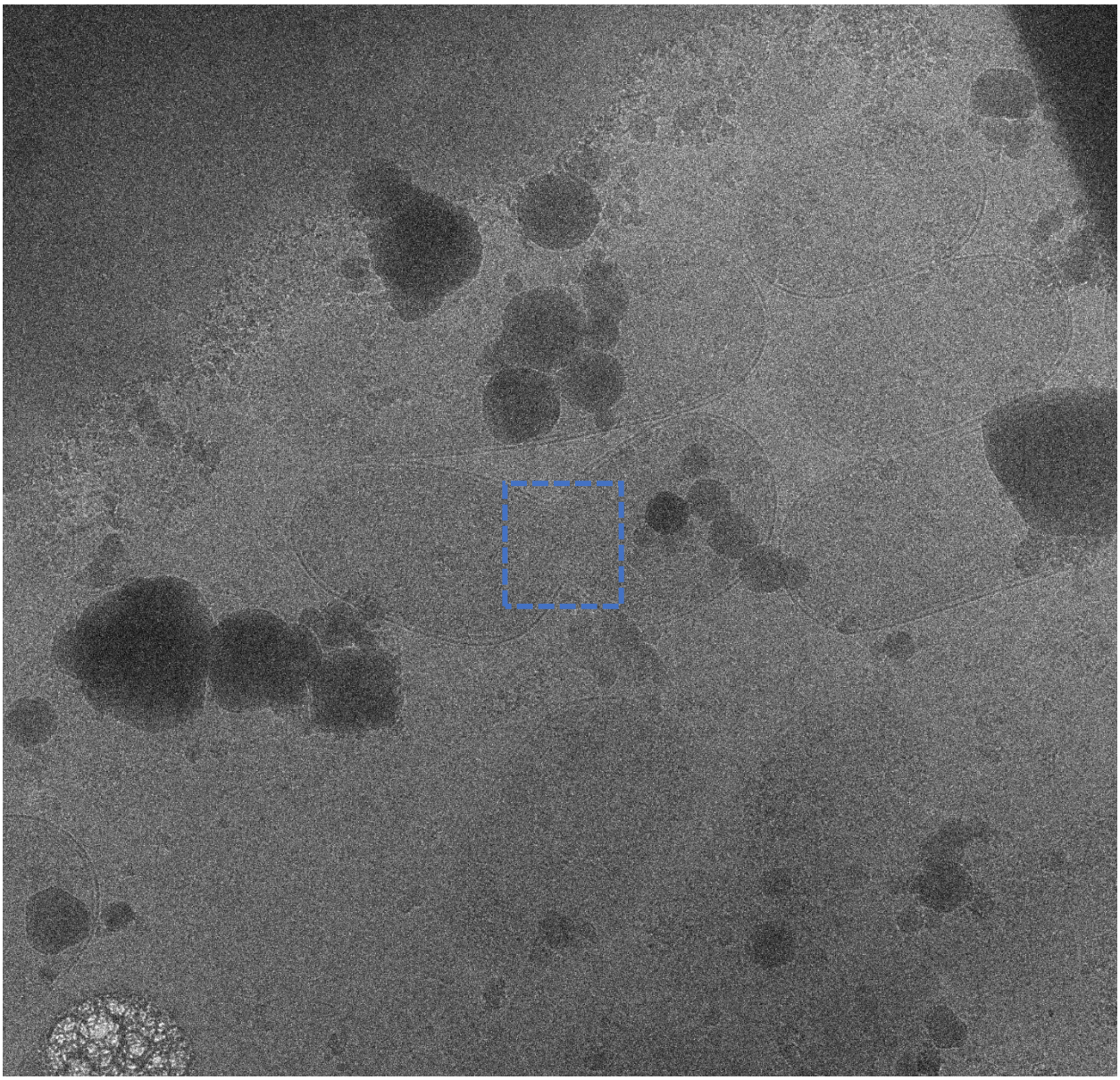

Figure 5.7. *Cryo-TEM image of FIB-milled lamella containing a dividing* E. coli *cell expressing the cSeNP-FtsZ construct. Approximate tilt-series location denoted with blue box.*

Figure 5.8. *Slice from tomogram collected in region highlighted in figure 5.7 at the pinch point of a dividing* E. coli *cell where FtsZ is expected to form filaments. The cell(s) are expressing the cSeNP-FtsZ construct and were plunge frozen following cloneable selenium nanoparticle synthesis. Only the membranes are clearly visible in this tomogram (and this tomographic slice).*

5.4 Discussion and Future Directions

Featureless tilt-series alignment

One of the crucial steps for tomogram reconstruction is the precise alignment of the images in the tilt series. Historically, this was done by adding electron dense fiducials to the sample—commonly gold nanoparticles (e.g., 10 nm immunogold). These fiducials could be tracked through the tilt series allowing for precise alignment of adjacent images through the tilt-series.[156] While fiducials are still used for tomogram alignment, marker-free tilt-series alignments are increasingly common in cryo-ET. With data that has lots of features (i.e., organelles, membranes) this technique works well.

Unfortunately, *E. coli* cells are relatively featureless aside from their outer membrane. In the tilt-series collection from figure 5.7 (and tomogram slice in figure 5.8) most of the image is of the featureless cytosol. This tilt-series was collected at higher magnifications than those presented in chapter 3. Adding fiducials to these samples would likely improve the alignment but would complicate the data analysis / segmentation since selenium particles might be confused with gold fiducials (and vice versa). By reducing the magnification used for data collection, tomogram alignment will likely improve because more features (i.e., membranes) will be in the frame. Further, converting the amorphous cSeNPs to crystalline particles or quantum dots (as described in chapter 3) would provide additional contrast to the particles such that they could once again be used as fiducials for tilt-series alignment.[76,109,122]

E. coli *are dense and lamella are thick*

It is easy to think about the downsides of plastic sectioning and ultramicrotomy in the context of cryo-ET. Ultramicrotomy is time consuming and plastic embedment introduces unknown artifacts into the sample structure. However, ultramicrotomy affords incredible control over sample

thickness (given enough time and patience). In chapter 3, *E. coli* samples were sectioned via ultramicrotomy following high pressure freezing and freeze-substitution resulting in ~ 100 nm thick sections. With the cryo-FIB-SEM, lamellae on the order of 200 nm are much more common. With the thicker section, there is more *volume* to reconstruct in a tomogram since the Z-dimension of the tomogram is related to the thickness of the sample (i.e., lamella or plastic section). With the additional thickness, there is more background signal from the ice and more signal from the thicker *E. coli* cell volume. The lamellae that were imaged with cryo-ET are roughly twice as thick as the plastic sections from chapter 3. *E. coli* are prokaryotic, meaning that they don't have membrane bound organelles and all (most) of the cellular contents float around in the cytosol. With cryo-ET then, we are trying to image through twice the thickness of an already dense cytosol—resulting in high background from other intracellular macromolecules.

Moreover, it was some combination of above factors that resulted in difficult to identify cSeNPs in cryo-ET generated tomograms. Most likely, the combination of decreased contrast from amorphous selenium nanoparticles (versus crystalline) and comparatively thicker samples had the greatest impact. This in turn caused tomogram alignment to suffer.

Future and on-going work

In the long-term, it probably makes the most sense to move away from *E. coli* as a model system for *imaging*; organisms such as *Saccharomyces cerevisiae* and *Chlamydomonas reinhardtii* are more commonly used for cryo-ET and are both easy to culture with easy to manipulate genomes.[159,160] Imaging at the leading edge of a mammalian cell would likely remove some need to FIB-mill since that region is very thin and contains few intracellular components making it very transparent to the electron beam.[161] *Caulobacter crescentus* would be another example organism that could be imaged without FIB-milling.[158,162]

The most exciting on-going work involves developing the cloneable selenium nanoparticle for use as a cryo-CLEM tag (initially described in chapter 3). The goal is to generate intracellular zinc selenide quantum dots using the cloneable selenium nanoparticle for imaging in cryo-CLEM. Cloneable zinc selenide quantum dots should be identifiable in cryo-electron tomograms—their crystallinity helping to add contrast beyond that of amorphous selenium nanoparticles. Zinc selenide quantum dots have proven to be visible in fluorescence micrographs, but adapting previous work for cryo-CLEM will still be challenging. Preliminary work shows that zinc selenide quantum dots have a distinct fluorescence signal and they are identifiable in cryo-fluorescence microscopy. These so-called 'cloneable quantum dots' are unique in that the contrast for both fluorescence and electron microscopy will originate from a single particle. It is likely that this on-going work developing cloneable quantum dots for cryo-CLEM will simultaneously address the application of cloneable selenium nanoparticles in cryo-ET and the need for cryo-CLEM labels.

CHAPTER 6: LABORATORY EVOLUTION OF METALLOID REDUCTASE SUBSTRATE RECOGNITION AND NANOPARTICLE PRODUCT SIZE

6.0 Synopsis

Glutathione Reductase-Like Metalloid Reductase (GRLMR) is an enzyme that reduces selenodiglutathione (GS-Se-SG), forming zerovalent Se nanoparticles (SeNPs). Error prone polymerase chain reaction was used to create a library of ~10,000 GRLMR variants. The library was expressed in BL21 *Escherichia coli* in liquid culture with 50 mM of SeO_3^{2-} present, under the hypothesis that the enzyme variants with improved GS-Se-SG reduction kinetics would emerge. The selection resulted in a GRLMR variant with 2 mutations. One of the mutations (D to E) lacks an obvious functional role, whereas the other mutation is L to H within 5 Å of the enzyme active site. This mutation places a second H residue within 5 Å of an active site dicysteine. This GRLMR variant was characterized for NADPH dependent reduction of GS-Se-SG, GSSG, SeO_3^{2-}, SeO_4^{2-}, GS-Te-SG and TeO_3^{2-}. The evolved enzyme demonstrated enhanced reduction of SeO_3^{2-} and gained ability to reduce SeO_4^{2-}. This variant is named Selenium Reductase (SeR) because of its emergent broad activity for a wide variety of Se substrates, whereas the parent enzyme was specific for GS-Se-SG. This study overall suggests that new biosynthetic routes are possible for inorganic nanomaterials using laboratory directed evolution methods.

6.1 Introduction

Biocatalysts accomplish a staggering variety of chemical reactions at physiological (mild) temperatures, pH, and aqueous conditions. Directed evolution methods expand the sequence space frontiers for biocatalysis.[58,163] Diverse examples of evolved enzymes include those that facilitate enantioselective synthesis of active pharmaceutical ingredients[164–166], the design of more

environmentally conscious and greener reaction conditions[167–170], and the further development of chemical tools which can be used to study complex biological systems.[61,171–173]

Enzymes developed using directed evolution, such as those in the cytochrome p450 family, now facilitate reactions that were previously unavailable or otherwise practiced with less efficiency, enantioselectivity, or yield.[174–176] Flavin-dependent halogenases such as RebH have been evolved to halogenate an array of small molecules with high site-specificity.[177–179] Notably, a few well-placed mutations can provoke dramatic changes in both enzyme substrate specificity and the reaction catalyzed (e.g., hydroxylation vs. dealkylation). Thus, significant precedent exists for engineering enzymes toward novel biocatalyzed reactions. There are nevertheless many un- and under explored biocatalyzed reactions.

One relatively unexplored area is in enzymes that synthesize inorganic nanomaterials. Naturally occurring examples of such enzymes are common. For example, multimeric iron-storing ferritin and ferritin-like proteins oxidize soluble and highly bioavailable Fe^{2+} into uniform ferric nanoparticles as a means of promoting cellular Fe^{2+} homeomostasis.[31,180,181] Multicopper oxidases such as manganese oxidase are thought to play primary roles in the bacterial formation of geological manganese oxide materials.[182–184] Enzymes involved in the metabolization/release of sulfur compounds such as cystathionine-y-lyase are implicated in several biosynthetic routes to quantum dots (QDs), the compositions of which include cadmium sulfides.[77,78,185,186] In our previous work, a glutathione reductase-like metalloid reductase (GRLMR) discovered in selenium tolerant microorganisms generated amorphous selenium[31,32] nanoparticles as determined by energy dispersive x-ray spectroscopy (EDS) in the presence of ionic selenium precursors such as SeO_3^{2-} (selenite) and selenodiglutathione (GS-Se-SG).[65,67,73,105]

Enzymes that produce inorganic materials have not yet been substantially subject to directed evolution methods; such experiments might modify the elements (bio-coordination complexes) that are preferred by the enzyme (substrate selectivity).

We are aware of only two prior efforts at directed evolution of inorganic oxidoreductases: In one instance, a chromate reductase was evolved using a 96-well plate NAD(P)H assay to increase reduction kinetics for Cr(IV) and U(VI).[187] In a second example, ferritin was evolved to exhibit improved physical attraction to magnets through altered biomineralization of iron.[188] Notably, these examples did not change substrate selectivity. Rather these studies altered enzyme kinetics toward existing substrates or altered the physicochemical nature of the product. Therefore, to the extent of our knowledge, there are no known examples where metal(loid) reductase substrate specificities are altered through laboratory directed evolution.

It is expected that modification of metal(loid) reductase enzyme substrate specificities will benefit several academic and industrial applications. Biomining and bioremediation of metals are nascent fields which currently rely on intact microbes to extract metals from heterogeneous mixtures.[64,189–192] Molecular mechanisms underlying the microbial extractions are scarcely characterized.[193,194] Identification, improvement, or alteration of enzymatic processes underlying biomining may facilitate use of 'greener' approaches to metal(loid) mining.

Our motivation for altering metal(loid) reductase substrate specificity is driven by our interest in producing cloneable nanoparticles of distinct size/shape/elemental composition.[195] A cloneable inorganic nanoparticle is synthesized in physiological conditions, has well-defined elemental composition, size, shape, and crystal structure. Because the protein determines these nanoparticle properties, and proteins are encoded in DNA, the properties of the nanoparticle are encoded in DNA.

Our cloneable nanoparticle approach relies on a combination of NADPH-dependent metal(loid) reducing enzymes (e.g., GRLMR[105], mercuric reductase[196,197], etc.) combined with metal nanoparticle binding peptides.[51,198] In this context, the elemental composition of the resulting nanoparticles is determined by the preferred enzymatic bio-coordination complex (i.e., substrate). Altering the substrate selectivity of a metal-reducing enzyme, therefore, can alter the elemental composition of a cloneable nanoparticle in which the enzyme is a component.

Herein we report the first directed evolution of a metal(loid) reductase that changes its substrate specificity. We began with GRLMR, whose preferred substrate is selenodiglutathione. A library of DNA mutants encoding the enzyme was created by error prone polymerase chain reaction (PCR). The library was expressed in *E. coli* and screened for isolates that survive in otherwise lethal concentrations of SeO_3^{2-}. An evolved enzyme was isolated, in which the substrate selectivity for SeO_3^{2-} was greatly increased as measured by catalytic efficiency (k_{cat}/K_m). There was a corresponding decrease in the catalytic efficiency of GS-Se-SG reduction. In addition, the parent enzyme had no measurable activity towards SeO_4^{2-} (selenate), while the evolved enzyme could reduce selenate. Overall, this suggests that substrate selectivity of metal-reducing enzymes can be altered using laboratory directed evolution methods. Notably the enzyme now acts on Se in 3 different coordination environments (GS-Se-SG, SeO_3^{2-}, and SeO_4^{2-}). In light of the findings that metal(loid) reductases can be evolved to act on a diverse range of metal(loid) coordination complexes (as opposed to free ions), the door is opened towards developing enzymes capable of acting on more dramatic ranges of inorganic coordination compound substrates – such as those with different metal(loid) centers.

6.2 Results and Discussion

Table 6.1. *Kinetics values K_m (mM), Vmax ($\frac{\mu M}{min * \mu g\ enzyme}$), and K_{cat}/K_m ($M^{-1}s^{-1}$) for GRLMR and SeR. Algorithmic fits to Michaelis-Menten models failed for some datasets due to marked product inhibition. Values marked with † were estimated from plots in figure 1. Examples of algorithmic fits may be found in figures S2 and S3.*

Substrate	GRLMR Km	SeR Km	GRLMR Vmax	SeR Vmax	GRLMR Kcat/Km	SeR Kcat/Km
$HNaSeO_3$	16.9 ± 3	4.09 ± 0.8	0.0298±0.004	0.102 ±0.009	$8.82 * 10^4 \pm 2 * 10^4$	$1.25 * 10^6 \pm 3 * 10^5$
GSSG	0.411 ± 0.3	1.08 ± 0.8	0.257 ± 0.08	0.14†	$3.13 * 10^7 \pm 3 * 10^7$	$6.48 * 10^6 \pm 6 * 10^6$
GS-Se-SG	0.233 ± 0.03	0.934 ± 0.166	0.265 ± 0.0157	0.05†	$5.69 * 10^7 \pm 9 * 10^6$	$2.68 * 10^6 \pm 9 * 10^5$
K_2TeO_3	12†	12†	0.007†	0.025†	$2.92 * 10^4$	$1.04 * 10^5$
GS-Te-SG	0.1†	0.22†	0.015†	0.01†	$7.5 * 10^6$	$2.3 * 10^6 \pm 3 * 10^6$
Na_2SeO_4	-	6.36 ± 2	-	.005†	-	$3.93 * 10^4 \pm 1 * 10^4$

The evolved enzyme contains two mutations: L314H and D408E. The evolved enzyme and its parent homologue (GRLMR) were evaluated with the substrates oxidized glutathione (GSSG), selenodiglutathione, and selenite. Enzymatic reactions were started by addition of NADPH to a final concentration of 200 μM. Enzyme activity was quantified spectrophotometrically by observing depletion of the characteristic NADPH absorption maximum at 340 nm. Typical raw kinetic data for GRLMR and SeR reduction of Selenite is shown in figure D1. The enzyme reactions were terminated upon observation of steady state reaction kinetics.

Plots of initial enzyme velocity vs. concentration for both GRLMR and SeR with all 3 substrates are shown in figure 6.1. The data was fitted with the Michaelis-Menten enzyme kinetic model in the Origin software package (OriginLab Corporation, Northampton, MA, USA). Table 6.1 gives the K_m, V_{max} and k_{cat}/K_m values derived for each enzyme/substrate pair. Relative to the parent enzyme (GRLMR), the evolved enzyme has dramatically increased catalytic efficiency toward Selenite, coupled with substantially decreased activities toward GSSG and GS-

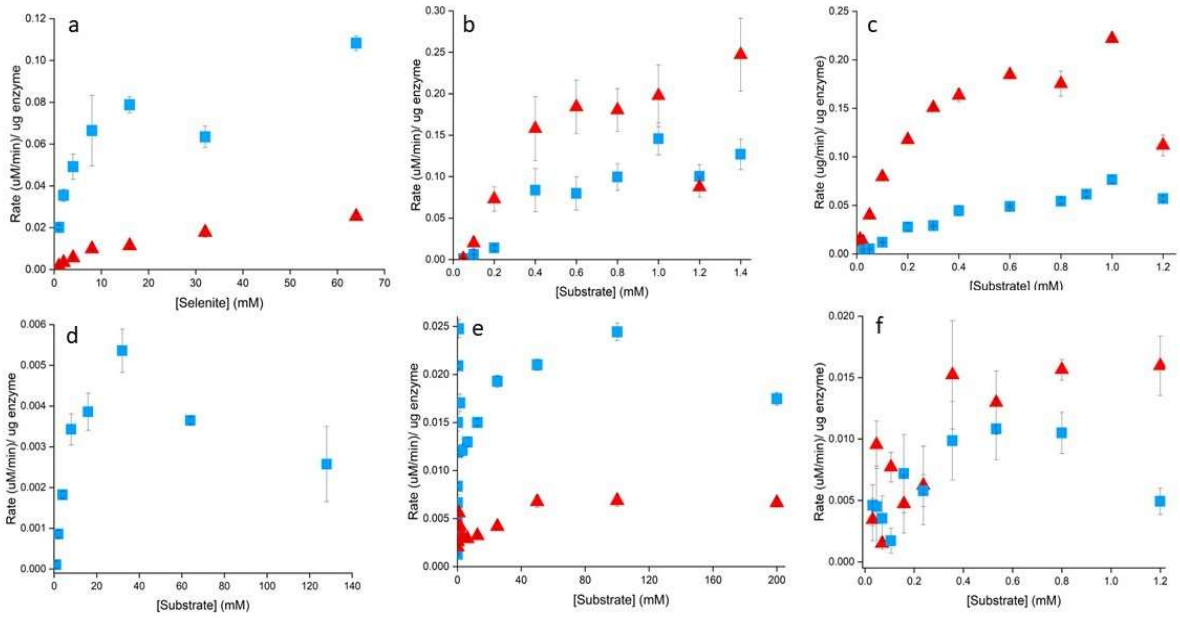

Figure 6.1. *Enzyme rate plotted against substrate concentration of GRLMR (red triangles) and SeR (blue squares) comparing (A) $SeO3^{2-}$, (B) GSSG, (C) GS-Se-SG, (D) $SeO4^{2-}$, (E) $TeO3^{2-}$, and (F) GS-Te-SG.*

Se-SG, and a new activity, not observed in the parent enzyme, toward reduction of Selenate. Because the catalytic efficiency for SeO_3^{2-} is indistinguishable from that for GSSG and GS-Se-SG, and the new activity for reduction of SeO_4^{2-} is now observable, we name the evolved enzyme Selenium Reductase (SeR), as the enzyme has clearly become biased toward reduction of various Se species in a way that the parent (GRLMR) enzyme is not.

GRLMR and SeR, like glutathione reductase (GSHR), do not conform perfectly to Michaelis-Menten enzyme kinetics. The main deviation from classic Michaelis-Menten kinetics is substrate inhibition of the enzyme at higher substrate concentrations.[48] Other known deviations from Michaelis-Menten kinetics may arise from a ping-pong/branching mechanism.[199]

The substrate inhibition of the enzyme leads to some uncertainty in V_{max} determination. In some cases (noted with † in Table 6.1), the algorithmic fits to Michaelis-Menten models were clearly flawed due to substrate inhibition resulting in artifactually low V_{max} values. These nonlinear

regression fits are shown in figures D2 and D3, accompanied by an explanation for which V_{max} values were estimated.

This uncertainty in Michaleis-Menten modeling – arising from product inhibition, is systematic – applying to both enzymes. Therefore, the comparative values are robust, but the absolute V_{max} values (and subsequent k_{cat} and k_{cat}/K_m interpretations) have some uncertainty that we cannot quantify. In addition, the experimental variability measured for the GSSG substrate is significantly larger than for the other substrates. This may be consistent with a ping-pong/branching mechanism suggested previously for this enzyme/substrate pair.[199] Notably, reduced experimental variability among other substrates suggests the putative mechanism of reduction for GSSG may change for other enzyme/substrate pairs.

Enzyme substrate selectivity

Catalytic efficiency (k_{cat} / K_m) of an enzyme for any substrate can allow comparison of substrate preference. Table 6.1 shows the k_{cat}/K_m values for both GRLMR and SeR for the substrates GS-Se-SG, GSSG, selenite, and selenate. The parent enzyme (GRLMR) has catalytic efficiency for the 4 substrates that follows the trend GS-Se-SG > GSSG >> SeO_3^{2-}. In comparison, SeR is much more promiscuous in substrate catalytic efficiency. For SeR, considering quantifiable experimental error, the k_{cat}/K_m are indistinguishable (GSSG = GS-Se-SG = SeO_3^{2-} >> SeO_4^{2-}).

This increase in promiscuity arises from a ~50% decrease in V_{max} for GSH based substrates, along with a ~300% increase in K_m for GS-Se-SG. Combined the k_{cat}/K_m for the GSH based substrates becomes less favorable by a factor of ~20 for GS-Se-SG and a factor of ~5 for GSSG. In contrast the V_{max} for SeO_3^{2-} increases by a factor of ~5 and the K_m decreases by a factor of 4. The overall catalytic efficiency of SeR increases from 8.82 x 10^4 to 1.25x10^6 $M^{-1}s^{-1}$ for SeO_3^{2-}. Overall, the catalytic efficiency of SeR is similar for the GSSG, GS-Se-SG, and SeO_3^{2-} substrates.

Superficially, the overall effect of the enzyme evolution appears to broaden Se substrate specialization (given that all 3 substrates show similar catalytic efficiency).

Combined, this analysis shows the enzyme evolving towards a broad capacity to use selenium as a preferred substrate, instead of GS-Se-SG which is preferred by the parent enzyme[200]. This could imply that at very high concentrations of selenite (50 mM in liquid culture), intracellular concentrations of selenite may exceed the usual form of intracellular selenium (GS-Se-SG), resulting in selective pressure for enzymes preferring SeO_3^{2-} over GS-Se-SG.

Tellurium Substrates

In addition to Se-based substrates, GRLMR can reduce (with less efficiency) Te based substrates such as GS-Te-SG, and TeO_3^{2-}. To gain further insight into how substrate selectivity evolved with the two mutations found in SeR, we determined enzymatic constants (K_m, V_{max}, k_{cat}/K_m) for the known tellurium substrates. Figure 6.1, panels e and f, give plots of initial reaction rate vs substrate concentration for GRLMR and SeR with tellurite and GS-Te-SG substrates.

Michaelis-Menten analysis was performed on these enzyme/substrate pairs. Table 6.1 lists the K_m, V_{max} and k_{cat}/K_m of each. Overall, catalytic efficiency for Te reduction is notably less than for Se reduction, indicating that the SeR is specialized for Se reduction. Among the Te species, catalytic efficiency for TeO_3^{2-} improves by a factor of ~4, whereas catalytic efficiency for GS-Te-SG is unchanged within experimental error. Overall, the evolution of catalytic efficiency from favoring oxidized glutathione substrates to increasingly favor chalcogenide oxyanion substrates is consistent for both Se and Te based substrates.

Structural Basis for Chalcogenide Oxyanion Selection

Structural predictions for SeR and GRLMR homodimers were generated through AlphaFold2-multimer[201,202] (AF2). LocalColabFold[203] was used in conjunction with the MMseqs[204] server to

rapidly prepare a multiple sequence alignment. Remaining calculations were performed on local machinery. With respect to calculation configuration, Template and Amber modes were selected to supply AF2 with template structural models to aid in prediction[205,206] (PDB entries 3DJJ, 3DK9, 4GRT, 5VDN, 5V36, 6DU7, 6N7F, 6N7F, 2R9Z, 6B4O, 1GEU, 2RAB, 2EQ6, 2EQ8, 2X8C, 7B02, 3QFA, 3EAN, and 4KPR). Final predicted structures were subjected to a molecular mechanics energy minimization step with Amber to refine bond geometry.

AF2 assesses its confidence in each amino acid prediction by the "predicted local-distance difference test" (pLDDT). The pLDDT metric ranges from 0 to 100, with higher values reflecting greater confidence in predicted structures. Typically, pLDDT values above 90 indicate a reliable prediction. Correctness of domain alignments for GRLMR and SeR were also assessed with the "predicted aligned error" (PAE) metric, which is standard practice for multimeric proteins. Low PAE values, indicating relatively

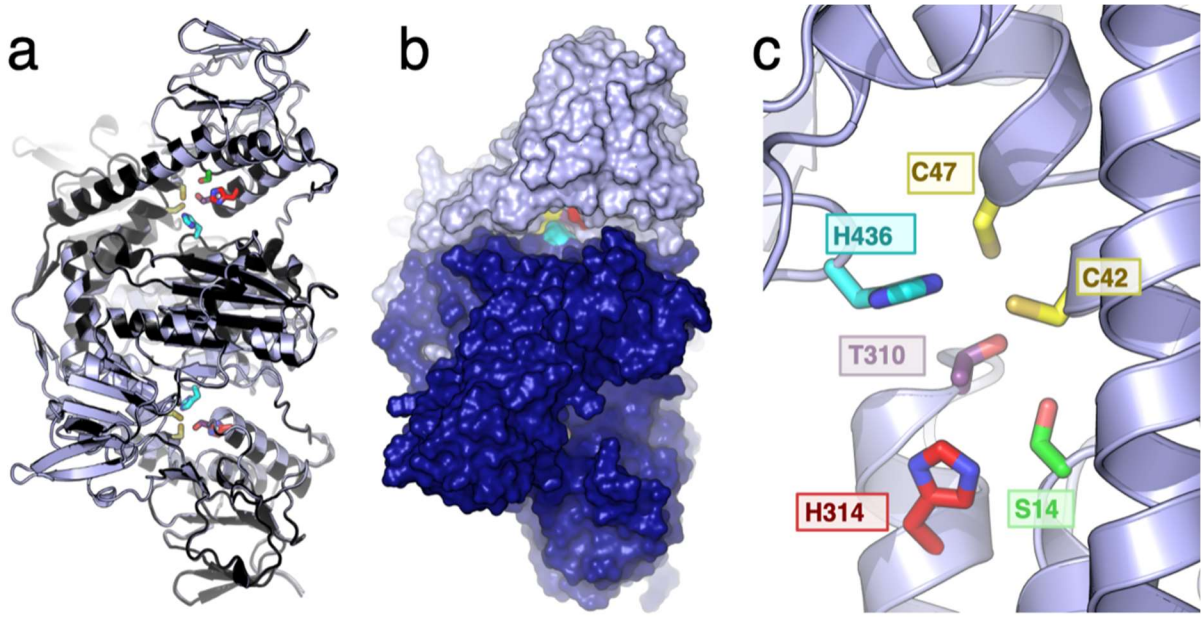

Figure 6.2. *AlphaFold2 models of SeR and GRLMR homodimers. a) a 3D superposition of SeR (light blue) and GRLMR (black). Active site residues are shown in sticks: H314 (red), S14 (green), C42 (yellow), C47 (yellow), T310 (purple) and H436 (cyan). This color scheme is used to highlight these residues in all panels. b) a surface rendering of the SeR homodimer, reveals the putative substrate entry channel into the active site, with H436 (cyan) provided by chain B (dark blue). c) active site close-up rendering with residues labels.*

high prediction correctness among alignment positions, are ideally within the 0-10 Å range (blue in Figure D4). On the other hand, higher values above 15 Å (red in Figure D4) would indicate low inter-domain sequence quality.

Five structure prediction models for both GRLMR and SeR were generated; the average pLDDT value for each structure was above 96 (Table D1), indicating a high prediction reliability. The predicted dimer alignment was also of very high confidence, with average PAE scores of 4.61 and 4.72 for GRLMR and SeR, respectively (Figure D4).

Because of the possibility that the template structures used in the AF2 modeling could bias the resulting models, we also generated structures without homology templates. The template-free models resulted in structures with similar pLDDT values compared to those generated with templates; without templates, the highest confidence models maintained average pLDDT values greater than 95 – as compared to above 96 when templates were used (Table D2). Structural alignment of the template-free models showed both templated and non-templated models were very similar. We compared the templated and non-templated models by calculating the root-mean-square-deviation of α-carbon positions ($RMSD_{C\alpha}$) of the top ranked structures made with and without templates. For GRLMR and SeR the $RMSD_{C\alpha}$ difference between template and without template was 1.357 Å and 0.933 Å respectively. These small $RMSD_{C\alpha}$ values indicate that use of templates did not bias the resulting models. For downstream analysis, we selected the GRLMR and SeR models with the most favorable pLDDT and PAE metrics from the AlphaFold2 calculations (generated with homology templates).

GRLMR and SeR models were aligned in PyMOL[207] to assess their similarity. The $RMSD_{C\alpha}$ between models was calculated to be 0.963 Å, indicating very high structural homology as shown visually in figure 6.2a. The main differences between GRLMR and SeR result from two

amino acid mutations: L314H and D408E. The D408E mutation sits at the homodimer interface and is 16 Å away from the closest catalytic cysteine residue (C45). The chemical change is small (aspartic acid being replaced by glutamic acid) and there is no obvious change between the GRLMR and SeR models at this position. Combined this analysis suggests that the D408E mutation is functionally a silent mutation.

Conversely, the L314H mutation sits in a position that has large implications for enzyme function. Residue 314 sits in a likely substrate entry channel in the enzyme (Figure 6.2b, red patch) and is just 5 Å from the disulfide active site of the enzyme (Figure 6.2c). The leucine to histidine mutation significantly alters the chemistry of this residue – from hydrophobic to an acid-base active aromatic residue. We therefore hypothesize that enzyme activity alterations can be attributed to the L314H mutation, and we focus our analysis on this mutation.

As shown in figure 6.2, the L314H mutation of SeR positions the histidine sidechain in the substrate entry channel. The Histidine sidechain is oriented toward the enzyme's putative disulfide active site. Only 3 other residues (T310, H236, and S14) are closer to the active side disulfide, at distances of 3.5 Å, 3.8 Å, and 4.8 Å respectively. All 3 of these residues bear functional groups implicated in enzymatic catalysis.

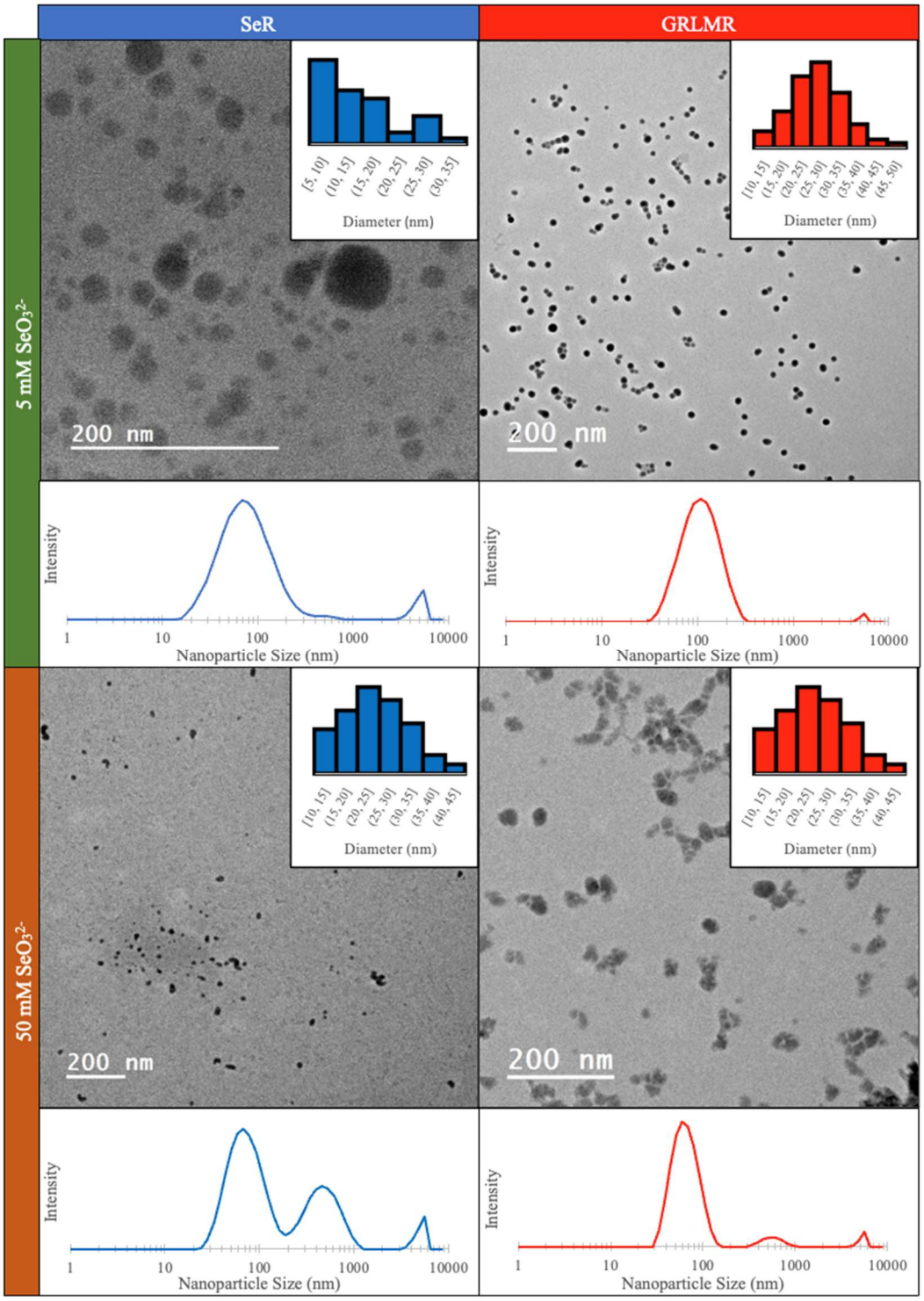

Figure 6.3. *Transmission electron microscopy images of amorphous selenium nanoparticles produced by SeR (left column) and GRLMR (right column) at 5 mM SeO_3^{2-} (top row) and 50 mM SeO_3^{2-} (bottom row). DLS intensity graphs of amorphous selenium nanoparticles produced by SeR (left column) and GRLMR (right column) at 5 mM SeO_3^{2-} (top row) and 50 mM SeO_3^{2-} (bottom row). The major peaks for each, reading from left to right, characterize the particle sizes at 90.49 nm, 114.20 nm, 76.29 nm, and 66.60 nm respectively.*

To assess the role of these 4 active-site proximal residues – T310, H236, S14 and H314 – we examined their homology in related enzymes in the Type-I pyridine nucleotide-disulfide oxidoreductase family. An analysis of 13 GSHRs, GRLMR, Mercuric Reductase, and Tellurite reductase shows that the disulfide is universally conserved, as expected for a catalytic active site. Similarly, S14 is conserved in all analyzed enzymes except for mercuric reductase where it is Alanine. T310 is conserved in all considered enzymes except for mercuric reductase and tellurite reductase, where it is V and K respectively. The highly conserved nature of S14 and T310 implicates these residues in catalysis.

Interestingly, the closest residue to the active site, H236, is not conserved among these enzymes. In fact, the only enzymes in which residue 236 is histidine are GRLMR and SeR -- the two Se specialized reductases present in this analysis. This implicates H236 in selectivity of chalcogenide substrates – both glutathione ligated and oxyanions – where GRLMR out-performs GSHR in terms of catalytic efficiency for the metal(loid) reduction. Similar to residue 236, the mutation in the SeR variant – L314H also occurs at a non-conserved amino acid position. Sequence alignments for these enzymes can be found in the Supporting Information.

This analysis reveals that SeR, interestingly, positions 2 histidine residues within 5Å of the enzyme active site (H236, H314). This location of two histidine residues proximal to the enzyme active site is likely to be significant for catalytic efficiency toward Se substrates. Histidine is an aromatic residue that is well-known to interact with metal cations (e.g., sequential His residues form the basis for immobilized metal affinity chromatography[208]). As an aromatic residue it participates in π-π interactions; addition of a nearby aromatic residue in SeR, coupled with the H236 already present in GRLMR (and retained in SeR) facilitates π-π interactions between Se substrates and the enzyme. The two active-site proximal histidine residues may help to position

the SeO_3^{2-} and other Se substrates through π-Se interactions in a way that makes both K_m (substrate binding) and k_{cat} (substrate->product rate) significantly more favorable.[209] Furthermore, the size increase in a mutation of leucine to histidine may disfavor the active-site approach of GSSG and GS-Se-SG, which are significantly larger substrates than selenite. This 'steric bulk' hypothesis is supported by the enzyme kinetic analysis, where changes in K_m are significant in the evolved enzyme for GS-Se-SG and GSSG, whereas the changes in k_{cat} for these substrates are antagonistic but small. Combined the L314H mutation appears to underlie all of the observed changes in SeR catalytic efficiency relative to SeO_3^{2-}, GSSG and GS-Se-SG.

Histidine is known to interact with chalcogen with diminishing preference correlated to relative atomic size, i.e., S > Se > Te.[209] This is corroborated by our experimental results, as the mutated histidine drastically increased selenite preference and modestly increased tellurite preference.

SeR and GRLMR SeNP product characterization.

Enzymatic products can change when enzymes evolve.[188] To determine if the enzymatic product had changed in any substantial way, we compared the GRLMR and SeR enzymatic products produced with SeO_3^{2-} substrates. GRLMR is known to produce approximately spherical red Se nanoparticles (SeNPs) whose size depends upon the initial concentration of SeO_3^{2-}. Modifying GRLMR could potentially change product size, morphology, and allotrope of the resulting SeNPs.

Both enzymes produce a red solution upon NADPH dependent reduction of SeO_3^{2-}, indicating that both enzymes produce the red allotrope of Se – which is amorphous, as compared to the crystalline black allotrope. The red solutions were drop-cast on carbon-coated transmission

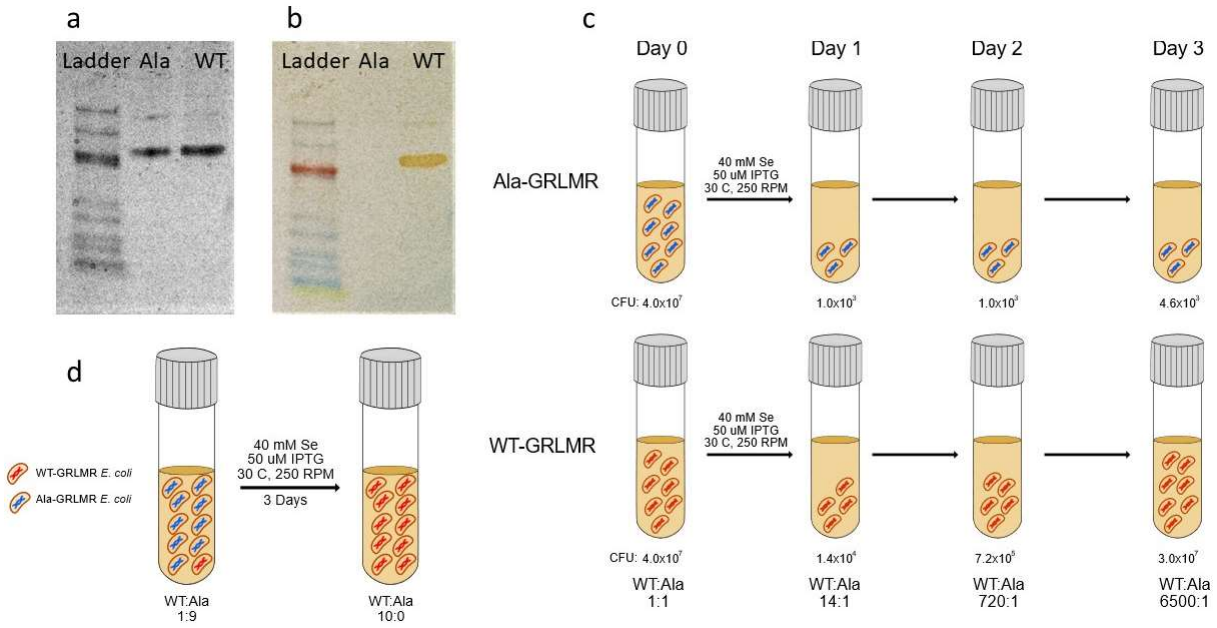

Figure 6.4. *(A) Native PAGE of wild-type GRLMR and an inactivated enzyme variant (Ala-GRLMR) stained with selenite and NADPH, (B) Native-PAGE of WT-GRLMR and Ala-GRLMR stained with Coomassie, (C) Scheme depicting growth of Ala-GRLMR and WT-GRLMR in 40 mM Se, (D) Scheme depicting enrichment of WT-GRLMR from a population of Ala-GRLMR in 40 mM Se.*

electron microscopy (TEM) grids and examined by TEM (Figure 6.3). This showed that SeR produced approximately spherical SeNPs of diameter 14.5 ± 7.4 nm and 11.2 ± 5.5 nm at 5 mM, and 50 mM SeO_3^{2-} respectively. In contrast GRLMR produced spherical SeNPs of diameter 26.8 ± 7.2 nm and 24.1 ± 7.4 nm at 5 mM and 50 mM SeO_3^{2-} respectively. SeNP aggregation was more commonly observed with SeR but was seen with both SeR and GRLMR synthesized particles at 50 mM SeO_3^{2-}.

This trend in size can also be observed by dynamic light scattering measurements (DLS). The particle sizes determined by DLS are significantly larger than those observed by TEM. We attribute this larger particle size to the inclusion of nanoparticle-associated enzymes in the DLS diameter measurement.

The smaller size of SeNPs produced by SeR compared to GRLMR can be rationalized by classical nucleation theory. Here, we hypothesize that SeO_3^{2-} is reduced to either Se^{2-} or Se^0 by the enzymes. Se^{2-} is rapidly oxidized to Se^0 by dissolved oxygen.[76] The Se^0 species is essentially

insoluble in water, so it has a very high propensity to nucleate and grow into SeNPs.[76] In classical nucleation theory, the critical nucleus size describes the size of a particle at which growth becomes favored over dissolution. Particles larger than the critical nucleus size tend to grow while particles smaller than the critical nucleus size tend to shrink. The critical nucleus size depends on how saturated a solution is with a given solute; for a saturated solution, the critical nucleus size becomes zero.

Because the V_{max} (k_{cat}) of SeR is improved for SeO_3^{2-} relative to GRLMR, we suggest that local concentrations of Se^0 enzymatic product are higher for SeR than for GRLMR. This makes the solutions produced by SeR locally more 'saturated', shrinking the critical nucleus size of the resulting SeNPs. The smaller SeNPs observed for SeR enzymatic products can therefore be rationalized by the higher SeR k_{cat} resulting in a smaller critical nucleus size. Increased number of nuclei leads to increased competition for growth, leading to a larger number of smaller nanoparticles.

It's at first surprising that the observed SeNP diameters do increase when [SeO_3^{2-}] increases. We attribute this to SeNP passivation by enzymes present in the mixtures exerting more influence over SeNP size than [SeO_3^{2-}]. Because SeR and GRLMR surfaces are essentially identical, the difference in SeNP size is attributed to the increased k_{cat} of SeR.

GRLMR Variant Library Creation

Error-prone polymerase chain reaction (EP-PCR) was used to create a library of approximately 10,000 GRLMR variants. EP-PCR is a widely adopted and relatively straightforward means of introducing random mutations into defined gene segments.[210] Genes of interest ranging from hundreds to thousands of base pairs can be replicated into diversified libraries through this technique.

We used the commercially available Genemorph II Random Mutagenesis Kit (Agilent Technologies #200550) setting error-prone replication parameters to generate approximately 3-5 nucleotide mutations per 1000 bp. The resulting EP-PCR library product was ligated into pET20b. The ligation product was purified on a 1% agarose gel.

Electrocompetent E. coli cells (New England BioLabs #c3020K) were transformed with the EP-PCR library of GRLMR mutants. The library was subsequently transformed into T7 Express lysY (New England BioLabs #C3010I) for downstream selection experiments. To validate the mutational load of our WT-GRLMR DNA library, we picked 5 random colonies from the transformed library for sequencing. Of the randomly picked colonies, each displayed 3-9 point mutations within the ~1,400 bp gene sequence of GRLMR confirming our expected mutational load.

Library Selection Strategy

Enzymatic reduction of ionic metal(loids) into lower redox states (and in many instances zero-valent nanoparticulate form) is a documented detoxification mechanism for cells. While selenium is an essential nutrient, it is also toxic at higher concentrations.[200,211]

Previous work has demonstrated that transformation of GRLMR into laboratory expression cells increases tolerance to selenite supplementation in the culture by nearly 10-fold, as judged by IC90 values.[105] We therefore reasoned that a selection environment could be developed wherein the survivability and proliferation of host cells could be directly correlated to the kinetic profile of mutated GRLMR.

Under this hypothesis, GRLMR variants with altered substrate specificity (e.g., altered catalytic efficiency) could be isolated by challenging host *E. coli* cells with toxic concentrations of substrate. The hypothesis is that cells expressing GRLMR variants with improved catalytic

efficiency toward toxic Se will out-compete cells expressing variants with unchanged or decreased catalytic efficiency.

In the particular selection described here, we hypothesized that we could improve GRMLR reduction of the intracellular form of Selenium, GS-Se-SG, by challenging the cells with 50mM selenite in liquid culture. The basis for this selection is to find GRLMR variants that reduce more bio-active intracellular Se (4+) into less available Se (0) at a greater rate, promoting a competitive advantage and thus generating selective pressure in favor of the host cell. As shown above, however, this initial hypothesis was not entirely correct, as we instead unexpectedly evolved an enzyme with decreased activity toward GS-Se-SG and improved activity toward SeO_3^{2-}.

A previous study demonstrated evolution of chromate reductase in a 96-well plate format to become a catalytically more efficient enzyme toward chromate.[187] We opted to develop the selection method described here because it can accommodate much larger library sizes, with higher throughput and reduced labor. We additionally rationalized that a free-floating culture (as opposed to solid media) would prevent cells from depleting their local exterior selenite concentration, placing more selection emphasis on intracellular chemistry.

Inactivating GRLMR with C42A and C47A mutations

As a first step in library screening, we found an SeO_3^{2-} culture concentration in which cells expressing WT-GRMLR could consistently outcompete cells expressing a disabled GRLMR enzyme. Like its highly characterized parent analogue GSHR, GRLMR contains a cysteine-based disulfide which is described as the putative active site. In GRLMR, SeR, and GSHR, among others, the active site sequence motif is CXXXXC. In GRLMR, the active site cysteine residues are C42 and C47.

We used site directed mutagenesis to make C42A and C47A mutations. While the exact mechanism of metal(loid) reduction by GRLMR is currently unknown, we hypothesized that the C42A and C47A mutations would abolish GRLMR catalytic activity, with minimal perturbations to expression strength, intracellular solubility, or other factors that might confound experimental / control paired experiments.

C42A, C47A mutants to GRLMR do not reduce SeO_3^{2-}

Figure 6.4A shows a Coomassie stained Native-PAGE gel of purified the GRLMR-C42A-C47A (Ala-GRLMR) and GRLMR side-by-side. To assay activity of the C42A, C47A mutant, we used an *in situ* assay of SeO_3^{2-} reduction capability. In this assay, a non-denaturing gel containing SeO_3^{2-} reducing enzymes is stained with a combination of SeO_3^{2-} and NADPH. The result of this assay is shown in figure 6.4B. The assay shows a band comprised of selenium precipitates in the GRLMR lane, whereas there is no evidence of selenium precipitates in for the Ala-GRLMR mutant. This comprises strong evidence that the mutant GRLMR is catalytically inactive.

Development of live/dead selection system

We proceeded to determine a level of SeO_3^{2-} supplementation where intracellularly expressed GRLMR endows survival and proliferation of host cells in comparison to cells expressing inactivated GRLMR. Previous studies showed that functional GRLMR conveys SeO_3^{2-} tolerance by enzymatic formation of intracellular SeNPs.[32]

As illustrated in figure 6.4C, liquid cultures of WT-GRLMR and Ala-GRLMR were each inoculated and induced with an initial concentration of 4×10^7 colony forming units (CFUs) in 2.5 mL of LB with 40 mM $HNaSeO_3$ and 50 μM IPTG. The cultures were incubated at 30 ºC for 3 days. At regular intervals, the cell population was assessed in each culture. This was done by determining the number of CFUs as measured by serial dilution of 10 μL culture samples. For

robustness, this experiment was done in triplicate. Cells expressing inactivated GRLMR lost population, resulting in only 400 CFU/mL by day 3. In contrast GRLMR expressing cells comparatively declined on day 1 and rebounded to the initial CFU value by day 3, resulting in a WT:Ala ratio of 6,500:1.

We subsequently tested our selection conditions by mixing a subpopulation of GRLMR expressing cells into a culture containing 10-fold more cells expressing inactivated GRLMR, as shown in figure 6.4D. At day 3, a portion of the culture was plated on LB-Agar. From the LB-Agar, 10 colonies were grown in liquid culture, from which plasmids were purified and sequenced. This sequencing revealed that all 10 isolates contained only active GRLMR sequence. This shows that in the selection condition (40 mM SeO_3^{2-}), GRLMR expressing cells outcompete those cells that express inactivated GRLMR. This condition, then, is expected to put selective pressure on cells containing a GRLMR mutant library, favoring those cells with more effective Se-reducing GRLMR variants.

Selection for improved Se reduction

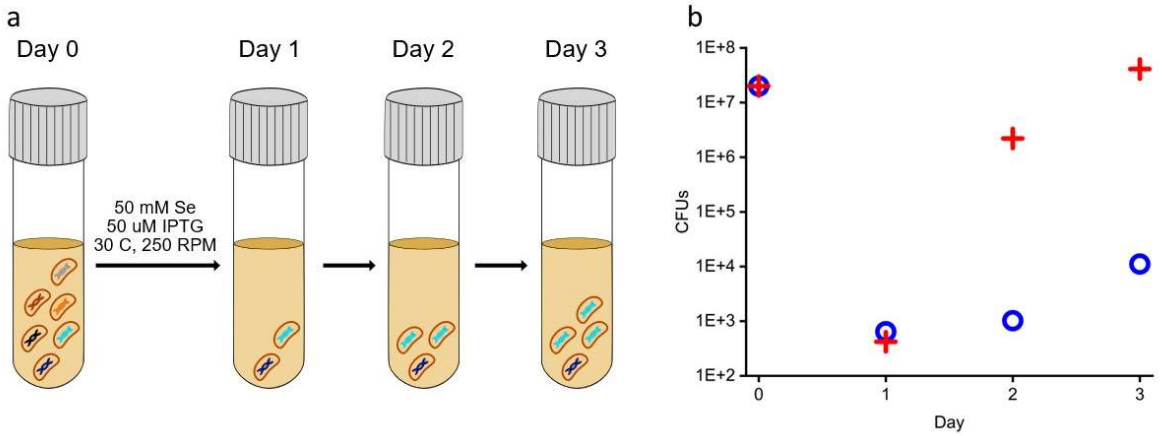

Figure 6.5. *(A) Initial EP-PCR GRLMR library loses population members through the first day of Se challenge. High performing variants repopulate the overall culture over the following days. (B) Library culture CFUs over two rounds of selection; first round marked by blue circles, second round marked by red cross symbols.*

Because supplementation of liquid culture with 40 mM sodium selenite creates a condition where GRLMR expressing cells proliferate whereas inactivated GRLMR cells do not, we attempted selections of the EP-PCR library at 50 mM sodium selenite concentration (10 mM higher than in the proof-of-concept experiments), under the hypothesis that GRLMR mutants with improved activity will out-compete WT-GRLMR in these conditions in the same way that WT-GRLMR outcompeted Ala-GRLMR.

The EP-PCR library was transformed into BL21 *E. coli* cells, and library expression was induced with 50 μM IPTG. To determine the number of cells that survived the 50mM selenite challenge, serial dilutions of 10 μL in triplicate were plated on LB-agar at 24 h intervals allowing determination of the CFU count of the culture. Similarly to earlier experiments, CFU count of the library decreased several orders of magnitude through the first day of selection, followed by rebound growth in the following days. As is shown in figure 6.5A, we infer that an initial drop in CFU correlates to a loss in the overall library diversity. Subsequent cell proliferation therefore occurs from a 'fitter' subsection of the initial library, which forms the basis of evolutionary selection.

After allowing the library three days to repopulate, we inoculated 50 μL of the selection culture into 2.5 mL fresh LB/carb in preparation for a second round of selection. The outgrowth was subsequently grown to an OD of 0.5, then a 100 μL aliquot was inoculated into 2.5 mL LB/carb containing 50 mM selenite and 50 uM IPTG. The 50 mM selenite concentration was maintained in the second round to directly compare growth rates and assess if selection had occurred in the first round – under the hypothesis that a fitter population would better withstand an equal challenge.

As shown in figure 6.5B, the cell population in this second round of selection grew to become several orders of magnitude larger than observed in the first round of selection at the same time interval and Se concentration. This much faster growth during the second round of selection implied that we had enriched the presence of GRLMR variants that had improved Se reduction capability – therefore endowing host cells with an improved ability to survive/proliferate in 50 mM selenite.

A total of 10 individual plasmid preparations from the second-round selection were sequenced. All 10 sequences of the encoded GRLMR mutants were identical, containing the two-point mutations (L314H and D408E) that were characterized above. We thus reasoned that GRLMR variants had converged to the most fit variant throughout the two rounds of selection. This GRLMR variant (SeR) was fully characterized as described above.

Manuscript adapted for dissertation submission[104]*. Author contributions: ARH (lead author) and RSC (2nd author) conducted experiments, wrote initial draft, and edited. GE, TT,* ***BFG****, and AA (co-authors) conducted experiments and wrote initial draft. CJA (principal investigator) wrote initial draft and edited. CS (co-principal investigator) edited.*

CHAPTER 7: CONCLUSIONS

The work presented in this dissertation entitled "Cryo-Electron Microscopy of Cloneable Inorganic Nanoparticles" highlights the application and prospects for cloneable nanoparticles as cloneable contrast labels for cryo-electron microscopy. First, the grand challenge with low innate contrast in biological imaging was established. Second, the cloneable nanoparticle paradigm was defined and development of the cloneable selenium nanoparticle was detailed through previous work from the Ackerson lab. In the third chapter, the cloneable selenium nanoparticle is revealed and demonstrated in cellular electron tomography, correlative light-electron microscopy, and X-ray tomography. This work serves as a powerful proof-of-concept for deployment of the cloneable selenium nanoparticle as an intracellular contrast label for electron microscopy in addition to other biological imaging modalities. Then, an on-going project to determine a near-atomic resolution structure of GRLMR via single particle cryo-EM showed promising results. The single particle cryo-EM structure of GRLMR—alongside structural information about substrate binding (i.e., selenium, NADPH) will illuminate fundamental understanding of enzymatic nanoparticle synthesis. Chapter 5 chronicles current progress adapting the cloneable selenium nanoparticle in cryo-electron tomography and reveals promising preliminary data alongside current challenges and adjacent work developing cloneable quantum dots as cryo-CLEM labels. And in chapter 6, we saw a glimpse towards the future expansion of cloneable nanoparticles with a first-of-its-kind directed evolution project of GRLMR. The cloneable nanoparticles platform has a promising future to enhance biological imaging for many imaging modalities, chiefly in cryo-electron tomography and cryo-CLEM.

REFERENCES

(1) Shimomura, O. Structure of the Chromophore of *Aequorea* Green Fluorescent Protein. *FEBS Lett.* **1979**, *104* (2), 220–222. https://doi.org/10.1016/0014-5793(79)80818-2.

(2) Chalfie, M.; Tu, Y.; Euskirchen, G.; Ward, W. W.; Prasher, D. C. Green Fluorescent Protein as a Marker for Gene Expression. *Science* **1994**, *263* (5148), 802–805. https://doi.org/10.1126/science.8303295.

(3) Gray, N. Knowing the Limit: Diffraction Limit Theory. *Nat. Cell Biol.* **2009**, *11* (S1), S8–S8. https://doi.org/10.1038/ncb1940.

(4) Rust, M. J.; Bates, M.; Zhuang, X. Sub-Diffraction-Limit Imaging by Stochastic Optical Reconstruction Microscopy (STORM). *Nat. Methods* **2006**, *3* (10), 793–796. https://doi.org/10.1038/nmeth929.

(5) De Boer, P.; Hoogenboom, J. P.; Giepmans, B. N. G. Correlated Light and Electron Microscopy: Ultrastructure Lights Up! *Nat. Methods* **2015**, *12* (6), 503–513. https://doi.org/10.1038/nmeth.3400.

(6) Kisielowski, C.; Freitag, B.; Bischoff, M.; van Lin, H.; Lazar, S.; Knippels, G.; Tiemeijer, P.; van der Stam, M.; von Harrach, S.; Stekelenburg, M.; Haider, M.; Uhlemann, S.; Müller, H.; Hartel, P.; Kabius, B.; Miller, D.; Petrov, I.; Olson, E.; Donchev, T.; Kenik, E.; Lupini, A.; Bentley, J.; Pennycook, S.; Anderson, I.; Minor, A.; Schmid, A.; Duden, T.; Radmilovic, V.; Ramasse, Q.; Watanabe, M.; Erni, R.; Stach, E.; Denes, P.; Dahmen, U. Detection of Single Atoms and Buried Defects in Three Dimensions by Aberration-Corrected Electron Microscope with 0.5-Å Information Limit. *Microsc. Microanal.* **2008**, *14* (5), 469–477. https://doi.org/10.1017/S1431927608080902.

(7) Chen, Z.; Jiang, Y.; Shao, Y.-T.; Holtz, M. E.; Odstrčil, M.; Guizar-Sicairos, M.; Hanke, I.; Ganschow, S.; Schlom, D. G.; Muller, D. A. Electron Ptychography Achieves Atomic-Resolution Limits Set by Lattice Vibrations. *Science* **2021**, *372* (6544), 826–831. https://doi.org/10.1126/science.abg2533.

(8) Schnell, U.; Dijk, F.; Sjollema, K. A.; Giepmans, B. N. G. Immunolabeling Artifacts and the Need for Live-Cell Imaging. *Nat. Methods* **2012**, *9* (2), 152–158. https://doi.org/10.1038/nmeth.1855.

(9) Reth, M. Matching Cellular Dimensions with Molecular Sizes. *Nature Immunology*. 2013, pp 765–767. https://doi.org/10.1038/ni.2621.

(10) Sarraf, C. E. Immunolabeling for Electron Microscopy; 2000; Vol. 4, pp 439–452. https://doi.org/10.1385/1-59259-076-4:439.

(11) Shu, X.; Lev-Ram, V.; Deerinck, T. J.; Qi, Y.; Ramko, E. B.; Davidson, M. W.; Jin, Y.; Ellisman, M. H.; Tsien, R. Y. A Genetically Encoded Tag for Correlated Light and Electron Microscopy of Intact Cells, Tissues, and Organisms. *PLoS Biol.* **2011**, *9* (4). https://doi.org/10.1371/journal.pbio.1001041.

(12) Fogel, A. I.; Akins, M. R.; Krupp, A. J.; Stagi, M.; Stein, V.; Biederer, T. SynCAMs Organize Synapses through Heterophilic Adhesion. *J. Neurosci.* **2007**, *27* (46), 12516–12530. https://doi.org/10.1523/JNEUROSCI.2739-07.2007.

(13) Doh, J. K.; Tobin, S. J.; Beatty, K. E. MiniVIPER Is a Peptide Tag for Imaging and Translocating Proteins in Cells. *Biochemistry* **2020**, *59* (33), 3051–3059. https://doi.org/10.1021/acs.biochem.0c00526.

(14) Los, G. V.; Encell, L. P.; McDougall, M. G.; Hartzell, D. D.; Karassina, N.; Zimprich, C.; Wood, M. G.; Learish, R.; Ohana, R. F.; Urh, M.; Simpson, D.; Mendez, J.; Zimmerman, K.; Otto, P.; Vidugiris, G.; Zhu, J.; Darzins, A.; Klaubert, D. H.; Bulleit, R. F.; Wood, K. V. HaloTag: A Novel Protein Labeling Technology for Cell Imaging and Protein Analysis. *ACS Chem. Biol.* **2008**, *3* (6), 373–382. https://doi.org/10.1021/cb800025k.

(15) Gautier, A.; Juillerat, A.; Heinis, C.; Corrêa, I. R.; Kindermann, M.; Beaufils, F.; Johnsson, K. An Engineered Protein Tag for Multiprotein Labeling in Living Cells. *Chem. Biol.* **2008**, *15* (2), 128–136. https://doi.org/10.1016/j.chembiol.2008.01.007.

(16) Keppler, A.; Gendreizig, S.; Gronemeyer, T.; Pick, H.; Vogel, H.; Johnsson, K. A General Method for the Covalent Labeling of Fusion Proteins with Small Molecules in Vivo. *Nat. Biotechnol.* **2003**, *21* (1), 86–89. https://doi.org/10.1038/nbt765.

(17) Zakeri, B.; Fierer, J. O.; Celik, E.; Chittock, E. C.; Schwarz-Linek, U.; Moy, V. T.; Howarth, M. Peptide Tag Forming a Rapid Covalent Bond to a Protein, through Engineering a Bacterial Adhesin. *Proc. Natl. Acad. Sci.* **2012**, *109* (12). https://doi.org/10.1073/pnas.1115485109.

(18) Morphew, M. K.; O'Toole, E. T.; Page, C. L.; Pagratis, M.; Meehl, J.; Giddings, T.; Gardner, J. M.; Ackerson, C.; Jaspersen, S. L.; Winey, M.; Hoenger, A.; Mcintosh, J. R. Metallothionein as a Clonable Tag for Protein Localization by Electron Microscopy of Cells. *J. Microsc.* **2015**, *260* (1), 20–29. https://doi.org/10.1111/jmi.12262.

(19) Si, M.; Lang, J. The Roles of Metallothioneins in Carcinogenesis. *J. Hematol. Oncol.J Hematol Oncol* **2018**, *11* (1), 1–20. https://doi.org/10.1186/s13045-018-0645-x.

(20) Mercogliano, C. P.; DeRosier, D. J. Gold Nanocluster Formation Using Metallothionein: Mass Spectrometry and Electron Microscopy. *J. Mol. Biol.* **2006**, *355* (2), 211–223. https://doi.org/10.1016/j.jmb.2005.10.026.

(21) Fukunaga, Y.; Hirase, A.; Kim, H.; Wada, N.; Nishino, Y.; Miyazawa, A. Electron Microscopic Analysis of a Fusion Protein of Postsynaptic Density-95 and Metallothionein in Cultured Hippocampal Neurons. *J. Electron Microsc. (Tokyo)* **2007**, *56* (4), 119–129. https://doi.org/10.1093/jmicro/dfm027.

(22) Martell, J. D.; Deerinck, T. J.; Sancak, Y.; Poulos, T. L.; Mootha, V. K.; Sosinsky, G. E.; Ellisman, M. H.; Ting, A. Y. Engineered Ascorbate Peroxidase as a Genetically Encoded Reporter for Electron Microscopy. *Nat. Biotechnol.* **2012**, *30* (11), 1143–1148. https://doi.org/10.1038/nbt.2375.

(23) Ramachandra, R.; Mackey, M. R.; Hu, J.; Peltier, S. T.; Xuong, N. H.; Ellisman, M. H.; Adams, S. R. Elemental Mapping of Labelled Biological Specimens at Intermediate Energy Loss in an Energy-Filtered TEM Acquired Using a Direct Detection Device. *J. Microsc.* **2021**, *283* (2), 127–144. https://doi.org/10.1111/jmi.13014.

(24) Schmitt, F. J.; Renger, G.; Friedrich, T.; Kreslavski, V. D.; Zharmukhamedov, S. K.; Los, D. A.; Kuznetsov, V. V.; Allakhverdiev, S. I. Reactive Oxygen Species: Re-Evaluation of Generation, Monitoring and Role in Stress-Signaling in Phototrophic Organisms. *Biochim. Biophys. Acta - Bioenerg.* **2014**, *1837* (6), 835–848. https://doi.org/10.1016/j.bbabio.2014.02.005.

(25) Chen, X.; Winters, C.; Crocker, V.; Lazarou, M.; Sousa, A. A.; Leapman, R. D.; Reese, T. S. Identification of PSD-95 in the Postsynaptic Density Using miniSOG and Em Tomography. *Front. Neuroanat.* **2018**, *12* (December). https://doi.org/10.3389/fnana.2018.00107.

(26) Adams, S. R.; Mackey, M. R.; Ramachandra, R.; Palida Lemieux, S. F.; Steinbach, P.; Bushong, E. A.; Butko, M. T.; Giepmans, B. N. G.; Ellisman, M. H.; Tsien, R. Y. Multicolor Electron Microscopy for Simultaneous Visualization of Multiple Molecular Species. *Cell Chem. Biol.* **2016**, *23* (11), 1417–1427. https://doi.org/10.1016/j.chembiol.2016.10.006.

(27) Lučić, V.; Rigort, A.; Baumeister, W. Cryo-Electron Tomography: The Challenge of Doing Structural Biology in Situ. *J. Cell Biol.* **2013**, *202* (3), 407–419. https://doi.org/10.1083/jcb.201304193.

(28) Clarke, N. I.; Royle, S. J. FerriTag Is a New Genetically-Encoded Inducible Tag for Correlative Light-Electron Microscopy. *Nat. Commun.* **2018**, *9* (1), 1–10. https://doi.org/10.1038/s41467-018-04993-0.

(29) Dieudonné, A.; Pignol, D.; Prévéral, S. Magnetosomes: Biogenic Iron Nanoparticles Produced by Environmental Bacteria. *Appl. Microbiol. Biotechnol.* **2019**, *103* (9), 3637–3649. https://doi.org/10.1007/s00253-019-09728-9.

(30) Jogler, C.; Lin, W.; Meyerdierks, A.; Kube, M.; Katzmann, E.; Flies, C.; Pan, Y.; Amann, R.; Reinhardt, R.; Schüler, D. Toward Cloning of the Magnetotactic Metagenome: Identification of Magnetosome Island Gene Clusters in Uncultivated Magnetotactic Bacteria from Different Aquatic Sediments. *Appl. Environ. Microbiol.* **2009**, *75* (12), 3972–3979. https://doi.org/10.1128/AEM.02701-08.

(31) Wang, Q.; Mercogliano, C. P.; Löwe, J. A Ferritin-Based Label for Cellular Electron Cryotomography. *Structure* **2011**, *19* (2), 147–154. https://doi.org/10.1016/j.str.2010.12.002.

(32) Clarke, N. I.; Royle, S. J. FerriTag Is a New Genetically-Encoded Inducible Tag for Correlative Light-Electron Microscopy. *Nat. Commun.* **2018**, *9* (1), 2604. https://doi.org/10.1038/s41467-018-04993-0.

(33) Jiang, B.; Fang, L.; Wu, K.; Yan, X.; Fan, K. Ferritins as Natural and Artificial Nanozymes for Theranostics. *Theranostics* **2020**, *10* (2), 687–706. https://doi.org/10.7150/thno.39827.

(34) Karas, V. O.; Westerlaken, I.; Meyer, A. S. The DNA-Binding Protein from Starved Cells (Dps) Utilizes Dual Functions To Defend Cells against Multiple Stresses. *J. Bacteriol.* **2015**, *197* (19), 3206–3215. https://doi.org/10.1128/JB.00475-15.

(35) Orban, K.; Finkel, S. E. Dps Is a Universally Conserved Dual-Action DNA-Binding and Ferritin Protein. *J. Bacteriol.* **2022**, *204* (5), e00036-22. https://doi.org/10.1128/jb.00036-22.

(36) Capeness, M. J.; Echavarri-Bravo, V.; Horsfall, L. E. Production of Biogenic Nanoparticles for the Reduction of 4-Nitrophenol and Oxidative Laccase-Like Reactions. *Front. Microbiol.* **2019**, *10*, 997. https://doi.org/10.3389/fmicb.2019.00997.

(37) Sawant, S. Y.; Sayed, M. S.; Han, T. H.; Karim, M. R.; Shim, J.-J.; Cho, M. H. Bio-Synthesis of Finely Distributed Ag Nanoparticle-Decorated TiO2 Nanorods for Sunlight-Induced Photoelectrochemical Water Splitting. *J. Ind. Eng. Chem.* **2019**, *69*, 48–56. https://doi.org/10.1016/j.jiec.2018.09.002.

(38) Singh, P.; Garg, A.; Pandit, S.; Mokkapati, V.; Mijakovic, I. Antimicrobial Effects of Biogenic Nanoparticles. *Nanomaterials* **2018**, *8* (12), 1009. https://doi.org/10.3390/nano8121009.

(39) Fayaz, A. M.; Balaji, K.; Girilal, M.; Yadav, R.; Kalaichelvan, P. T.; Venketesan, R. Biogenic Synthesis of Silver Nanoparticles and Their Synergistic Effect with Antibiotics: A Study against Gram-Positive and Gram-Negative Bacteria. *Nanomedicine Nanotechnol. Biol. Med.* **2010**, *6* (1), 103–109. https://doi.org/10.1016/j.nano.2009.04.006.

(40) Zambonino, M. C.; Quizhpe, E. M.; Mouheb, L.; Rahman, A.; Agathos, S. N.; Dahoumane, S. A. Biogenic Selenium Nanoparticles in Biomedical Sciences: Properties, Current Trends, Novel Opportunities and Emerging Challenges in Theranostic Nanomedicine. *Nanomaterials* **2023**, *13* (3), 424. https://doi.org/10.3390/nano13030424.
(41) Nayak, V.; Singh, K. R.; Verma, R.; Pandey, M. D.; Singh, J.; Pratap Singh, R. Recent Advancements of Biogenic Iron Nanoparticles in Cancer Theranostics. *Mater. Lett.* **2022**, *313*, 131769. https://doi.org/10.1016/j.matlet.2022.131769.
(42) Heuer-Jungemann, A.; Feliu, N.; Bakaimi, I.; Hamaly, M.; Alkilany, A.; Chakraborty, I.; Masood, A.; Casula, M. F.; Kostopoulou, A.; Oh, E.; Susumu, K.; Stewart, M. H.; Medintz, I. L.; Stratakis, E.; Parak, W. J.; Kanaras, A. G. The Role of Ligands in the Chemical Synthesis and Applications of Inorganic Nanoparticles. *Chem. Rev.* **2019**, *119* (8), 4819–4880. https://doi.org/10.1021/acs.chemrev.8b00733.
(43) Fricker, S. P. Metal Based Drugs: From Serendipity to Design. *Dalton Trans.* **2007**, No. 43, 4903. https://doi.org/10.1039/b705551j.
(44) Haas, K. L.; Franz, K. J. Application of Metal Coordination Chemistry To Explore and Manipulate Cell Biology. *Chem. Rev.* **2009**, *109* (10), 4921–4960. https://doi.org/10.1021/cr900134a.
(45) Jozefczak, M.; Remans, T.; Vangronsveld, J.; Cuypers, A. Glutathione Is a Key Player in Metal-Induced Oxidative Stress Defenses. *Int. J. Mol. Sci.* **2012**, *13* (3), 3145–3175. https://doi.org/10.3390/ijms13033145.
(46) Mittl, P. R. E.; Schulz, G. E. Structure of Glutathione Reductase from Escherichia Coli at 1.86 Å Resolution: Comparison with the Enzyme from Human Erythrocytes. *Protein Sci.* **2008**, *3* (5), 799–809. https://doi.org/10.1002/pro.5560030509.
(47) Carlberg, I.; Mannervik, B. [59] Glutathione Reductase. In *Methods in Enzymology*; Elsevier, 1985; Vol. 113, pp 484–490. https://doi.org/10.1016/S0076-6879(85)13062-4.
(48) Fox, B.; Walsh, C. T. Mercuric Reductase. Purification and Characterization of a Transposon-Encoded Flavoprotein Containing an Oxidation-Reduction-Active Disulfide. *J. Biol. Chem.* **1982**, *257* (5), 2498–2503. https://doi.org/10.1016/S0021-9258(18)34951-2.
(49) Butz, Z. J.; Hendricks, A.; Borgognoni, K.; Ackerson, C. J. Identification of a TeO32− Reductase/Mycothione Reductase from *Rhodococcus Erythropolis* PR4. *FEMS Microbiol. Ecol.* **2020**, *97* (1), fiaa220. https://doi.org/10.1093/femsec/fiaa220.
(50) Nemeth, R.; Neubert, M.; Ni, T.; Ackerson, C. J. The Metalloid Reductase of Pseudomonas Moravenis Stanleyae Conveys Nanoparticle Mediated Metalloid Tolerance. **2018**. https://doi.org/10.26434/chemrxiv.6267383.v1.
(51) Whaley, S. R.; English, D. S.; Hu, E. L.; Barbara, P. F.; Belcher, A. M. Selection of Peptides with Semiconductor Binding Specificity for Directed Nanocrystal Assembly. *Nature* **2000**, *405* (6787), 665–668. https://doi.org/10.1038/35015043.
(52) Carter, C. J.; Ackerson, C. J.; Feldheim, D. L. Unusual Reactivity of a Silver Mineralizing Peptide. *ACS Nano* **2010**, *4* (7), 3883–3888. https://doi.org/10.1021/nn100630v.
(53) Chandra, K.; Culver, K. S. B.; Werner, S. E.; Lee, R. C.; Odom, T. W. Manipulating the Anisotropic Structure of Gold Nanostars Using Good's Buffers. *Chem. Mater.* **2016**, *28* (18), 6763–6769. https://doi.org/10.1021/acs.chemmater.6b03242.
(54) Xie, J.; Lee, J. Y.; Wang, D. I. C. Seedless, Surfactantless, High-Yield Synthesis of Branched Gold Nanocrystals in HEPES Buffer Solution. *Chem. Mater.* **2007**, *19* (11), 2823–2830. https://doi.org/10.1021/cm0700100.

(55) Payne, C. K. A Protein Corona Primer for Physical Chemists. *J. Chem. Phys.* **2019**, *151* (13), 130901. https://doi.org/10.1063/1.5120178.
(56) Pino, P. del; Pelaz, B.; Zhang, Q.; Maffre, P.; Nienhaus, G. U.; Parak, W. J. Protein Corona Formation around Nanoparticles – from the Past to the Future. *Mater Horiz* **2014**, *1* (3), 301–313. https://doi.org/10.1039/C3MH00106G.
(57) Lenz, M.; Kolvenbach, B.; Gygax, B.; Moes, S.; Corvini, P. F. X. Shedding Light on Selenium Biomineralization: Proteins Associated with Bionanominerals. *Appl. Environ. Microbiol.* **2011**, *77* (13), 4676–4680. https://doi.org/10.1128/AEM.01713-10.
(58) Chen, K.; Arnold, F. H. Engineering New Catalytic Activities in Enzymes. *Nat. Catal.* **2020**, *3* (3), 203–213. https://doi.org/10.1038/s41929-019-0385-5.
(59) Chalfie, M.; Tu, Y.; Euskirchen, G.; Ward, W.; Prasher, D. Green Fluorescent Protein as a Marker for Gene Expression. *Science* **1994**, *263* (5148), 802–805. https://doi.org/10.1126/science.8303295.
(60) Chudakov, D. M.; Matz, M. V.; Lukyanov, S.; Lukyanov, K. A. Fluorescent Proteins and Their Applications in Imaging Living Cells and Tissues. *Physiol. Rev.* **2010**, *90* (3), 1103–1163. https://doi.org/10.1152/physrev.00038.2009.
(61) Shu, X.; Lev-Ram, V.; Deerinck, T. J.; Qi, Y.; Ramko, E. B.; Davidson, M. W.; Jin, Y.; Ellisman, M. H.; Tsien, R. Y. A Genetically Encoded Tag for Correlated Light and Electron Microscopy of Intact Cells, Tissues, and Organisms. *PLoS Biol.* **2011**, *9* (4), e1001041. https://doi.org/10.1371/journal.pbio.1001041.
(62) Lam, S. S.; Martell, J. D.; Kamer, K. J.; Deerinck, T. J.; Ellisman, M. H.; Mootha, V. K.; Ting, A. Y. Directed Evolution of APEX2 for Electron Microscopy and Proximity Labeling. *Nat. Methods* **2015**, *12* (1), 51–54. https://doi.org/10.1038/nmeth.3179.
(63) Mercogliano, C. P.; DeRosier, D. J. Concatenated Metallothionein as a Clonable Gold Label for Electron Microscopy. *J. Struct. Biol.* **2007**, *160* (1), 70–82. https://doi.org/10.1016/j.jsb.2007.06.010.
(64) Staicu, L. C.; van Hullebusch, E. D.; Ackerson, C. Editorial: Microbial Biominerals: Toward New Functions and Resource Recovery. *Front. Microbiol.* **2021**, *12*, 796374. https://doi.org/10.3389/fmicb.2021.796374.
(65) Staicu, L. C.; Ackerson, C. J.; Cornelis, P.; Ye, L.; Berendsen, R. L.; Hunter, W. J.; Noblitt, S. D.; Henry, C. S.; Cappa, J. J.; Montenieri, R. L.; Wong, A. O.; Musilova, L.; Sura-de Jong, M.; van Hullebusch, E. D.; Lens, P. N. L.; Reynolds, R. J. B.; Pilon-Smits, E. A. H. *Pseudomonas Moraviensis* Subsp. Stanleyae, a Bacterial Endophyte of Hyperaccumulator *Stanleya Pinnata* , Is Capable of Efficient Selenite Reduction to Elemental Selenium under Aerobic Conditions. *J. Appl. Microbiol.* **2015**, *119* (2), 400–410. https://doi.org/10.1111/jam.12842.
(66) Noblitt, S. D.; Staicu, L. C.; Ackerson, C. J.; Henry, C. S. Sensitive, Selective Analysis of Selenium Oxoanions Using Microchip Electrophoresis with Contact Conductivity Detection. *Anal. Chem.* **2014**, *86* (16), 8425–8432. https://doi.org/10.1021/ac502013k.
(67) Ni, T. W.; Staicu, L. C.; Nemeth, R. S.; Schwartz, C. L.; Crawford, D.; Seligman, J. D.; Hunter, W. J.; Pilon-Smits, E. A. H.; Ackerson, C. J. Progress toward Clonable Inorganic Nanoparticles. *Nanoscale* **2015**, *7* (41), 17320–17327. https://doi.org/10.1039/C5NR04097C.
(68) Kashyap, S.; Woehl, T. J.; Liu, X.; Mallapragada, S. K.; Prozorov, T. Nucleation of Iron Oxide Nanoparticles Mediated by Mms6 Protein *in Situ*. *ACS Nano* **2014**, *8* (9), 9097–9106. https://doi.org/10.1021/nn502551y.

(69) Mingos, D. M. P.; Wales, D. J. *Introduction to Cluster Chemistry*; Prentice Hall advanced reference series; Prentice Hall: Englewood Cliffs, N.J, 1990.
(70) Scott, D.; Toney, M.; Muzikár, M. Harnessing the Mechanism of Glutathione Reductase for Synthesis of Active Site Bound Metallic Nanoparticles and Electrical Connection to Electrodes. *J. Am. Chem. Soc.* **2008**, *130* (3), 865–874. https://doi.org/10.1021/ja074660g.
(71) Mavis, R. D.; Stellwagen, E. Purification and Subunit Structure of Glutathione Reductase from Bakers' Yeast. *J. Biol. Chem.* **1968**, *243* (4), 809–814. https://doi.org/10.1016/S0021-9258(19)81737-4.
(72) Yu, J.; Zhou, C.-Z. Crystal Structure of Glutathione Reductase Glr1 from the Yeast Saccharomyces Cerevisiae. *Proteins Struct. Funct. Bioinforma.* **2007**, *68* (4), 972–979. https://doi.org/10.1002/prot.21354.
(73) Butz, Z. J.; Borgognoni, K.; Nemeth, R.; Nilsson, Z. N.; Ackerson, C. J. Metalloid Reductase Activity Modified by a Fused Se ^{0} Binding Peptide. *ACS Chem. Biol.* **2020**, *15* (7), 1987–1995. https://doi.org/10.1021/acschembio.0c00387.
(74) Adams, S. R.; Mackey, M. R.; Ramachandra, R.; Palida Lemieux, S. F.; Steinbach, P.; Bushong, E. A.; Butko, M. T.; Giepmans, B. N. G.; Ellisman, M. H.; Tsien, R. Y. Multicolor Electron Microscopy for Simultaneous Visualization of Multiple Molecular Species. *Cell Chem. Biol.* **2016**, *23* (11), 1417–1427. https://doi.org/10.1016/j.chembiol.2016.10.006.
(75) Scotuzzi, M.; Kuipers, J.; Wensveen, D. I.; de Boer, P.; Hagen, K. W.; Hoogenboom, J. P.; Giepmans, B. N. G. Multi-Color Electron Microscopy by Element-Guided Identification of Cells, Organelles and Molecules. *Sci. Rep.* **2017**, *7* (1), 45970. https://doi.org/10.1038/srep45970.
(76) Riskowski, R. A.; Nemeth, R. S.; Borgognoni, K.; Ackerson, C. J. Enzyme-Catalyzed in Situ Synthesis of Temporally and Spatially Distinct CdSe Quantum Dots in Biological Backgrounds. *J. Phys. Chem. C* **2019**, *123* (44), 27187–27195. https://doi.org/10.1021/acs.jpcc.9b05519.
(77) Dunleavy, R.; Lu, L.; Kiely, C. J.; McIntosh, S.; Berger, B. W. Single-Enzyme Biomineralization of Cadmium Sulfide Nanocrystals with Controlled Optical Properties. *Proc. Natl. Acad. Sci.* **2016**, *113* (19), 5275–5280. https://doi.org/10.1073/pnas.1523633113.
(78) Wang, Y.; Chen, H.; Huang, Z.; Yang, M.; Yu, H.; Peng, M.; Yang, Z.; Chen, S. Structural Characterization of Cystathionine γ-Lyase smCSE Enables Aqueous Metal Quantum Dot Biosynthesis. *Int. J. Biol. Macromol.* **2021**, *174*, 42–51. https://doi.org/10.1016/j.ijbiomac.2021.01.141.
(79) Hamedi, S.; Ghaseminezhad, M.; Shokrollahzadeh, S.; Shojaosadati, S. A. Controlled Biosynthesis of Silver Nanoparticles Using Nitrate Reductase Enzyme Induction of Filamentous Fungus and Their Antibacterial Evaluation. *Artif. Cells Nanomedicine Biotechnol.* **2017**, *45* (8), 1588–1596. https://doi.org/10.1080/21691401.2016.1267011.
(80) Morphew, M. K.; O'Toole, E. T.; Page, C. L.; Pagratis, M.; Meehl, J.; Giddings, T.; Gardner, J. M.; Ackerson, C.; Jaspersen, S. L.; Winey, M.; Hoenger, A.; Mcintosh, J. R. Metallothionein as a Clonable Tag for Protein Localization by Electron Microscopy of Cells: METALLOTHIONEIN FOR PROTEIN LOCALIZATION IN CELLS. *J. Microsc.* **2015**, *260* (1), 20–29. https://doi.org/10.1111/jmi.12262.
(81) Morphew, M.; He, W.; Bjorkman, P. J.; McINTOSH, J. R. Silver Enhancement of Nanogold Particles during Freeze Substitution for Electron Microscopy: ENHANCEMENT OF

NANOGOLD DURING FREEZE SUBSTITUTION. *J. Microsc.* **2008**, *230* (2), 263–267. https://doi.org/10.1111/j.1365-2818.2008.01983.x.
(82) Choi, Y.; Lee, S. Y. Biosynthesis of Inorganic Nanomaterials Using Microbial Cells and Bacteriophages. *Nat. Rev. Chem.* **2020**, *4* (12), 638–656. https://doi.org/10.1038/s41570-020-00221-w.
(83) Choi, Y.; Park, T. J.; Lee, D. C.; Lee, S. Y. Recombinant *Escherichia Coli* as a Biofactory for Various Single- and Multi-Element Nanomaterials. *Proc. Natl. Acad. Sci.* **2018**, *115* (23), 5944–5949. https://doi.org/10.1073/pnas.1804543115.
(84) Carothers, D. J.; Pons, G.; Patel, M. S. Dihydrolipoamide Dehydrogenase: Functional Similarities and Divergent Evolution of the Pyridine Nucleotide-Disulfide Oxidoreductases. *Arch. Biochem. Biophys.* **1989**, *268* (2), 409–425. https://doi.org/10.1016/0003-9861(89)90309-3.
(85) Swulius, M. T.; Jensen, G. J. The Helical MreB Cytoskeleton in Escherichia Coli MC1000/pLE7 Is an Artifact of the N-Terminal Yellow Fluorescent Protein Tag. *J. Bacteriol.* **2012**, *194* (23), 6382–6386. https://doi.org/10.1128/JB.00505-12.
(86) Huang, Z.; Zhang, C.; Chen, S.; Ye, F.; Xing, X.-H. Active Inclusion Bodies of Acid Phosphatase PhoC: Aggregation Induced by GFP Fusion and Activities Modulated by Linker Flexibility. *Microb. Cell Factories* **2013**, *12* (1), 25. https://doi.org/10.1186/1475-2859-12-25.
(87) Mirzaei, S. A.; Yazdi, M. T.; Sepehrizadeh, Z. Secretory Expression and Purification of a Soluble NADH Cytochrome B5 Reductase Enzyme from Mucor Racemosus in Pichia Pastoris Based on Codon Usage Adaptation. *Biotechnol. Lett.* **2010**, *32* (11), 1705–1711. https://doi.org/10.1007/s10529-010-0348-z.
(88) Setayesh, N. A.; Sepehrizadeh, Z.; Jaberi, E.; Yazdi, M. T. Cloning, Molecular Characterization and Expression of a cDNA Encoding a Functional NADH-Cytochrome B5 Reductase from Mucor Racemosus PTCC 5305 in E. Coli. *Biol. Res.* **2009**, *42* (2). https://doi.org/10.4067/S0716-97602009000200001.
(89) Mukhopadhyay, R.; Rosen, B. P. Arsenate Reductases in Prokaryotes and Eukaryotes. *Environ. Health Perspect.* **2002**, *110* (suppl 5), 745–748. https://doi.org/10.1289/ehp.02110s5745.
(90) Hendricks, A. R.; Guilliams, B. F.; Cohen, R. S.; Tien, T.; McEwen, G. A.; Borgognoni, K. M.; Ackerson, C. J. Cloneable Inorganic Nanoparticles. *Chem. Commun.* **2023**, 10.1039.D3CC01319G. https://doi.org/10.1039/D3CC01319G.
(91) Yuste, R. Fluorescence Microscopy Today. *Nat. Methods* **2005**, *2* (12), 902–904. https://doi.org/10.1038/nmeth1205-902.
(92) Sali, A. From Integrative Structural Biology to Cell Biology. *J. Biol. Chem.* **2021**, *296*, 100743. https://doi.org/10.1016/j.jbc.2021.100743.
(93) Ziemianowicz, D. S.; Kosinski, J. New Opportunities in Integrative Structural Modeling. *Curr. Opin. Struct. Biol.* **2022**, *77*, 102488. https://doi.org/10.1016/j.sbi.2022.102488.
(94) Schiøtz, O. H.; Kaiser, C. J. O.; Klumpe, S.; Morado, D. R.; Poege, M.; Schneider, J.; Beck, F.; Klebl, D. P.; Thompson, C.; Plitzko, J. M. Serial Lift-Out: Sampling the Molecular Anatomy of Whole Organisms. *Nat. Methods* **2024**, *21* (9), 1684–1692. https://doi.org/10.1038/s41592-023-02113-5.
(95) Nguyen, H. T. D.; Perone, G.; Klena, N.; Vazzana, R.; Kaluthantrige Don, F.; Silva, M.; Sorrentino, S.; Swuec, P.; Leroux, F.; Kalebic, N.; Coscia, F.; Erdmann, P. S. Serialized On-

Grid Lift-in Sectioning for Tomography (SOLIST) Enables a Biopsy at the Nanoscale. *Nat. Methods* **2024**, *21* (9), 1693–1701. https://doi.org/10.1038/s41592-024-02384-6.

(96) Doh, J. K.; White, J. D.; Zane, H. K.; Chang, Y. H.; López, C. S.; Enns, C. A.; Beatty, K. E. VIPER Is a Genetically Encoded Peptide Tag for Fluorescence and Electron Microscopy. *Proc. Natl. Acad. Sci.* **2018**, *115* (51), 12961–12966. https://doi.org/10.1073/pnas.1808626115.

(97) Silvester, E.; Vollmer, B.; Pražák, V.; Vasishtan, D.; Machala, E. A.; Whittle, C.; Black, S.; Bath, J.; Turberfield, A. J.; Grünewald, K.; Baker, L. A. DNA Origami Signposts for Identifying Proteins on Cell Membranes by Electron Cryotomography. *Cell* **2021**, *184* (4), 1110-1121.e16. https://doi.org/10.1016/j.cell.2021.01.033.

(98) Fung, H. K. H.; Hayashi, Y.; Salo, V. T.; Babenko, A.; Zagoriy, I.; Brunner, A.; Ellenberg, J.; Müller, C. W.; Cuylen-Haering, S.; Mahamid, J. Genetically Encoded Multimeric Tags for Subcellular Protein Localization in Cryo-EM. *Nat. Methods* **2023**, *20* (12), 1900–1908. https://doi.org/10.1038/s41592-023-02053-0.

(99) Lee, S.-Y.; Kang, M.-G.; Park, J.-S.; Lee, G.; Ting, A. Y.; Rhee, H.-W. APEX Fingerprinting Reveals the Subcellular Localization of Proteins of Interest. *Cell Rep.* **2016**, *15* (8), 1837–1847. https://doi.org/10.1016/j.celrep.2016.04.064.

(100) Ellisman, M. H.; Deerinck, T. J.; Shu, X.; Sosinsky, G. E. Picking Faces out of a Crowd. In *Methods in Cell Biology*; Elsevier, 2012; Vol. 111, pp 139–155. https://doi.org/10.1016/B978-0-12-416026-2.00008-X.

(101) Diestra, E.; Fontana, J.; Guichard, P.; Marco, S.; Risco, C. Visualization of Proteins in Intact Cells with a Clonable Tag for Electron Microscopy. *J. Struct. Biol.* **2009**, *165* (3), 157–168. https://doi.org/10.1016/j.jsb.2008.11.009.

(102) Jiang, Z.; Jin, X.; Li, Y.; Liu, S.; Liu, X.-M.; Wang, Y.-Y.; Zhao, P.; Cai, X.; Liu, Y.; Tang, Y.; Sun, X.; Liu, Y.; Hu, Y.; Li, M.; Cai, G.; Qi, X.; Chen, S.; Du, L.-L.; He, W. Genetically Encoded Tags for Direct Synthesis of EM-Visible Gold Nanoparticles in Cells. *Nat. Methods* **2020**, *17* (9), 937–946. https://doi.org/10.1038/s41592-020-0911-z.

(103) Naseri, N.; Ajorlou, E.; Asghari, F.; Pilehvar-Soltanahmadi, Y. An Update on Nanoparticle-Based Contrast Agents in Medical Imaging. *Artif. Cells Nanomedicine Biotechnol.* **2018**, *46* (6), 1111–1121. https://doi.org/10.1080/21691401.2017.1379014.

(104) Hendricks, A. R.; Cohen, R. S.; McEwen, G. A.; Tien, T.; Guilliams, B. F.; Alspach, A.; Snow, C. D.; Ackerson, C. J. Laboratory Evolution of Metalloid Reductase Substrate Recognition and Nanoparticle Product Size. *ACS Chem. Biol.* **2024**, *19* (2), 289–299. https://doi.org/10.1021/acschembio.3c00493.

(105) Nemeth, R.; Neubert, M.; Butz, Z. J.; Ni, T. W.; Ackerson, C. J. Metalloid Reductase of *Pseudomonas Moravenis* Stanleyae Conveys Nanoparticle Mediated Metalloid Tolerance. *ACS Omega* **2018**, *3* (11), 14902–14909. https://doi.org/10.1021/acsomega.8b00826.

(106) Chiancone, E.; Ceci, P.; Ilari, A.; Ribacchi, F.; Stefanini, S. Iron and Proteins for Iron Storage and Detoxification. *BioMetals* **2004**, *17* (3), 197–202. https://doi.org/10.1023/B:BIOM.0000027692.24395.76.

(107) Fox, B. S.; Walsh, C. T. Mercuric Reductase: Homology to Glutathione Reductase and Lipoamide Dehydrogenase. Iodoacetamide Alkylation and Sequence of the Active Site Peptide. *Biochemistry* **1983**, *22* (17), 4082–4088. https://doi.org/10.1021/bi00286a014.

(108) Tomczak, M. M.; Slocik, J. M.; Stone, M. O.; Naik, R. R. Bio-Based Approaches to Inorganic Material Synthesis. *Biochem. Soc. Trans.* **2007**, *35* (3), 512–515. https://doi.org/10.1042/BST0350512.

(109) Borgognoni, K.; Nilsson, Z.; Ackerson, C. In Situ Synthesis of Metal Selenide Nanoparticles by Selenium Nanoparticle Disproportionation. July 4, 2023. https://doi.org/10.26434/chemrxiv-2023-vrbdb.
(110) Cormode, D. P.; Naha, P. C.; Fayad, Z. A. Nanoparticle Contrast Agents for Computed Tomography: A Focus on Micelles. *Contrast Media Mol. Imaging* **2014**, *9* (1), 37–52. https://doi.org/10.1002/cmmi.1551.
(111) Lucas, B. A.; Himes, B. A.; Xue, L.; Grant, T.; Mahamid, J.; Grigorieff, N. Locating Macromolecular Assemblies in Cells by 2D Template Matching with cisTEM. *eLife* **2021**, *10*, e68946. https://doi.org/10.7554/eLife.68946.
(112) Chari, A.; Stark, H. Prospects and Limitations of High-Resolution Single-Particle Cryo-Electron Microscopy. *Annu. Rev. Biophys.* **2023**, *52* (1), 391–411. https://doi.org/10.1146/annurev-biophys-111622-091300.
(113) Ma, X.; Ehrhardt, D. W.; Margolin, W. Colocalization of Cell Division Proteins FtsZ and FtsA to Cytoskeletal Structures in Living *Escherichia Coli* Cells by Using Green Fluorescent Protein. *Proc. Natl. Acad. Sci.* **1996**, *93* (23), 12998–13003. https://doi.org/10.1073/pnas.93.23.12998.
(114) Margolin, W. FtsZ and the Division of Prokaryotic Cells and Organelles. *Nat. Rev. Mol. Cell Biol.* **2005**, *6* (11), 862–871. https://doi.org/10.1038/nrm1745.
(115) Graumann, P. L. Cytoskeletal Elements in Bacteria. *Annu. Rev. Microbiol.* **2007**, *61* (1), 589–618. https://doi.org/10.1146/annurev.micro.61.080706.093236.
(116) Oliva, M. A.; Cordell, S. C.; Löwe, J. Structural Insights into FtsZ Protofilament Formation. *Nat. Struct. Mol. Biol.* **2004**, *11* (12), 1243–1250. https://doi.org/10.1038/nsmb855.
(117) McDonald, K.; Morphew, M. K. Improved Preservation of Ultrastructure in Difficult-to-fix Organisms by High Pressure Freezing and Freeze Substitution: I. *Drosophila Melanogaster* and *Strongylocentrotus Purpuratus* Embryos. *Microsc. Res. Tech.* **1993**, *24* (6), 465–473. https://doi.org/10.1002/jemt.1070240603.
(118) Kremer, J. R.; Mastronarde, D. N.; McIntosh, J. R. Computer Visualization of Three-Dimensional Image Data Using IMOD. *J. Struct. Biol.* **1996**, *116* (1), 71–76. https://doi.org/10.1006/jsbi.1996.0013.
(119) Schorb, M.; Haberbosch, I.; Hagen, W. J. H.; Schwab, Y.; Mastronarde, D. N. Software Tools for Automated Transmission Electron Microscopy. *Nat. Methods* **2019**, *16* (6), 471–477. https://doi.org/10.1038/s41592-019-0396-9.
(120) Kora, A. J.; Rastogi, L. Bacteriogenic Synthesis of Selenium Nanoparticles by *Escherichia Coli* ATCC 35218 and Its Structural Characterisation. *IET Nanobiotechnol.* **2017**, *11* (2), 179–184. https://doi.org/10.1049/iet-nbt.2016.0011.
(121) Gong, S.-L.; Tian, Y.; Sheng, G.-P.; Tian, L.-J. Dual-Mode Harvest Solar Energy for Photothermal Cu2-xSe Biomineralization and Seawater Desalination by Biotic-Abiotic Hybrid. *Nat. Commun.* **2024**, *15* (1), 4365. https://doi.org/10.1038/s41467-024-48660-z.
(122) Borgognoni, K.; Guilliams, B.; Cohen, R.; Ackerson, C. Cloneable Selenium Nanoparticles As Multi-Modal Bio-Imaging Contrast Agents. July 4, 2023. https://doi.org/10.26434/chemrxiv-2023-7sm53.
(123) Baran, M. C.; Huang, Y. J.; Moseley, H. N. B.; Montelione, G. T. Automated Analysis of Protein NMR Assignments and Structures. *Chem. Rev.* **2004**, *104* (8), 3541–3556. https://doi.org/10.1021/cr030408p.
(124) Shi, Y. A Glimpse of Structural Biology through X-Ray Crystallography. *Cell* **2014**, *159* (5), 995–1014. https://doi.org/10.1016/j.cell.2014.10.051.

(125) Punjani, A.; Rubinstein, J. L.; Fleet, D. J.; Brubaker, M. A. cryoSPARC: Algorithms for Rapid Unsupervised Cryo-EM Structure Determination. *Nat. Methods* **2017**, *14* (3), 290–296. https://doi.org/10.1038/nmeth.4169.
(126) Bepler, T.; Kelley, K.; Noble, A. J.; Berger, B. Topaz-Denoise: General Deep Denoising Models for cryoEM and cryoET. November 12, 2019. https://doi.org/10.1101/838920.
(127) Suloway, C.; Pulokas, J.; Fellmann, D.; Cheng, A.; Guerra, F.; Quispe, J.; Stagg, S.; Potter, C. S.; Carragher, B. Automated Molecular Microscopy: The New Leginon System. *J. Struct. Biol.* **2005**, *151* (1), 41–60. https://doi.org/10.1016/j.jsb.2005.03.010.
(128) Glaeser, R. M. Limitations to Significant Information in Biological Electron Microscopy as a Result of Radiation Damage. *J. Ultrastruct. Res.* **1971**, *36* (3–4), 466–482. https://doi.org/10.1016/S0022-5320(71)80118-1.
(129) Glaeser, R. M. Retrospective: Radiation Damage and Its Associated "Information Limitations." *J. Struct. Biol.* **2008**, *163* (3), 271–276. https://doi.org/10.1016/j.jsb.2008.06.001.
(130) Rubinstein, J. L.; Brubaker, M. A. Alignment of Cryo-EM Movies of Individual Particles by Optimization of Image Translations. *J. Struct. Biol.* **2015**, *192* (2), 188–195. https://doi.org/10.1016/j.jsb.2015.08.007.
(131) Zivanov, J.; Nakane, T.; Scheres, S. H. W. A Bayesian Approach to Beam-Induced Motion Correction in Cryo-EM Single-Particle Analysis. *IUCrJ* **2019**, *6* (1), 5–17. https://doi.org/10.1107/S205225251801463X.
(132) Scheres, S. H. Beam-Induced Motion Correction for Sub-Megadalton Cryo-EM Particles. *eLife* **2014**, *3*, e03665. https://doi.org/10.7554/eLife.03665.
(133) Nakane, T.; Kotecha, A.; Sente, A.; McMullan, G.; Masiulis, S.; Brown, P. M. G. E.; Grigoras, I. T.; Malinauskaite, L.; Malinauskas, T.; Miehling, J.; Uchański, T.; Yu, L.; Karia, D.; Pechnikova, E. V.; De Jong, E.; Keizer, J.; Bischoff, M.; McCormack, J.; Tiemeijer, P.; Hardwick, S. W.; Chirgadze, D. Y.; Murshudov, G.; Aricescu, A. R.; Scheres, S. H. W. Single-Particle Cryo-EM at Atomic Resolution. *Nature* **2020**, *587* (7832), 152–156. https://doi.org/10.1038/s41586-020-2829-0.
(134) Zheng, S. Q.; Palovcak, E.; Armache, J.-P.; Verba, K. A.; Cheng, Y.; Agard, D. A. MotionCor2: Anisotropic Correction of Beam-Induced Motion for Improved Cryo-Electron Microscopy. *Nat. Methods* **2017**, *14* (4), 331–332. https://doi.org/10.1038/nmeth.4193.
(135) Grant, T.; Grigorieff, N. Measuring the Optimal Exposure for Single Particle Cryo-EM Using a 2.6 Å Reconstruction of Rotavirus VP6. *eLife* **2015**, *4*, e06980. https://doi.org/10.7554/eLife.06980.
(136) Li, X.; Mooney, P.; Zheng, S.; Booth, C. R.; Braunfeld, M. B.; Gubbens, S.; Agard, D. A.; Cheng, Y. Electron Counting and Beam-Induced Motion Correction Enable near-Atomic-Resolution Single-Particle Cryo-EM. *Nat. Methods* **2013**, *10* (6), 584–590. https://doi.org/10.1038/nmeth.2472.
(137) Thorne, R. E. Hypothesis for a Mechanism of Beam-Induced Motion in Cryo-Electron Microscopy. *IUCrJ* **2020**, *7* (3), 416–421. https://doi.org/10.1107/S2052252520002560.
(138) Cheng, Y. Single-Particle Cryo-EM at Crystallographic Resolution. *Cell* **2015**, *161* (3), 450–457. https://doi.org/10.1016/j.cell.2015.03.049.
(139) Cheng, Y.; Grigorieff, N.; Penczek, P. A.; Walz, T. A Primer to Single-Particle Cryo-Electron Microscopy. *Cell* **2015**, *161* (3), 438–449. https://doi.org/10.1016/j.cell.2015.03.050.

(140) Mindell, J. A.; Grigorieff, N. Accurate Determination of Local Defocus and Specimen Tilt in Electron Microscopy. *J. Struct. Biol.* **2003**, *142* (3), 334–347. https://doi.org/10.1016/S1047-8477(03)00069-8.
(141) Rohou, A.; Grigorieff, N. CTFFIND4: Fast and Accurate Defocus Estimation from Electron Micrographs. *J. Struct. Biol.* **2015**, *192* (2), 216–221. https://doi.org/10.1016/j.jsb.2015.08.008.
(142) Woolford, D.; Hankamer, B.; Ericksson, G. The Laplacian of Gaussian and Arbitrary Z-Crossings Approach Applied to Automated Single Particle Reconstruction. *J. Struct. Biol.* **2007**, *159* (1), 122–134. https://doi.org/10.1016/j.jsb.2007.03.003.
(143) Scheres, S. H. W. A Bayesian View on Cryo-EM Structure Determination. *J. Mol. Biol.* **2012**, *415* (2), 406–418. https://doi.org/10.1016/j.jmb.2011.11.010.
(144) Scheres, S. H. W.; Chen, S. Prevention of Overfitting in Cryo-EM Structure Determination. *Nat. Methods* **2012**, *9* (9), 853–854. https://doi.org/10.1038/nmeth.2115.
(145) Henderson, R.; Sali, A.; Baker, M. L.; Carragher, B.; Devkota, B.; Downing, K. H.; Egelman, E. H.; Feng, Z.; Frank, J.; Grigorieff, N.; Jiang, W.; Ludtke, S. J.; Medalia, O.; Penczek, P. A.; Rosenthal, P. B.; Rossmann, M. G.; Schmid, M. F.; Schröder, G. F.; Steven, A. C.; Stokes, D. L.; Westbrook, J. D.; Wriggers, W.; Yang, H.; Young, J.; Berman, H. M.; Chiu, W.; Kleywegt, G. J.; Lawson, C. L. Outcome of the First Electron Microscopy Validation Task Force Meeting. *Structure* **2012**, *20* (2), 205–214. https://doi.org/10.1016/j.str.2011.12.014.
(146) Wang, X.; Zhu, H.; Terashi, G.; Taluja, M.; Kihara, D. DiffModeler: Large Macromolecular Structure Modeling in Low-Resolution Cryo-EM Maps Using Diffusion Model. January 23, 2024. https://doi.org/10.1101/2024.01.20.576370.
(147) Meng, E. C.; Goddard, T. D.; Pettersen, E. F.; Couch, G. S.; Pearson, Z. J.; Morris, J. H.; Ferrin, T. E. UCSF ChimeraX : Tools for Structure Building and Analysis. *Protein Sci.* **2023**, *32* (11), e4792. https://doi.org/10.1002/pro.4792.
(148) Bhattacharjee, S.; Feng, X.; Maji, S.; Dadhwal, P.; Zhang, Z.; Brown, Z. P.; Frank, J. Time Resolution in Cryo-EM Using a PDMS-Based Microfluidic Chip Assembly and Its Application to the Study of HflX-Mediated Ribosome Recycling. *Cell* **2024**, *187* (3), 782-796.e23. https://doi.org/10.1016/j.cell.2023.12.027.
(149) Zhong, E. D.; Bepler, T.; Berger, B.; Davis, J. H. CryoDRGN: Reconstruction of Heterogeneous Cryo-EM Structures Using Neural Networks. *Nat. Methods* **2021**, *18* (2), 176–185. https://doi.org/10.1038/s41592-020-01049-4.
(150) Gilles, M. A.; Singer, A. Cryo-EM Heterogeneity Analysis Using Regularized Covariance Estimation and Kernel Regression. November 1, 2023. https://doi.org/10.1101/2023.10.28.564422.
(151) Russo, C. J.; Scotcher, S.; Kyte, M. A Precision Cryostat Design for Manual and Semi-Automated Cryo-Plunge Instruments. *Rev. Sci. Instrum.* **2016**, *87* (11), 114302. https://doi.org/10.1063/1.4967864.
(152) Parisi, G. The Physics of the Glass Transition. *Phys. Stat. Mech. Its Appl.* **2000**, *280* (1–2), 115–124. https://doi.org/10.1016/S0378-4371(99)00626-3.
(153) Al-Amoudi, A.; Norlen, L. P. O.; Dubochet, J. Cryo-Electron Microscopy of Vitreous Sections of Native Biological Cells and Tissues. *J. Struct. Biol.* **2004**, *148* (1), 131–135. https://doi.org/10.1016/j.jsb.2004.03.010.
(154) Kuba, J.; Mitchels, J.; Hovorka, M.; Erdmann, P.; Berka, L.; Kirmse, R.; König, J.; De Bock, J.; Goetze, B.; Rigort, A. Advanced Cryo-tomography Workflow Developments –

Correlative Microscopy, Milling Automation and Cryo-lift-out. *J. Microsc.* **2021**, *281* (2), 112–124. https://doi.org/10.1111/jmi.12939.
(155) Wolff, G.; Limpens, R. W. A. L.; Zheng, S.; Snijder, E. J.; Agard, D. A.; Koster, A. J.; Bárcena, M. Mind the Gap: Micro-Expansion Joints Drastically Decrease the Bending of FIB-Milled Cryo-Lamellae. *J. Struct. Biol.* **2019**, *208* (3), 107389. https://doi.org/10.1016/j.jsb.2019.09.006.
(156) Mastronarde, D. N.; Held, S. R. Automated Tilt Series Alignment and Tomographic Reconstruction in IMOD. *J. Struct. Biol.* **2017**, *197* (2), 102–113. https://doi.org/10.1016/j.jsb.2016.07.011.
(157) Mastronarde, D. N. Dual-Axis Tomography: An Approach with Alignment Methods That Preserve Resolution. *J. Struct. Biol.* **1997**, *120* (3), 343–352. https://doi.org/10.1006/jsbi.1997.3919.
(158) Szwedziak, P.; Wang, Q.; Bharat, T. A. M.; Tsim, M.; Löwe, J. Architecture of the Ring Formed by the Tubulin Homologue FtsZ in Bacterial Cell Division. *eLife* **2014**, *3*, e04601. https://doi.org/10.7554/eLife.04601.
(159) McCafferty, C. L.; Klumpe, S.; Amaro, R. E.; Kukulski, W.; Collinson, L.; Engel, B. D. Integrating Cellular Electron Microscopy with Multimodal Data to Explore Biology across Space and Time. *Cell* **2024**, *187* (3), 563–584. https://doi.org/10.1016/j.cell.2024.01.005.
(160) Rathore, S.; Berndtsson, J.; Marin-Buera, L.; Conrad, J.; Carroni, M.; Brzezinski, P.; Ott, M. Cryo-EM Structure of the Yeast Respiratory Supercomplex. *Nat. Struct. Mol. Biol.* **2019**, *26* (1), 50–57. https://doi.org/10.1038/s41594-018-0169-7.
(161) Dillard, R. S.; Hampton, C. M.; Strauss, J. D.; Ke, Z.; Altomara, D.; Guerrero-Ferreira, R. C.; Kiss, G.; Wright, E. R. Biological Applications at the Cutting Edge of Cryo-Electron Microscopy. *Microsc. Microanal.* **2018**, *24* (4), 406–419. https://doi.org/10.1017/S1431927618012382.
(162) Li, Z.; Trimble, M. J.; Brun, Y. V.; Jensen, G. J. The Structure of FtsZ Filaments in Vivo Suggests a Force-Generating Role in Cell Division. *EMBO J.* **2007**, *26* (22), 4694–4708. https://doi.org/10.1038/sj.emboj.7601895.
(163) Esvelt, K. M.; Carlson, J. C.; Liu, D. R. A System for the Continuous Directed Evolution of Biomolecules. *Nature* **2011**, *472* (7344), 499–503. https://doi.org/10.1038/nature09929.
(164) Engström, K.; Nyhlén, J.; Sandström, A. G.; Bäckvall, J.-E. Directed Evolution of an Enantioselective Lipase with Broad Substrate Scope for Hydrolysis of α-Substituted Esters. *J. Am. Chem. Soc.* **2010**, *132* (20), 7038–7042. https://doi.org/10.1021/ja100593j.
(165) Reetz, M. T. Directed Evolution of Enantioselective Enzymes: An Unconventional Approach to Asymmetric Catalysis in Organic Chemistry. *J. Org. Chem.* **2009**, *74* (16), 5767–5778. https://doi.org/10.1021/jo901046k.
(166) Prier, C. K.; Zhang, R. K.; Buller, A. R.; Brinkmann-Chen, S.; Arnold, F. H. Enantioselective, Intermolecular Benzylic C–H Amination Catalysed by an Engineered Iron-Haem Enzyme. *Nat. Chem.* **2017**, *9* (7), 629–634. https://doi.org/10.1038/nchem.2783.
(167) Ma, S. K.; Gruber, J.; Davis, C.; Newman, L.; Gray, D.; Wang, A.; Grate, J.; Huisman, G. W.; Sheldon, R. A. A Green-by-Design Biocatalytic Process for Atorvastatin Intermediate. *Green Chem* **2010**, *12* (1), 81–86. https://doi.org/10.1039/B919115C.
(168) Bell, E. L.; Smithson, R.; Kilbride, S.; Foster, J.; Hardy, F. J.; Ramachandran, S.; Tedstone, A. A.; Haigh, S. J.; Garforth, A. A.; Day, P. J. R.; Levy, C.; Shaver, M. P.; Green, A. P. Directed Evolution of an Efficient and Thermostable PET Depolymerase. *Nat. Catal.* **2022**, *5* (8), 673–681. https://doi.org/10.1038/s41929-022-00821-3.

(169) Wu, S.; Xiang, C.; Zhou, Y.; Khan, M. S. H.; Liu, W.; Feiler, C. G.; Wei, R.; Weber, G.; Höhne, M.; Bornscheuer, U. T. A Growth Selection System for the Directed Evolution of Amine-Forming or Converting Enzymes. *Nat. Commun.* **2022**, *13* (1), 7458. https://doi.org/10.1038/s41467-022-35228-y.
(170) Vaud, S.; Pearcy, N.; Hanževački, M.; Van Hagen, A. M. W.; Abdelrazig, S.; Safo, L.; Ehsaan, M.; Jonczyk, M.; Millat, T.; Craig, S.; Spence, E.; Fothergill, J.; Bommareddy, R. R.; Colin, P.-Y.; Twycross, J.; Dalby, P. A.; Minton, N. P.; Jäger, C. M.; Kim, D.-H.; Yu, J.; Maness, P.-C.; Lynch, S.; Eckert, C. A.; Conradie, A.; Bryan, S. J. Engineering Improved Ethylene Production: Leveraging Systems Biology and Adaptive Laboratory Evolution. *Metab. Eng.* **2021**, *67*, 308–320. https://doi.org/10.1016/j.ymben.2021.07.001.
(171) Tran, J. R.; Paulson, D. I.; Moresco, J. J.; Adam, S. A.; Yates, J. R.; Goldman, R. D.; Zheng, Y. An APEX2 Proximity Ligation Method for Mapping Interactions with the Nuclear Lamina. *J. Cell Biol.* **2021**, *220* (1), e202002129. https://doi.org/10.1083/jcb.202002129.
(172) Lam, S. S.; Martell, J. D.; Kamer, K. J.; Deerinck, T. J.; Ellisman, M. H.; Mootha, V. K.; Ting, A. Y. Directed Evolution of APEX2 for Electron Microscopy and Proximity Labeling. *Nat. Methods* **2015**, *12* (1), 51–54. https://doi.org/10.1038/nmeth.3179.
(173) Xu, S.; Chisholm, A. D. Highly Efficient Optogenetic Cell Ablation in C. Elegans Using Membrane-Targeted miniSOG. *Sci. Rep.* **2016**, *6* (1), 21271. https://doi.org/10.1038/srep21271.
(174) Li, Z.; Jiang, Y.; Guengerich, F. P.; Ma, L.; Li, S.; Zhang, W. Engineering Cytochrome P450 Enzyme Systems for Biomedical and Biotechnological Applications. *J. Biol. Chem.* **2020**, *295* (3), 833–849. https://doi.org/10.1016/S0021-9258(17)49939-X.
(175) Otey, C. R.; Bandara, G.; Lalonde, J.; Takahashi, K.; Arnold, F. H. Preparation of Human Metabolites of Propranolol Using Laboratory-Evolved Bacterial Cytochromes P450. *Biotechnol. Bioeng.* **2006**, *93* (3), 494–499. https://doi.org/10.1002/bit.20744.
(176) Zhou, Q.; Chin, M.; Fu, Y.; Liu, P.; Yang, Y. Stereodivergent Atom-Transfer Radical Cyclization by Engineered Cytochromes P450. *Science* **2021**, *374* (6575), 1612–1616. https://doi.org/10.1126/science.abk1603.
(177) Payne, J. T.; Poor, C. B.; Lewis, J. C. Directed Evolution of RebH for Site-Selective Halogenation of Large Biologically Active Molecules. *Angew. Chem. Int. Ed.* **2015**, *54* (14), 4226–4230. https://doi.org/10.1002/anie.201411901.
(178) Prakinee, K.; Phintha, A.; Visitsatthawong, S.; Lawan, N.; Sucharitakul, J.; Kantiwiriyawanitch, C.; Damborsky, J.; Chitnumsub, P.; Van Pée, K.-H.; Chaiyen, P. Mechanism-Guided Tunnel Engineering to Increase the Efficiency of a Flavin-Dependent Halogenase. *Nat. Catal.* **2022**, *5* (6), 534–544. https://doi.org/10.1038/s41929-022-00800-8.
(179) Snodgrass, H. M.; Mondal, D.; Lewis, J. C. Directed Evolution of Flavin-Dependent Halogenases for Site- and Atroposelective Halogenation of 3-Aryl-4(3 *H*)-Quinazolinones via Kinetic or Dynamic Kinetic Resolution. *J. Am. Chem. Soc.* **2022**, *144* (36), 16676–16682. https://doi.org/10.1021/jacs.2c07422.
(180) Jutz, G.; Van Rijn, P.; Santos Miranda, B.; Böker, A. Ferritin: A Versatile Building Block for Bionanotechnology. *Chem. Rev.* **2015**, *115* (4), 1653–1701. https://doi.org/10.1021/cr400011b.
(181) Haikarainen, T.; Papageorgiou, A. C. Dps-like Proteins: Structural and Functional Insights into a Versatile Protein Family. *Cell. Mol. Life Sci.* **2010**, *67* (3), 341–351. https://doi.org/10.1007/s00018-009-0168-2.

(182) Butterfield, C. N.; Soldatova, A. V.; Lee, S.-W.; Spiro, T. G.; Tebo, B. M. Mn(II,III) Oxidation and MnO 2 Mineralization by an Expressed Bacterial Multicopper Oxidase. *Proc. Natl. Acad. Sci.* **2013**, *110* (29), 11731–11735. https://doi.org/10.1073/pnas.1303677110.
(183) Soldatova, A. V.; Romano, C. A.; Tao, L.; Stich, T. A.; Casey, W. H.; Britt, R. D.; Tebo, B. M.; Spiro, T. G. Mn(II) Oxidation by the Multicopper Oxidase Complex Mnx: A Coordinated Two-Stage Mn(II)/(III) and Mn(III)/(IV) Mechanism. *J. Am. Chem. Soc.* **2017**, *139* (33), 11381–11391. https://doi.org/10.1021/jacs.7b02772.
(184) Liu, J.; Feng, L.; Wu, Y. Enzymatically Synthesised MnO 2 Nanoparticles for Efficient near-Infrared Photothermal Therapy and Dual-Responsive Magnetic Resonance Imaging. *Nanoscale* **2021**, *13* (25), 11093–11103. https://doi.org/10.1039/D1NR02400K.
(185) Yang, Z.; Lu, L.; Kiely, C. J.; Berger, B. W.; McIntosh, S. Single Enzyme Direct Biomineralization of CdSe and CdSe-CdS Core-Shell Quantum Dots. *ACS Appl. Mater. Interfaces* **2017**, *9* (15), 13430–13439. https://doi.org/10.1021/acsami.7b00133.
(186) Huang, S.; Chua, J. H.; Yew, W. S.; Sivaraman, J.; Moore, P. K.; Tan, C.-H.; Deng, L.-W. Site-Directed Mutagenesis on Human Cystathionine-γ-Lyase Reveals Insights into the Modulation of H2S Production. *J. Mol. Biol.* **2010**, *396* (3), 708–718. https://doi.org/10.1016/j.jmb.2009.11.058.
(187) Barak, Y.; Ackerley, D. F.; Dodge, C. J.; Banwari, L.; Alex, C.; Francis, A. J.; Matin, A. Analysis of Novel Soluble Chromate and Uranyl Reductases and Generation of an Improved Enzyme by Directed Evolution. *Appl. Environ. Microbiol.* **2006**, *72* (11), 7074–7082. https://doi.org/10.1128/AEM.01334-06.
(188) Liu, X.; Lopez, P. A.; Giessen, T. W.; Giles, M.; Way, J. C.; Silver, P. A. Engineering Genetically-Encoded Mineralization and Magnetism via Directed Evolution. *Sci. Rep.* **2016**, *6* (1), 38019. https://doi.org/10.1038/srep38019.
(189) Rawlings, D. E. Heavy Metal Mining Using Microbes. *Annu. Rev. Microbiol.* **2002**, *56* (1), 65–91. https://doi.org/10.1146/annurev.micro.56.012302.161052.
(190) Gumulya, Y.; Boxall, N.; Khaleque, H.; Santala, V.; Carlson, R.; Kaksonen, A. In a Quest for Engineering Acidophiles for Biomining Applications: Challenges and Opportunities. *Genes* **2018**, *9* (2), 116. https://doi.org/10.3390/genes9020116.
(191) Hoque, E.; Fritscher, J. Multimetal Bioremediation and Biomining by a Combination of New Aquatic Strains of Mucor Hiemalis. *Sci. Rep.* **2019**, *9* (1), 10318. https://doi.org/10.1038/s41598-019-46560-7.
(192) Verma, S.; Kuila, A. Bioremediation of Heavy Metals by Microbial Process. *Environ. Technol. Innov.* **2019**, *14*, 100369. https://doi.org/10.1016/j.eti.2019.100369.
(193) Elahian, F.; Reiisi, S.; Shahidi, A.; Mirzaei, S. A. High-Throughput Bioaccumulation, Biotransformation, and Production of Silver and Selenium Nanoparticles Using Genetically Engineered Pichia Pastoris. *Nanomedicine Nanotechnol. Biol. Med.* **2017**, *13* (3), 853–861. https://doi.org/10.1016/j.nano.2016.10.009.
(194) Shakibaie, M.; Amiri-Moghadam, P.; Ghazanfari, M.; Adeli-Sardou, M.; Jafari, M.; Forootanfar, H. Cytotoxic and Antioxidant Activity of the Biogenic Bismuth Nanoparticles Produced by Delftia Sp. SFG. *Mater. Res. Bull.* **2018**, *104*, 155–163. https://doi.org/10.1016/j.materresbull.2018.04.001.
(195) Hendricks, A. R.; Guilliams, B. F.; Cohen, R. S.; Tien, T.; McEwen, G. A.; Borgognoni, K. M.; Ackerson, C. J. Cloneable Inorganic Nanoparticles. *Chem Comm Accepted June 2nd, 2023*. https://doi.org/10.1039/D3CC01319G.

(196) Lian, P.; Guo, H.-B.; Riccardi, D.; Dong, A.; Parks, J. M.; Xu, Q.; Pai, E. F.; Miller, S. M.; Wei, D.-Q.; Smith, J. C.; Guo, H. X-Ray Structure of a Hg^{2+} Complex of Mercuric Reductase (MerA) and Quantum Mechanical/Molecular Mechanical Study of Hg^{2+} Transfer between the C-Terminal and Buried Catalytic Site Cysteine Pairs. *Biochemistry* **2014**, *53* (46), 7211–7222. https://doi.org/10.1021/bi500608u.
(197) Distefano, M. D.; Au, K. G.; Walsh, C. T. Mutagenesis of the Redox-Active Disulfide in Mercuric Ion Reductase: Catalysis by Mutant Enzymes Restricted to Flavin Redox Chemistry. *Biochemistry* **1989**, *28* (3), 1168–1183. https://doi.org/10.1021/bi00429a035.
(198) Naik, R. R.; Stringer, S. J.; Agarwal, G.; Jones, S. E.; Stone, M. O. Biomimetic Synthesis and Patterning of Silver Nanoparticles. *Nat. Mater.* **2002**, *1* (3), 169–172. https://doi.org/10.1038/nmat758.
(199) Pannala, V. R.; Bazil, J. N.; Camara, A. K. S.; Dash, R. K. A Biophysically Based Mathematical Model for the Catalytic Mechanism of Glutathione Reductase. *Free Radic. Biol. Med.* **2013**, *65*, 1385–1397. https://doi.org/10.1016/j.freeradbiomed.2013.10.001.
(200) Painter, E. P. The Chemistry and Toxicity of Selenium Compounds, with Special Reference to the Selenium Problem. *Chem. Rev.* **1941**, *28* (2), 179–213. https://doi.org/10.1021/cr60090a001.
(201) Jumper, J.; Evans, R.; Pritzel, A.; Green, T.; Figurnov, M.; Ronneberger, O.; Tunyasuvunakool, K.; Bates, R.; Žídek, A.; Potapenko, A.; Bridgland, A.; Meyer, C.; Kohl, S. A. A.; Ballard, A. J.; Cowie, A.; Romera-Paredes, B.; Nikolov, S.; Jain, R.; Adler, J.; Back, T.; Petersen, S.; Reiman, D.; Clancy, E.; Zielinski, M.; Steinegger, M.; Pacholska, M.; Berghammer, T.; Bodenstein, S.; Silver, D.; Vinyals, O.; Senior, A. W.; Kavukcuoglu, K.; Kohli, P.; Hassabis, D. Highly Accurate Protein Structure Prediction with AlphaFold. *Nature* **2021**, *596* (7873), 583–589. https://doi.org/10.1038/s41586-021-03819-2.
(202) Evans, R.; O'Neill, M.; Pritzel, A.; Antropova, N.; Senior, A.; Green, T.; Žídek, A.; Bates, R.; Blackwell, S.; Yim, J.; Ronneberger, O.; Bodenstein, S.; Zielinski, M.; Bridgland, A.; Potapenko, A.; Cowie, A.; Tunyasuvunakool, K.; Jain, R.; Clancy, E.; Kohli, P.; Jumper, J.; Hassabis, D. *Protein Complex Prediction with AlphaFold-Multimer*; preprint; Bioinformatics, 2021. https://doi.org/10.1101/2021.10.04.463034.
(203) Mirdita, M.; Schütze, K.; Moriwaki, Y.; Heo, L.; Ovchinnikov, S.; Steinegger, M. ColabFold: Making Protein Folding Accessible to All. *Nat. Methods* **2022**, *19* (6), 679–682. https://doi.org/10.1038/s41592-022-01488-1.
(204) Mirdita, M.; Steinegger, M.; Söding, J. MMseqs2 Desktop and Local Web Server App for Fast, Interactive Sequence Searches. *Bioinformatics* **2019**, *35* (16), 2856–2858. https://doi.org/10.1093/bioinformatics/bty1057.
(205) Berman, H.; Henrick, K.; Nakamura, H. Announcing the Worldwide Protein Data Bank. *Nat. Struct. Mol. Biol.* **2003**, *10* (12), 980–980. https://doi.org/10.1038/nsb1203-980.
(206) Steinegger, M.; Meier, M.; Mirdita, M.; Vöhringer, H.; Haunsberger, S. J.; Söding, J. HH-Suite3 for Fast Remote Homology Detection and Deep Protein Annotation. *BMC Bioinformatics* **2019**, *20* (1), 473. https://doi.org/10.1186/s12859-019-3019-7.
(207) The PyMOL Molecular Graphics System, Version 2.5.5, Schrödinger, LLC.
(208) Bornhorst, J. A.; Falke, J. J. [16] Purification of Proteins Using Polyhistidine Affinity Tags. In *Methods in Enzymology*; Elsevier, 2000; Vol. 326, pp 245–254. https://doi.org/10.1016/S0076-6879(00)26058-8.
(209) Chivers, T.; Laitinen, R. S. Tellurium: A Maverick among the Chalcogens. *Chem. Soc. Rev.* **2015**, *44* (7), 1725–1739. https://doi.org/10.1039/C4CS00434E.

(210) Cadwell, R. C.; Joyce, G. F. Randomization of Genes by PCR Mutagenesis. *Genome Res.* **1992**, *2* (1), 28–33. https://doi.org/10.1101/gr.2.1.28.
(211) Hunter, W. J.; Manter, D. K. Reduction of Selenite to Elemental Red Selenium by Pseudomonas Sp. Strain CA5. *Curr. Microbiol.* **2009**, *58* (5), 493–498. https://doi.org/10.1007/s00284-009-9358-2.
(212) Bi, E.; Lutkenhaus, J. FtsZ Ring Structure Associated with Division in Escherichia Coli. *Nature* **1991**, *354* (6349), 161–164. https://doi.org/10.1038/354161a0.
(213) Mückl, A.; Schwarz-Schilling, M.; Fischer, K.; Simmel, F. C. Filamentation and Restoration of Normal Growth in Escherichia Coli Using a Combined CRISPRi sgRNA/Antisense RNA Approach. *PLOS ONE* **2018**, *13* (9), e0198058. https://doi.org/10.1371/journal.pone.0198058.
(214) Lutkenhaus, J. Assembly Dynamics of the Bacterial MinCDE System and Spatial Regulation of the Z Ring. *Annu. Rev. Biochem.* **2007**, *76* (1), 539–562. https://doi.org/10.1146/annurev.biochem.75.103004.142652.

APPENDIX A: SUPPLEMENTAL TO CHAPTER 3

A1 Supplementary Materials and Methods

Whole cell in vivo SeNP formation expressing the cSeNP-FtsZ chimera

T7 Expression lysY/I^q Competent E. coli cells containing a pD441-CH expression vector encoding the N- or C-term tagged cSeNP-FtsZ chimera were grown in a shaking incubator at 225 – 275 rpm for 16 – 24 hours at 37 °C in 2 mL Miller's Luria Broth (LB) containing kanamycin (25 μg/mL) and chloramphenicol (34 μg/mL) (Kan/Cam) antibiotics. After cells reach confluency, the culture was diluted $1/100^{th}$ by volume into 5 mL fresh antibiotic containing LB and allowed to grow 30 – 37 °C for an additional 3 – 6 hours to reach log phase. After an apparent optical density of 0.2 – 0.4 was reached, cells were treated with a final concentration of 1 μM – 10 mM SeO_3^{2-} and 1 μM – 1 mM isopropyl-β-D-thiogalactopyranoside (IPTG) to promote nanoparticle formation and expression of the cSeNP-FtsZ construct.

After an induction period (30 – 360 minutes) cells were collected by centrifugation at 3000 xg at 4 °C for 3 minutes and washed 3-5x with ice cold filter sterilized 0.1 M phosphate buffer (PB) pH 6.9 – 7.0. Cells were then fixed in buffered 1.5 – 2.5% glutaraldehyde (25% Electron Microscopy Sciences) for 1 hour at 4 °C. A final wash 3 – 5x in ice cold buffer at 3000 xg at 4 °C for 3 minutes was done before reconstituting the sample into 100 – 200 μL buffer to either plate cells or prepare them for dehydration. Cells were drop-cast onto negatively glow-discharged C-coated 200 mesh Cu grids for 1 – 2 minutes followed by 2 washes with 5 μL filtered UpH_2O for 1 minute each.

Formation of AgSe and CuSe particles post-fixation using the cSeNP-FtsZ construct

Following SeNP formation, the sample was washed 4x in ice cold filtered 0.1 M phosphate buffer at pH 7 at 3000 xg at 4 °C for 3 minutes each. Samples were fixed using 1.5 – 2.5% buffered glutaraldehyde for 1 hour. Samples were then washed 3x with ice cold filtered 0.1 M acetate pH 5.6 at 3000 xg at 4 °C for 3 minutes each. Samples were then incubated with either $AgNO_3$ or $Cu(OAc)_2$ at a final concentration of 1 mM for 1 – 4 hours at 4 °C. Samples were washed 3x in acetate buffer and prepared for embedment. Controls did not contain Se supplement.

In another preparation of CuSeNPs, a "ramp up" protocol was performed. A starter culture was inoculated with 10 μM IPTG and 1 μM SeO_3^{2-} for an overnight low level induction. After subsequent dilution and growth to OD 0.4, we induced with 100 μM IPTG and 2 mM SeO_3^{2-} for 3 hours. For disproportionation reactions performed post-fixation, the sample was first fixed as described above, washed 3x with filtered 0.1 M acetate pH 5.6 and immediately soaked with 1mM $Cu(OAc)_2$ overnight at 4 °C. The control was treated identically except the [SeO_3^{2-}] was kept at 1 μM.

Dehydration Protocol

Fixed cells were first encapsulated into 2-3% low melting temperature Agarose by centrifugation. Once firm enough to handle, 1 mm^3 cubes were diced and placed in the dehydration solvent. Serial dehydration occurred in ethanol according to the following series with at least two solvent changes during each step: 5 minutes in 30%, 5 minutes in 50%, 10 minutes in 70%, 10 minutes in 80%, 10 minutes in 90%, 10 minutes in 100%, 10 minutes in 100%. Following traditional preparations, ethanol was replaced with propylene oxide for 1 hour with 1 change.

Embedment procedure

Following traditional embedment, the samples were transferred from propylene oxide to a 1:1 mixture of propylene oxide to catalyzed resin (Luft's formulation of 10 g Araldite, 7.5 g DDSA,

and 1.5% w/w DMP-30) for 1 hour with one solution change. The sample was moved to complete resin for 2 hours with one resin change, after which the sample was moved to molds for curing described below.

In a non-standard procedure, ethanol was used as the transition solvent. Because ethanol is not miscible with the resin, the sample was transferred to a 1:1 mixture of ethanol to uncatalyzed resin for 16 – 18 hours with constant agitation until all ethanol had evaporated to allow enough time for infiltration. The sample was transferred to 100% uncatalyzed resin for an additional 4 – 8 hours with one change, then transferred to complete (catalyzed) resin for 2 hours with one change. The sample was placed into either an Easy-Mold™ or a BEEM size 3 capsule and set into a prewarmed oven to either cure for 16 hours at 60 °C or for 3 – 5 days at 42 – 45 °C as a low temperature alternative.

High Pressure Freeze Substitution

Alternatively, live cells were immediately spun down and plated into brass PELCO® freezer hats, vitrified in a Wohlwend Compact 02 High Pressure Freezer, and transferred to a liquid nitrogen (LN_2) cooled freeze substitution cocktail composed of anhydrous 0.25% glutaraldehyde in ethanol. Samples were slowly brought up to -20 °C over the course of 4 – 5 days by surrounding the samples with dry ice in a Styrofoam box in a -20 °C freezer. The sample was removed from the freezer and placed in a refrigerator for 4 hours at 4 °C followed by 1 hour at room temperature. The samples were carefully washed 3x with molecular biology grade ethanol and removed from their freezer hats followed by embedment described above.

Formation of ZnSe particles in vivo using the cSeNP-FtsZ construct

To show that the construct could be used to form fluorescent ZnSe particles in live cells, we modified SeNP formation by doing a "fast particle" growth protocol. *E. coli* containing the cSeNP-

FtsZ construct were grown to log phase as described above. At OD 0.4, cells were induced with 250 μM IPTG and 10 mM SeO_3^{2-} for 1 hour at 37 °C and 275 rpm. After, cells were spun down at 3000 xg at 22 °C for 3 minutes and fresh, room temperature LB containing antibiotics was used to replenish the decanted supernatant. Cells were resuspended and allowed to recover for 20 minutes at 22 °C with agitation. Following recovery, $Zn(OAc)_2$ was added to the media at a final concentration of 1 mM for an additional 2 hours. The control was treated identically to the sample, except no SeO_3^{2-} was added to the media.

Following the Zn addition, cells were washed 1x with 4 °C LB, then 2x 4 °C 0.1 M filtered PB pH 7 at 3000 xg for 3 minutes at 4 °C. The sample was then fixed with buffered 2.5% glutaraldehyde for 1 hour at 4 °C, washed 3x with 1 mL PB, and plated onto TEM grids for analysis.

Mock Tissue Preparation for microCT Analysis Using cSeNP as a Cellular Marker

For these studies, T7 express *E. coli* that contained only the cSeNP gene or wild type GRLMR gene were used. Starter cultures were grown at 37 °C 275 rpm overnight in LB with Kan/Cam. The next day, cultures were diluted 100x to 200 mL total volume of LB/Kan/Cam and grown for 2 – 3 hours at 37 °C 225 rpm until OD 0.4 was reached. Bacteria containing the enzyme were induced with 1 mM IPTG and either 10 mM, 2 mM, 1 mM, 500 μM, 250 μM, 100 μM, 10 μM, or 1 μM SeO_3^{2-} and allowed to grown overnight. The next day, samples were washed 3x with 10 mL ice cold, filtered 1x PBS pH 7.4 at 3000 xg for 5 minutes followed by fixation in 10 mL buffered 2.5% glutaraldehyde overnight at 4 °C. For the control, T7 express E. coli that did not contain the cSeNP gene (blank T7s) were treated identically to the samples made above, except these were not grown in either 10 mM or 2 mM SeO_3^{2-} to avoid cell stress. Additionally, the blank T7s were not exposed to kanamycin, as this antibiotic resistance is only present in the cSeNP plasmid.

In these studies, the goal was to simulate a tissue sample. Therefore, to maintain cell stability throughout the CT scan, cells were kept in glutaraldehyde. For data collection, mock tissue was prepared by pelleting cells in 2 mL Eppendorf tubes. From 100 mL of culture, a 500 – 750 mm^3 volume of pelleted cells was collected and analyzed.

Micro-Computed Tomography (MicroCT) Analysis

Quantitative analysis of X-ray attenuation within the sample tubes was performed using Scanco μCT 80 analysis software suite (Scanco μCT 80, Scanco USA Inc. Wayne, PA; Scanco Medical Evaluator 1.1.15.0). A low density volume rendering was performed to segment material within a range of 0-400 Hounsfield units, and a higher density rendering was performed to segment material within a range of 800-1800 Hounsfield units.

Bone mineral density analysis done in the Scanco software suite against the standard hydroxyapatite (HA) phantom was used to quantify low (<400 HU) and high density (>800 HU) materials in a 55 mm^3 volume of interest (VOI) of each sample. The volume chosen was within the same Z plane that contained material in both the control and SeNP containing samples (i.e. no

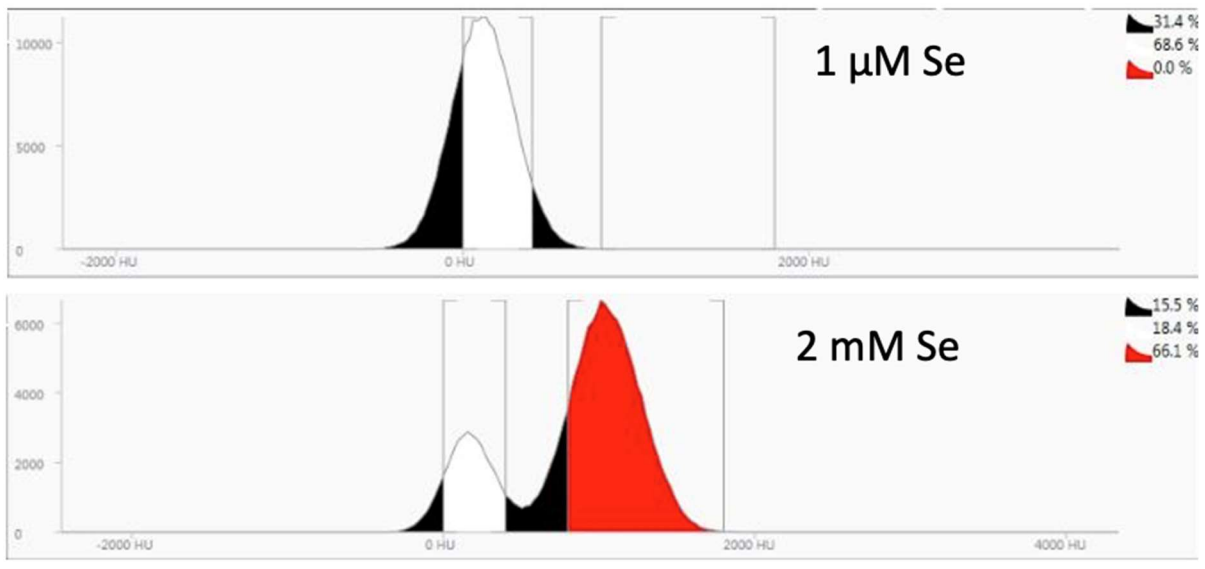

Figure A1. *Plots of X-ray attenuation (HU, x-axis) versus intensity (arbitrary units). Bracketed are the regions rendered in blue (0-400HU) and red (800-1800HU) in figure 5, panels E and F.*

air was captured in the analysis). In the 0 – 400 HU range, 60.5% of the control showed scattering intensity with respect to the total VOI, and 4% of the SeNP containing sample attenuated in that range. In the 800 – 1800 HU range, 0% of the control attenuated versus 77.7% of the SeNP sample with respect to the total VOI.

X-ray renderings (Figure 3.5) were produced by coloring voxels according to attenuation using the Scanco μCT 80 analysis software. Figure A1 shows the attenuation curve and the HU range used for tomogram construction. We chose a control range of 0 – 400 HU (bracketed with white), representing attenuation from soft tissue, and a nanoparticle range from 800 – 1800 HU (bracketed with red) for the SeNPs.

Materials

T7 Expression lysY/I^q Competent *E. coli* cells (Cat no. C3013I) were purchased from New England Biolabs, Inc. Original plasmids containing GRLMR and F-cSeNP-His were designed and purchased from ATUM (DNA Twopointo, Inc.) in their pD441-CH expression vector. Luria Broth was purchased from Fisher Scientific. Kanamycin, Chloramphenicol, and IPTG were purchased from GoldBio. Sodium hydrogen selenite was purchased from Alfa Aesar. Molecular Biology grade ethanol and HPLC grade acetone were purchased from Fisher Scientific. Araldite 502 Kit; Araldite, EMbed 812 Kit; 25% aqueous EM grade glutaraldehyde, and 0.25% aqueous Toluidine Blue O Solution were purchased from Electron Microscopy Sciences.

Sterile snap cap culture tubes (max volume 12 mL) were used for initial growth and induction experiments. 15 mL falcon tubes were used during centrifugation and fixation. 1.5 mL microfuge tubes were used for fixation and encapsulation in agarose. 20 mL glass scintillation vials with screw tops were used during dehydration and embedment. BEEM® size 3 Embedding

Capsules were used during high pressure freeze substitution protocols, and either BEEM® Flat Embedding Molds or Easy-Molds™ were used for standard fixation and embedment procedures.

The PELCO easiGlow™ Glow Discharge system was used to prepare EM grids. Either 200 mesh C-coated (5-6 nm thick) Cu grids or Cu slot grids coated in house-prepared Formvar were used for sample mounting.

A2 Instrumentation, Equipment, and Software

EM Grid Preparation

200 mesh C-coated Cu grids were prepared for sample mounting by glow discharging in air for 45 seconds using the PELCO easiGlow™ apparatus.

Ultramicrotomy

The blocks were removed from the oven and roughly trimmed under a dissection scope using injector blades followed by fine trimming using a glass knife made with a LKB Type 7801B KnifeMaker. A Reichert-Jung Ultracut E Microtome was used with either a DiATOME Ultra 35° Diamond Knife or a glass knife to make thin (50 – 100 nm) sections for EM analysis. In some instances, semi-thin (100 – 200 nm) sections were made for better elemental mapping.

Scanning Electron Microscopy (SEM) Imaging

A JEOL JSM-6500 Field Emission Scanning Electron Microscope with an In-Lens thermal field emission electro gun (TFEG) was used for SEM imaging. It is also equipped with an Oxford Instruments energy dispersive X-ray spectrometer (EDS) and uses Oxford Aztec software for qualitative and quantitative elemental analysis. STEM mode was used in bright field to collect all data by mounting an EM grid onto the STEM sample holder.

Transmission Electron Microscopy (TEM) Imaging and Energy Dispersive X-ray Spectroscopy Characterization (EDS)

A JEOL JEM-2100F Transmission Electron Microscope equipped with a Gatan Ultrascan 2K x 2K CCD camera to capture images in TEM mode and diffraction patterns was used. For STEM mode, a JEOL annular dark field (ADF) detector was used. For elemental analysis, an Oxford Instruments SSD EDS detector with Aztec software was used.

Electron Tomography Acquisition and Modeling

All data collection and tomogram reconstruction was done by Eileen O'Toole and Garry Morgan at the University of Colorado in Boulder. Tomograms were reconstructed from a tilt series collected from a 200 – 300 nm thick section using SerialEM and ETomo software. No post-fixation stain was applied and no gold fiducials were added. This means that there is no question that the contrast we are observing is from the intracellular particles and not from salts or fiducials added ex situ.

The tilt series were collected with SerialEM using 2° steps over 120° at 31 kX, 39 kX, and 59 kX magnification corresponding to 6.436 Å, 5.144 Å, and 3.338 Å pixel sizes respectively on a FEI Tecnai F30 FEG-TEM equipped with a Gatan OneView IS (4k) CCD at 300 kV. Tilts were reconstructed with the IMOD software package by inputting the Setup parameters into Etomo. Of particular note is that Etomo was able to align tilts using intracellular particles as the fiducial markers for the seed model. Following tomogram generation, a nonlinear anisotropic diffusion filter was applied to improve contrast, which is not usual but was necessary for our samples since they were not stained with heavy metals. The 3dmod package was used to semi-automatically segment the tomographic reconstructions to reproduce models of the nanoparticles and cell membrane. The script findbeads3d was used to automatically identify and segment nanoparticles. Example input:

```
findbeads3d -I CuSeF_gF4_cell5a_rec.mrc_nad.mrc -size 10 -o cell5a_findbeads.mod
```

Fluorescence Microscopy

Fluorescence images were acquired on an inverted Olympus IX73 microscope (Olympus IX73) in an epi-fluorescence illumination set-up. Immediately before imaging, the sample was placed on a quartz slide and a coverslip was placed over the sample. The edges of the coverslip "sandwich" were sealed. The sample was placed on to the inverted microscope with the coverslip side facing down and brought into focus using transmitted white light. The sample was excited with a 50 mW 355 nm laser (Co-herent Genesis CX) and the emission was spectrally filtered (585 ± 40 nm band-pass). Photons emitted from the sample were collected through a water-immersion 60x microscope objective (Olympus) at either 1.6X or 2X magnification before passing through a long pass filter (cutoff wavelength: 364 nm). The pixel length at 60X corresponds to 216 nm. Emission was collected onto a 512 x 512 pixel electron-multiplying charge-coupled device camera (Andor iXon 897). Movies were recorded at an acquisition rate of 10 fps. Images were processed using ImageJ version 1.51j8 by importing the movie stacks and Z-projecting the average intensity value.

A3 Supplementary Figures and Discussion

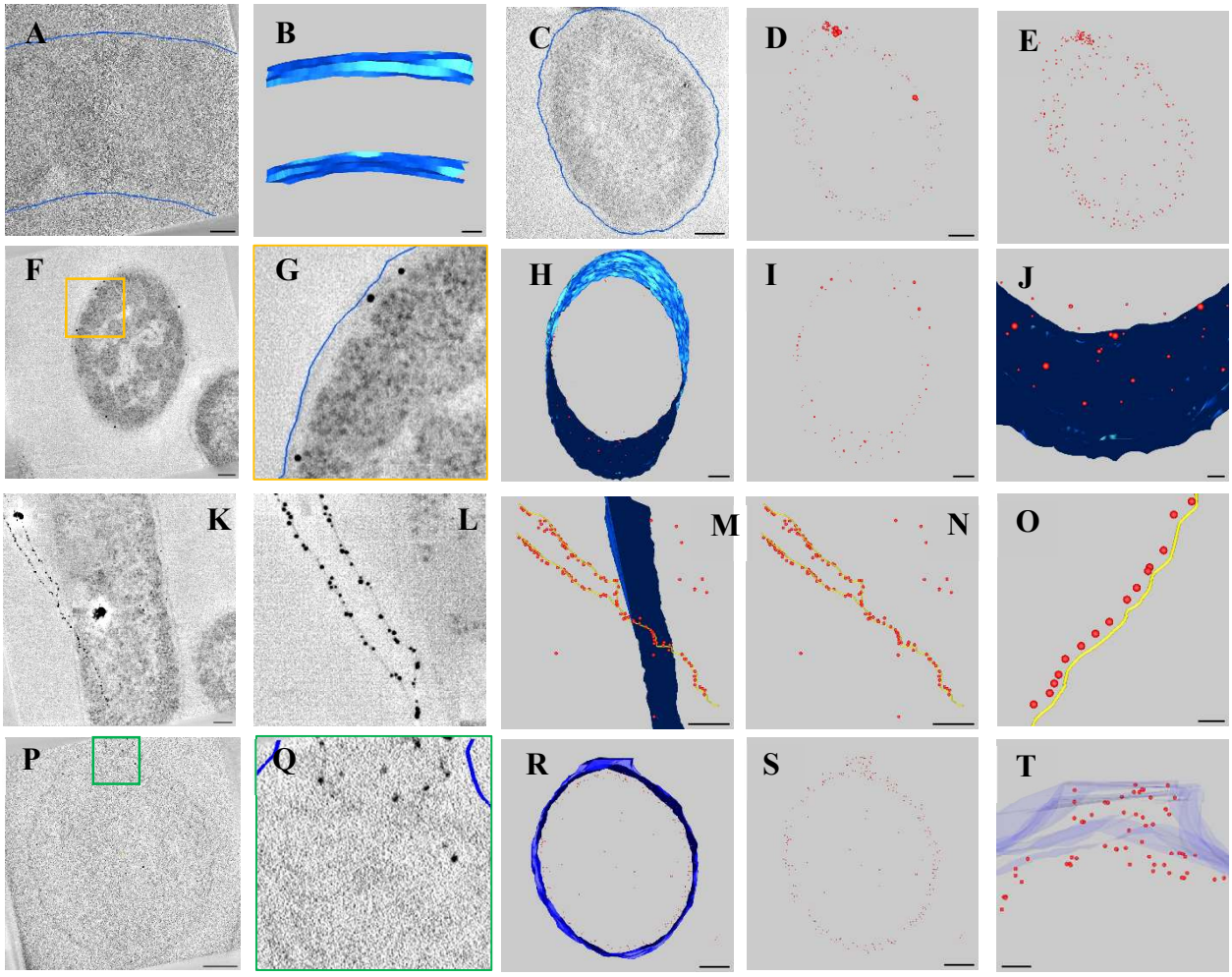

Figure A2. *Montage of tomograms collected. A&B) control cell C) Same cell as Fig 3.3A in text. D) Manual segmentation of particles from cell in C. E) Autosegmented particles using findbeads3d script. F) Cell containing Ag2Se particles labeling FtsZ. G) Zoomed in view of panel F orange box. H) Whole cell model of F. I) Autosegmented particles from panel F using findbeads3d script. J) Zoomed in view of part of the membrane of the model view in H. K) Another cell containing Ag2Se-FtsZ. L) close up view of large particle-decorated filaments in K. M) model view of filaments and part of the membrane. N) View of just filaments and membrane from M. O) Zoomed in view of filament. P) Another CuSe-FtsZ cell. Q) Zoom in view of portion boxed in green from P. R) Whole cell model view of P. S) Autosegmented particles from findbeads3d script. T) Model view of Q with transparent membrane. In all models, nanoparticles are segmented in red and membranes are blue. Scale bars of whole cell views are 100 nm, and scale bars of zoomed in view are 25 nm (J, O, T).*

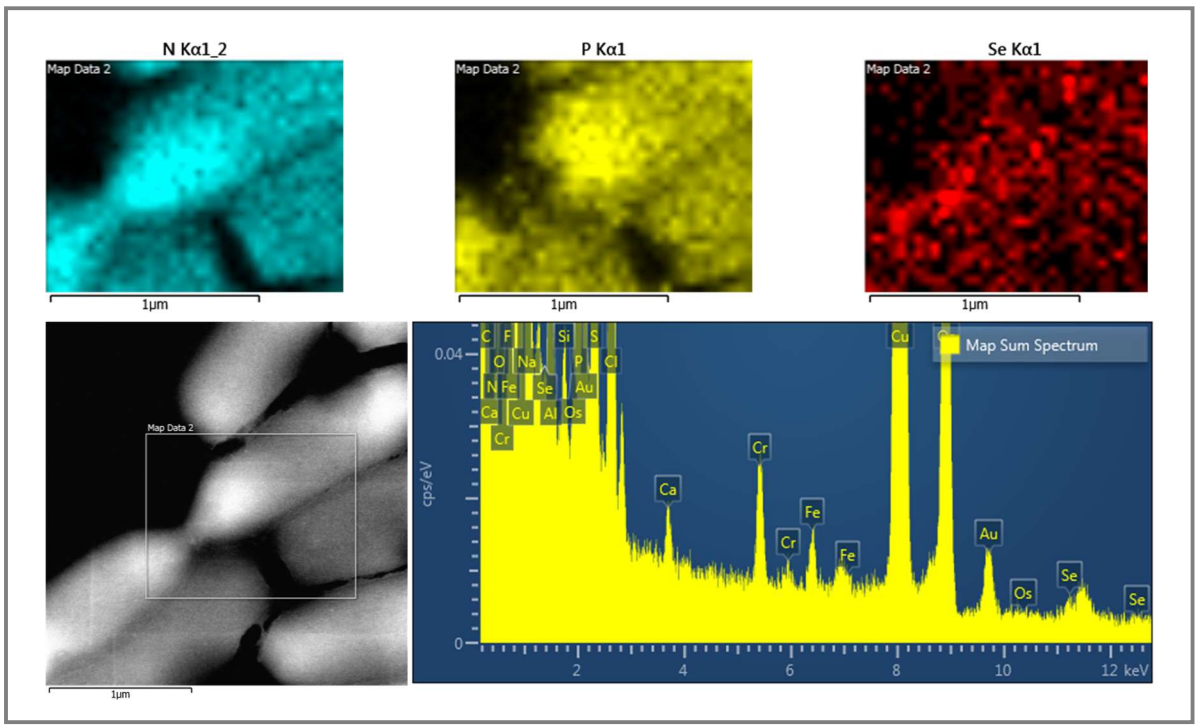

Figure A3. *Extended EDS analysis of Figure 3.2 in main text.*

Optimization of [SeO_3^{2-}], FtsZ-cSeNP expression level, and cSeNP formation time using a high throughput EM workflow

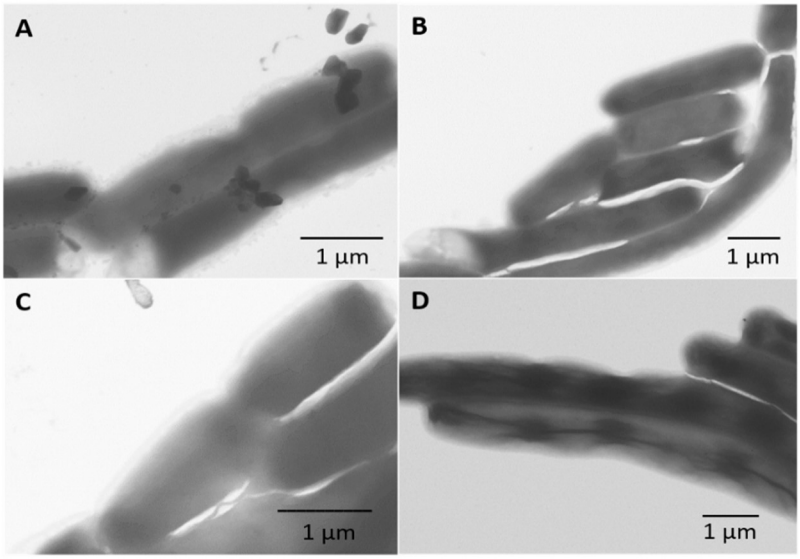

Figure A4. *Selenite concentration screen. (A) Control incubated with no SeO_3^2 (B) sample incubated with 250 µM SeO_3^2 (C) sample incubated with 1 mM SeO_3^2 and (D) sample incubated with 2 mM SeO_3^{2-}.*

To determine the optimum concentration of SeO_3^{2-} in cell culture, the optimum FtsZ over-expression level, the optimum time for cSeNP nanoparticle formation and whether FtsZ should be modified at the C- or N- terminus with the cSeNP fusion, we implemented a high-throughput screening strategy. The strategy uses traditional EM preparation methods. We chemically fixed E. coli with glutaraldehyde and drop cast them on EM grids for Scanning Transmission Electron Microscopy (STEM) analysis. We acquired images on a JEOL JSM-6500 SEM with a FEG source operating at 25 kV at a working distance of 4 mm. The theoretical Kanaya-Okayama electron beam penetration depth at this accelerating voltage is ~5 μm. However, multiple scattering events within the cell degrades final resolution. Thus, our goal for these initial screens was to identify whole cells with cSeNP contrast localizing to known FtsZ-cSeNP locations, as supported by fluorescence microscopy literature on FtsZ-Fluorescent Protein fusions.

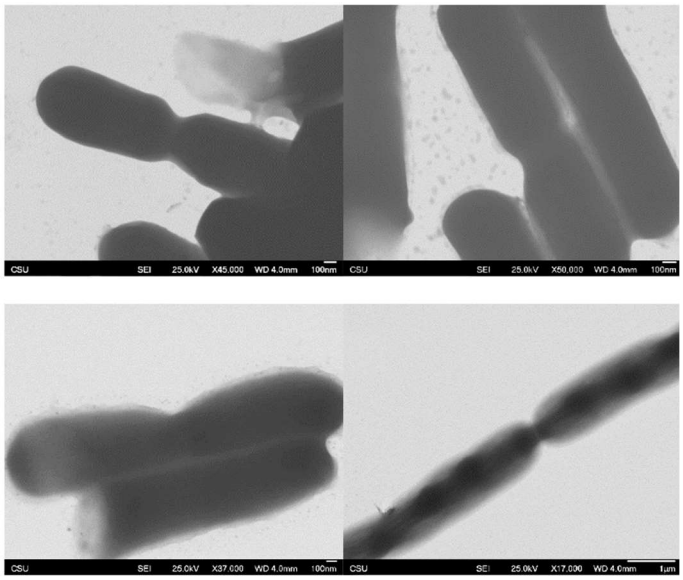

Figure A5. *[IPTG] Screen - 1 uM, 10 uM, 100 uM, 1 mM IPTG all with 2 mM SeO_3^{2-}*

Optimization of [SeO_3^{2-}]

Using the cSeNP-FtsZ (c-terminal fusion of the cSeNP to FtsZ), we tested optimal selenite concentrations (1 μM – 10 mM) that would produce macroscopic color changes in the cell culture (from tan to red/orange) and high contrast in an electron micrograph while maintaining cell viability. Shown in Figure A4 are STEM images of samples overexpressing the chimera in the presence of 250 μM, 1 mM, and 2 mM SeO_3^{2-}. As a control, we grew one sample with no SeO_3^{2-}

present. In Figure A4, it is apparent that incremental increase of the concentration SeO_3^{2-} in cell culture results in an increase in the contrast observed at the cleavage point of dividing cells, where the FtsZ-cSeNP constructs should localize. In addition, at high concentrations, longitudinal filaments appear, which are most distinct in the sample incubated with 2 mM SeO_3^{2-} (Figure A4D).

Optimization of FtsZ-cSeNP expression level.

To assess optimal FtsZ-cSeNP expression level, 1 mM, 100 µM, 10 µM, and 1 µM IPTG were added to *E. coli* containing the expression plasmid for 1 hour at 28 - 30 ℃ in the presence of 2 mM SeO_3^{2-} during log phase growth. Expression level was qualitatively assessed based on cell morphology and EM contrast (Figure A5). Both 1 mM and 100 µM IPTG expression produced cells with noticeable contrast in FtsZ locations, as observed by STEM. The samples treated with 1 µM and 10 µM IPTG did not express enough of the FtsZ-cSeNP to observe contrast distinctive of FtsZ localization. Comparing the 100 µM sample with the 1 mM sample, we observe a qualitative difference in FtsZ expression level by cell morphology. The 100 µM sample results in an apparent moderate expression level of the chimera, where cells are elongated up to 10 µm but not excessively extended to 20 – 30 µm as is shown previously with FtsZ overexpression.[113,212,213] These extended cells are indeed present in the 1 mM IPTG high expression level sample, where we also see long filamentous structures with high contrast running throughout the cell (Figure A5).

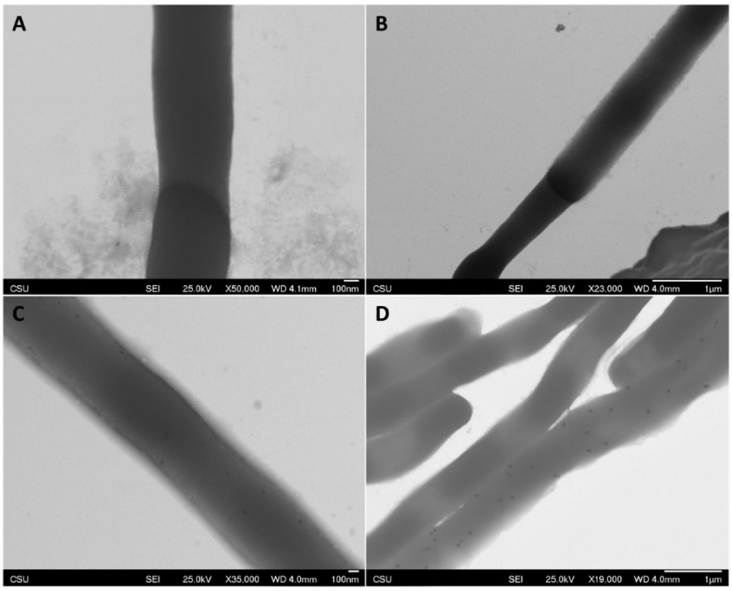

Figure A6. *Extended induction in 1 mM SeO_3^{2-} and 100 µM IPTG for (A) 3h (B) 4h (C) 5h (D) 6h.*

Optimization of Expression Time For Punctate Nanoparticle Formation.

In the presence of 1 mM SeO_3^{2-} and 100 μM IPTG, expression of FtsZ-cSeNP was induced for 3, 4, 5, and 6 hours. From this induction-time screen, punctate particles were not observed until hour 5 or 6 (Figure A6, panels C, D). Formation of particles was inconsistent as seen in Figure A6 panel D, where particles are distinct in the center cell but indistinct in the surrounding cells. It is possible that the inconsistency in particle formation was due to the extended induction time, as biochemical experiments have shown that FtsZ begins to degrade after 3 hours (data not shown).

Optimization of Chimera Function By Comparing C- vs N- terminal fusions.

It is reported in literature that C-terminally labeled GFP-FtsZ fusions are not fully functional in vivo, which could be due to the inability of FtsZ to properly tether to the membrane.[214] We hypothesized that similar artifactual FtsZ behavior could arise from C-terminal fusions of the cSeNP to FtsZ. To test this hypothesis, we fused the cSeNP to the N-terminus of FtsZ (cSeNP-FtsZ). Experiments were repeated by inducing cultures with 1 mM IPTG and 2 mM SeO_3^{2-} for 1 and 2 hours and are shown in Figure A7. The control sample does not contain any SeO_3^{2-} and is shown in Figure A5A and A5D, in which we see no distinct particle formation. One sample was incubated with SeO_3^{2-} for 1 hour as seen in Figure A7B and A7E, in which we begin to see small particles forming throughout the cell and also at the cleavage furrow of dividing cells. In the sample marinated with SeO_3^{2-} for 2 hours, particles become much more distinct as illustrated in Figure A7C and A7F. Elemental mapping was done using (S)TEM-EDS on a sample induced in the presence of 1 mM SeO_3^{2-} and 100 μM IPTG for 1 hour, where analysis of both large internal particles and pinch points confirmed Se presence (data not shown).

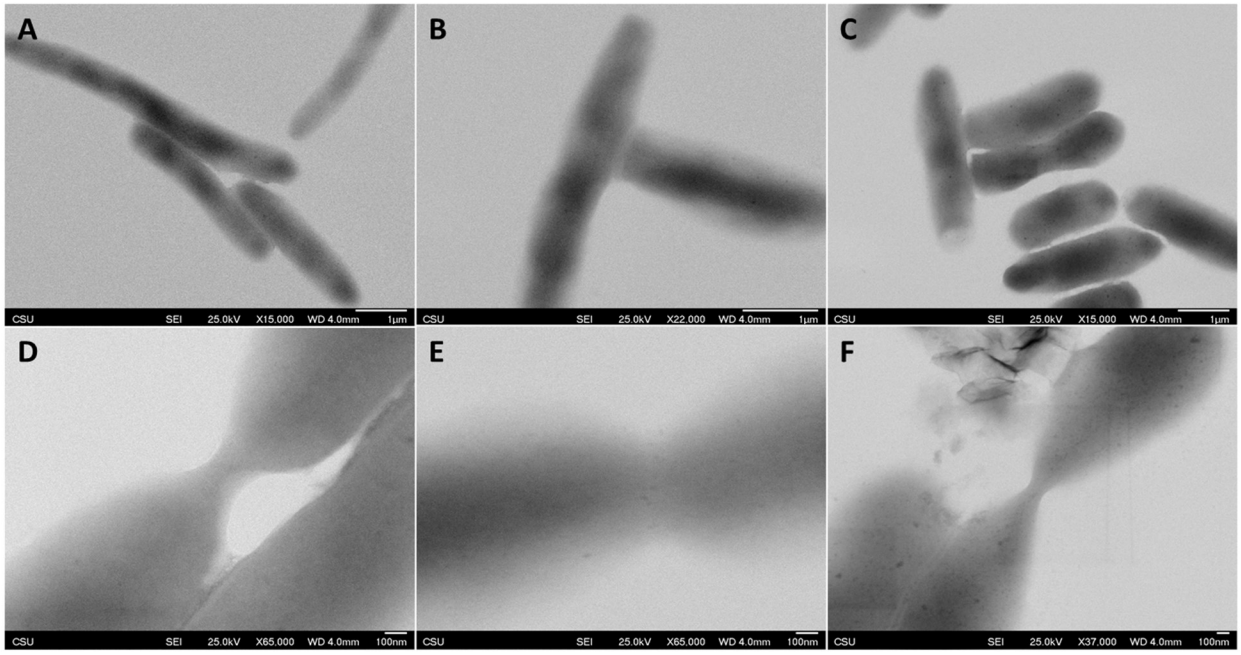

Figure A7. *N-Terminal (FtsZ-cSeNP) construct induction screen. (A&D) control (B&E) sample incubated with selenite for 1 hour (C&F) sample incubated with selenite for 2 hours.*

Optimization of Induction Parameters for Increased SeNP Growth

An additional experiment was conducted to test whether prolonged, low expression of the chimera before adding SeO_3^{2-} would impact nanoparticle formation. Cells were grown in 10 µM IPTG and 1 µM SeO_3^{2-} overnight followed by a ramp up where either 250 µM or 100 µM IPTG and 2 mM SeO_3^{2-} (none for the control) were added to cultures for approximately 2 hours. The two different concentrations of IPTG represent two distinct levels of high and medium expression.[213] High expression level is shown in Figure A8A (control) and A8B, where cells are elongated and extremely filamentous determined by apparent cell thickness. In Figure A8C, medium expression

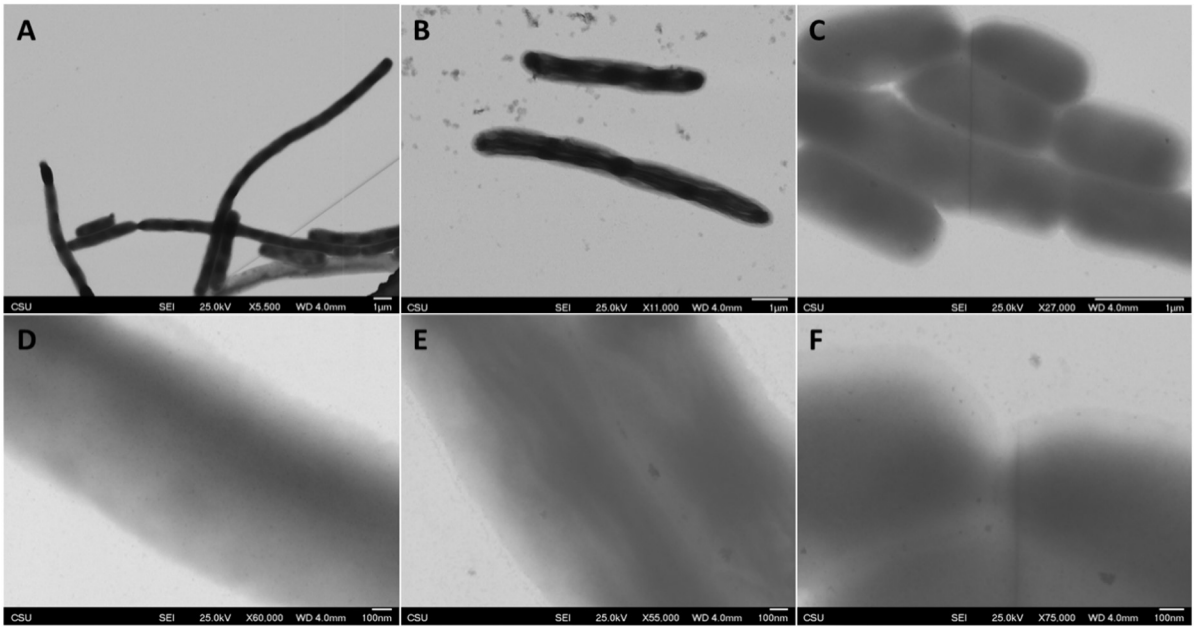

Figure A8. *Extended expression experiment. Low magnification images of the control (A), the sample induced with 250 µM IPTG (B), and the sample induced with 100 µM IPTG (C) are shown in the top row. Higher magnification images of the control (D), the sample induced with 250 µM IPTG (E), and the sample induced with 100 µM IPTG (F) are shown in the bottom row.*

cells are also elongated but are not as filamentous, as is deducted by the lower level of contrast throughout the cell and at specific points where cleavage furrows seem to be forming.

Shown in Figure A8D-F are higher magnification images of the high express control (D), the high express sample (E), and the medium express sample (F). In the control, it is possible that small SeNPs are being formed, since it was necessary to supplement the medium with 1 µM SeO_3^{2-} to avoid cell death due to the prolonged expression period. Nonetheless, there is far less contrast in the control compared with the high express sample incubated with 2 mM SeO_3^{2-}. As is apparent in Figure A8E, obvious SeNP formation is observed along the edge of the membrane and along the filaments as expected. Finally, in the medium expression sample, the particles are much more distinct along the membrane and at the division points within the cell (Figure A8F).

Overall, this set of optimization experiments uncovered a range of conditions that allow for observable FtsZ expression and punctate SeNP formation. We found that 100 – 250 µM IPTG

was ideal for FtsZ expression to produce cells with both hyper-extended filaments and pinch points. We found that incubation with 1 – 2 mM SeO_3^{2-} for 1 – 2 hours produced punctate SeNPs with sufficient contrast for EM observation. Despite both C- and N-terminal fusions appearing functional, we believe the N-terminal construct is better in our case for punctate SeNP observation to demonstrate our theory-to-practice method.

Cellular Preservation: Dehydration and resin embedment optimization

We prepared samples induced with 100 µM IPTG and 2 mM SeO_3^{2-} for 2 hours. After the induction period, we performed a high-pressure freeze followed by freeze-substitution into a

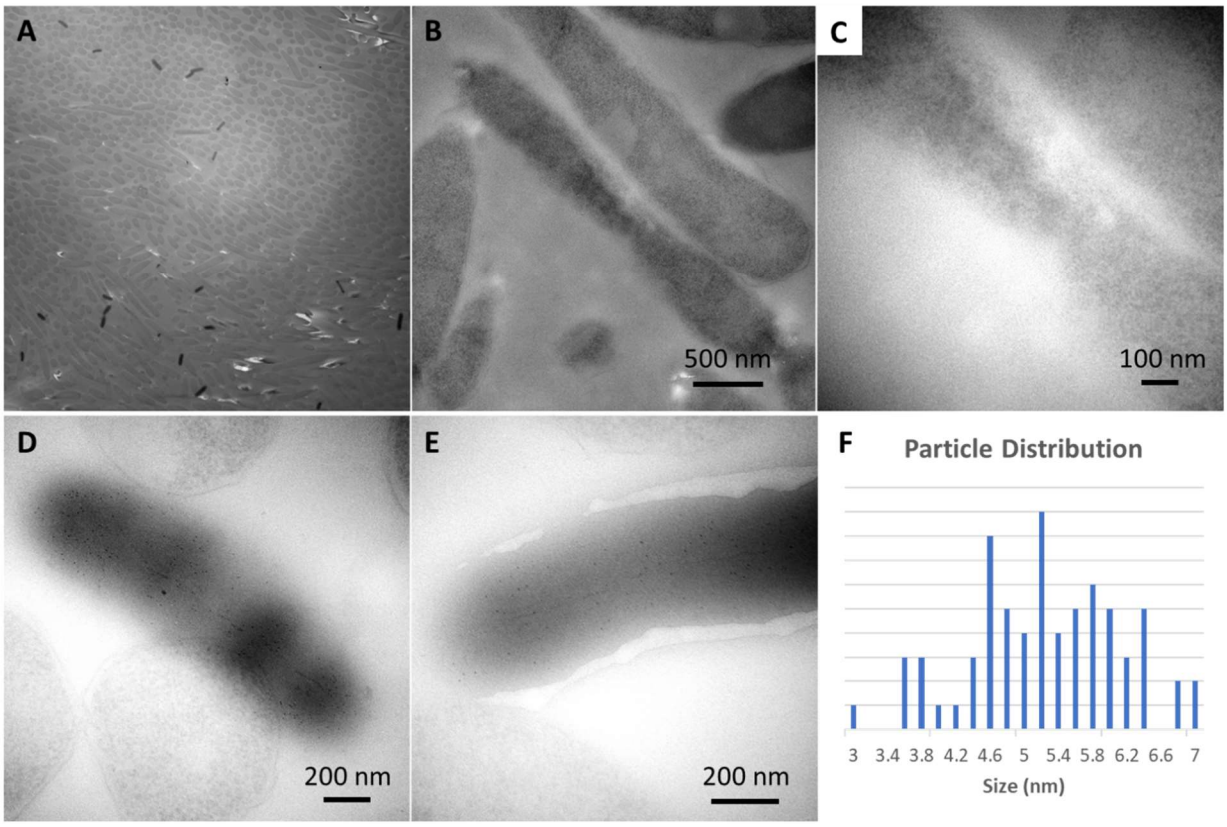

Figure A9. *(A) Low magnification overview of the sample. (B) higher magnification view of a midpoint where we expect FtsZ to localize. (C) The pinch point of a cell is in full view where FtsZ is expected to localize. (D&E) Images of cytoplasmic bodies. (F) A particle distribution graph of a small sample of particles (n = 70) observed in the cytoplasmic bodies.*

glutaraldehyde/acetone cocktail for simultaneous fixation and dehydration. After dehydration, the sample was infiltrated using an epoxy-based resin followed by a curing. The results from this

experiment are shown in Figure A9. The overview of the sample is given in panel A, where we see a typical view of the sample in light grey along with a few odd cells appearing as dark grey entities. During sample processing, it is possible for some cytoplasmic bodies to pop out of their cellular membranes, resulting in smaller anomalies that have not been exposed to acetone or glutaraldehyde. Viewing Figure A9B and A9C, there do not appear to be punctate SeNPs like we saw previously in Figures A4 and A6 or high contrast regions within the normal cells. However, upon inspection of the cytoplasmic bodies shown in Figure A8D and A8E, we do observe ~5nm particles running throughout the entity. SEM-EDS was done on the cytoplasmic bodies, as one is boxed in white shown in Figure A10. Looking at the elemental maps, these anomalies are Se rich and P poor, which further supports that these bodies are cells that contain SeNPs and that have popped out of their membranes.

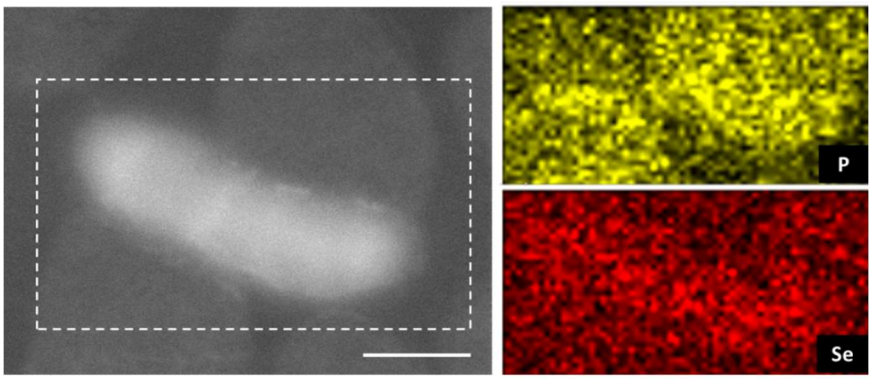

Figure A10. *SEM-EDS analysis of cytoplasmic bodies boxed in white. Elemental mapping shows that the bodies are Se rich and P poor, indicating that these bodies have popped out of their membranes and contain SeNPs.*

Comparing the samples prepared using high pressure freeze-substitution (HPFS) and embedment versus chemically fixed whole cell samples, somewhere downstream during sample processing the SeNPs are degrading. We suspected that acetone could be causing this degradation, since this solvent was not present during the initial whole cell experiments. To test the stability of SeNPs in acetone, a dissolution study was performed by mimicking a typical freeze substitution temperature ramp. SeNPs were synthesized via a borohydride reduction method as described previously and

transferred into 100% acetone that had been prechilled to -80 °C and immediately placed in a -80 °C freezer for 5 days.[109] At this temperature, particles remained stable and unchanged. Once the particles were brought back up to room temperature, they dissolved in acetone within 1 – 2 hours as inferred by a color change from red to colorless.

To observe this dissolution, SeNPs were exposed to acetone for 5 minutes and 20 minutes. Shown in Figure A11, when comparing SeNPs that have not been exposed to acetone (Figure A11A) versus those that have been exposed for 5 minutes (Figure A11B), the acetone-exposed particles appear to contain much less mass as is obviated by the lesser contrast. When comparing the SeNPs exposed to acetone for 5 minutes versus 20 minutes (Figure A11C), we see that particles begin to aggregate and grow, as it seems at this point most of the smaller particles have either dissolved or fused into larger particles following an Ostwald ripening mechanism. We suspect that eventually these larger particles will also dissolve in accordance with the visual observations noted previously.

In vivo *SeNP dissolution screening*

We used a high throughput conventional fixation and embedment method to screen alternative approaches. Extensive optimization was attempted to stabilize as-biosynthesized amorphous

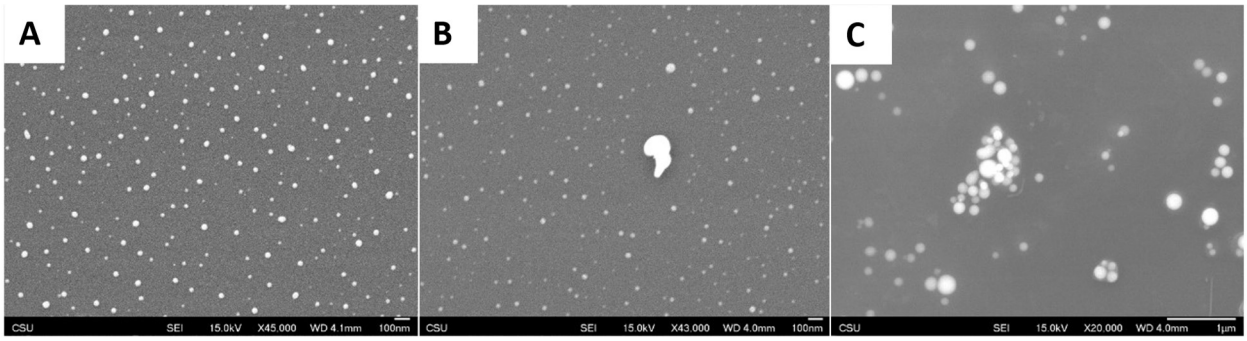

Figure A11. *Acetone dissolution trials. (A) SeNPs before exposure to acetone, (B) SeNPs exposed to acetone for 5 minutes, and (C) SeNPs exposed to acetone for 20 minutes.*

SeNPs by changing dehydration and embedment conditions. Some example images are shown in Fig A12. Panels A – C are representative controls to an ethanol and propylene oxide (PO)

alternative (A and B) or ethanol only (C) dehydration. Panel D is an EDS map of control cells that do not contain SeNPs. Panels E – L are cells containing SeNPs exposed to ethanol and PO dehydration (A12F – H) or ethanol only dehydration (A12E, A12 I – L). SeNP-containing cells exposed to ethanol and PO dehydration, where cells contained locally "stained" Se-rich filaments (fig A12 F – H). As in, no punctate particle were observed. When omitting PO as the transition solvent during dehydration/infiltration, we extended the infiltration time from a 1 hour step to an overnight step because the resin is immiscible with ethanol. The results of those experiments are shown in Fig A12E and A12N. Panel E is an ethanol only dehydration sample of the C-terminal construct, and Panels I-N are of the N-terminal construct. Comparing panels E, I and J, both C- and N-terminal fusions appear to produce SeNPs that are destabilized during sample processing since we observe SeNP aggregates and dissolution along filaments and membranes. From these experiments we concluded that the solvent conditions rather than tag location were the cause of SeNP destabilization.

In addition to changing solvent conditions, previous reports have noted that the surface of amorphous SeNPs can become "soft" when heated to 50 ℃, causing particles to fuse together.[6] Standard resin curing temperatures range from 60 – 70 ℃. Therefore, we changed our curing temperature from 60 ℃ to 42 ℃. Under the new conditions we no longer saw large aggregates of SeNP. However, the particles present were ultrasmall in size and difficult to detect (data not shown). This was not consistent with the particles we were producing in the whole cell experiments (Figures A6, A7), which appeared to be larger and produce higher contrast. Because of these discrepancies, we presumed that SeNPs were still degrading despite significant changes made to the preservation procedure.

To improve the stability of the SeNPs, we used a disproportionation reaction previously described to transform SeNPs into CuSeNPs (Fig A11M and N) and other metal selenides.[109] Shown in Fig A11M are punctate CuSeNPs aligning the cell membrane with the corresponding elemental spectrum. The size of these particles more closely matches that from our whole cell experiments (Fig A5 and A6). Fig A11N is an example of particle overgrowth, which was also observed in whole cell experiments (data not shown). Overall, we optimized conditions suitable for SeNP formation and preservation by modifying the dehydration and curing procedures and by transforming SeNPs into metal selenides.

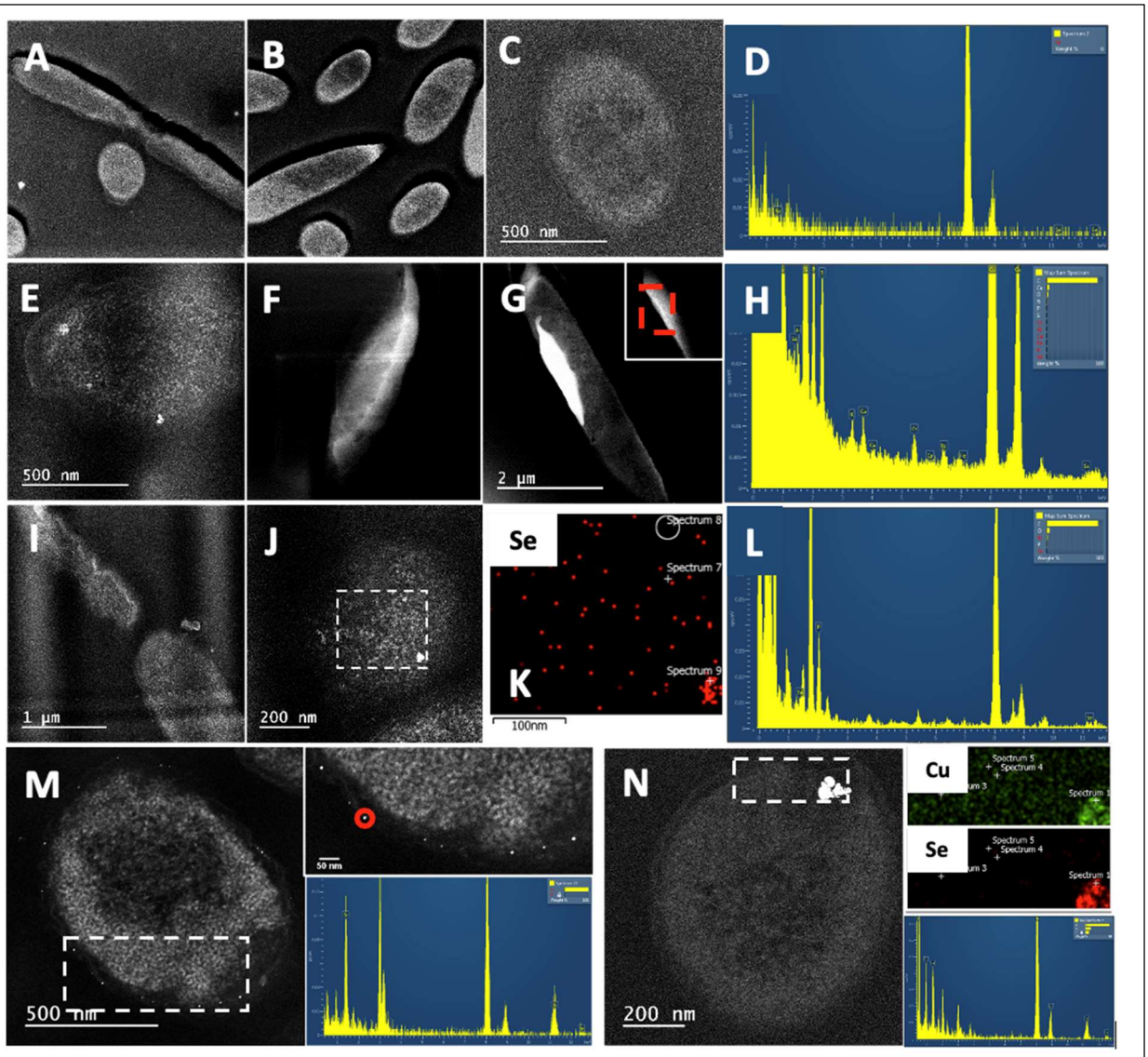

Figure A12. *Example of dissolution experiments. A & B) HPFS control (no SeO_3^{2-}) to ethanol and propylene oxide dehydration and infiltration. C) Control to CuSe disproportionation. D) Control EDS map of plastic background. E) C-term construct containing SeNPs prepared with EtOH dehydration and infiltration. F&G) HPFS C-term construct containing SeNPs prepared with EtOH dehydration and propylene oxide infiltration. H) EDS mapping of G inset boxed in white. I&J) HPFS N-term construct prepared with EtOH dehydration and infiltration. K) Se elemental map in red and L) EDS spectrum of white boxed area of J. F&G) N-term construct used with SeNP disproportionation to form CuSeNPs and dehydrated and embedded with EtOH.*

APPENDIX B: SUPPLEMENTAL TO CHAPTER 4

Supplemental Figures

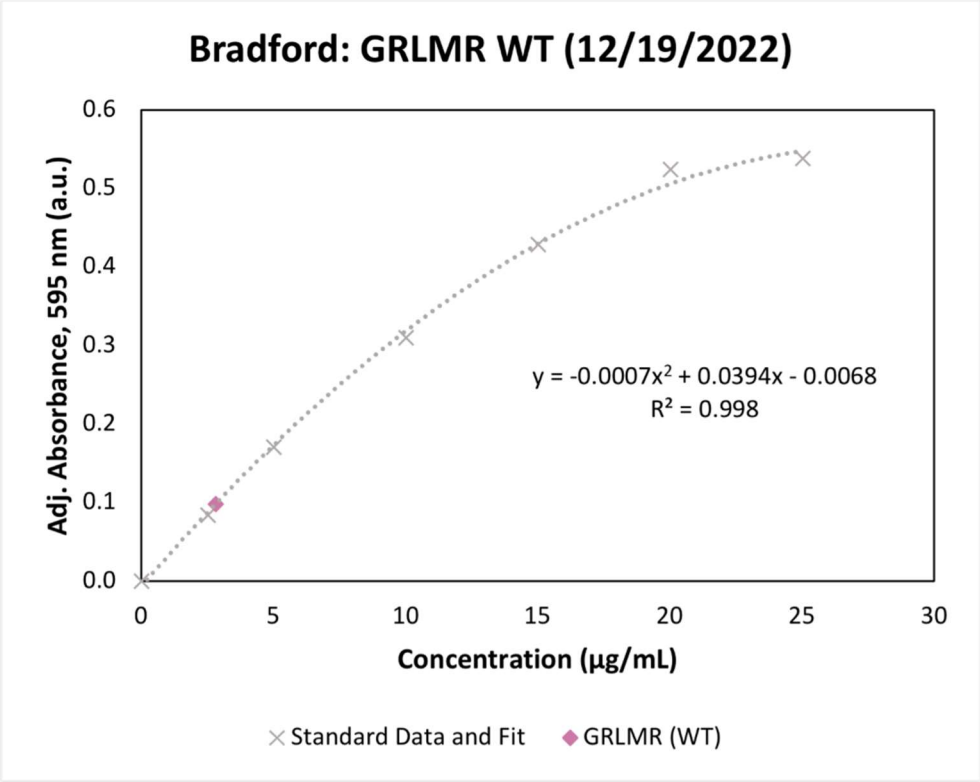

Figure B1. *Example Bradford Assay from GRLMR WT expression and purification; ~3.8 mg/mL is typical for our purifications. Purification is described elsewhere (Appendix D)*

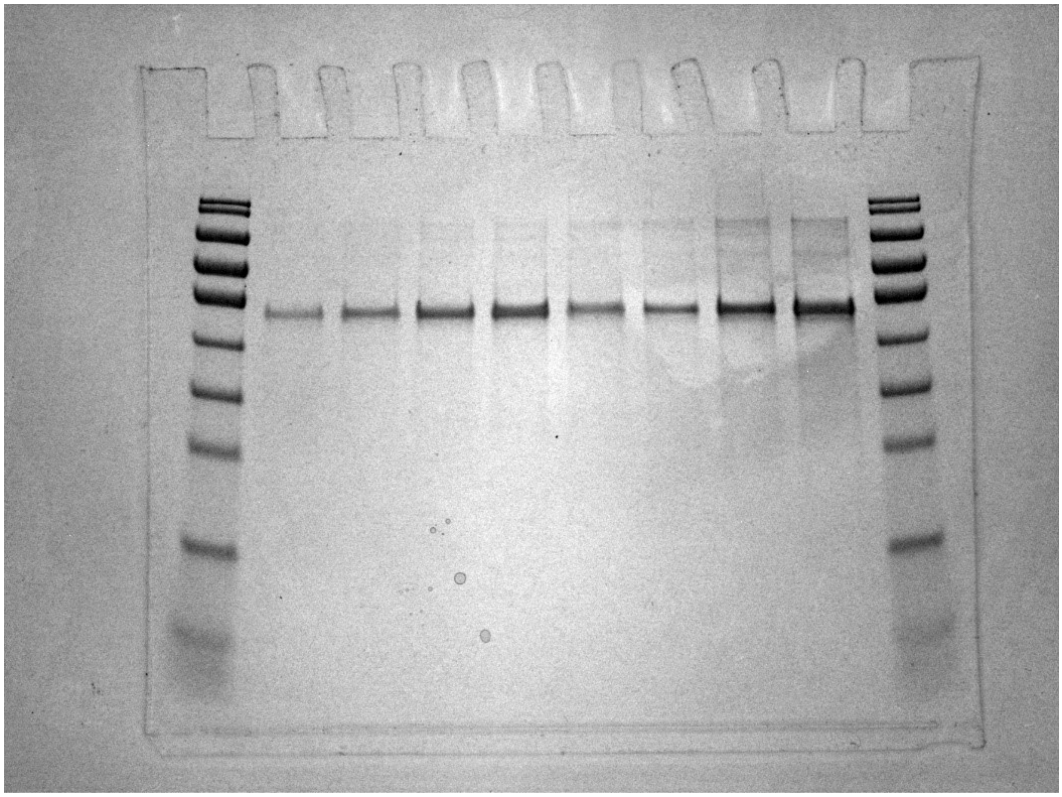

Figure B2. *SDS-PAGE gel of purified GRLMR WT (lanes 6 thru 9) at (2 ug -5 ug). Ladders are in the 1st and last lane. Primary bands in each lane correspond to (1) copy of the protein, additional bands correspond to 2x or 4x monomers. Lane 1: Ladder, Lane 2: 2 µg GRLMR (alanine mutant), Lane 3: 3 µg GRLMR (alanine mutant), Lane 4: 4 µg GRLMR (alanine mutant), Lane 5: 5 µg GRLMR (alanine mutant), Lane 6: 2 µg GRLMR WT, Lane 7: 3 µg GRLMR WT, Lane 8: 4 µg GRLMR WT, Lane 9: 5 µg GRLMR WT, Lane 10: Ladder. Purification is described elsewhere (Appendix D).*

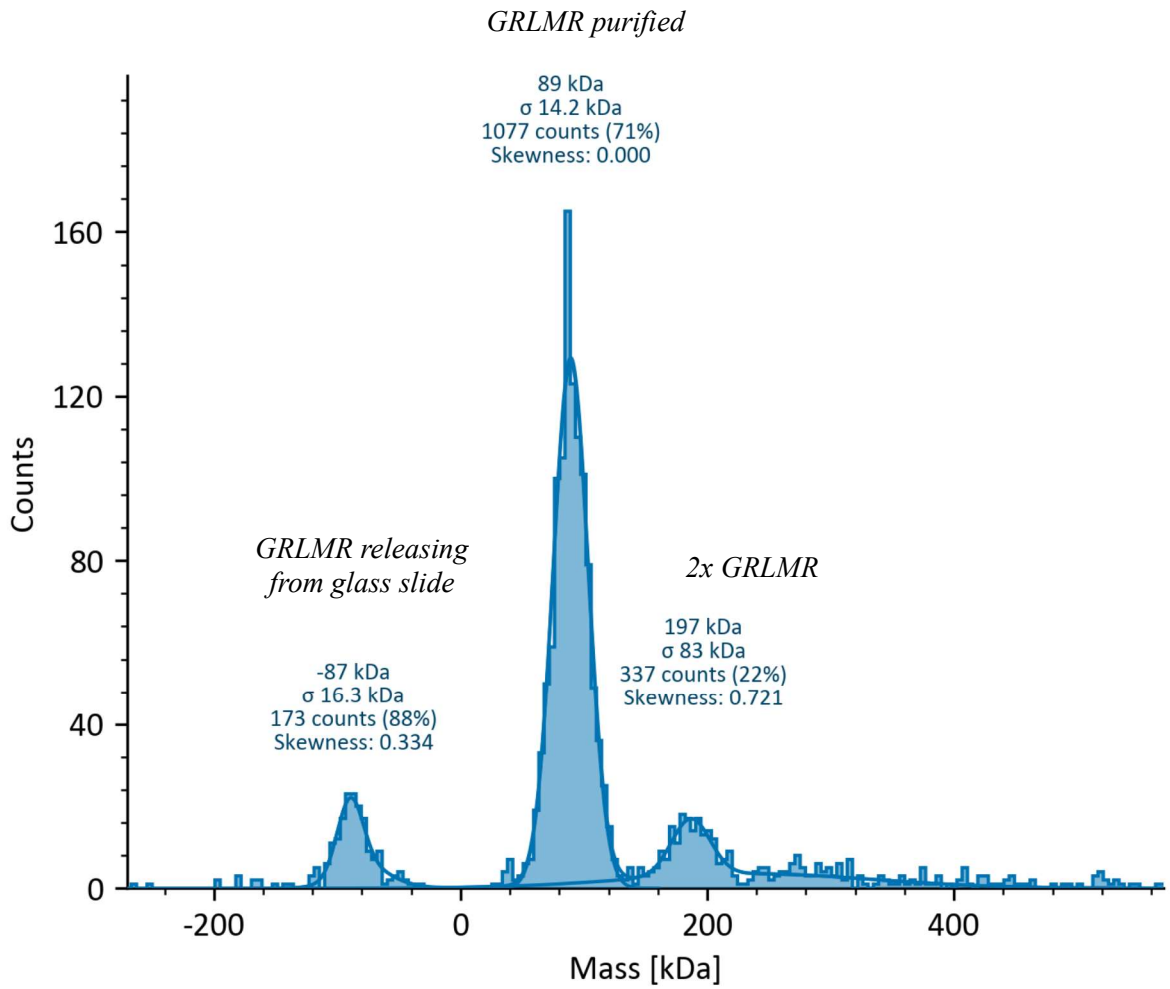

Figure B3. *Mass photometry data of purified GRLMR sample used to generate some of the single particle cryo-EM data presented in chapter 4. The primary peak corresponds to the expected homodimer of GRLMR and the peak at -87 kDa corresponds to the signal from GRLMR unbinding from the glass slide used in this technique. The peak at ~197 kDa corresponds to a population of 'dimer of dimers' and represents a somewhat significant portion of the sample. This species is thus far uncharacterized and has appeared in the single particle cryo-EM data processing.*

APPENDIX C: SUPPLEMENTAL TO CHAPTER 5

Supplemental Figures

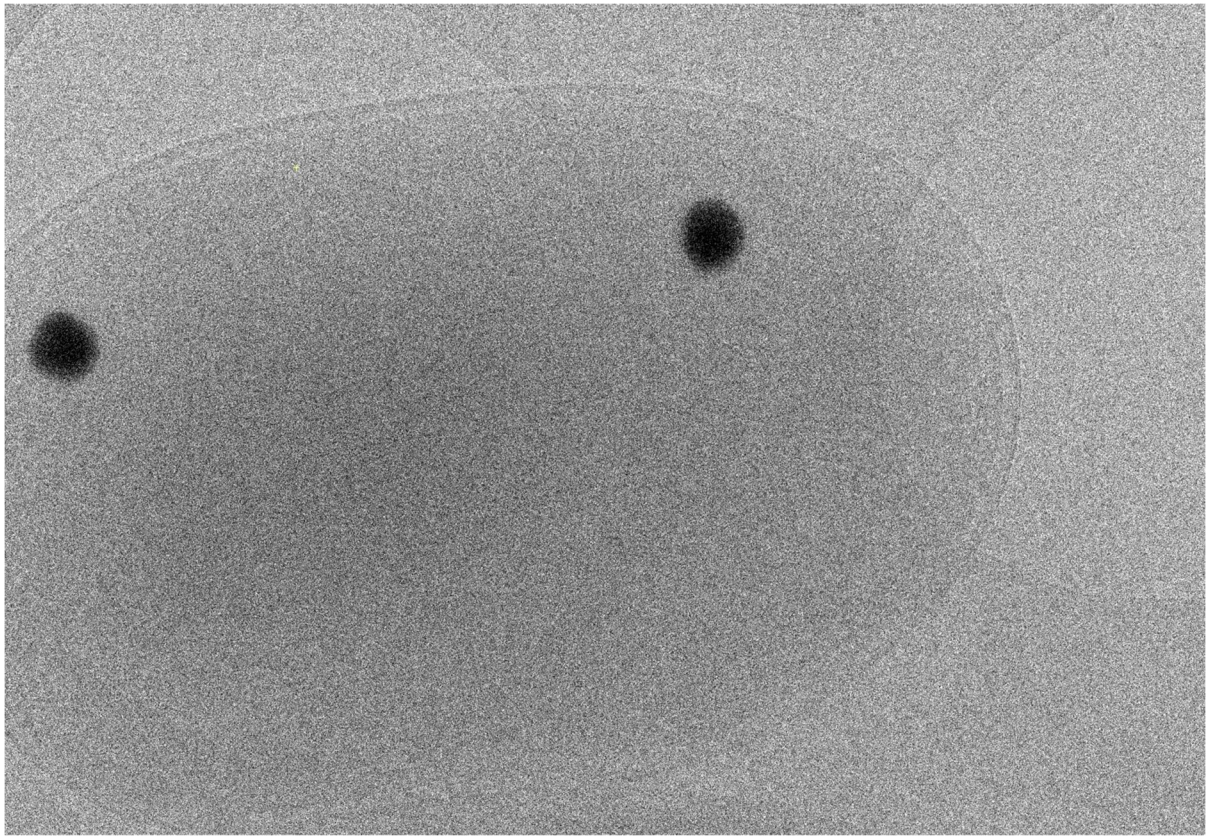

Figure C1. *Cryo-TEM image of* E. coli *cell expressing GRLMR-wildtype and supplemented with selenite. The dark densities are attributed to large selenium nanoparticles that unmodified GRLMR makes inside of bacteria cells.*[67] *This experiment served as a positive control.*

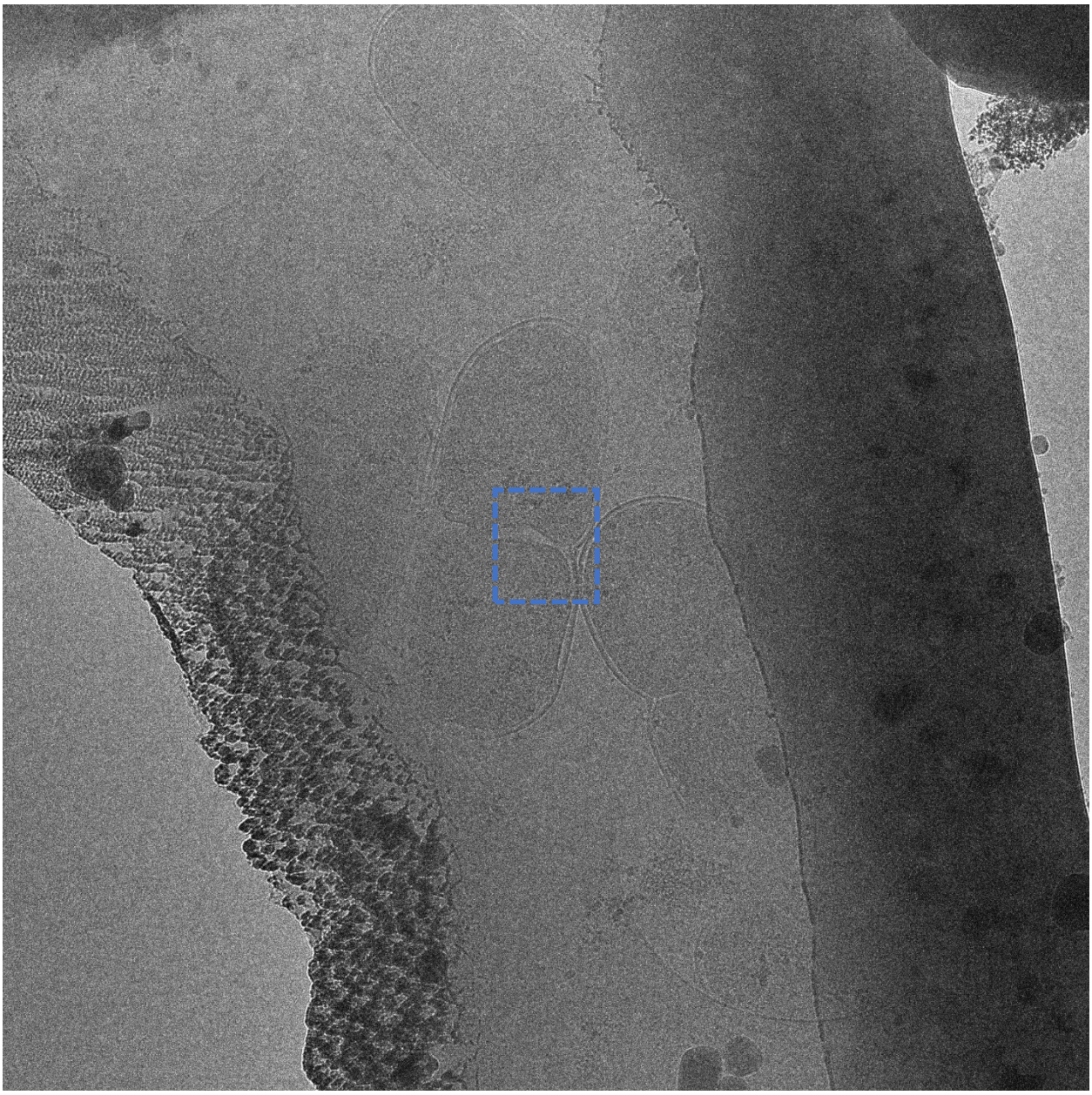

Figure C2. *FIB-milled lamella containing* E. coli *cells expressing the inactive alanine variant of GRLMR and with added selenite. A tilt series was collected in the area within the blue square. This represented a negative control.*

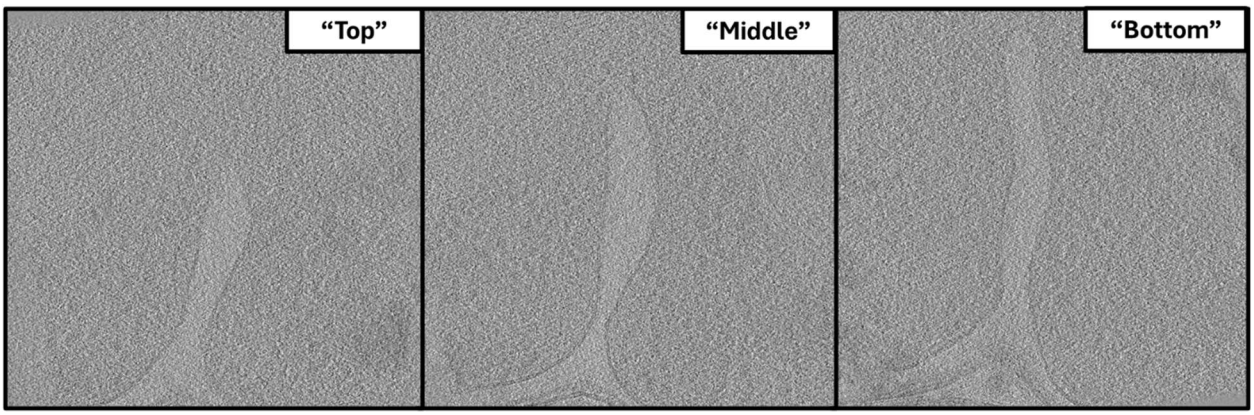

Figure C3. *Tomographic slices of the reconstructed tomogram from figure C2 at the pinch point of dividing cells. The panels correspond to 3 different locations within the volume and this figure highlights the sort of 3-dimensional structure that can be regained through electron tomography.*

Cloneable nanoparticles in D. melanogaster

While exploring the use of cloneable nanoparticles in new organisms, we initiated a collaboration with Susan Tsunoda whose primary research uses *D. melanogaster* as a model organism to study neuronal signaling. Through this collaboration, Lauren Young from the Tsunoda lab worked to generate fly lines incorporating the cloneable selenium nanoparticle. She showed evidence that the cloneable selenium nanoparticle expressed within the *D. melanogaster* brain and trafficked to many of the different cell types within the brain (Figure C4). She also showed that *D. melanogaster* food could be supplemented with selenite and concentrations suitable for nanoparticle production by the cloneable selenium nanoparticle could be found in the brains. Since *D. melanogaster* brains are sufficiently large to require high-pressure freezing for fixation, samples could not easily be prepared for cryo-electron tomography. However, with recent advancements in cryo-lift-out and CLEM, preparing *D. melanogaster* brains for cryo-electron tomography should be much more straightforward than it was even a year ago—though still quite challenging.[94] For this sample, fluorescent antibodies will highlight regions of interest for milling in the cryo-FIB-SEM that can be isolated for thin lamellae preparation followed by cryo-ET imaging. Once again, this work is on-going.

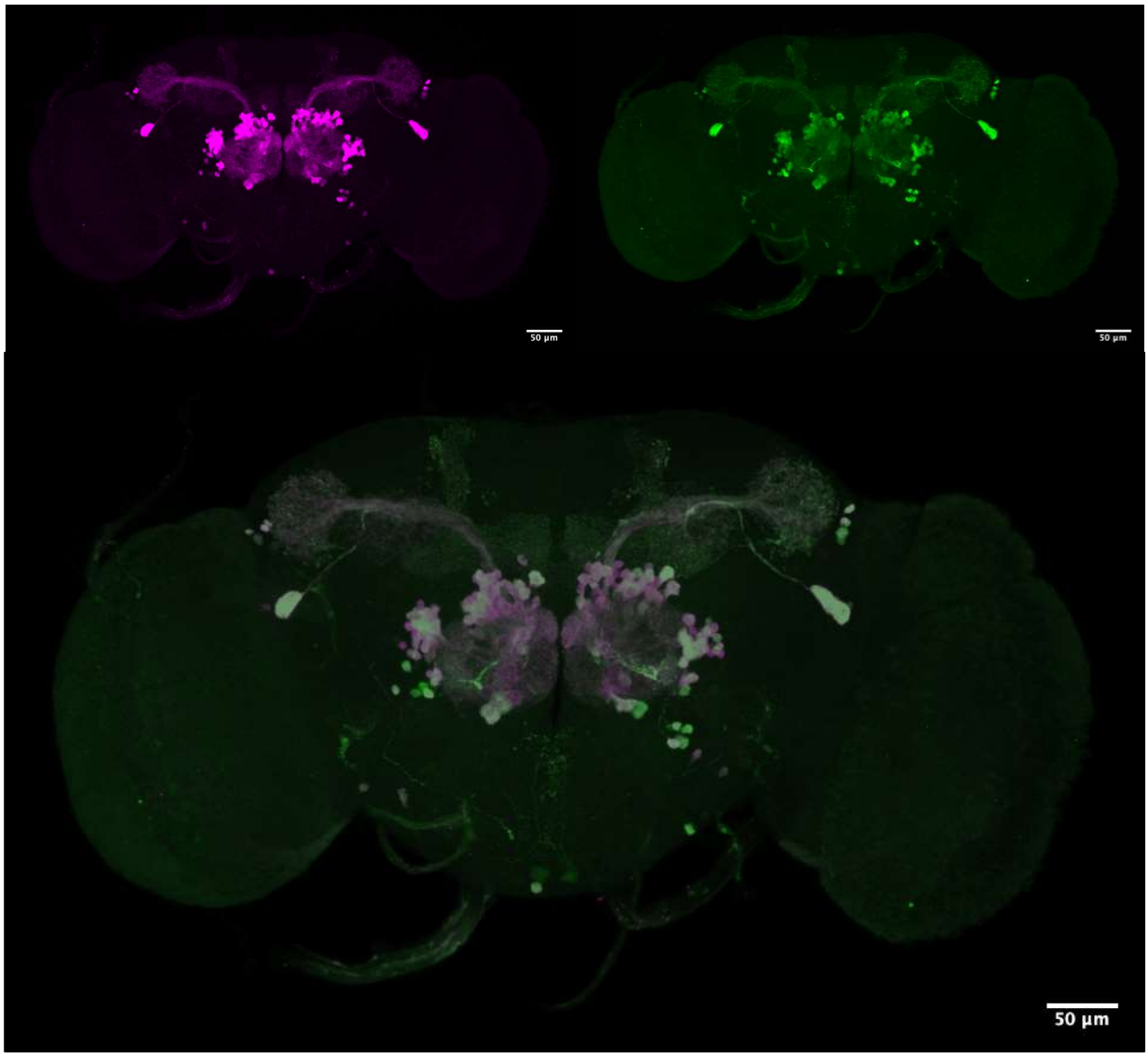

Figure C4. *We attached an HA tag to GRLMR so that we could easily do fluorescent imaging using an anti-HA antibody. GRLMR expression is under the control of an upstream activation sequence (UAS) so that we can drive expression of GRLMR to a specific cell type using the UAS/Gal4 binary expression system. In this case we have GRLMR being driven in the projection neurons, whose dendrites and cell bodies reside in and around the antennal lobe, and whose axons project upward to innervate the lateral horn. The magenta is UAS-DsRed expression, which is being driven in the projection neurons. This is used as a cell marker to show which cells we are looking at, and to show that our driver/genetic system is what we expect it to be. The green image is showing UAS-GRLMR-HA being driven in the projection neurons in the same brain. Merge: Expression of GRLMR overlaps with the cell marker (green + magenta = white). This shows that GRLMR is where we expect it to be, and it is being driven in the correct cells. Our genetic system is validated. Also note that GRLMR is being trafficked out to the processes (dendrites and axons); it's not only expressed in the cell bodies.*

APPENDIX D: SUPPLEMENTAL TO CHAPTER 6

D1 Materials and Methods

Molecular cloning

Unless stated otherwise, all restriction enzymes used in molecular cloning were purchased through New England Biolabs, and DNA primers were purchased from Integrated DNA technologies (IDT, Inc.). Polymerase chain reaction (PCR) and digestion products were purified on 1% agarose (Thermo Fischer) gels run at 115 V for 40 min and imaged on a Bio-Rad Molecular Imager Gel Dox XR+ for further analysis and purification.

Error-prone PCR library

An error-prone polymerase chain reaction (PCR) library of GRLMR was constructed using the GeneMorph™ II Random Mutagenesis Kit (Agilent) with parameters set for 3-5 mutations per 1000 bp using pET20b-GRLMR as a template and primers listed in the Supporting Information. After purification on a 1.0% agarose gel, the PCR product and pET20b plasmid were restriction digested using NdeI and XhoI (New England Biolabs) and subject to another round of purification following calf alkaline phosphatase (New England Biolabs) treatment of the plasmid. Digested PCR product and plasmid were combined at a 100 ng to 100 ng ratio and ligated overnight at 16 C using T4 Ligase (New England Biolabs). After heat inactivation at 65 C for 10 min, the ligation sample buffer was exchanged to Millipore water using a Monarch™ PCR and DNA Cleanup Kit (New England Biolabs) and electroporated to electrocompetent NEB-10Bs (New England Biolabs) using a Gene Pulser Xcell (Bio-Rad) according to factory settings. Serial dilution of the rescued cells yielded a total transformation number of ~100,000 library colony forming units (CFUs). The following day, library DNA was collected using a ZymoPURE™ Plasmid Maxiprep Kit (Zymo

Research) and a sampling of 10 random colonies were sent for sequencing (Azenta Biosciences, LLC), which confirmed a mutational load in the desired range. Purified library plasmid was subsequently transformed to chemically competent T7 Express lysY cells (New England Biolabs), yielding transformation efficiency 5x higher than the electroporated cells (500,000 library transformants). After rescue, cells were grown to an optical density at 600 nm (OD600) of 0.4 and aliquoted to 15% glycerol stocks for storage at –80 C.

The ePCR library of GRLMR was set up according to the specifications of the GeneMorph II Random Mutagenesis Kit with parameters set for approximately 5 mutations per gene. A random selection of 10 plated colonies were grown to confluency in 5 mL LB media, miniprepped, and DNA sent for sequencing (Azenta Biosciences).

Protein expression, purification, and characterization

All protein expressions were conducted in T7 Express lysY cells with pET20b. Cells were grown from glycerol stocks overnight in 5 mL LB/carb cultures at 37 C and 250 RPM. 1 mL aliquots were dispensed into 1 L fresh LB/carb for a 1:000 inoculation. The cells were then grown to an OD600 of ~0.5 to 0.6 prior to addition of 50 uM IPTG and grown at RT at ~200 RPM. 50 uM selenite was added to expression vessels to supplement nutritional levels of selenium.

After expressing overnight, cells were centrifuged at 3,000 g then resuspended in 10 mL pH 6 100 mM MES lysate buffer containing 100 mM NaCl, 5% glycerol, and 0.5% triton x100 (Sigma Aldritch). Resuspended cells were sonicated at 70% in iterative cycles of 3 seconds on followed by 7 seconds off. Crude lysate was centrifuged at 10,000 g for 1 h, and the supernatant was filtered through a 0.2 um sterile filter.

Filtered lysate was combined at 1:1 volume with 10 mM imidazole/PBS buffer. A bed of 4 mL HisPur Nickel NTA resin (Thermo Fischer) was prepared by washing with 10 mM

imidazole/PBS. The combined lysate/buffer solution was added to the prepared Ni-NTA resin and incubated at 4 C with stirring on an orbital shaker for 1 h. Crude lysate was discarded, and the column washed 4x with 40 mM imidazole/PBS, followed by an elution with 2 mL 300 mM imidazole. The buffer was exchanged to PBS through use of centrifugal filters (10,000 MWCO – Amicon). Protein purity was assessed with SDS-PAGE at 150 V for 40-60 min followed by Coomassie staining. Protein concentration was determined through use of the Bradford assay (Thermo Fischer) using bovine serum albumin as a control.

Alanine mutations of GRLMR

As a negative control, a soluble and expressible inactive GRLMR mutant was cloned. The two active site cysteines in GRLMR were exchanged to alanine residues with a Q5® Site Directed Mutagenesis Kit (New England Biolabs) using primers listed in the Appendix. Lack of activity of the purified enzyme was indicated by an absence of color change in the presence of NADPH and selenite.

Selenium reduction selection protocol

An assay correlating enzyme-mediated selenium nanoparticle formation with cell survival in toxic quantities of sodium hydrogen selenite was developed in Luria Low Salt LB growth medium (Sigma Aldrich). Starter cultures of transformed T7 lysY cells containing ampicillin-resistant pET20b plasmids were grown overnight in 5 mL LB medium containing carbenicillin (LB/carb). The following morning, 100 uL of the overnight growths were inoculated to a fresh 2.5 mL low salt LB/carb and grown to an OD600 of 0.5 in an incubating shaker set to 250 RPM and 37 C. Subsequently, 100 uL of the resulting cultures were again inoculated to fresh low salt LB/carb containing 50 uM isopropyl β-D-1-thiogalactopyranoside (IPTG, Thermo Fischer) and sodium hydrogen selenite in varying amounts ranging from 30 mM to 60 mM. Cell quantities were

determined over subsequent days through plating serial dilutions of 10 uL spots in triplicate on carbenicillin LB plates until notable culture growth or death was observed. In cases where cell growth was observed, 100 uL of the selection growth medium was inoculated to fresh LB/carb and grown to confluency for further DNA collection, sequencing, and in some cases additional rounds of selection.

Selenodiglutathione and tellurodiglutathione syntheses

A reaction mixture was prepared with sequential addition of 394 uL Millipore water, 660 uL 0.1 M HCl, 110 uL 100 mM sodium hydrogen selenite or potassium tellurite (Alfa Aesar), and 440 uL 100 mM reduced glutathione (Sigma Aldrich) at room temperature. After 1 h the reaction mixture was loaded to a Alltima 3 um 150 x 4.6 mm C18 column equilibrated at 5% methanol in 0.05% acetic acid on an Cytiva UPC10 fast protein liquid chromatographer. Selenodiglutathione/tellurodiglutathione fractions were collected from 20-24 min as the 3rd of three total peaks absorbing in the UV range.

Enzyme kinetics

Kinetics data was obtained via NADPH depletion (solution concentration 200 uM) using 50 ug enzyme in the presence of varying amount of substrate per reaction. Each reaction was run in a 1 mL plastic cuvette in a NanoDrop 2000 (Thermo Fischer) in triplicate. Data was fitted and plotted using Origin Software[124].

Enzymatic SeNP formation

At 25ºC, four aliquots of enzymatic SeNPs were made using wild type GRLMR and turbo GRLMR. Two concentrations of Se were compared for each type of enzyme, yielding a 5 mM Se sample set and a 50 mM Se sample set. Additionally, a 0.934 M NADPH solution was made with PBS at a pH of 7.4.

To make 1 mL enzymatic solutions, the following was added. To make a 5 mM wild type solution, 5 µL 1 M $HNaSeO_3$ and 250 µL of a 3.87 mg/mL wild type stock were added to 650 µL PBS. To make a 50 mM wild type solution, 50 µL 1 M $HNaSeO_3$ and 250 µL of wild type stock were added to 600 µL PBS. To make a 5 mM turbo solution, 5 µL 1 M $HNaSeO_3$ and 100 µL of a 23.1 ng/mL turbo stock were added to 850 µL PBS. To make a 50 mM turbo solution, 50 µL 1 M $HNaSeO_3$ and 100 µL of turbo stock were added to 800 µL PBS. To all four solutions, 50 µL of the NADPH solution was introduced to start the reaction; all four tubes were allowed to react for three hours. Following reaction, the SeNP samples were all centrifuged at 7,000 rpm at 4°C for 5 minutes for purification purposes; the supernatant was removed and an orange nanoparticle pellet was retained. The nanoparticles were rinsed twice with 500 µL fresh PBS and centrifuged according to the same parameters as mentioned before. Final resuspension was achieved with 100 µL fresh PBS.

Performing DLS on enzymatic SeNPs for size distribution

DLS was conducted for all four SeNP samples listed in the previous section. Using Zetasizer 7.12 for data collection and analysis of particle sizes, each measurement parameter was set up under the 'measurement' tab of the program. After naming the sample for each trial, the materials manager function allowed for the selection of Se nanoparticles in a PBS dispersant. Having set the material and dispersant, the machine was allowed to select an optimized equilibration temperature for sample equilibration over 2 minutes. The cell type set for these experiments was a disposable cuvette and the measurement angle was set to 173o backscatter. The DLS machine was set to automatic parameters for the optimization of number of runs and run duration. Automatic attenuation was also used, and the machine was set to three run sets per sample input. Finally, under the data processing setting, the default general purpose setting was utilized.

Each SeNP sample was loaded into a clean disposable cuvette and fresh PBS was used to bring each cuvette to the appropriate sample volume. Once filled appropriately, the cuvettes were capped and inserted into the machine. Using the parameters described above, each sample was run in a set of three measurements for a duration of 12-16 10 second runs. This data was then extrapolated and analyzed with Zetasizer 7.12.

TEM methods

200 mesh copper TEM grids with carbon support film (Electron Microscopy Sciences) were glow discharged in a PELCO easiGlow (Ted Pella) to make them hydrophilic and to clean them. TEM samples were prepared by drop-casting 5 µL of enzymatically produced SeNP samples onto the 200 mesh copper TEM grids for 3-minutes before blotting the excess solution. Grids were washed twice with 5 µL filtered ultrapure water for 1 minute each. After samples air-dried for 5 minutes, they were ready for imaging. Imaging was conducted in a JEOL 2100F Transmission Electron Microscope at 200 kV equipped with an Ultra-High Resolution (UHR) pole-piece and Gatan Ultrascan 2K x 2K CCD camera. Elemental analysis was conducted using an Oxford Instruments EDS detector operating while operating in STEM mode with a JEOL HAADF detector.

D2 Supplementary Figures

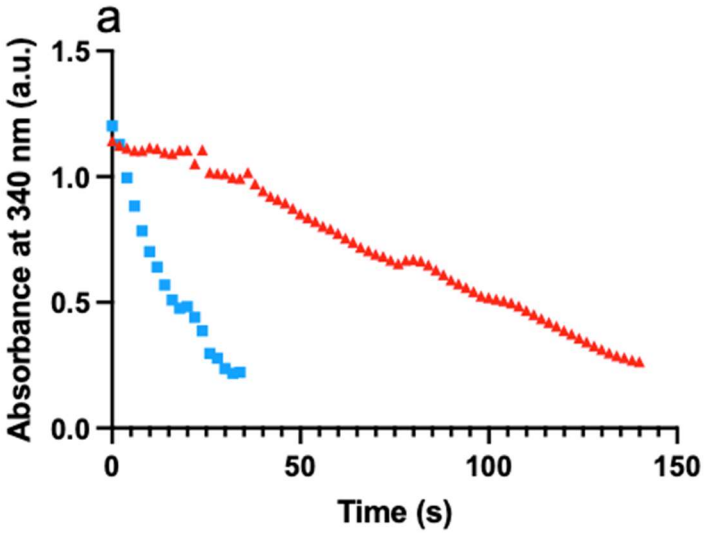

Figure D1. *Absorbance at 340 nm plotted against time, showing a depletion of NADPH by the enzymatic activity of GRLMR (red triangles) and SeR (blue squares) for reduction of selenite.*

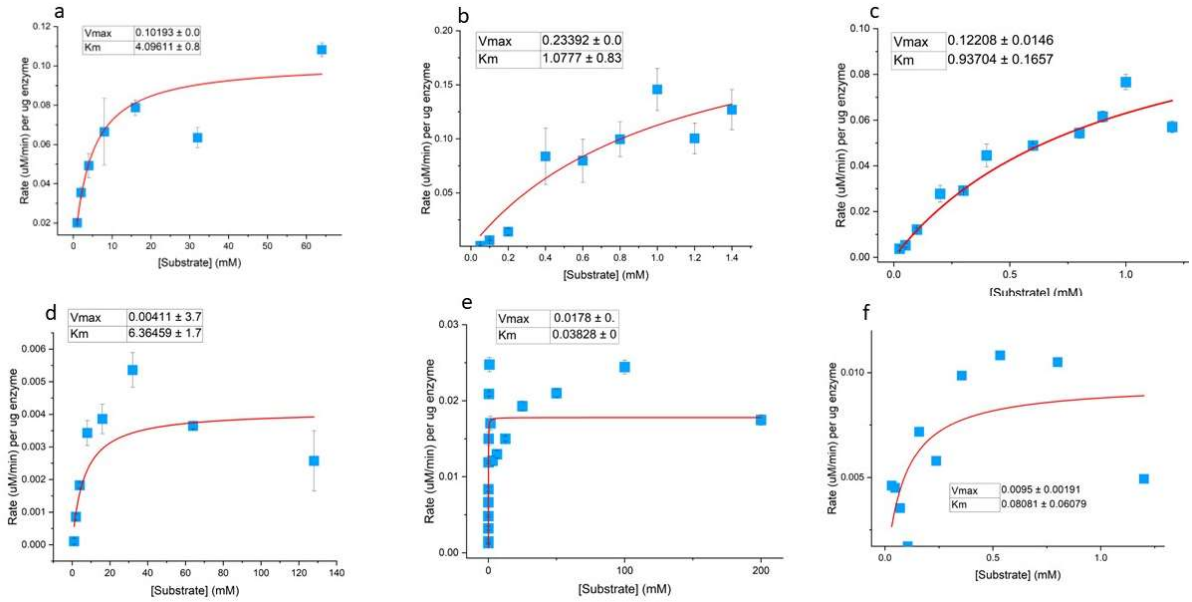

Figure D2*: SeR nonlinear regression analysis of a) selenite, b) GSSG, c) GS-Se-SG, d) selenate, e) tellurite, f) GS-Te-SG. For panels d, e, and f, the substrate inhibition aspect of the enzyme mechanism causes a clear under-estimation of* V_{max}.

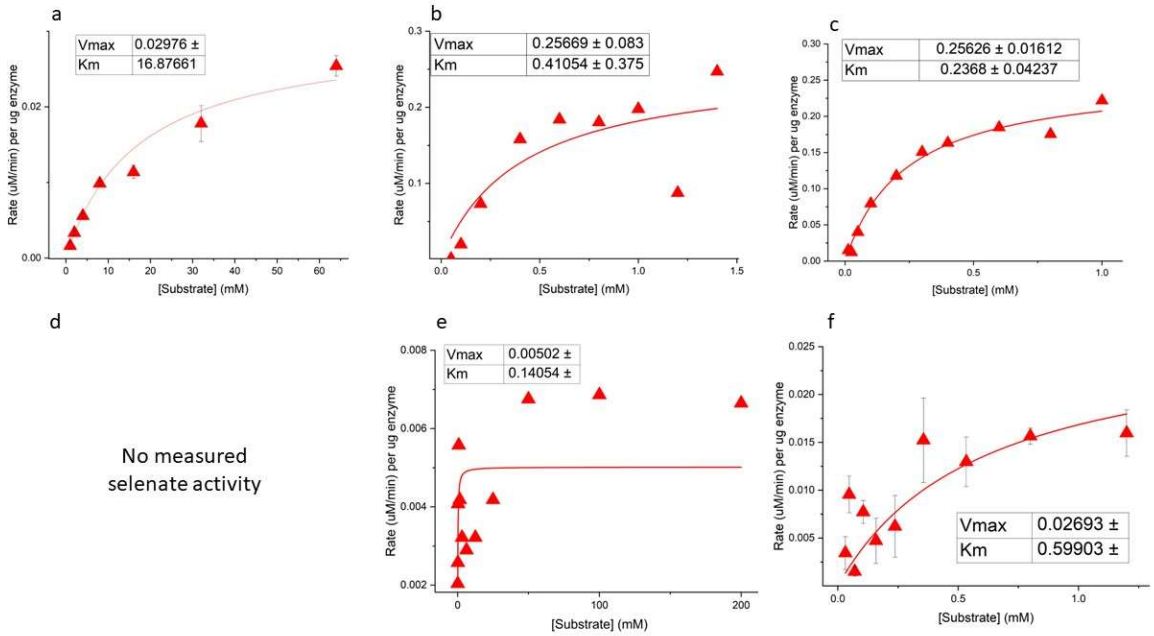

Figure D3*: GRLMR nonlinear regression analysis of a) selenite, b) GSSG, c) GS-Se-SG, d) selenate, e) tellurite, f) GS-Te-SG. For panel e the substrate inhibition aspect of the enzyme mechanism causes a clear under-estimation of* V_{max}.

D3 Protein modeling

Sequences utilized

> WT-GRLMR
MAYDFDLYVIGAGSGGVRAARFAAGFGAKVAVAESRYLGGTCVNVGCVPKKLLVYG
AHFAEDFEQASGFGWNLGEANFDWATLIANKDREINRLNGIYRNLLVNSGVTLHEAHA
KIVGPHEVEVNGERFTAKNILIATGGWPQIPGIPGHEHAIGSNEAFFLKELPKRVLVVGGG
YIAVEFAGIFHGLGANTTLLYRGDLFLRGFDGSVRKHLQEELTKRGLDLQFNADIARIDK
QADGSLKATLKDGRVLEADCVFYATGRRPMLDNLGLENIDVQLDDKGFIKVDGEYQTT
EPSILALGDVIGRVQLTPVALAEGMAVARRLFKPEQYRPVDYKMIPTAVFSLPNIGTVGL
SEEEARECGHEVVIFESRFRPMKLTLTDCQEKTLMKLVVDARTDKVLGCHMVGPDAGE
IVQGLAIALKAGATKRDFDDTIGVHPTAAEEFVTMRTPVSALEHHHHHH:MAYDFDLYV
IGAGSGGVRAARFAAGFGAKVAVAESRYLGGTCVNVGCVPKKLLVYGAHFAEDFEQA
SGFGWNLGEANFDWATLIANKDREINRLNGIYRNLLVNSGVTLHEAHAKIVGPHEVEV
NGERFTAKNILIATGGWPQIPGIPGHEHAIGSNEAFFLKELPKRVLVVGGGYIAVEFAGIF
HGLGANTTLLYRGDLFLRGFDGSVRKHLQEELTKRGLDLQFNADIARIDKQADGSLKAT
LKDGRVLEADCVFYATGRRPMLDNLGLENIDVQLDDKGFIKVDGEYQTTEPSILALGDV
IGRVQLTPVALAEGMAVARRLFKPEQYRPVDYKMIPTAVFSLPNIGTVGLSEEEARECG
HEVVIFESRFRPMKLTLTDCQEKTLMKLVVDARTDKVLGCHMVGPDAGEIVQGLAIAL
KAGATKRDFDDTIGVHPTAAEEFVTMRTPVSALEHHHHHH

> SeR
MAYDFDLYVIGAGSGGVRAARFAAGFGAKVAVAESRYLGGTCVNVGCVPKKLLVYG
AHFAEDFEQASGFGWNLGEANFDWATLIANKDREINRLNGIYRNLLVNSGVTLHEAHA
KIVGPHEVEVNGERFTAKNILIATGGWPQIPGIPGHEHAIGSNEAFFLKELPKRVLVVGGG
YIAVEFAGIFHGLGANTTLLYRGDLFLRGFDGSVRKHLQEELTKRGLDLQFNADIARIDK
QADGSLKATLKDGRVLEADCVFYATGRRPMLDNLGLENIDVQLDDKGFIKVDGEYQTT
EPSILALGDVIGRVQLTPVAHAEGMAVARRLFKPEQYRPVDYKMIPTAVFSLPNIGTVGL
SEEEARECGHEVVIFESRFRPMKLTLTDCQEKTLMKLVVDARTDKVLGCHMVGPEAGEI
VQGLAIALKAGATKRDFDDTIGVHPTAAEEFVTMRTPVSALEHHHHHH:MAYDFDLYVI
GAGSGGVRAARFAAGFGAKVAVAESRYLGGTCVNVGCVPKKLLVYGAHFAEDFEQAS
GFGWNLGEANFDWATLIANKDREINRLNGIYRNLLVNSGVTLHEAHAKIVGPHEVEVN
GERFTAKNILIATGGWPQIPGIPGHEHAIGSNEAFFLKELPKRVLVVGGGYIAVEFAGIFH
GLGANTTLLYRGDLFLRGFDGSVRKHLQEELTKRGLDLQFNADIARIDKQADGSLKATL
KDGRVLEADCVFYATGRRPMLDNLGLENIDVQLDDKGFIKVDGEYQTTEPSILALGDVI
GRVQLTPVAHAEGMAVARRLFKPEQYRPVDYKMIPTAVFSLPNIGTVGLSEEEARECGH
EVVIFESRFRPMKLTLTDCQEKTLMKLVVDARTDKVLGCHMVGPEAGEIVQGLAIALK
AGATKRDFDDTIGVHPTAAEEFVTMRTPVSALEHHHHHH

> mycothione reductase from *rhodococcus erythropolis* (strain PR4/ NBRC 100887)
MTHYDLAIIGSGSGNSLPDERFDGKKIAILEEGTFGGTCLNVGCIPTKMFVYAAEVARTIT
TAEKYGVDATLDGVRWSDIVKRVFGRIDPISAGGERYRSEDSPNTTVYRGHATFTGDKTI
DTGTGETITADQVVIAAGSRPIIPEEIASSGVKYYTNEDIMRLPELPEHLVIVGSGFIATEFA
HVFSALGSRVSIIGRSQRLLRHLDDEISERFTELAEQKWDVHLGSPLTSVRGDGDNIAVEL
ANGTVVSGDVLLVAVGRQPNGDLLGLDKAGVELDDKGSVVVDEYQRTTAEGVFALGD
VSSPYQLKHVANHEARVVQHNLLQDAWKDTSGLRSTDHRFVPAAVFTDPQIADVGMTE
KQARDAGLDITVKVQAYGDVAYGWAMEDQEGICKVIAERGTGRILGAHVMGTQAPTVI
QPLIQAMSFGLSAQDMARGQYWIHPALAEVVENALLGLDI

> mercuric reductase, merA, from *streptomyces lividans*
MLQAHTGYDLAIIGSGAGAFAAAIAARNKGRSVVMVERGTTGGTCVNVGCVPSKALLA
AAEARHGAQAASRFPGIQATEPALDFPALISGKDTLVGQLRAEKYTDLAAEYGWQIVHG
TATFADGPMLEVALNDGGTATVEAAHYLIATGSAPTAPHIDGLDQVDYLTSTTAMELQQL
PEHLLILGGGYVGLEQAQLFARLGSRVTLAVRSRLASREEPEISAGIENIFREEGITVHTRT
QLRAVRRDGEGILATLTGPDGDQQVRASHLLIATGRRSVTNGLGLERVGVKTGERGEVV
VDEYLRTDNPRIWAAGDVTCHPDFVYVAAAHGTLVADNALDGAERTLDYTALPKVTFT
SPAIASVGLTEAQLTEAGIAHQTRTLSLENVPRALVNRDTRGLVKLIAERGTGKLLAAHV
LAEGAGDVITAATYAITAGLTVDQLARTWHPYLTMAEALKLAAQTFTSDVAKLSCCAG

Clustal Omega Sequence Alignment

```
WT_GRLMR                    ----------------------MAYDFDLYVIGAGSGGVRAARFAAGFGAKVAVAESRYL
        38
3O0H,                       MAHHHHHHMGTLEAQTQGPGSMGSFDFDLFVIGSGSGGVRAARLAGALGKRVAIAEEYRI
        60
```

```
4DNA,                   ----------------------XSAFDYDLFVIGGGSGGVRSGRLAAALGKKVAIAEEFRY
        39
1ONF,                   ------------------------MVYDLIVIGGGSGGMAAARRAARHNAKVALVEKSRL
        36
2HQM,                   ---------------YVEFMSTNTKHYDYLVIGGGSGGVASARRAASYGAKTLLVEAKAL
        45
GR_homo                 ------ACRQEPQPQGPPPAAGAVASYDYLVIGGGSGGLASARRAAELGARAAVVESHKL
        54
6B4O,                   --------------------SNAMKTYDYIVIGGGSGGIASANRAGMHGANVLLIEGNEI
        40
6DU7,                   ----------------------MREYDIIAIGGGSGGIATMNRAGEHGAQAAVIEEKKL
        37
5V36,                   -------------------SNAMTKQYDYIVIGGGSGGIASANRAAMHGAKVILFEGKQV
        41
6N7F,                   -------------------SNAMVIPYDYIVIGGGSAGIASANRAAMHGAKVLLAEGKEI
        41
5U1O,                   ---------------SNAMEKVMATHFDYICIGGGSGGIASANRAAMYGAKVALIEAQDL
        45
5VDN,                   ---------SNAMTGYLMETTLMTKHYDYLAIGGGSGGIASINRAAMYGKKCALIEAKQL
        51
1GER,                   ----------------------MTKHYDYIAIGGGSGGIASINRAAMYGQKCALIEAKEL
        38
1GES,                   ----------------------MTKHYDYIAIGGGSGGIASINRAAMYGQKCALIEAKEL
        38
mercuric_reductase,     -------------------MLQAHTGYDLAIIGSGAGAFAAAIAARNKGRSVVMVERGTT
        41
mycothione_reductase    ----------------------MTHYDLAIIGSGSGNSLP--DERFDGKKIAILEEGTF
        35
                                               :*   **.*:.         .  : *

WT_GRLMR                GGTCVNVGCVPKKLLVYGAHFAEDFE-QASGFG------WNLGEANFDWATLIANKDREI
        91
3O0H,                   GGTCVIRGCVPKKLYFYASQYAQEFS-KSIGFG------WKYADPIFNWEKLVAAKNKEI
        113
4DNA,                   GGTCVIRGCVPKKLYVYASQFAEHFE-DAAGFG------WTVGESRFDWAKLVAAKEQEI
        92
1ONF,                   GGTCVNVGCVPKKIMFNAASVHDILE-NSRHYG------FDT-KFSFNLPLLVERRDKYI
        88
2HQM,                   GGTCVNVGCVPKKVMWYASDLATRVS-HANEYGLYQNLPLDKEHLTFNWPEFKQKRDAYV
        104
GR_homo                 GGTCVNVGCVPKKVMWNTAVHSEFMH-DHADYG------FPSCEGKFNWRVIKEKRDAYV
        107
6B4O,                   GGTCVNVGCVPKKVMWQASSMMEMMERDTAGYG------FDVEIKNFSFKQLVENREKYI
        94
6DU7,                   GGTCVNVGCVPKKIMWYGAQIAETFHQFGEDYG------FKTTDLNFDFATLRRNRESYI
        91
5V36,                   GGTCVNVGCVPKKVMWYGAQVAETINNYAADYG------FDVTTQAFHFDVLKQNRQAYI
        95
6N7F,                   GGTCVNLGCVPKKVMWYGAQVADILGTYAKDYG------FDFKEKAFDFKQLKANRQAYI
        95
5U1O,                   GGTCVNVGCVPKKVMWHGAQIAEAMNLYAEDYG------FDVDVKGFDWSKLVESRQAYI
        99
5VDN,                   GGTCVNVGCVPKKVMWHAAQIAEAIHLYGPDYG------FDTTVNHFDWKKLIANRTAYI
        105
1GER,                   GGTCVNVGCVPKKVMWHAAQIREAIHMYGPDYG------FDTTINKFNWETLIASRTAYI
        92
1GES,                   GGTCVNVGCVPKKVMWHAAQIREAIHMYGPDYG------FDTTINKFNWETLIASRTAYI
        92
mercuric_reductase,     GGTCVNVGCVPSKALLAAAEARHGAQAASRFPG------IQATEPALDFPALISGKDTLV
        95
mycothione_reductase    GGTCLNVGCIPTKMFVYAAEVARTITTAEKY-G------VDATLDGVRWSDIVKRVFGRI
        88
                       ****:  **:*.*     :            *            .   :      :
```

```
WT_GRLMR                NRLN---GIYRNLLVNSGVTLHEAHAKIVGPHEVE--------------VNGERFTAKNI
        134
3O0H,                   SRLE---GLYREGLQNSNVHIYESRAVFVDEHTLEL------------SVTGERISAEKI
        158
4DNA,                   ARLE---GLYRKGLANAGAEILDTRAELAGPNTVKL------------LASGKTVTAERI
        137
1ONF,                   QRLN---NIYRQNLSKDKVDLYEGTASFLSENRILIKGTKDNNNKDNGPLNEEILEGRNI
        145
2HQM,                   HRLN---GIYQKNLEKEKVDVVFGWARFNKDGNVEVQ---------KRDNTTEVYSANHI
        152
GR_homo                 SRLN---AIYQNNLTKSHIEIIRGHAAFTSDPKPTI------------EVSGKKYTAPHI
        152
6B4O,                   DFLH---GAYNRGLDSNNIERIHGYATFTGE--QTI------------EVNGTEYTAPHI
        137
6DU7,                   DRAR---SSYDGSFKRNGVDLIEGHAEFVDS--HTV------------SVNGELIRAKHI
        134
5V36,                   DRIH---DSYERGFDSNGVERVYGYATFVDA--HTV------------EVAGEHYTAPHI
        138
6N7F,                   DRIH---ASYERGFEQNGVDRIYDYAVFKDA--HTV------------EIAGQLYTAPHI
        138
5U1O,                   GRIH---QSYDRVLGNNKVNVIKGFAKFVDE--KTV------------EVNGEHYTADHI
        142
5VDN,                   DRIH---QSYERGLGNNKVDVIQGFARFVDA--HTV------------EVNGETITADHI
        148
1GER,                   DRIH---TSYENVLGKNNVDVIKGFARFVDA--KTL------------EVNGETITADHI
        135
1GES,                   DRIH---TSYENVLGKNNVDVIKGFARFVDA--KTL------------EVNGETITADHI
        135
mercuric_reductase,     GQL--RAEKYTDLAAEYGWQIVHGTATFADGPMLEVA---------LNDGGTATVEAAHY
        144
mycothione_reductase    DPISAGGERYRSED-SPNTTVYRGHATFTGDK----T---------IDTGTGETITADQV
        134
                                *               * :                          . .

WT_GRLMR                LIATGGWPQI---PGIPGHEHAIGSNEAFFLKELPKRVLVVGGGYIAVEFAGIFHGLGAN
        191
3O0H,                   LIATGAKIVSN--SAIKGSDLCLTSNEIFDLEKLPKSIVIVGGGYIGVEFANIFHGLGVK
        216
4DNA,                   VIAVGGHPSPH--DALPGHELCITSNEAFDLPALPESILIAGGGYIAVEFANIFHGLGVK
        195
1ONF,                   LIAVGNKPVFP---PVKGIENTISSDEFFNIKES-KKIGIVGSGYIAVELINVIKRLGID
        201
2HQM,                   LVATGGKAIFP--ENIPGFELGTDSDGFFRLEEQPKKVVVVGAGYIGIELAGVFHGLGSE
        210
GR_homo                 LIATGGMPSTPHESQIPGASLGITSDGFFQLEELPGRSVIVGAGYIAVEMAGILSALGSK
        212
6B4O,                   LIATGGRPKKL---GIPGEEYALDSNGFFALEEMPKRVVFVGAGYIAAELAGTLHGLGAE
        194
6DU7,                   VIATGAHPSIP---NIPGAELGGSSDDVFAWEELPESVAILGAGYIAVELAGVLHTFGVK
        191
5V36,                   LIATGGHALLP---DIPGSEYGITSDGFFELDAIPKRTAVVGAGYIAVEISGILHALGSE
        195
6N7F,                   LIATGGHPVFP---DIEGAQYGISSDGFFALDEVPKRTAVVGAGYIAVELAGVLHALGSK
        195
5U1O,                   LIAVGGRPTIP---NIPGAEYGIDSNGFFDLAEQPKRVAVVGAGYIAVEIAGVLHALGTE
        199
5VDN,                   LIATGGRPSHP---DIPGAEYGIDSDGFFELDEMPKRVAVVGAGYIAVEIAGVLNGLGTE
        205
1GER,                   LIATGGRPSHP---DIPGVEYGIDSDGFFALPALPERVAVVGAGYIAVELAGVINGLGAK
        192
1GES,                   LIATGGRPSHP---DIPGVEYGIDSDGFFALPALPERVAVVGAGYIGVELGGVINGLGAK
        192
```

```
mercuric_reductase,        LIATGSAPTAPHIDGLDQVDYL-TSTTAMELQQLPEHLLILGGGYVGLEQAQLFARLGSR
        203
mycothione_reductase       VIAAGSRPIIPEEIASSGVKYY-TNEDIMRLPELPEHLVIVGSGFIATEFAHVFSALGSR
        193
                           ::*.*              .   .  :          . *.*::. *    :  :*

WT_GRLMR                   TTLLYRGDLFLRGFDGSVRKHLQEELTKRGLDLQFNADIARIDKQADGSL-KATLK----
        246
3O0H,                      TTLLHRGDLILRNFDYDLRQLLNDAMVAKGISIIYEATVSQVQSTENCYN-VV-LT----
        270
4DNA,                      TTLIYRGKEILSRFDQDXRRGLHAAXEEKGIRILCEDIIQSVSADADGRR-VATTX----
        250
1ONF,                      SYIFARGNRILRKFDESVINVLENDMKKNNININVTFADVVEIKKVSDKNL-SIHLS----
        256
2HQM,                      THLVIRGETVLRKFDECIQNTITDHYVKEGINVHKLSKIVKVEKNVETDKLKIHMN----
        266
GR_homo                    TSLMIRHDKVLRSFDSMISTNCTEELENAGVEVLKFSQVKEVKKTLSGLE-VSMVTAVPG
        271
6B4O,                      THWAFRHERPLRSFDDMLSEKVVERYQEMGMQIHPNATPAKIEKTAQNEY-VITFE----
        249
6DU7,                      TDLFVRRDRPLRGFDSYIVEGLVKEMERTNLPLHTHKVPVKLEKTTDG-I-TIHFE----
        245
5V36,                      THLFVRRDRPLRKFDKEIVGTLVDEMKKDGPHLHTFSVPKEVIKNTDNSL-TLILE----
        250
6N7F,                      TDLFIRHDRPLRSFDKTIVDVLVDEMAVNGPRLHTHAEVAKVVKNTDESL-TLYLK----
        250
5U1O,                      THLFVRKESPLRSFDPMIIDTLVEVMEAEGPTLHTHSVPKEVVKEADGSL-TLHLE----
        254
5VDN,                      THLFVRKHAPLRTFDPLIVETLLEVMNTEGPKLHTESVPKAVIKNADGSL-TLQLE----
        260
1GER,                      THLFVRKHAPLRSFDPMISETLVEVMNAEGPQLHTNAIPKAVVKNTDGSL-TLELE----
        247
1GES,                      THLFEMFDAPLPSFDPMISETLVEVMNAEGPQLHTNAIPKAVVKNTDGSL-TLELE----
        247
mercuric_reductase,        VTLAVRSRLASRE-EPEISAGIENIFREEGITVHTRTQLRAVRRDGEGILATLT------
        256
mycothione_reductase       VSIIGRSQRLLRHLDDEISERFT-ELAEQKWDVHLGSPLTSVRGDGDNIAVELA------
        246
                                       :                 :       :    .

WT_GRLMR                   ----DGRVLEADCVFYATGRRPMLDNLGLENIDVQLDDKGFIKVDGEYQTTEPSILALGD
        302
3O0H,                      ----NGQTICADRVMLATGRVPNTTGLGLERAGVKVNEFGAVVVDEKMTTNVSHIWAVGD
        326
4DNA,                      ----KHGEIVADQVXLALGRXPNTNGLGLEAAGVRTNELGAIIVDAFSRTSTPGIYALGD
        306
1ONF,                      ---DGRIYEHFDHVIYCVGRSPDTENLKLEKLNVETN-NNYIVVDENQRTSVNNIYAVGD
        312
2HQM,                      ---DSKSIDDVDELIWTIGRKSHL-GMGSENVGIKLNSHDQIIADEYQNTNVPNIYSLGD
        322
GR_homo                    RLPVMTMIPDVDCLLWAIGRVPNTKDLSLNKLGIQTDDKGHIIVDEFQNTNVKGIYAVGD
        331
6B4O,                      ----NGESITTDAVIFGTGRQPNTDQLGLENTKVALDEKGYVKVDKFQNTTQNGIYAVGD
        305
6DU7,                      ----DGTSHTASQVIWATGRRPNVKGLQLEKAGVTLNERGFIQVDEYQNTVVEGIYALGD
        301
5V36,                      ----NGEEYTVDTLIWAIGRAANTKGFNLEVTGVTLDSRGFIATDAFENTNVEGLYALGD
        306
6N7F,                      ----DGQEVEVDQLIWAIGRKPNLEGFSLDKTGVTLNDKGYIETDAYENTSVKGIYAVGD
        306
5U1O,                      ----NGESQNVDQLIWAIGRHPATDAINLASTGVATNEKGYIKVDEYQETNVKGIYCVGD
        310
```

```
5VDN,                    ----NGTEVTVDHLIWAIGREPATDNLNLSVTGVKTNDKGYIEVDKFQNTNVKGIYAVGD
        316
1GER,                    ----DGRSETVDCLIWAIGREPANDNINLEAAGVKTNEKGYIVVDKYQNTNIEGIYAVGD
        303
1GES,                    ----DGRSETVDCLIWAIGREPANDNINLEAAGVKTNEKGYIVVDKYQNTNIEGIYAVGD
        303
mercuric_reductase,      -GPDGDQQVRASHLLIATGRRSVTNGLGLERVGVKTGERGEVVVDEYLRTDNPRIWAAGD
        315
mycothione_reductase     -N---GTVVSGDVLLVAVGRQPNGDLLGLDKAGVELDDKGSVVVDEYQRTTAEGVFALGD
        302
                                   . :    **     :     :  . . : .*    *    : . **

WT_GRLMR                 V-I---------------------------------GRVQLTPVALAEGMAVARRLFKPE
        328
3O0H,                    V-T---------------------------------GHIQLTPVAIHDAMCFVKNAFENT
        352
4DNA,                    V-T---------------------------------DRVQLTPVAIHEAXCFIETEYKNN
        332
1ONF,                    CCMVKKSKEIEDLNLLKLYNEERYLNKKENVTEDIFYNVQLTPVAINAGRLLADRLFLKK
        372
2HQM,                    V-V---------------------------------GKVELTPVAIAAGRKLSNRLFGPE
        348
GR_homo                  V-C---------------------------------GKALLTPVAIAAGRKLAHRLFEYK
        357
6B4O,                    V-I---------------------------------GKIDLTPVAIAAGRRLSERLFNGQ
        331
6DU7,                    V-T---------------------------------GEKELTPVAIKAGRTLSERLFNGK
        327
5V36,                    V-N---------------------------------GKLELTPVAVKAGRQLSERLFNHK
        332
6N7F,                    V-N---------------------------------GKLALTPVAVAAGRRLSERLFNGK
        332
5U1O,                    IME---------------------------------GGIELTPVAVKAGRQLSERLFNNK
        337
5VDN,                    N-T---------------------------------GVVELTPVAVAAGRRLSERLFNNK
        342
1GER,                    N-T---------------------------------GAVELTPVAVAAGRRLSERLFNNK
        329
1GES,                    N-T---------------------------------GAVELTPVAVAAGRRLSERLFNNK
        329
mercuric_reductase,      V-T---------------------------------CHPDFVYVAAAHGTLVADNALDG-
        340
mycothione_reductase     V-S---------------------------------SPYQLKHVANHEARVVQHNLLQDA
        328
                                                             :  **   . .

WT_GRLMR                 -----QYRPVDYKMIPTAVFSLPNIGTVGLSEEEARECGH--EVVIFESRFRPMKLTLT-
        380
3O0H,                    -----ST-TPDYDLITTAVFSQPEIGTVGLSEEDALHRYK--RVEIYRTVFRPMRNVLS-
        403
4DNA,                    -----PT-SPDHDLIATAVFSQPEIGTVGITEEEAARKFQ--EIEVYRAEFRPXKATLS-
        383
1ONF,                    ------TRKTNYKLIPTVIFSHPPIGTIGLSEEAAIQIYGKENVKIYESKFTNLFFSVYD
        426
2HQM,                    K---FRNDKLDYENVPSVIFSHPEAGSIGISEKEAIEKYGKENIKVYNSKFTAMYYAML-
        404
GR_homo                  -----EDSKLDYNNIPTVVFSHPPIGTVGLTEDEAIHKYGIENVKTYSTSFTPMYHAVT-
        411
6B4O,                    -----TDLYLDYNLVPTVVFTHPPVATIGLTEKAALEEYGEDQVKIYRSSFTPMYFALG-
        385
6DU7,                    -----TTAKMDYSTIPTVVFSHPAIGTVGLTEEQAIKEYGQDQIKVYKSSFASMYSACT-
        381
```

```
5V36,                    -----PQAKMDYKDVATVIFSHPVIGSIGLSEEAALDQYGEENVTVYRSTFTSMYTAVT-
        386
6N7F,                    -----TDEKLDYQNVATVIFSHPVIGSVGLSEEAAVKQYGQEAVKTYQSRFTSMFTAIT-
        386
5U1O,                    -----PNAKMDYDLVPTVVFSHPPIGTIGLTTQEAEEKYGKDNIKVYTSGFTAMYTAVT-
        391
5VDN,                    -----PDEHLDYSNIPTVVFSHPPIGTIGLTEPQAREKFGDDQVKVYTSSFTAMYSAVT-
        396
1GER,                    -----PDEHLDYSNIPTVVFSHPPIGTVGLTEPQAREQYGDDQVKVYKSSFTAMYTAVT-
        383
1GES,                    -----PDEHLDYSNIPTVVFSHPPIGTVGLTEPQAREQYGDDQVKVYKSSFTAMYTAVT-
        383
mercuric_reductase,      -----AERTLDYTALPKVTFTSPAIASVGLTEAQLTEAGIAHQTRTLS--LENVPRALV-
        392
mycothione_reductase     WKDTSGLRSTDHRFVPAAVFTDPQIADVGMTEKQARDAGLDITVKVQA--YGDVAYGWA-
        385
                                   ::  :  . *: *  . :*::

WT_GRLMR                 ---DCQEKTLMKLVVDARTDKVLGCHMVGPDAGEIVQGLAIALKAGATKRDFDDTI-GVH
        436
3O0H,                    ---GSPEKMFMKLVVDGESRIVVGAHVLGENAGEIAQLIGISLKGKLTKDIFDKTM-AVH
        459
4DNA,                    ---GRKEKTIXKLVVNAADRKVVGAHILGHDAGEXAQLLGISLRAGCTKDDFDRTX-AVH
        439
1ONF,                    IEPELKEKTYLKLVCVGKDELIKGLHIIGLNADEIVQGFAVALKMNATKKDFDETI-PIH
        485
2HQM,                    ---SEKSPTRYKIVCAGPNEKVVGLHIVGDSSAEILQGFGVAIKMGATKADFDNCV-AIH
        460
GR_homo                  ---KRKTKCVMKMVCANKEEKVVGIHMQGLGCDEMLQGFAVAVKMGATKADFDNTV-AIH
        467
6B4O,                    ---EYRQKCDMKLICVGKEEKIVGLHGIGIGVDEMLQGFAVAIKMGATKADFDNTV-AIH
        441
6DU7,                    ---RNRQESRFKLITAGSEEKVVGLHGIGYGVDEMIQGFAVAIKMGATKADFDATV-AIH
        437
5V36,                    ---SHRQACKMKLVTVGEDEKIVGLHGIGYGVDEMIQGFAVAIKMGATKADFDNTV-AIH
        442
6N7F,                    ---NHRQPCLMKLVTVGDTEKIVGLHGIGYGVDEMIQGFAVAIKMGATKADFDNTV-AIH
        442
5U1O,                    ---KHRQPCKMKLVCAGEEETVVGLHGIGFTVDEMIQGFGVAMKMGATKADFDSVV-AIH
        447
5VDN,                    ---QHRQPCRMKLVCVGAEEKIVGIHGIGFGMDEILQGFAVAMKMGATKKDFDNTV-AIH
        452
1GER,                    ---THRQPCRMKLVCVGSEEKIVGIHGIGFGMDEMLQGFAVALKMGATKKDFDNTV-AIH
        439
1GES,                    ---THRQPCRMKLVCVGSEEKIVGIHGIGFGMDEMLQGFAVALKMGATKKDFDNTV-AIH
        439
mercuric_reductase,      ---NRDTRGLVKLIAERGTGKLLAAHVLAEGAGDVITAATYAITAGLTVDQLART--W-H
        446
mycothione_reductase     ---MEDQEGICKVIAERGTGRILGAHVMGTQAPTVIQPLIQAMSFGLSAQDMARGQYWIH
        442
                                    *::       : . *  .           ::    :   :       *

WT_GRLMR                 PTAAEE-FVTMRTPVSAGS----------    454
3O0H,                    PTMSEE-LVTMYKPSYVYENGEKLDN---    484
4DNA,                    PTAAEE-LVTXYQPSYRVRNGERVG----    463
1ONF,                    PTAAEE-FLTLQPWMK-------------    500
2HQM,                    PTSAEE-LVTMRGSHHHHHH---------    479
GR_homo                  PTSSEE-LVTLR-----------------    478
6B4O,                    PTGSEE-FVTMR-----------------    452
6DU7,                    PTSSEE-FVTMR-----------------    448
5V36,                    PTGSEE-FVTMR-----------------    453
6N7F,                    PTGSEE-FVTMR-----------------    453
5U1O,                    PTGSEE-FVTMR-----------------    458
```

```
5VDN,                    PTAAEE-FVTMR-----------------    463
1GER,                    PTAAEE-FVTMR-----------------    450
1GES,                    PTAAEE-FVTMR-----------------    450
mercuric_reductase,      PYLTMAEALKLAAQ-TFTSDVAKLSCCAG    474
mycothione_reductase     PALA--EVVENA---LLGLDI--------    458
                         *  :    :
```

AlphaFold modeling

A)

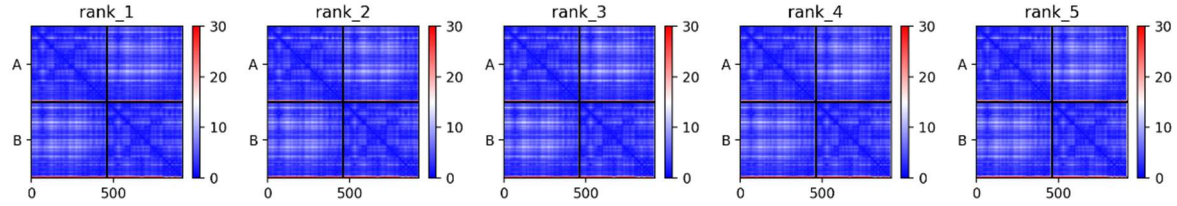

B)

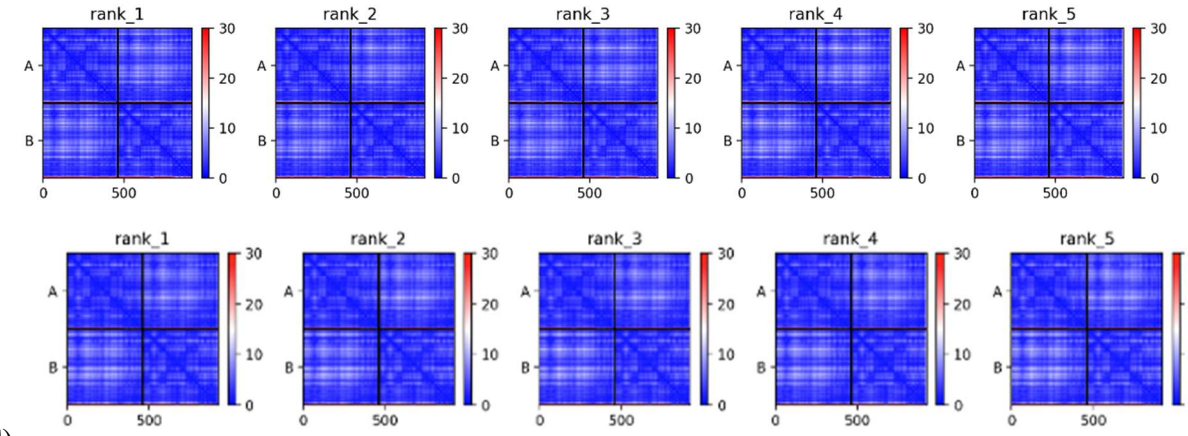

C)

D)

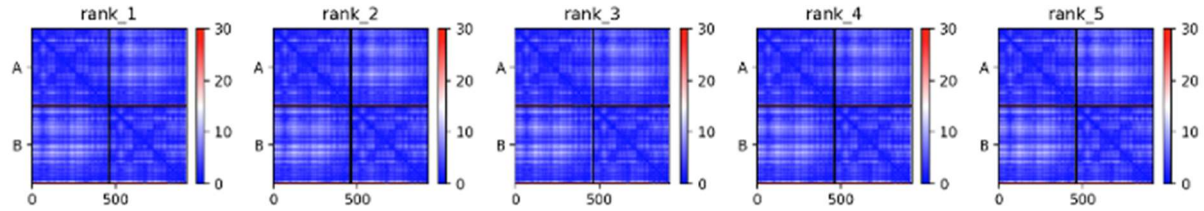

Figure D4. *The PAE scores are plotted for each of the five alphafold2 ranked models generated for (A) GRLMR with templates, (B) SeR with templates, (C) GRLMR without templates, (D) SeR without templates. Each axis corresponds to individual amino acid positions and "A" and "B" indicate the chain ID. These plots are separated into four quadrants. The top left quadrant corresponds to residue distance errors between residues within chain A, top right to chain A residues and chain B residues, bottom left in chain B residues to chain A and lower right one represents errors within residues in chain B. The error is displayed on a color spectrum going from blue (0 angstroms) to white (15 angstroms) to red (30 angstroms). A) the wildtype metrics and B) the SeR metrics. There are low PAE scores overall with the highest error consistently being at the C-termini of both chains with respect to all of the rest of the residues (two horizontal red lines at the bottom of all four quadrants). There are also some white shaded regions in the two quadrants which would relate chains A and B relative errors but within a single chain the PAE are very low (almost a block of blue shading).*

***Table D1**: pLDDT scores for each of 5 models generated for GRLMR and SeR with templates.*

GRLMR	Average alpha-Carbon pLDDT	Average PAE (angstroms)
Rank 1 model 5	96.54	4.61
Rank 2 model 3	96.17	4.76
Rank 3 model 1	96.36	4.74
Rank 4 model 4	96.40	4.78
Rank 5 model 2	96.29	4.85
SeR	Average alpha-Carbon pLDDT	Average PAE (angstroms)
Rank 1 model 3	96.22	4.72
Rank 2 model 5	96.48	4.62
Rank 3 model 4	96.43	4.71
Rank 4 model 1	96.38	4.75
Rank 5 model 2	96.26	4.87

***Table D2**: pLDDT scores for each of 5 models generated for GRLMR and SeR without templates*

GRLMR	Avg plddt	Average PAE (angstroms)
Rank 1 model 3	95.99	4.71
Rank 2 model 5	96.34	4.72
Rank 3 model 1	96.45	4.69
Rank 4 model 4	96.40	4.75
Rank 5 model 2	96.17	4.94
SeR	Avg plddt	Average PAE (angstroms)
Rank 1 model 3	96.25	4.72
Rank 2 model 5	96.30	4.76
Rank 3 model 1	96.45	4.70
Rank 4 model 4	96.37	4.82
Rank 5 model 2	96.10	5.00